Catarina Sofia Henriques de Jesus

KINETICS AND ENERGETICS OF FUNDAMENTAL EVENTS IN PEPTIDE AND PROTEIN (UN)FOLDING

Tese de Doutoramento em Química, especialidade Química Biológica,
orientada por Professor Doutor Rui Manuel Pontes Meireles Ferreira de Brito
e por Doutor Carlos Alberto Lourenço da Serpa Soares e apresentada
à Faculdade de Ciências e Tecnologia da Universidade de Coimbra

Coimbra 2013

· U C ·

UNIVERSIDADE DE COIMBRA

Catarina Sofia Henriques de Jesus

KINETICS AND ENERGETICS OF FUNDAMENTAL EVENTS IN PEPTIDE AND PROTEIN (UN)FOLDING

Coimbra 2013

· U   C ·

UNIVERSIDADE DE COIMBRA

Catarina Sofia Henriques de Jesus

CINÉTICA E ENERGÉTICA DE EVENTOS FUNDAMENTAIS NO (DES)ENROLAMENTO DE PEPTÍDEOS E PROTEÍNAS

Tese de Doutoramento em Química, especialidade Química Biológica,
orientada por Professor Doutor Rui Manuel Pontes Meireles Ferreira de Brito
e por Doutor Carlos Alberto Lourenço da Serpa Soares e apresentada
à Faculdade de Ciências e Tecnologia da Universidade de Coimbra

Coimbra 2013

· U C ·

UNIVERSIDADE DE COIMBRA

Aos meus Pais e ao meu Irmão,
pelo carinho e pelo exemplo de coragem,
força e determinação perante tantas adversidades...

À memória do meu Pai,
simplesmente porque embora
ausente estará sempre Presente!

This thesis is based on the following in manuscripts:

Jesus, C. S. H., Vaz, D. C., Saraiva, M. J. M., & Brito, R. M. M. (2012). The V30M Amyloidogenic Mutation Decreases the Rate of Refolding Kinetics of the Tetrameric Protein Transthyretin. *Spectroscopy: An International Journal*, *27*(5-6), 343–348. doi:10.1155/2012/502497

Jesus, C. S. H., De Almeida, Z. L., Vaz, D. C., Saraiva M. J. M., & Brito, R. M. M. Transthyretin Folding Kinetics: Could Slower Refolding Imply Enhanced Amyloidogenicity? (*In preparation*)

Jesus, C. S. H., Nunes, R. M. D., Brito, R. M. M., Luís G. Arnaut, L. G., Serpa, C. Amino acids structural volume changes upon photoinduced pH jump (*In preparation*)

Jesus, C. S. H., Cruz, P. F., Brito, R. M. M., Serpa, C. Role of ionizable residues on α-helix conformational stability and folding dynamics (*In preparation*)

Contributions to the following work, not include in the thesis, were also made:

Harley, C. A., Jesus, C. S. H., Carvalho, R., Brito, R. M. M., & Morais-Cabral, J. H. (2012). Changes in channel trafficking and protein stability caused by LQT2 mutations in the PAS domain of the HERG channel. *PloS One*, *7*(3), e32654. doi:10.1371/journal.pone.0032654

Maia, J., Vazão, H., Pedroso, D. C. S., Jesus, C. S. H., Brito, R. M. M., Grãos, M., Gil, M. H., Ferreira, L. (2012). VEGF-functionalized dextran has longer intracellular bioactivity than VEGF in endothelial cells. *Biomacromolecules*, *13*(9), 2906–16. doi:10.1021/bm3009268

Jesus, C. S. H., Henriques, E. S., Simões, C. J. V., Moniz, C. V. S., Cruz, P. F., Velázquez-Campoy, A. & Brito, R. M. M. Binding Energetics of Four Transthyretin Stabilizers: guidelines for the rational design of anti-amyloid agents (*In preparation*)

Acknowledgments / Agradecimentos

Gostaria de agradecer aos meus orientadores Professor Rui Brito e Doutor Carlos Serpa pela disponibilidade para a orientação do projecto de doutoramento reunindo os conhecimentos da área de bioquímica e da fotoquímica. Em particular, agradeço ao Professor Rui Brito pela oportunidade de contactar com uma grande diversidade de técnicas, e pela oportunidade de participar em diferentes projectos de investigação, incluindo visita a laboratórios ao estrangeiro da Universidade de Saragoça e da Universidade de Leeds. Ao Doutor Carlos Serpa agradeço a sua total disponibilidade quer na orientação do trabalho quer na ajuda de resolução de problemas nas experiências de PAC, interpretação de resultados, e por sempre transmitir todo o seu entusiasmo e positivismo.

Ao Professor Arnaut agradeço a disponibilidade para discussão de resultados e todas as questões e críticas pertinentes que motivaram novas experiências e permitiram a evolução do trabalho de PAC. Ao Fábio Schaberle e ao Rui Nunes agradeço a disponibilidade para me ajudarem quer na montagem da PAC, quer na resolução dos diversos problemas experimentais que foram surgindo.

A special thanks to Adrián Velazquez-Campoy for his hospitality on my visits to University of Saragoça and for his supervision and help in all the isothermal titration calorimetry experiments.

I would like to thank to the supervision of Professor Sheena Radford, Professor Allison Ashcroft, and specially to Charlotte for the help in the mass spectrometry lab, during my visit to their group in the University of Leeds.

Aos meus colegas de trabalho pela colaboração na resolução de diversos problemas. Em particular, à Cândida pela ajuda a nível da Matemática e da Química Computacional e ao Pedro na ajuda das experiências de RMN, interpretação de resultados, e a disponibilidade para ser "bombardeado" com perguntas sobre RMN. Agradeço também à Elsa por todas as explicações sobre Química Computacional e ajuda durante a sua estadia pelo RMBLab…e também pela sua paciência para as nossas brincadeiras! É claro que também não posso deixar de relembrar todas as pausas divertidas no horário de café

com o *núcleo* Cândida, Pedro e Zaida e quem mais estivesse presente…claro está que a nossa série "The Lab!" está destinada ao sucesso. Também a todos os outros elementos do RMBLab ao longo destes últimos anos: o chefinho Tiago, Daniela, Nuno, Carlos, Raquel, Cláudia, …

Às minhas antigas colegas de casa e amigas de longa data Lucy, Patrícia e Daniela por todas as conversas divertidas, agradáveis e relaxantes após um longo dia no laboratório! Pelo apoio incondicional, pelas aventuras e principalmente pela amizade. À Sandra e à Isabel por estarem sempre no sítio certo à altura certa….obrigada pelo apoio!

Aos meus Pais e ao meu Irmão por todo o amor, amizade, coragem e força perante tantas adversidades… Ao meu Pai que embora agora ausente está sempre presente em tudo o que faço…obrigada pelo exemplo de força, coragem, capacidade de luta e pela vontade de viver! À minha Mãe e ao meu Manito por todo o apoio ao longo destes anos, por serem um verdadeiro suporte, um exemplo de coragem e uma fonte de inspiração. Ao João por todo o carinho, apoio e paciência infinita ao longo dos últimos anos.

Contents

Abstract

One of the major challenges in the field of biophysical chemistry is the study of the mechanisms of protein folding, i.e., how an unstructured polypeptide chain can rapidly adopt an unique, densely packed, three-dimensional structure. Modifications in the folding kinetics and transitions to "misfolded" states are thought to be involved in the pathogenesis of many diseases commonly known as conformational disorders, including cystic fibrosis, type II diabetes, Alzheimer's and Parkinson's diseases. The global folding of proteins typically occurs in the millisecond to second time scale, but the underlying fundamental molecular events such as β-hairpin or α-helix folding occur in the microsecond or faster time scale. The methods generally employed for studying folding or unfolding kinetics are typically limited to the time range of milliseconds or slower because the process usually involves mixing buffers in stopped-flow apparatus. A new generation of kinetic experiments has emerged to investigate the mechanisms of protein folding on the previously inaccessible sub-millisecond time scale. As a result, the earliest conformational events related to folding, occurring within microseconds or less may now be measured experimentally and interpreted. Laser-triggered fast initiation of the folding/unfolding reaction coupled with fast detection techniques provides the tools to probe these events in detail.

As the native conformations of peptides and proteins are normally sensitive to pH, conformational changes can be initiated by a pH change. Here, we propose to use a laser-triggered pH change, which provides an interesting way to probe the early events in protein folding/unfolding. With this technique, the pH jump occurs in few a nanoseconds and lasts for several milliseconds. This fast proton gradient protonates/deprotonates ionizable residues of a protein or peptide producing different charged species, and consequently conformational changes. Photothermal methods, like time-resolved photoacoustic calorimetry (TR-PAC) have the ability to measure accurately enthalpy and molar volume changes for reactions occurring with lifetimes in the nanoseconds to tens of microsecond time range. TR-PAC is likely the technique of choice to study fast events in protein folding when a spectroscopic technique is not applicable either because the intermediates are "dark" or too short lived. In this work, we proposed to use a pH-jump methodology to trigger the folding/unfolding events, coupled with TR-PAC to monitor the energetics and kinetics of pH-dependent folding/unfolding of peptides and proteins.

Throughout this thesis, simple molecules such as amino acid models, an α-helical peptide and proteins were subjects of study to investigate protein folding, using a combination of pH-jump and TR-PAC detection, and fluorescence spectroscopy. Complementary equilibrium structural information was obtained by methodologies such as nuclear magnetic resonance (NMR) and circular dichroism (CD). In the first stage, the association of pH-jump and TR-PAC detection was used to investigate the protonation of amino acids models, which corresponds to the earliest step in protein or peptide pH-induced folding/unfolding events. Our results suggest that the protonation of negatively charged carboxylic acids is accompanied by a volume expansion, while the protonation of the uncharged inidazole groups leads to a volume contraction. On a second stage, a small peptide similar to the C-peptide of RNase A, forming a stable α-helix in aqueous solution, was selected as a model system to explore the energetics and dynamics of α-helix formation. The C-peptide analogue investigated was RN80 synthesized with specific side-chain interactions, namely a salt-bridge and a π-stacking interaction that contributes to the α-helix stability. Finally, we proposed the application of these methods to the study of proteins, searching for intermediate states during their folding/unfolding processes, such as molten globule states. As a protein system model, bovine serum albumin (BSA) has been selected because it undergoes partial unfolding transitions under acid conditions.

In a parallel effort, the influence of refolding kinetics on amyloid formation by transthyretin (TTR) variants was studied. TTR is a homotetramer and one of the many proteins known to be involved in human amyloid diseases. Numerous studies showed that dissociation of the native tetrameric structure into partially unfolded monomeric species precedes amyloid formation. Since the small structural differences observed in the crystal structures of TTR variants do not seem to justify their varying amyloidogenic potential, a significant effort has been devoted to search for thermodynamic and kinetic factors that may play a critical role on TTR stability, in order to fully understand the molecular mechanism of amyloid formation by TTR. Here, we have performed refolding kinetics assays, using intrinsic tryptophan fluorescence, with WT-TTR and its most common amyloidogenic variant V30M-TTR, to investigate the potential role of refolding kinetics on amyloid formation by TTR. Our results show that, in conditions close to physiological, tetramerization of the amyloidogenic variant occurs at a rate significantly slower than WT-TTR.

Resumo

Um dos maiores desafios na área da biofísica é o estudo de mecanismos de enrolamento de proteínas, isto é, como é que uma cadeia polipetídica se enrola rapidamente adquirindo a estrutura tridimensional nativa. Alterações na cinética de enrolamento e transições para estados conformacionais não funcionais ou incorrectos estão envolvidas na patogenia de doenças graves como fibrose cística, diabetes de tipo II, e doenças de Alzheimer e de Parkinson. Tipicamente, o enrolamento global de proteínas ocorre numa escala de tempo entre os milisegundos e os segundos. No entanto, eventos fundamentais no processo de enrolamento, tal como a formação de elementos de estrutura secundária como α-hélices e folhas-β, ocorrem na gama temporal dos microsegundos ou menos. Apesar das técnicas experimentais tradicionalmente aplicadas no estudo da cinética de enrolamento/desenrolamento de proteínas estarem limitados à escala de tempo dos milisegundos, nas últimas décadas foi desenvolvida uma nova geração de experiências para investigar estes processos na escala dos sub-milisegundos. Nomeadamente, técnicas baseadas no uso de fontes de irradiação rápidas (lasers) que provocam uma mudança súbita das condições do meio e promovem o enrolamento/desenrolamento, tornando possível investigar em detalhe os eventos fundamentais nestes processos.

A conformação nativa de uma cadeia polipeptídica é normalmente sensível ao pH, e a dinâmica entre duas condições de pH pode ser explorada usando uma variação súbita de pH. Neste trabalho, propomos a utilização de uma variação súbita de pH fazendo incidir um pulso de luz laser sobre uma molécula que liberte protões rapidamente. Esta variação de pH ocorre em poucos nanosegundos e induz a protonação dos resíduos de aminoácidos, promovendo de seguida o processo de enrolamento/desenrolamento. Métodos de detecção como a calorimetria fotoacústica resolvida no tempo (TR-PAC) permitem determinar mudanças de volume e deposições rápidas de calor em solução que ocorrem na escala de tempo entre os nanosegundos e os microsegundos. Esta técnica pode ser particularmente útil quando as técnicas espectroscópicas não são apropriadas porque os intermediários não são detectáveis ou porque têm tempos de vida muito curtos. Assim, a combinação de TR-PAC com o rápido salto de pH apresenta potencialidades excepcionais para a monitorização da cinética e a energética das primeiras etapas do enrolamento/desenrolamento de proteínas.

Neste trabalho, diversas moléculas foram objecto de estudo, incluindo moléculas modelo de aminoácidos, um peptídeo com estrutura em α-hélice e proteínas. As duas metodologias aplicadas para explorar a cinética, nomeadamente a combinação de TR-PAC com o rápido salto de pH e a espectroscopia de fluorescência. Outras técnicas, como ressonância magnética nuclear (RMN) e dicroísmo circular (CD), foram utilizadas para obter informação estrutural.

Numa primeira fase, a combinação da técnica TR-PAC e o salto de pH foi utilizada para investigar a protonação de moléculas modelo de aminoácidos, uma vez que a protonação dos aminoácidos é o primeiro evento observado com uma variação súbita de pH. Enquanto que a protonação grupos carboxílicos promovem uma expansão de volume, a protonação do grupo imidazole no aminoácido modelo da histidina é caracterizada por uma contracção de volume. Numa segunda fase, o peptídeo RN80 que apresenta estrutura estável em α-hélice foi seleccionado como um sistema modelo para investigar a energética e dinâmica da formação de α-hélices. Este peptídeo possui interacções específicas entre cadeias laterais, nomeadamente uma ponte salina e uma interacção de emparelhamento entre anéis que contribuem para a estabilização da α-hélice em solução aquosa. Por fim, aplicámos estas metodologias ao estudo de proteínas para investigar estados intermediários no processo de enrolamento/desenrolamento. Como proteína modelo, foi seleccionada a albumina do soro bovino (BSA) que sofre alterações para estados conformacionais parcialmente desenrolados em diferentes pHs.

Paralelamente, de forma a explorar o efeito da cinética de enrolamento na formação de amilóide foram realizados estudos com a proteína homotetramérica transtirretina (TTR), que é uma das muitas proteínas envolvidas em doenças amilóides. Vários estudos demonstraram que ocorre a dissociação dos tetrâmeros em espécies monoméricas parcialmente desenroladas, que subsequentemente agregam, originando oligómeros solúveis e posteriormente fibras amilóides. As estruturas de diversas variantes de TTR revelam pequenas diferenças que não justificam a variação no potencial amiloidogénico. Assim, tem sido feito um esforço na procura de factores cinéticos e termodinâmicos que desempenhem um papel importante na estabilidade da TTR, de forma a compreender em detalhe o mecanismo molecular associado à formação de amilóide. Usando a técnica de fluorescência intrínseca, foram comparadas as cinéticas de enrolamento da TTR normal e da variante amiloidogénica V30M-TTR e possível relação com o potencial amiloidogénico. Os resultados revelaram que a cinética de enrolamento da variante amiloidogénica é mais lenta.

List of abbreviations

ApoMb	Apomyoglobin
BP	Bromocresol purple
BSA	Bovine serum albumin
BSE	Bovine spongiform encephalopathy
CD	Circular dichroism
Con-T	Conantokin-T
COSY	Correlated spectroscopy
DQF	Double quantum filtered
EPR	Pulsed electron paramagnetic resonance
FAC	Familial amyloid cardiomyopathy
FAP	Familial amyloidotic polyneuropathy
FRET	Foster resonance energy transfer
GdmSCN	Guanidinium thiocyanide
GuHCl	Guanidinium chloride
HSA	Human serum albumin
IL-4	Interleukin-4
IR	Infrared spectroscopy
L55P-TTR	Transthyretin with a proline replacing a leucine in position 55
NMR	Nuclear magnetic resonance
o-NBA	*ortho*-nitrobenzaldehyde
PAC	Photoacoustic calorimetry
PAT	Photoacoustic tomography
PLG	Poly-L-glutamic acid
PLL	Poly-L-lysine
RBP	Retinol binding protein
RNase A	Bovine pancreatic ribonuclease A
ROESY	Rotating-frame nuclear overhauser effect correlation spectroscopy
SAXS	Small-angle X-ray scattering
SSA	Senile systemic amyloidosis
STD-NMR	Saturation transfer difference NMR
T119M	Transthyretin with a methionine replacing a threonine in position 119

T_4	Thyroxine
T-Jump	Temperature jump
TOCSY	Total correlated spectroscopy
TR-PAC	Time-resolved photoacoustic calorimetry
TTR	Transthyretin
V122I	Transthyretin with an isoleucine replacing a valine in position 122
V30M-TTR	Transthyretin with a methionine replacing a valine in position 30
WT-TTR	Wild-type transthyretin
Y78P	Transthyretin with a proline replacing a tyrosine in position 78

Chapter 1

Objectives and Thesis Outline

The general objective of the present study was to characterize the early molecular events in protein folding and unfolding. The understanding of the energetics and kinetics of these fundamental first events will certainly contribute to a deeper understanding of the overall protein folding and unfolding processes. In order to probe the very fast early events in protein folding and unfolding, we used time-resolved photoacoustic calorimetry (TR-PAC) coupled with a laser triggered pH-jump technique to initiate the folding or unfolding processes of the biomolecules under study. This allowed to characterize kinetics, enthalpy and volume changes upon folding/unfolding, in model peptides and in proteins. To characterize the equilibrium conformational states of the biomolecules, at several pHs, we used two-dimensional homonuclear magnetic resonance (2D-NMR) and circular dichroism (CD). We have applied these methodologies first to amino acid models and then to a α-helical model peptide and a α-helix rich protein. Furthermore, experiments conducted with a conventional method to measure protein folding - intrinsic tryptophan fluorescence - emphasizes differences in the folding rates of two transthyretin (TTR) variants, which may be related with their amyloidogenic potential.

The work developed focused on four main points:

1. Establishing the experimental setup necessary to perform laser induced pH-jump experiments coupled with time-resolved photoacoustic calorimetry detection in aqueous solutions, and apply the methodology to the study of simple molecules, namely ionizable amino acid models.

2. Investigating folding/unfolding events on α-helices using a small model peptide similar to the C-peptide, a protein fragment from the protein bovine pancreatic ribonuclease A (RNase A) forming a stable α-helix in aqueous solution, previously characterized by NMR and CD. Analyse the role of specific interactions such as salt-bridges and π-stacking interactions on the α-helix folding/unfolding kinetics and stability.

3. Applying our methodology to more complex biological systems, such as the study of early events of folding/unfolding in proteins. As a system model we used bovine serum albumin (BSA), which undergoes a partial unfolding transition at low pH, losing a fraction of its α-helical content.

4. Investigating a possible relation between folding rates and amyloid formation propensity. As a case study we compared the folding rates of wild-type transthyretin (WT-TTR) and one of its most common amyloidogenic variants, V30M-TTR. Intrinsic tryptophan fluorescence was the detection method selected to follow the refolding kinetics of both TTR variants.

The thesis consists of eight chapters, including a general introduction and a final chapter containing an overall discussion, conclusions, and perspectives. A more detailed description of the main chapters follows.

Chapter 2 gives a brief introduction on proteins, the complexity of the protein folding problem and how it can be dissected by studying early events in protein folding such as the formation of regular secondary structural elements, including α-helices and *β*-structures. A short glimpse on theoretical models developed to explain protein folding and experimental strategies currently employed are also presented. The relation between protein misfolding and disease is highlighted, in particular the amyloid diseases promoted by the homotetrameric protein transthyretin and its variants.

Chapter 3 describes the theoretical background of the main detection method employed throughout the thesis, time-resolved photoacoustic calorimetry (TR-PAC), along with relevant methodological issues such as the experimental setup, analysis of time-resolved photoacoustic data, as well as, the principal properties of photocalorimetric reference compounds, especially required for acoustic detection. In addition, the chapter aims to give an introduction in the combination of laser-induced pH jump with TR-PAC, which enables the study of folding processes on the nanosecond and microsecond timescales. The mechanistic details about the *o*-nitrobenzaldehyde (*o*-NBA) photolysis, which is directly responsible for the creation of the pH jump, along with the typical photoacoustic signals resulting from its photolysis at 355 nm are also presented.

Chapter 4 introduces the importance of amino acids with ionizable side chains and how their acid-base behaviour can play important roles in enzyme catalysis, substrate binding and protein structure. In this chapter our primary purpose was to fully understand, at molecular level, fundamental events occurring during the protonation of individual amino acid models. The protonation of amino acids correspond to the earliest step in protein or peptide pH-induced folding/unfolding processes. Hence, it is essential to characterize the energetics and kinetics of these protonation reactions.

Chapter 5 presents a classical NMR work on the determination of a peptide structure, in different pH conditions. A protein fragment forming a stable α-helix in aqueous solution, RN80 (an analogue of the C-Peptide from RNase A), has been selected as a model system to explore the energetics and dynamics of α-helix formation. In addition, far-UV and near-UV CD have been used to report further structural details. These structural details were essential to select the initial pH conditions to perform the pH jump experiments. Detection of folding/unfolding events using TR-PAC measurements

allowed the determination of folding and unfolding kinetics, volume changes and enthalpy changes for these events. Moreover, correlations between structure and folding could be inferred.

In Chapter 6, we explore conformational changes of bovine serum albumin (BSA), a mainly α-helical protein, which undergoes a partial unfolding transition at low pH essentially due to protonation of Asp and Glu residues. TR-PAC allowed the determination of rates of protonation and an estimate of the number of Asp and/or Glu carboxylate groups being protonated could be inferred from the kinetic data. Further conformational changes were not detected by nanosecond resolved PAC. However, using the 0.5 MHZ transducer a slow conformational change on a microsecond timescale has been detected.

Chapter 7 describes intrinsic tryptophan fluorescence studies to explore the folding of the homotetrameric protein transthyretin (TTR), one of the many proteins known to be involved in human amyloid diseases. The chapter focuses on the differences in folding rates of two TTR variants, WT and V30M-TTR, and the possible implications in amyloid formation.

Finally, Chapter 8 highlights the main conclusions from all previous chapters. Each chapter is constructed so that it can be read independently. As a consequence, in every chapter the problem is briefly introduced and a relevant background history of prior results is presented. Being so, the reader will notice that some important background information is repeated on several occasions, especially when directly related with the data interpretation and where it is critical for the discussion.

Chapter *2*

General Introduction

Proteins are polymers of amino acids covalently linked through peptide bonds into a linear chain. Each of the twenty common naturally-occurring amino acids contains a central α-carbon, an α-amino group, an α-carboxylic acid group, and an α-side chain. These side chains (or R groups) may be either nonpolar, polar and uncharged, or charged, depending on the pH and pK_a of the ionizable group. Proteins are the most versatile macromolecules in living systems and serve crucial functions in essentially all biological processes. In addition to serve as structural materials in all living organisms, proteins are involved in such diverse functions as gene expression, metabolic regulation, transport, defense, and catalysis. Given the multitude of their roles, it is not surprising that proteins are the most abundant molecules in biology, apart from water, and that even the simplest organism contains about 1000 different types of proteins (Dobson 2004).

Chain-polymers of amino acids are synthesized in the ribosomes based on genetic information. Upon synthesis, a newly translated polypeptide chain must fold into its unique three-dimensional conformation, bind any small molecule cofactors required for its activity, be appropriately modified by protein kinases, glycosylases, or other protein-modifying enzymes, and in the case of oligomeric proteins, assemble correctly with the other protein subunits with which it functions. The information needed for these maturation steps of the protein is ultimately contained in the sequence of linked amino acids that the ribosome produces when it translates an mRNA molecule into a polypeptide chain. However, proteins do not always fold correctly, despite the existence of a complex cellular machinery of protein control. Incorrect folding is being recognized as the cause for

an increasing number of age-related diseases, including Alzheimer's and Parkinson's diseases as well as other neurodegenerative disorders.

The native conformation of a biologically active protein must be energetically stable and from a thermodynamic point of view it is influenced by several contributions, such as the hydrophobic effect, the energy of hydrogen bonds, the energy of electrostatic interactions, and the conformational entropy due to the restricted motion of the main chain and the side chains.

The hydrophobic effect has long been considered the major driving force of protein folding as it leads to a rapid collapse of the polypeptide chain, thereby largely reducing the conformational space to explore (Dill 1990). Basically, it demonstrates the tendency of hydrophobic amino acids to hide away from the aqueous environment and form a hydrophobic core, while the hydrophilic amino acids remain at the surface. Large proteins can complete this task within minutes, while small proteins can do it in less than milliseconds.

Hydrogen bonds have also been recognized as having a contribution to protein stability as important as the hydrophobic effect (Pace et al. 1996). In fact, the secondary structure of proteins, which is defined as the local conformations of the polypeptide backbone, and characterized by regular repeating structures such as α-helices and *β*-sheets, is the result of hydrogen bonding between the amide proton of one peptide bond and the carbonyl oxygen of another peptide bond in close proximity to the first.

While hydrogen bonds and hydrophobic forces are essentially nonspecific, electrostatic interactions are largely specific, and therefore play an important role in specifying the fold of a protein as well as in protein flexibility and function (Kumar & Nussinov 2002). While conventional chemical intuition expects salt bridges to contribute favorably to protein stability, computational and experimental evidence shows that salt bridges can be stabilizing or destabilizing.

Folding a long chain into a specific, compact structure clearly results in a significant conformational entropy decrease. This is counterbalanced by the various intrachain interactions contributing to enthalpy decrease, such as hydrogen bonds and electrostatic interactions but also by the entropy increase due to the hydrophobic effect. The resulting overall stability of the protein is marginal, being on the order of 5 - 10 kcal mol^{-1} (Dill et al. 2008). Qualitatively, it is known that the hydrophobic effect and hydrogen bonds are the major stabilizing contributions and the conformational entropy is the major destabilizing one (Jaenicke 2000).

2.1 The Protein Folding Problem

The protein folding "problem" or the question of how a protein's amino acid sequence dictates its three-dimensional atomic structure first emerged around 1960, with the appearance of the first atomic-resolution protein structures. Since the work of Christian Anfinsen in the 1960s and 1970s, it has been clear that the essential information that encodes the structure of proteins is contained within the amino acid sequence (Anfinsen 1973). The way in which such information is encoded, however, has only recently begun to emerge, as a result of the combined application of a wide range of experimental and computational approaches.

Protein folding can be viewed as three different problems: *(1)* the folding code: the thermodynamic question of what balance of interatomic forces dictates the structure of the protein for a given amino acid sequence; *(2)* protein structure prediction: the computational problem of how to predict the native structure of a protein from its amino acid sequence; *(3)* folding speed (Levinthal's paradox): the kinetic question of how a protein can fold so fast and what routes or pathways some proteins use to fold so quickly (Dill et al. 2007; Dill et al. 2008; Dill & MacCallum 2012). An important goal in the study of folding is to develop models that can make quantitative predictions about the effects of different factors such as amino acid sequences, chain topology, pH, salt concentration and temperature on the kinetics and thermodynamics of the folding process. Thus, the development of suitable experimental and computational methodologies to assess the structural and thermodynamic properties of the different species involved in folding, as well as the kinetics that relate them is of critical importance. In particular, one of our main goals in the present work is to investigate the early events occurring in protein and peptide folding induced by ultrafast pH changes. These experiments allow the investigation of the role of ionizable amino acids and the effect of their protonation in peptide and protein folding/unfolding, as well as, their contribution for the formation of basic structural elements such as α-helices, β-hairpins and loops.

Over the years, the concept of folding pathways motivated a large number of experimental and theoretical studies and several models describing the folding process have emerged, such as the nucleation/growth model, diffusion–collision–adhesion model, framework model, among many others. Table 2.1 describes the most important aspects of some theoretical models used to describe the folding process. The many models of protein

folding are not mutually exclusive and try to explain different aspects of folding, and experimental results give some support to each model. In the 1990s, a new view of protein folding gained popularity: the energy landscape view (Wolynes et al. 1995; Dill & Chan 1997). This theoretical formalism describes the progression of unfolded polypeptide chains along an energy landscape towards the compact native structure (Figure 2.1). In this landscape view of folding, the denatured state of the protein populates a large ensemble of structures. The polypeptide chain may then fold by numerous pathways, potentially adopting multiple partially folded ensembles en route to the native state (Onuchic & Wolynes 2004). For small proteins this landscape appears to be funnel-like and represents the evolutionary selection of polypeptide sequences able to fold rapidly and reliably towards a unique native state (Figure 2.1(A)) (Watters et al. 2007). On the other hand, larger polypeptide sequences have rougher energy landscapes, allowing the population of partially folded states that may be on- or off- pathway to the native state (Figure 2.1(B)) (Vendruscolo et al. 2003; Brockwell & Radford 2007). Furthermore, in must cases a point mutation represents a small perturbation to the energy landscape. Being so, the basic shape of the funnel and the location of the global minimum is similar, and the mutant protein will fold into essentially the same structure as the wild-type protein (Nelson & Onuchic 1998). This observation underlies the most commonly used method of predicting structures: homology modeling (Zhang & Skolnick 2004).
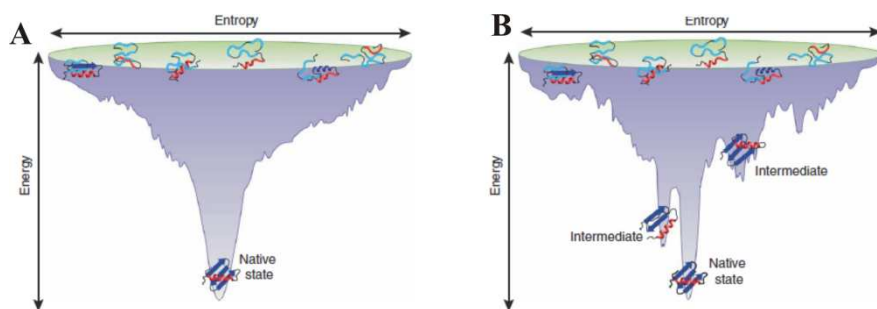
Figure 2.1: Schematic representation of funnel-shaped energy landscapes. The width of the funnel represents the conformational freedom of the chain. The vertical axis represents the free energy: as free energy decreases, the nativeness of the chain increases. Denatured (unfolded) states are at the top of the funnel including a broad ensemble of structures containing both elements of native and non-native interactions, while the native state is the global minimum. (A) Example of a smooth energy landscape, through which the polypeptide chain is effectively funneled to the native structure. (B) Example of a more rugged landscape, through which the polypeptide chain has to navigate, possibly via one or more populated intermediates, to the native state. (Adapted from Bartlett & Radford 2009).

Table 2.1: Examples of some theoretical models used to describe the protein folding process.

Model	Mechanism	References
Nucleation/growth	The rate-limiting step of the folding process is a nucleation event, presumably the formation of structural units, and once nucleation occurs the nuclei grow fast and the folding process rapidly completes.	(Wetlaufer 1973)
Diffusion-collision	Fluctuating microdomains (portions of secondary structure or hydrophobic clusters) move diffusively and repeatedly collide with each other. Collisions can lead to a coalescence of the microdomains into larger units.	(Karplus & Weaver 1976) (Karplus & Weaver 1994)
Framework	The folding process is hierarchical, starting with the formation of the secondary structure elements, and the docking of the pre-formed secondary structure units yield the native, folded protein.	(Baldwin 1989)
Hydrophobic collapse	The hydrophobic effect is the main driving force of folding, and the process starts with a rapid collapse of the chain, followed by the formation of the secondary structure.	(Dill 1985)
Nucleation-condensation	Combine the features of both the framework and the hydrophobic collapse mechanisms; Long-range and other native hydrophobic interactions form in the transition state to stabilize the otherwise weak secondary structure.	(Fersht 1995) (Fersht 1997)

2.1.1 Dynamics of Elementary Events in Protein Folding

One solution to reduce the magnitude of the folding problem is to divide the folding process into elementary events, whose dynamic properties can be investigated using suitable model compounds (Eaton et al. 2000; Ferguson & Fersht 2003). One of the essential events during the folding of a protein is the formation of regular secondary structural elements, such as α-helices and *β*-structures, or even the formation of loops in oligopeptides. Estimates of the timescales of these relevant early events in protein folding

can therefore be of critical importance for the understanding of the overall folding process of a protein, which results from a complex series of events including specific and nonspecific chain collapse, formation of secondary and tertiary contacts and desolvation of the polypeptide chain (Ferguson & Fersht 2003).

The α-helix is a structural element highly ordered, stabilized by local interactions. In particular, backbone hydrogen bonds between the *i*th and the (i + 4)th residues are responsible for the integrity of an α-helix. Almost 50 years ago, the kinetics of helix-coil transition in polypeptides was first investigated using ultrasonic relaxation methods and found to occur in nanoseconds (Schwarz 1965; Hammes & Roberts 1969). More recently, using infrared spectroscopy (IR) (Williams et al. 1996), fluorescence (Thompson et al. 2000) and UV resonance Raman (Lednev et al. 1999), laser T-jump experiments determined the folding rates for Ala-rich oligopeptide helices to be on the order of 500 ns. Furthermore, T-jump experiments were also applied to investigate the folding kinetics of the neuroactive peptide Conantokin-T (Con-T) revealing a folding rate around 700 ns (Du et al. 2007), and Gai and coworkers (Mukherjee et al. 2008) found that the helix from the ribosomal protein L9 from Bacillus stearothermophilus exhibits a much slower T-jump relaxation kinetics, about 2 μs, than equivalent Ala-rich peptide helices. Much slower relaxation kinetics in stable, protein-like helices has been suggested due to a higher entropic cost associated with the alignment of non-alanine side chains, and breaking of stronger side chain interactions (Eaton et al. 2000). However, bulky side chains were found to have no effect on the α-helix folding kinetics in oligopeptides (Petty & Volk 2004) and α-helices in proteins also appear to form on the same timescales as those in Ala-rich peptides (Gilmanshin et al. 1997). In addition, experiments using laser induced pH-jump and photoacoustic detection showed that the folding rate of poly-L-lisine and poly-L-glutamic polypeptide is around 300 ns (Abbruzzetti et al. 2000; Bonetti et al. 1997). In the present work, an analogue of the well studied C-peptide from bovine pancreatic ribonuclease A (RNase A) has been selected as a system model to investigate the role of ionizable amino acids on its folding dynamics (Chapter 5).

β-hairpins correspond to the simplest *β*-sheet, and formed with just two antiparallel *β*-strands. Compared to the α-helices, peptide models for the *β*-sheet structure presente more of a challenge, predominantly due to their tendency to aggregate. A suitable model was found in the C-terminal *β*-hairpin from the GB1 protein (Blanco et al. 1994). From laser T-jump experiments, the GB1 *β*-hairpin was found to fold in a few microseconds (Muñoz et al. 1997). The *β*-hairpin folds much slower due to a significant

entropy barrier, which arises because non-local inter-residue contacts must form. More recently, other β-hairpin peptide models have appeared, such as tryptophan zippers (trpzips), stabilized by two pairs of Trp residues, whose folding kinetics has been intensively studied using laser T-jump methods (Snow et al. 2004; Du et al. 2004; Yang & Gruebele 2004). Investigation of several trpzips suggests that turn formation is the rate-limiting factor in β-hairpin folding.

In Table 2.2 is shown the rate of formation of some peptide fragments forming α-helices, β-hairpins and loops previously studied. These studies suggest that the folding rate of β-hairpins is in general slower than the estimated for α-helical peptides, and loop formation times are less than 0.16 μs, much faster than the formation of α-helices and β-hairpins of comparable length (Kubelka et al. 2004).

Table 2.2: Rate of formation of different structural elements of proteins (Adapted from Kubelka et al. 2004).

Loop sequences	$\tau_{contact}$ (μs)	References
C-(AGQ)$_n$-W-NH$_2$; n = 1-6	0.02-0.1	(Lapidus et al. 2002)
Xan-(GS)$_n$-NAla-GS; n = 1-28	0.007-0.16	(Krieger et al. 2003)
Xan-S$_n$-NAla-GS; n = 2-11	0.012-0.03	(Krieger et al. 2003)
α-helical peptides	$\tau_{folding}$ (μs)	
Ac-YG(AKA$_3$)$_2$AG-NH$_2$	2.0	(Wang et al. 2003)
Ac-YGG(KA$_4$)$_3$K-NH$_2$	0.7	(Werner et al. 2002)
A$_5$(A$_3$RA)$_3$A	0.8	(Lednev et al. 1999)
Ac-WA$_3$H$^+$(A$_3$RA)$_3$A-NH$_2$	0.4	(Thompson et al. 2000)
β-hairpin peptides	$\tau_{folding}$ (μs)	
(GB1) GEWTYDDATKTFTVTE	6	(Muñoz et al. 1997)
(trpzip4) GEWTWDDATKTWTWTE	13	(Xu et al. 2003)
(peptide I) SESYINPDGTWTVTE	0.8	(Xu et al. 2003)

NAla – naphtylalanine; Xan – xanthone.

2.2 Experimental Methodologies to Monitor Protein Folding

Especially during the last two decades a series of considerable advances in both theory and experiment have lead to a significantly better understanding of the underlying principles behind protein folding, as documented in several reviews (Plaxco & Dobson 1996; Roder & Shastry 1999; Brockwell et al. 2000; Bartlett & Radford 2009; Buchner et al. 2011). The introduction of high temporal resolution experimental methods, such as laser-pulsed techniques to trigger folding processes in nanoseconds has had a major impact in experimental, theoretical and computational studies of protein folding. These techniques made possible the investigation of the mechanism of formation and time scales of the elementary events in folding, including polypeptide chain collapse and formation of the basic secondary structure elements such as α-helices, β-hairpins and loops. The dynamics of these elementary steps sets a lower limit for the timescale of folding. Table 2.3 is shows several experimental detection methods that have been used to probe specific properties of proteins or peptides during folding. Some are less common, as they required specialized resources. For example, small-angle X-ray scattering (SAXS), which provides information on the dimensions and the shape of the polypeptide chain (Lipfert & Doniach 2007), requires a synchrotron X-ray source. Pulsed electron paramagnetic resonance (EPR) techniques in combination with spin labeling as well as liquid flow EPR have also been applied to investigate protein folding (Grigoryants et al. 2000). Another example of a less commonly used technique is time-resolved photoacoustic calorimetry (TR-PAC) because it requires a cell specifically designed for photoacoustic measurements. However, this technique can provide in a single experiment, kinetics and enthalpy changes. In our laboratory, a new time-resolved photoacoustic calorimetry flow cell coupled with temperature control and automatic injection has been designed to avoid the large sample consumption associated with the sample flow system and improve the temperature control system (details in Chapter 3). In addition, other methods such as fluorescence, circular dichroism (CD) in the far- and near-UV regions and nuclear magnetic resonance (NMR) have been used to obtain either structural or kinetics information.

Table 2.3: Experimental techniques used to investigate protein folding (Adapted from Bartlett & Radford 2009).

Technique	Time scale	Information content
Fluorescence	$\geq$ ns[a]	- Environment of (predominantly) Trp side chains, through measurement of intensity and λ_{max}; Trp can be introduced (or removed to create a single-tryptophan protein) by protein engineering - Extrinsic fluorophores can also be engineered into the protein
Far-UV CD	$\geq$ μs[a]	- Overall protein secondary structural content
Near-UV CD	$\geq$ μs[a]	- Packing of aromatic residues - Only strong interactions give a near-UV CD signal
Infrared Spectroscopy (IR)	$\geq$ μs[a]	- Secondary structure content predominantly through the amide I band (mainly amide C=O stretch, 1600-1700 cm^{-1}), which is sensitive to the polypeptide backbone conformation due to characteristic couplings among local amide modes - Combined with solvent-exchange, information about hydrogen-exchange protection can be obtained
ANS (1-anilino-8-napthalene sulfonic acid) binding	$\geq$ μs[a]	- Exposure of aromatic surface area - ANS should not perturb folding
FRET (Foster resonance energy transfer)	$\geq$ ps[a]	- Molecular ruler, dependent on the distance between two fluorophores (r^{-6} assuming free rotation of the dyes) - Information about rapid fluctuations is possible - Intrinsic Trp, if present, often serves as a donor with several options for the acceptor; careful design needed to incorporate dyes without perturbing folding
Anisotropy	$\geq$ μs[a]	- Correlation time measurements provide information about the shape and size of the molecule
SAXS (Small-angle X-ray scattering)	$\geq$ μs[a]	- The average radius of gyration - Dimensions and shape of a polypeptide chain can be obtained
Absorbance	$\geq$ ns[a]	- Environment of chromophore (peptide bond, aromatic residue or extrinsic moiety may be used)
Real-time NMR	> min	- Structural information via chemical shifts and measurement of NOEs
Pulsed H/D exchange by NMR	$\geq$ ms	- Hydrogen exchange protection of folding intermediates on a per-residue basis
Pulsed H/D exchange by ESI-MS	$\geq$ ms	- Hydrogen exchange protection of folding populations - Quantification of the population of species within heterogeneous ensembles with different hydrogen-exchange properties
Protein engineering	Depens on the probe used	- Role of individual residue in determining the rate of folding and stability of species of interest - Probes the role of a specific contact in the stabilization of intermediates
Time-Resolved Photoacoustic Calorimetry (TR-PAC)	> ns	- Structural information of volume changes, enthalpy changes and kinetics upon folding/unfolding in a single experiment

[a] The timescale depends on the method used to initiate the folding: temperature jump (ns), pH jump (ns), pressure jump (μs), ultra-rapid mixing (μs), stopped-flow (ms) or manual mixing (s).

Table 2.4 shows several methodologies to initiate the process of protein folding on a short timescale. In the present work, we proposed the application of a pH jump technique to explore the role of ionizable amino acid residues on the folding of peptides and proteins. As an example, using this technique one can perturb a peptide on site specific regions and understand the importance of salt-bridges as well as π-stacking interactions when specific amino acids are involved, such as histidine (His), glutamic acid (Glu) and aspartic acid (Asp) (details in Chapter 4 and 5).

2.3 Protein Misfolding and Disease

Native states of proteins represent the most thermodynamically stable conformation under physiological conditions. In a cellular environment, molecular chaperones help to protect the incompletely folded polypeptide chains from aggregating (Frydman 2001). Even after the folding process is complete, a protein can subsequently experience conditions under which it unfolds, at least partially, and then it is again prone to aggregation. The failure of a specific protein to adopt or maintain its native functional conformation under all appropriate physiological conditions may lead to a wide range of diseases with different pathological mechanisms (Thomas et al. 1995). Examples of these diseases include cystic fibrosis, some forms of emphysema, and a variety of senile dementias including Alzheimer's disease. The later is a member of the family of diseases known as amyloidoses, which also includes the prion diseases such as bovine spongiform encephalopathy (BSE) and Creutzfeldt-Jakob disease, which are associated with the aggregation of normally soluble proteins and formation of insoluble amyloid fibrils.

Table 2.4: Techniques to trigger protein refolding/unfolding on sub-millisecond timescales. These methods of initiating folding when combined with a suitable detection method (described in Table 2.3) allow to resolve fast events in protein folding (Adapted from Brockwell et al. 2000).

Technique	Dead time	Comments
Optical triggering	< ns	- A rapid shift of the folding equilibrium can be caused by changes in the environment of the protein, in the protein molecule itself by photodissociation of a ligand, electron transfer or by specifically designed photoswitches. - Proteins with prosthetic groups are frequently studied by this technique.
Temperature jump	~ ns	- Laser used to rapidly heat water molecules, triggering folding/unfolding. - The temperature jump (T-jump) can only increase the sample temperature. As a consequence, the equilibrium shift is toward the unfolded states, except when the protein can be cold denatured.
Pressure jump	50 μs	- A sudden increase in pressure initiates protein unfolding, while for a pressure unfolded protein, the decrease in pressure triggers refolding. - The pressure jump can be induced as repetitive pressure pulses by a stack of piezoelectric crystals or as a single pressure jump using a mechanical valve. - No mixing artifacts and the experiment can be repeated many times on the same sample. - Only small changes in equilibrium can be measured however, as >1000 bar is required to fully denature proteins.
Ultrafast mixing	50 μs	- Turbulent flow causes rapid mixing. Easy to change solvent conditions. - Results can be compared directly with stopped-flow methods.
Laser-induced pH jump	< ns	- Photoacids and photobases can be applied to induce an ultrafast pH jump upon laser irradiation. - Only specific regions of the polypeptide chain are perturbed and relationships between protein structure and folding or unfolding can be inferred. - Proteins should not absorb at the excitation wavelength used to promote the pH jump.

Amyloidoses are classified based on the main protein forming amyloid fibrils and today include 30 different human proteins (Sipe et al. 2012). One of the many proteins involved in human amyloid diseases is transthyretin (TTR). TTR is a homotetrameric serum and cerebrospinal fluid protein that transports thyroxine (T_4) and retinol in association with retinol binding protein (RBP). Diseases such as familial amyloid cardiomyopathy (FAC), familial amyloid polyneuropathy (FAP) and senile systemic amyloidosis (SSA) are caused by the formation of TTR amyloid aggregates and fibrils, which accumulate in human tissue and interfere with the normal organ function (Brito et al. 2003). SSA is characterized by deposition of wild-type TTR amyloid in parenchymal organs in the elderly population. By contrast, the fibrillar aggregates in FAC and FAP are essentially constituted by TTR-variants resulting from hereditary point mutations, of which over 100 amyloidogenic ones have been described so far. Thus is the case of the V30M-TTR variant implicated in the most common FAP type, a very debilitating, with very poor prognosis, autossomal dominant disease affecting individuals from their twenties in several countries, including Portugal, Japan, Sweden and the USA (Brito et al. 2003). In Chapter 7, it is described not only the investigation into the folding pathway for WT-TTR tetramer, but also how the single point mutation V30M affects the TTR folding rate and if there is any correlation between folding and amyloid fibril-forming propensity. These experiments have been conducted monitoring the intrinsic tryptophan fluorescence of TTR.

Table 2.5: Human diseases associated with the formation of amyloid deposits (Adapted from Chiti & Dobson 2006).

Aggregating protein or peptide	Disease
Transthyretin	Familial amyloid cardiomyopathy Familial amyloid polyneuropathy Senile systemic amyloidosis
α-Synuclein	Parkinson's disease
Amyloid β peptide	Alzheimer's disease
β2-microglobulin	Hemodialysis-related amyloidosis
Amylin, also called islet amyloid polypeptide (IAPP)	Type II diabetes
Prion Protein	Creutzfeldt-Jakob disease
Keratins	Cutaneous lichen amyloidosis
Lysozyme	Lysozyme amyloidosis

Chapter 3

Time-Resolved Photoacoustic Calorimetry: Theory and Applications

3.1 Photoacoustic Effect

More than a century ago, Alexander Graham Bell first observed the photoacoustic effect (Bell 1881). According to the very terms used by its discoverer, the photoacoustic effect is *the production of sound by light*. Absorption of pulsed or modulated light by a sample (solid, liquid or gas) generates heat due to the radiationless processes that follows the excitation of a sample. Pressure waves (acoustic waves) are then produced as a result of the thermal expansion due to local heating and structural volume changes of the sample and the surrounding medium. The practical use of Bell's discovery had to wait almost one century until suitable measuring techniques were developed in the 1970s. These techniques use either continuous modulated light or flash excitation, and the pressure changes are detected by a microphone or a piezoelectric transducer.

The application of the photoacoustic effect to the study of time-resolved enthalpy and volume changes was introduced by Callis, Parson and Gouterman in the early 1970s by measuring flash-induced volume changes in photosynthetic materials, using a suspension of *Chromatium* chromatophores (Callis et al. 1972). The experiment employed a capacitor microphone that measures the volume changes promoted by the thermal expansion or contraction resulting from enthalpy changes as well as those caused by volume changes between reactants and products. The time resolution approached 100 μs.

In 1985, the time resolution of photoacoustic calorimetry was subsequently extended onto the 100 ns time scale following the introduction of piezoelectric transducers for the detection of acoustic waves and a nanosecond laser for light initiation of the reactions (Rudzki et al. 1985). The photoacoustic calorimetry technology was adapted from the photoacoustic spectroscopic methods developed by Patel and Tam (Patel & Tam 1981). Further modifications in cell design (Melton et al. 1989; Arnaut et al. 1992) and new materials such as thin films of polyvinylidene difluoride for detection of acoustic waves (Heihoff & Braslavsky 1986; Komorowski & Eyring 1987) have extended the time resolution of photoacoustic calorimetry to nearly 10 ns. Nowadays, we can listen to the sound produced by reacting molecules with the time resolution of a few nanoseconds (Peters 1994).

Currently, the photoacoustic effect has a broad range of applications from medicine to fundamental problems in chemistry. In particular, photoacoustic tomography (PAT) is a methodology that has been developed rapidly in the past decade and can be used to obtain *in vivo* imaging from organelles to organs, and have several promising applications explored in vascular biology, oncology and dermatology, among many others (Xu & Wang 2006; Wang & Hu 2012). In chemistry, several studies using time-resolved photoacoustic calorimetry (TR-PAC) have shown that PAC waves carry important information on structural volume changes (Callis et al. 1972; Westrick et al. 1987; Gensch & Braslavsky 1997; Chakrabarty et al. 2008), absorption coefficients of transient species (Arnaut & Pineiro 2003), the characterization of solid/liquid interfaces (Serpa et al. 2008), the thermodynamics of ligand binding to proteins (Larsen & Mikšovská 2007; Miksovská et al. 2008), among others.

3.2 Biochemical Applications of Time-Resolved Photoacoustic Calorimetry

Over the years, TR-PAC theory and its applications to a variety of reactions encountered in organic and organometallic chemistry, and biochemistry have been thoroughly reviewed by several authors (Tam 1986; Peters & Snyder 1988; Peters et al. 1991; Braslavsky & Heibel 1992; Peters 1994; McLean et al. 1998; Gensch & Viappiani

2003). Unlike time-resolved optical techniques, which are highly sensitive to the structural changes in the vicinity of a specific chromophore, the advantage of photoacoustic calorimetry is in its ability to monitor the magnitudes and time profiles of overall volume and enthalpy changes of a photo-initiated reaction by monitoring the acoustic waves. In fact, TR-PAC is useful not only to obtain a kinetic description, the energetics, and the conformational and hydration changes that occur during chemical and biochemical transformations, but also to detect conformational changes that are optically silent.

In organic chemistry, TR-PAC experiments allow to measure the reaction enthalpies for highly reactive species such as radicals, and bond dissociation enthalpies (Muralha et al. 2004; Nunes et al. 2006; Correia et al. 2004; Nunes et al. 2009), while in organometallic chemistry a number of metal-ligand, metal-hydrogen, and metal-metal bond enthalpies have been obtained (Peters 1994). Moreover, photoacoustic measurements have been applied to examine a great variety of biochemical processes. In particular, the dynamics of proton pumping in bacteriorhodopsin (Ort & Parson 1979), the dynamics of photodissociation of carbon monoxide from carboxymyoglobin (Norris & Peters 1993) and carboxyhemoglobin (Peters et al. 1992) and oxygen from human and bovine oxyhemoglobin (Chen et al. 2004), the energetics of the intermediates formed in the bleaching of the protein rhodopsin (Marr & Peters 1991), electron transfer in reaction centers and the photophysics and photochemistry of the plant photosensor pigments phytochrome and chlorophyll (Arata & Parson 1981; Jabben et al. 1986), among many other problems in biochemistry.

In the field of protein folding research, a number of methods have been developed to extend the time window of observation of the protein unfolding/folding processes from the microseconds to the nanosecond regime, and thus observe the early steps of protein folding. Among these methods, TR-PAC combined with either photolabile caging strategies or laser-induced pH jump tecnhiques is an increasingly popular method to study protein folding. The photochemical trigger typically used to promote an ultrafast pH jump is the caged photolabile compound *o*-nitrobenzaldehyde (*o*-NBA). One of the most extensively investigated proteins using the pH jump technique is apomyoglobin (ApoMb). Several experimental techniques have revealed the rapid, sub-millisecond development of a compact acid intermediate in the ApoMb folding kinetic pathway (Jennings & Wright 1993; Eliezer et al. 1995). Laser-induced pH jump with TR-PAC detection has been applied to examine the structural volume changes accompanying the early events leading to the formation of the compact acid intermediate of ApoMb in the presence of 200 mM

GuHCl (Abbruzzetti, Crema, et al. 2000), and in the absence of denaturant (Miksovská & Larsen 2003). Abbruzzetti and collaborators have shown that beside the volume and enthalpy changes associated with the proton release from o-NBA two additional processes were observed. The first process accompanied by an expansion occurred with a lifetime of 100 ns and was attributed to the protonation of carboxylic acids. This was followed by a large contraction of approximately -82 ml mol^{-1} with a lifetime of 2.4 μs, and the slower process was assigned to structural changes taking place during the ApoMb unfolding. In the absence of denaturant, Miksovská et al observed a smaller volume decrease of about -22 ml mol^{-1} with a lifetime of 620 ns.

Polypeptides that fold into α-helix structures, such as poly-L-glutamic Acid (PLG) and poly-L-lysine (PLL), were used as model systems to investigate the early events in acid-induced protein unfolding/folding processes. Despite the fact that PLG and PLL sequences are not found in naturally occurring polypeptides, they represent an interesting system for model studies because undergo pH-dependent unfolding/folding. In particular, PLL is an α-helical structure at pH 12 that completely unfolds into a random coil at neutral pH (Viappiani et al. 1998). The unfolding process is due to the strong electrostatic repulsive forces between the protonated ε-amino groups. The acid-induced local disruption of the helical structure of PLL is associated with a contraction of approximately -17 ml mol^{-1} and lifetime of 250 ns. On the contrary, PLG is unfolded at neutral pH but protonation of γ-carboxylates reduces the intramolecular electrostatic repulsive forces leading to formation of secondary structure (Abbruzzetti, Viappiani, et al. 2000). The coil to helix transition in PLG induced by pH jump and studied by PAC shows an expansion of approximately 7 ml mol^{-1} with a lifetime of 100 ns.

Recently, a method combining TR-PAC and a photolabile caging strategy was developed to study fast peptide folding. Photolabile linkers such as bromoacetyl-carboxymethoxybenzoin (BrAcCMB) and 4-(bromomethyl)-6,7-dimethoxycauramin (BrDMC) are used to cyclize short synthetic peptides or small proteins, constraining the structure of the "cage" peptide or protein in a well-defined non-native conformational state (R. P.-Y. Chen et al. 2004; Kuo et al. 2005; H.-L. Chen et al. 2010). To initiate the refolding, the photolabile linker is cleaved within 10^{-9} s by irradiation with pulses of UV-light from a laser. As an example TR-PAC studies revealed that synthetic β-sheet peptides refold in very different times. For example, the refolding of c-19merE11C (τ = 600 ns) is much slower than the refolding of c-20merE12C (τ = 40 ns) or c-20merDP6D peptide (τ = 150 ns) (Kuo et al. 2005). These differences in the refolding

kinetics reflect the contribution of the turn amino acid sequence. A less stable turn is associated with longer folding times.

3.3 Analysis of Photoacoustic Data

The physical principle behind PAC and its applications to chemical and biochemical reactions has been previously described in detail (Peters 1994; McLean et al. 1998; Gensch & Viappiani 2003). When a chemical reaction in solution is initiated by the absorption of light, the reacting molecules transfer part of their excess energy to the surrounding solution. The prompt increase in temperature leads to a pressure wave resulting from a volume expansion of the solvent, which propagates through the medium and can be detected by a pressure-sensitive detector. When the absorption of the laser light pulse results in additional processes, such as cleavage of a covalent bond or creation of charged species leading to electrostriction of the solvent about the charged centers, these processes also contribute to the overall volume change ($\Delta V_{overall}$), which can be expressed as

$$\Delta V_{overall} = \Delta V_{th} + \Delta V_{struct} \tag{3.1}$$

where ΔV_{th} represents the thermal volume change due to heat release to the solution and ΔV_{struct} includes volume changes other than those due to thermal heating, including volume changes due to conformational changes, electrostriction, etc. Thus both a thermal expansion, ΔV_{th}, and a structural rearrangement at the molecular level, ΔV_{struct}, contribute to the production of the acoustic wave.

The amplitude of the acoustic signal for the sample is given by Equation 3.2, where K is the instrumental response parameter.

$$S = K\left(\Delta V_{th} + \Delta V_{struct}\right) \tag{3.2}$$

The thermal component of the volume change is defined by Equation 3.3, where Q is the amount of heat released to the solvent, β is the thermal expansion coefficient of

the solution (K^{-1}), C_p is the heat capacity (cal g^{-1} K^{-1}), and ρ is the density (g ml^{-1}). The fraction ($\beta/C_p\rho$) is the thermoelastic parameter of the solution and for pure water can be obtained from tabulated values.

$$\Delta V_{th} = \left(\frac{\beta}{C_p\rho}\right)Q \qquad (3.3)$$

It is worth noting that in aqueous solutions $\beta/C_p\rho$ is highly temperature-dependent and approaches zero at 3.9 °C for pure water. Although ΔV_{th} is a function of temperature, ΔV_{struct} can be considered independent of temperature over a limited interval. Therefore in aqueous solutions the contributions of ΔV_{th} and ΔV_{struct} can be separated by examining the temperature dependence of the acoustic wave amplitude, S.

Considering Equation 3.3, the Equation 3.2 can be rewritten as in Equation 3.4

$$S = K\left[\left(\frac{\beta}{C_p\rho}\right)Q + \Delta V_{struct}\right] \qquad (3.4)$$

The instrumental response parameter K may be eliminated from the analysis by employing a calibration compound that converts the entire energy of the photon, E_λ, into heat, and undergoes no changes in its molecular structure ($\Delta V_{struct} = 0$) on the time scale of the instrument resolution. The calibration compounds are commonly designated as photocalorimetric references and are usually non-fluorescence, photochemically stable, and 100 % efficient in delivering the absorbed energy to the medium as heat when the excited molecules return to their ground state (Abbruzzetti et al. 1999). To eliminate K, the acoustic waves for the reference compound are measured under conditions identical to those used to obtain the samples signals. Therefore, the amplitude of the acoustic wave for the reference compound can be described by Equation 3.5, where E_λ is the energy of the photon at the excitation wavelength (e.g. 355 nm expressed in kcal mol^{-1} will have the corresponding value of 80.54 kcal mol^{-1}).

$$S_{ref} = K\left(\frac{\beta}{C_p\rho}\right)E_\lambda \qquad (3.5)$$

K is eliminated by dividing the acoustic wave amplitude S by S_{ref}. The ratio of the signal amplitude of the sample to that of the reference reflects the exact properties of the sample.

$$\frac{S}{S_{ref}} = \phi = \frac{Q}{E_\lambda} + \frac{\Delta V_{struct}}{\left(\dfrac{\beta}{C_p\rho}\right)E_\lambda} \qquad (3.6)$$

If the fraction $(\beta/C_p\rho)$ is defined by F(t), because these quantities are functions of temperature, Equation 3.6 can be rearranged to

$$E_\lambda\phi = Q + \frac{\Delta V_{struct}}{F(T)} \qquad (3.7)$$

For aqueous solutions, a plot of $E_\lambda\phi$ versus $C_p\rho/\beta$ leads to a linear relationship, with a slope corresponding to ΔV_{struct} and an intercept equals to Q. If ΔV_{struct} is negligible, then the heat released during the reaction, Q, equals $E_\lambda\phi$.

For processes with a quantum yield (Φ) less than unity, the volume changes are obtained using Equations 3.8.

$$\Delta V = \frac{\Delta V_{struct}}{\Phi} \qquad (3.8)$$

Subtracting Q from E_λ gives ΔH for processes occurring faster than the time resolution of the experimental setup (Equation 3.9a) (Larsen 2006). The Q values of the subsequence kinetic processes represent $-\Delta H$ for that step (*i.e.*, heat release) (Equation 3.9b).

$$\Delta H_1 = \frac{E_\lambda - Q}{\Phi} \qquad (3.9a)$$

$$\Delta H_2 = \frac{-Q}{\Phi} \qquad (3.9b)$$

The transducers used in the detection of acoustic waves are sensitive not only to the amplitude of the acoustic wave but also to their temporal profile. The observed time-dependent acoustic signal $E(t)$ is produced by the convolution of a time-dependent function of the decay process $H(t)$ with an instrument response function $T(t)$, which reflects the response of the transducer to a pressure wave.

$$E(t) = T(t) \otimes H(t) \qquad\qquad (3.10)$$

Experimentally, the function $T(t)$ can be obtained using a photocalorimetric reference compound such as bromocresol purple (BP), that releases nonradiatively (only heat deposition) all the radiative energy absorbed in a time faster than the transducer resolution.

The overall time-dependent volume change described by the function $H(t)$ can be written as the summation of sequential single exponential terms:

$$H(t) = \sum_i \frac{\phi_i}{\tau_i} e^{-(t/\tau_i)} \qquad\qquad (3.11)$$

where ϕ_i and τ_i are the respective energy fraction and decay time for the ith component in the sum of the exponentials.

Numerous algorithms have been developed to obtain the parameters ϕ_i and τ_i (Rudzki et al. 1985; Melton et al. 1989; Small et al. 1992; Schaberle et al. 2010). The free software *CPAC* available online (http://cpac.qui.uc.pt/) has been developed in our laboratory and used to obtain the parameters ϕ_i ($\phi_i = S/S_{ref}$) and τ_i (Schaberle et al. 2010). This software provides an analytical description for the instrumental response acoustic wave $T(t)$, and the analytical solution for the convolution between $T(t)$ and the heat function $H(t)$. The instructions to use *CPAC* and analytical solutions for the acoustic waves $T(t)$ and $E(t)$ have been previously described in detail by Schaberle et al (Schaberle et al. 2010). Briefly, the software first uploads the acoustic waves from the reference ($T(t)$), sample ($E(t)$), and solvent ($O(t)$). The user introduces the absorbance of the reference and sample solutions, previously matched at the the excitation wavelength. This absorbance is employed to correct the amplitude of the $O(t)$ wave before it is subtracted from the $T(t)$ and $E(t)$ waves, and the pre-signal amplitude is set to zero with a change in offset. The $T(t)$ and $E(t)$ waves are then normalized to the maximum excursion from zero

of the *T(t)* wave. Next, the user defines the number of points to be analyzed and sets the initial value of t_0. The accurate description of experimental *T(t)* waves requires a series containing the product of exponential and sine functions that are the base functions for PAC simulations. Schaberle et al found that *T(t)* waves are appropriately described by a linear combination of three base functions, with different frequencies, phases and damping parameters. Thus, the reference is fitted with a function in the form of Equation 3.12 to reproduce the observed *T(t)* wave, where t_0 is related to the time delay from the triggering of the signal acquiring oscilloscope and sets the function to zero when $t = t_0$. The parameter Y_0 is related with the rise time of the wave, *w* with the damping time of the transducer, *f* with the frequencies and θ with the phases.

$$T(t) = \frac{(t_0 - t)}{Y_0} \left[\begin{array}{l} \exp\left(\frac{(t_0 - t)}{w_1}\right) \sin(f_1(t + \theta_1)) + \exp\left(\frac{(t_0 - t)}{w_2}\right) \sin(f_2(t + \theta_2)) \\ + \exp\left(\frac{(t_0 - t)}{w_3}\right) \sin(f_3(t + \theta_3)) \end{array} \right] \qquad (3.12)$$

The user may change the initial values of the parameters t_0, Y_0, θ, *w* and *f* in order to obtain the best fit to the experimental reference wave, although the fitting procedure generally converges independently of the initial values. With the obvious exception of t_0, those parameters are properties of the transducer and can even be set from the transducer supplier data sheet. Conversely, the values of the parameters after convergence can be compared with the transducer supplier data sheet. Those parameters are then used in the estimation of *E(t)*, which is the convolution of the *T(t)* wave with the heat function *H(t)*, Equation 3.10. This calculation requires the choice of an appropriate kinetic model. Currently, three kinetic models are implemented in the *CPAC* software, differing in the number of sequential exponential decays. The convolution of *T(t)* and *H(t)* with fractions of thermal energy released, ϕ_i, and lifetimes, τ_i, is compared with the experimental wave *E(t)* and the sum of the square deviations between the experimental and calculated *E(t)* waves is minimized with an iterative procedure that changes the values of ϕ_i and τ_i. In the present work, the deconvolutions employed kinetic models consisting of one, two or three sequential exponential decays. For each exponential, values of lifetime, τ_i, and fraction of thermal energy released, ϕ_i, were obtained. The analytical solutions for *E(t)* for the kinetic models implemented in *CPAC* software have been determined by Schaberle et al

(Schaberle et al. 2010). As an example, considering the distributive properties of the integral, the partial derivative of w_1 and only the first member of the $T(t)$ equation (Equation 3.12), the convolution expression for a monoexponential decay is express thought Equation 3.13 (Schaberle et al. 2010), where t0 is related with the time delay from triggering of the oscilloscope and sets the function to zero when $t = t_0$, Y_0 is related with the rise time of the wave, w with the damping time of the transducer, f with the frequencies and θ with the phases, k_1 ($k = 1/\tau$) with the kinetic constant, and ϕ_1 corresponds to the fraction of thermal energy released.

$$E(t) = \frac{1}{Y_0} \frac{\partial}{\partial\left(1/w_1\right)} \left\{ \int_{t_0}^{t} \exp\left(\frac{\left(t_0 - t'\right)}{w_1} \right) \sin\left(f_1\left(t' - \theta_1\right)\right) \phi_1 k_1 \exp\left(k_1\left(t' - t\right)\right) dt' \right\} \qquad (3.13)$$

3.3.1 Two-Temperature and Multiple-Temperature Methods

One PAC experiment consists in measuring and averaging an appropriate number of acoustic waves of the sample $E(t)$, reference $T(t)$ and solvent $O(t)$ in the same conditions. At least three sets of averaged sample, reference and solvent waves were used for data analysis at a given laser intensity, and four laser intensities were obtained by interposing filters with transmissions in the 25-100 % range (see Figure 3.1).
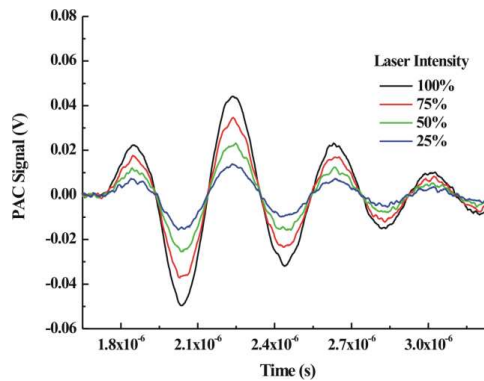
Figure 3.1: Acoustic waves from bromocresol purple (BP) (*T(t)* waves) acquired at different laser intensities, upon irradiation at 355 nm ($A_{355} = 0.65$, 1 cm path length cell). Each signal at the different laser intensities correspond to the average of 200 waves.

28

Using the *CPAC* software, the values of ϕ_i and τ_i were obtained for each ith process. Low laser intensities were used to minimize biphotonic processes, but they may still occur and contribute to heat release. This can be assessed comparing the values of ϕ_i obtained at different laser intensities. If significant laser intensity dependence is observed, the value of ϕ_i must to be extrapolated to zero laser intensity. Figure 3.2 shows typical experimental results obtained and the extrapolation to zero laser intensity of the ϕ_i values measured at four different laser intensities. In the particular cases of Figure 3.2 only a very slight dependence on laser intensity was detected.
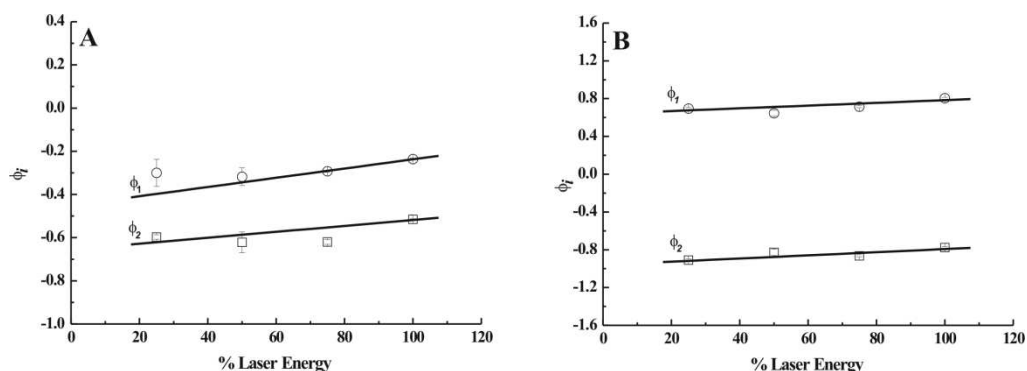
Figure 3.2: Values of ϕ_i obtained by deconvolution of the photoacoustic signals using the software *CPAC*, as a function of the fraction of energy absorbed, obtained from independent samples: 700 μM Ac-Glu-NH$_2$ (A) and 1 mM Ac-His-NHMe (B). Different laser intensities was obtained by interposing filters with transmissions in the 25 - 100 % range. The values of ϕ_1 and ϕ_2 correspond to different processes that are described in detail in Chapter 4.

In aqueous solutions, the structural volume changes can be assessed using a two-temperature method (Gensch & Braslavsky 1997). The sample acoustic waves ($E(t)$) were acquired at the temperature $T_{\beta=0}$, for which the thermal expansion coefficient of the solution, β, is zero. The value of $T_{\beta=0}$ can be determined experimentally by measuring the temperature at which the signal for the reference compound vanishes. The reference acoustic waves ($T(t)$) were measured at a slightly higher temperature, $T_{\beta\neq0} = 6.0$ °C. As previously described, the signals measured at $T_{\beta=0}$ originate solely from the structural volume changes in the solution and include no enthalpic contributions. The extent of the

observed structural volume change ΔV_i (estimated as milliliters per mole of absorbed photons) is calculated from ϕ_i as:

$$\Delta V_i = \phi_i E_\lambda \left(\frac{\beta}{C_p \rho} \right)_{\beta \neq 0} \qquad (3.14)$$

where E_λ is the energy of one mole of photons at the excitation wavelength (80.54 kcal mol^{-1} for 355 nm excitation) and $(\beta/C_p\rho)_{\beta \neq 0}$ is the thermoelastic parameter of the solution at $T_{\beta \neq 0}$. The two-temperature method also allowed the determination of the rate constants of protonation for each process, using τ_i values obtained from the fitting procedure.

Experiments conducted at multiple temperatures have been used to determine for each transient the heat release, the structural volume change and, from the temperature dependence of the rate constants, the activation energy (Callis et al. 1972; Peters & Snyder 1988; Braslavsky & Heibel 1992). This parameter was then plotted versus the fraction $(C_p\rho/\beta)_{\beta \neq 0}$. From the linear relation in Equation 3.15 (see also Equation 3.7) it is possible to determine the heat release after excitation per mole of photons absorbed Q_i (from the intercept) and the structural volume change per mole of photons absorbed ΔV_i (from the slope) for each ith process.

$$\phi_i E_\lambda = Q_i + \Delta V_i \left(\frac{C_p \rho}{\beta} \right) \qquad (3.15)$$

The temperature dependence of the rate constants can be analyzed by the following relationships:

$$k = k_0 e^{-E_a / RT} \qquad (3.16)$$

$$\ln k = \ln k_0 - \frac{E_a}{RT} \qquad (3.17)$$

where $k = 1/\tau$. The activation energy (E_a) and the pre-exponential factor k_0 could then be derived from a linear plot of $\ln k$ versus 1/T (Arrhenius plot).

3.4 Experimental Setup

Over the years, several cell designs for the time-resolved photoacoustic calorimetry have been developed (Rudzki et al. 1985; Melton et al. 1989; Arnaut et al. 1992; Braslavsky & Heibel 1992), but the front-face irradiation cell proved capable of determining both energy fractions and lifetimes with higher sensitivity. In the present work, a new temperature controlled front-face PAC flow cell was specifically built in our laboratory, following the front-face irradiation design described by Arnaut et al (Arnaut et al. 1992). Figure 3.3 shows a schematic representation of the PAC flow cell components. A dielectric mirror (10 mm thickness and 50 mm diameter) and an optical window that serves as the front surface of the cell (6 mm thickness and 25 mm diameter) were mounted in the aluminum block I and block II, respectively. Both the dielectric mirror and the optical window were sealed against the body aluminum frame by using indium wires partially embedded in circular cages drilled in the aluminum body. The aluminum blocks were pressed against each other with a thin copper spacer in between, which defines the thickness of the cell. We used an optical path length of 0.127 mm, which has been directly measured from the reflection of the acoustic waves generated on the cell by excitation of a photocalorimetric reference. Using this setup, more than 99 % of the light impinging on the front-face of the dielectric mirror is reflected back into the solution, thus minimizing the background signal.
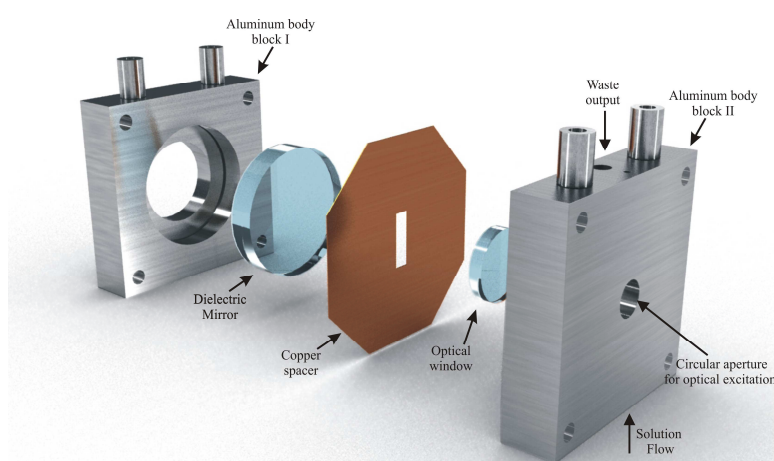
Figure 3.3: Schematic representation of the PAC flow cell components (Adapted from Reis 2011).

The aluminum frame (Block II) has two holes that allowed the flow of the solutions (see Figure 3.4). A circular aperture with 10 mm diameter allowed optical excitation through the optical window. The aperture in the aluminum block I allowed to mount the transducers (2.25 MHz or 0.5 MHz) against the back of the dielectric mirror. Good acoustic contact between the dielectric mirror and the transducer was facilitated using a thin layer of vacuum grease.
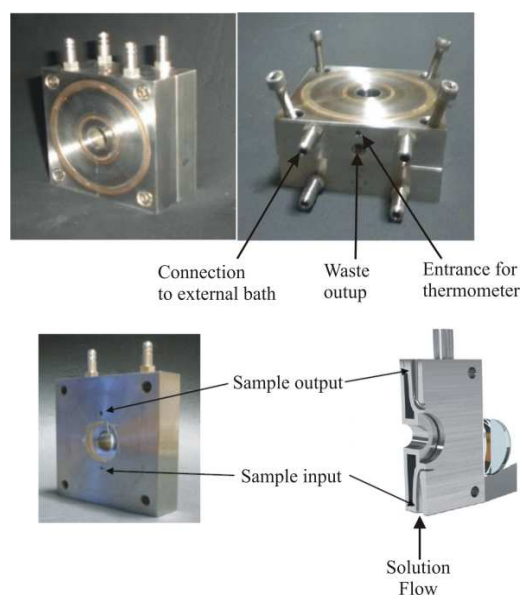
Figure 3.4: Technical details of design of the PAC flow cell related with solution flow and temperature control (Adapted from Reis 2011).

The cell temperature control was achieved by drilling channels all around the aluminum frame body and connecting them to a Julabo (model F-30C) thermostatic bath with external water circulation. The temperature was measured directly in the cell body using a Delta Ohm thermocouple thermometer (Figure 3.4). In order to achieve thermal stabilization, samples passed through a serpentine tube immersed in a temperature controlled water bath prior to enter the PAC flow cell. In the future, further improvements in the PAC flow cell may be implemented, such as a peltier device to control the temperature inside the cell (Reis 2011). In this new apparatus, the external thermostatic bath control is not necessary and the thermal stabilization will be achieved rapidly.

Prior to each PAC experiment, the absorbance of samples and reference solutions were carefully matched at the irradiation wavelength. Sample loading was performed using an automatic syringe pump (Kloehn model V6). The flow rate set-up allowed the average of a large number of laser shots (200-300) not only for the reference, but also for the samples and solvent, enabling an excellent signal to noise ratio. The solutions (samples, reference and solvent) were excited at 355 nm using the third harmonic of a nanosecond Q-switched Nd:YAG laser (Ekspla NL301G) (laser pulse width 6 ns). The spatial beam profile of the excitation laser has a circular shape (3.5 mm diameter) and its maximum energy per pulse was 1.0 mJ. Alternatively, the third harmonic of an Ekspla PL2143A Picosecond Nd:YAG Laser (30 ps pulse width) was used, with similar results. For all measurements we confirmed that the laser energy used was within the linear relationship between the acoustic signal and the energy of the laser. The signal was collected at four distinct laser intensities by interposing neutral density filters with transmissions in the 25-100 % range. Several combinations of liquid flow rate (1 ml min^{-1} to 2 ml min^{-1}), as well as, laser frequencies (from 1 Hz to 10 Hz) were used without any noticeable difference. The acoustic waves were detected using either 2.25 MHz (model A106S) or 0.5 MHz (model V101-RB) Panametrics transducers, amplified with a Panametrics ultrasonic amplifier (model 5676) and then recorded using a digital oscilloscope (Tektronix DPO7254). Figure 3.5 shows a schematic representation of the photoacoustic calorimetry apparatus used in this work.
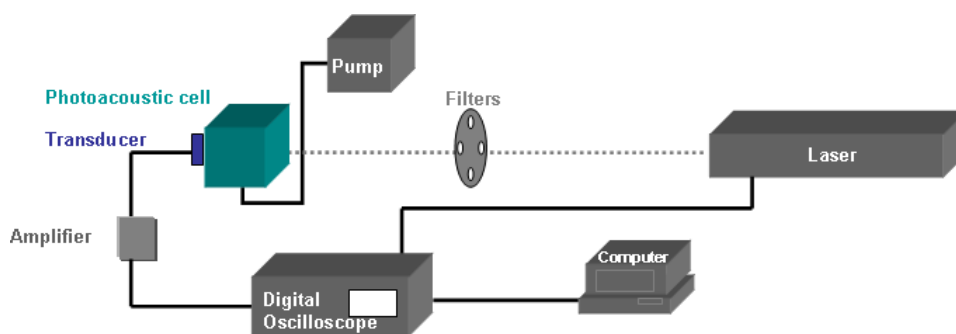
**Figure 3.5:** Schematic diagram of the time-resolved photoacaoustic calorimetry apparatus.

3.5 Photocalorimetric References

Photocalorimetric references are required for acoustic detection in TR-PAC experiments. Since the acoustic wave obtained with the reference compounds represents the instrumental response function $T(t)$ (Equation 3.10), they are of key importance in the determination of the thermodynamic and kinetic information contained in the acoustic wave obtained for the sample under investigation (Braslavsky & Heibel 1992; Rudzki et al. 1985; Abbruzzetti et al. 1999). Ideally, photocalorimetric references are compounds which are non-fluorescent, show no transients with a lifetime longer than a few nanoseconds, are photochemically stable and have unity efficiency in delivering the absorbed energy to the medium as heat, when the excited molecules return to their ground state (Abbruzzetti et al. 1999). These reference compounds should not exhibit multiphotonic or ground state depletion effects at the laser fluence used in the experiment. In addition, measurements of sample and reference acoustic waves must be performed in the same experimental conditions (temperature, ionic strength, solvent, excitation wavelength and cell geometry).

Several reference compounds have been identified for aqueous solutions and for organic solvents (Braslavsky & Heibel 1992; Abbruzzetti et al. 1999). Care must be taken not to use substances with low extinction coefficients at the excitation wavelength, since for these compounds, high concentrations are needed, which may affect the thermal expansion coefficient. Inorganic salts, such as Na_2CrO_4, $FeCl_3$ and $Fe(bpy)_3Cl_2$, are suitable as photocalorimetric references for UV-visible ($\lambda > 300$ nm) in aqueous solutions. However, most of the inorganic salts are toxic and of use over a limited wavelength range. Additionally, all of the inorganic salts show low molar absorption coefficient which requires the use of high concentrations, thus affecting the thermoelastic parameters of the solution. A set of non-toxic, water-soluble, compounds have been investigated to probe their viability as photocalorimetric references in aqueous solutions in the UV-visible region (Abbruzzetti et al. 1999). Among them are brilliant blue G, brilliant black BN, new coccine and indigo carmine. Bromocresol purple (BP) is one of the few organic photocalorimetric references recommended for these applications. Due to the pK_a of BP the use of the compound in unbuffered neutral aqueous solutions is difficult because the absorbance is unstable and therefore must be employed only at pH below 5 or above 9.

In the present work, the photocalorimetric reference used was BP that is frequently applied in TR-PAC experiments (Abbruzzetti, Crema, et al. 2000; Abbruzzetti

et al. 1999; Abbruzzetti, Viappiani, et al. 2000). As previously mentioned in section 3.3, the thermoelastic parameter of the solution ($\beta/C_p\rho$) depends strongly on temperature. In pure water, the signal for the reference compound vanishes at approximately 3.9 ºC ($T_{\beta=0}$), because the thermal expansion coefficient of water is zero, $\beta = 0$. The acoustic wave for reference compounds is positive above and negative below this temperature. Figures 3.6 (A) and 3.7(A) present the temperature dependence of the acoustic signals of BP solutions at pH 9 ($A_{355} \approx 0.65$, 1 cm path length cell), upon irradiation at 355 nm, and using 2.25 MHz and 0.5 MHz transducers. As can be observed, the acoustic waves of BP differ in shape when the experiments are performed with different transducers. Decreasing the temperature promotes a reduction in amplitude of the acoustic waves detected for BP. Using our experimental setup and either 2.25 MHz or 0.5 MHz transducers, there is no signal of BP at 3.0 ºC ($T_{\beta=0}$). At 2.0 ºC the first peak of the acoustic wave is negative (see Figure 3.6). Moreover, the superimposition of the theoretical values of temperature-dependent parameter ($\beta/C_p\rho$) for pure water and the relative intensity of the photoacoustic signals obtained using both transducers is shown in Figures 3.6(B) and 3.7 (B). Only slight deviations between the theoretical and experimental values are observed.
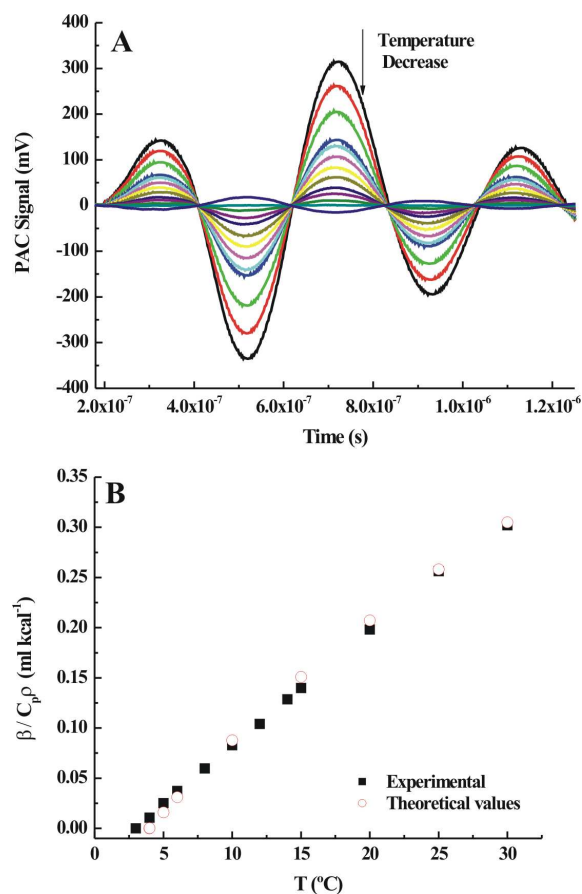
Figure 3.6: Temperature dependence of the acoustic waves of bromocresol purple (BP) upon irradiation at 355 nm, using the 2.25 MHz transducer. (A) BP acoustic waves collected at several temperatures, varying from 30.0 ℃ to 2.0 ℃. (B) Comparison between the theoretical values of temperature-dependent parameter $(\beta/C_p\rho)$ and the relative intensity of the photoacoustic signals shown in Figure 3.6(A), at each temperature. At the different temperatures, the maximum value of each photoacoustic signal was collected and then normalized against the $(\beta/C_p\rho)$ value at 30.0 ℃, the highest temperature.
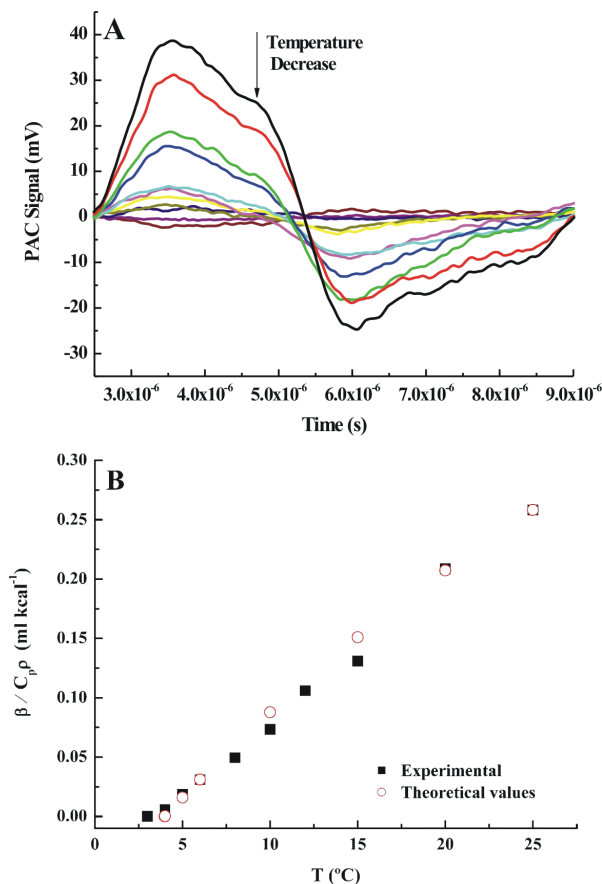
Figure 3.7: Temperature dependence of the acoustic waves of bromocresol purple (BP) upon irradiation at 355 nm, using the 0.5 MHz transducer. (A) BP acoustic waves collected at several temperatures, varying from 25.0 ℃ to 3.0 ℃. (B) Comparison between the theoretical values of temperature-dependent parameter ($\beta/C_p\rho$) and the relative intensity of the photoacoustic signals shown in Figure 3.7(A), at each temperature. At the different temperatures, the maximum value of each photoacoustic signal was collected and then normalized against the ($\beta/C_p\rho$) value at 25.0 ℃, the highest temperature.

For aqueous solutions containing salts or other additives at mM concentrations or higher, $(C_p\rho/\beta)_T$ and $T_{\beta=0}$ must be experimentally determined comparing the signal obtained for a calorimetric reference in the solvent of interest and in water (Braslavsky & Heibel 1992; Gensch & Viappiani 2003). Figure 3.8 shows the amplitude of the second positive peak versus the $C_p\rho/\beta$ in aqueous solution, at different temperatures. In aqueous solution the average amplitude of the second positive peak is close to 43 mV while in presence of NaCl the average value obtained is higher, corresponding to approximately 55 mV. Thus, there is an increase of approximately 20 % in amplitude in the presence of 100 mM NaCl. Moreover, the BP photoacoustic signal vanishes at a temperature lower than

37

3.0 ℃. Using a 100 mM NaCl as solution the temperature $T_{\beta=0}$ is 1.8 ℃. The BP waveform acquired in the presence of 100 mM NaCl is shifted relatively to the one detected in water, because the presence of dissolved salts in aqueous solutions produces an increase in the sound speed (Sigrist 1986), which accounts for the observed difference in the time it takes for the signal to reach the detector.
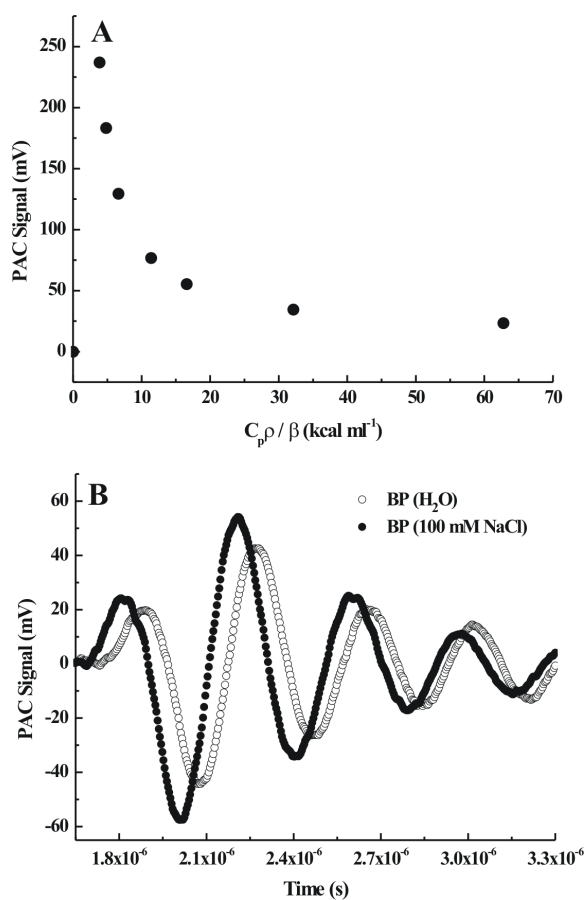

Figure 3.8: (A) Average amplitude of the second positive peak versus the thermoelastic parameter ($C_p\rho/\beta$), at different temperatures and in aqueous solution. (B) The photoacoustic signals of BP in the absence (open circles) and in presence of 100 mM NaCl (filled circles).

3.6 Laser-induced pH jump

The fast production of an acidic solution using a short laser pulse attracted much interest over the last 30 years. The acidification of a photoacid solution with a short laser pulse can be used to rapidly perturb the acid-base equilibria and to initiate acid-catalyzed reactions in less than 10 ns, which are of interest to uncover mechanisms of acid-base catalysis (Politi & Fendler 1984), study the initial steps of protein folding (Abbruzzetti, Crema, et al. 2000) or phototrigger drug delivery (Shum et al. 2001; Carvalho et al. 2011). In the present work, we have used a laser-induced pH jump technique coupled with TR-PAC detection to monitor directly the dynamics and energetics of early events in protein unfolding/folding due to site-specific protonation of ionizable amino acid side chains. In fact, the acid-base behavior of amino acids is an important subject of study due to their prominent role in enzyme catalysis, substrate binding and protein structure.

In our experiments, the acid pH jump was achieved through the photoexcitation of a caged compound, *o*-nitrobenzaldehyde (*o*-NBA), that transfer very rapidly a proton to the solution, being capable of transforming a neutral aqueous solution into an acidic one within nanoseconds. More than 100 years ago, Ciamician and Silber reported the photo-induced transformation of *o*-NBA into *o*-nitrosobenzoic acid (Figure 3.9) (Ciamician & Silber 1901). The proton release mechanism of *o*-NBA in water has been extensively studied using computational and experimental approaches (Bonetti et al. 1997; Viappiani et al. 1998; Leyva et al. 2008; Donten et al. 2011). Under irradiation, the *o*-NBA molecule is converted to *o*-nitrosobenzoic acid and protons are released with a quantum yield of about 0.40 in aqueous solutions. The reaction begins nearly instantly upon photoexcitation with the formation of the ketene intermediate (Figure 3.9(B)) on a time scale measured in hundreds of femtoseconds (Donten et al. 2011). This intermediate reacts in a solvent assisted way to produce *o*-nitrosobenzoic acid with a characteristic time of 7 ps. Finally, in the right pH conditions (pH > 3) the product (*o*-nitrosobenzoic acid) releases a carboxyl proton within a few nanoseconds. This step is directly responsible for the produced pH jump.
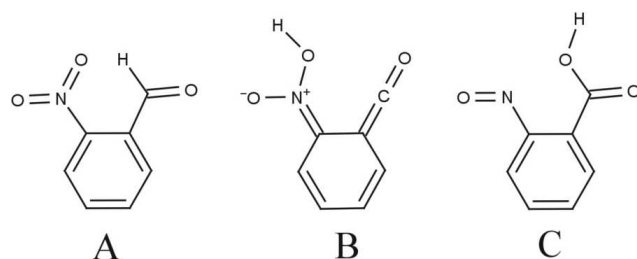
Figure 3.9: Molecular structures of *o*-NBA (A), the established ketene reaction intermediate (B), and the photoproduct *o*-nitrosobenzoic acid (C) (*o*-nitrosobenzoic acid $pK_a < 4$).

Figure 3.10 reports an example of the signal observed for *o*-NBA in water, at 3.0 ℃ and pH 7.0, using the PAC flow cell developed in our laboratory. As observed in previous studies (Bonetti et al. 1997; Viappiani et al. 1998), under pH conditions below 9, the proton release from *o*-NBA is accompanied by a prompt (lifetime below a few nanoseconds) volume contraction of the solution, induced by the solvation of the newly formed charges. Figure 3.10 shows that a negative oscillation dominates the photoacoustic signal of the *o*-NBA, which can be related to the volume contraction observed at pH 7. The value of ϕ_1 ($\phi_1 = -0.83$), associated with *o*-NBA photolysis, is obtained from the extrapolation to zero laser intensity of the ϕ_1 values measured at four different laser intensities. The corresponding structural volume change, calculated using Equation 3.14, is $\Delta V_1^{exp} = -2.2$ ml mol^{-1}. The measured volume contraction must be corrected for the quantum yield of the photo-induced reaction in aqueous solution (i.e. for a mole of photoreleased protons), $\Phi = 0.4$. Thus, the extent of the structural volume change for solvation of the formed ions is therefore calculated as $\Delta V = -5.4$ ml mol^{-1}. This value is in good agreement with previous results using TR-PAC, which report $\Delta V = -5.2$ ml mol^{-1} (Bonetti et al. 1997; Viappiani et al. 1998).

Between pH 9 and 12, two processes are observed and the prompt contraction due to ion solvation is followed by a large volume expansion ($\Delta V_2^{exp} = \sim 10$ ml mol^{-1}) occurring within lifetimes varying from 400 ns to 89 ns (Bonetti et al. 1997). This latter process is related with the reaction of the photodetached protons with hydroxyl ions, leading to water formation. However, above pH 10.25 the lifetimes of the two processes are too close to be resolved and single process is observed, which corresponds to the volume expansion.

In the present work, the pH conditions used varied between 5 and 8. The fit to the experimental data over this pH range is well represented by a single exponential decay

(see example in Figure 3.10). The prompt volume contraction of approximately -5 ml mol^{-1} varied slightly over the range of pH conditions used. Moreover, experiments performed in aqueous solutions containing 100 mM NaCl lead to a reduction of the structural volume contraction observed ($\Delta V = \sim$ -4 ml mol^{-1}). This effect is consistent with previous results that reported a decrease in the extent of the volume contraction (ΔV = -4.9 ml mol^{-1}) in the presence of 100 mM NaCl (Bonetti et al. 1997).
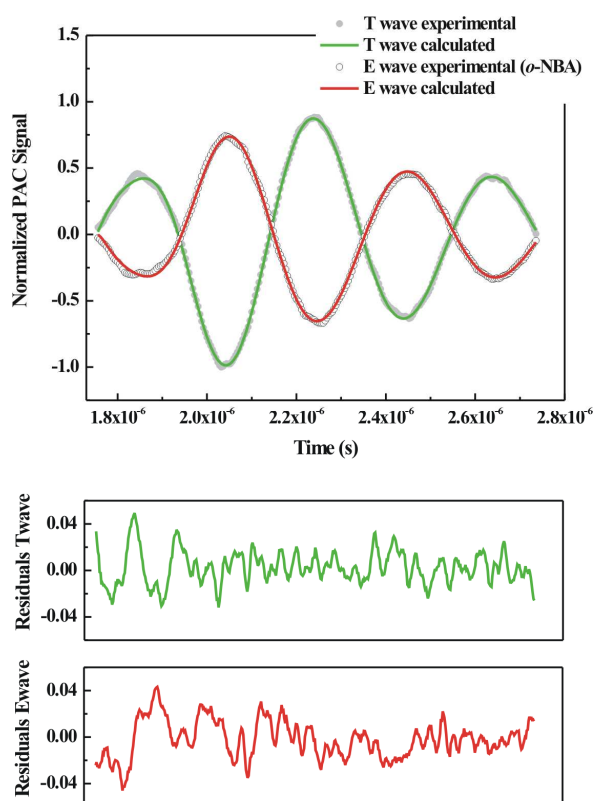
Figure 3.10: Examples of typical photoacoustic signals for bromocresol purple (BP) reference (T wave) and the photolysis of *o*-NBA (E wave) in water, at pH 7, and 100 % laser energy ($\sim$ 1 mJ). The E and T waves depicted were corrected for the background signal from the solvent (O wave), and normalized for the absorbance at the excitation wavelength (A_{355} = 0.65, 1 cm path length cell). The waveform for BP (filled circles) was acquired at 6.0 °C, whereas the sample waveform (open circles) was taken at 3.0 °C. The solid lines represent the calculated T and E waves obtained through the fitting procedure using the *CPAC* software. The best fit was obtained with a single exponential decay with ϕ_1 = - 0.75 and lifetime below the experimental resolution (< 10 ns).

To determine the magnitude of the pH jump is necessary to obtain the number of photons and the irradiated volume of the photoacid molecules in the experimental conditions used. Table 3.1 presents the calculations used to obtain the magnitude of the pH jump. In order to take into consideration the possibility of non-linear absorption processes under intense laser fluence (Arnaut et al. 1992). All photoacoustic measurements were performed under four distinct laser intensities. The laser energy per pulse varied between 1 mJ and 300 μJ, and the energy of one photon at 355 nm is 5.59 x 10^{-19} J ($E = h$ ν). Thus, the number of moles of photons produced per laser pulse is 8.91 x 10^{-10} mol at 300 μJ, and 2.97 x 10^{-9} mol at 1 mJ.

Considering the cell geometry, with a mirror enabling double irradiation of the sample, the very thin irradiation path length (cell thickness of 0.127 mm), and the photoacid absorbance at 355 nm (~0.6), the fraction of photoacid molecules that absorb photons can be calculated (Table 3.1). Thus, knowing the number of photons that irradiate the cell, the absolute number of photoacid molecules that absorb photons is calculated. As for *o*-NBA the photodissociation quantum yield is 0.4 (George & Scaiano 1980) one can calculate the number of injected protons in the absorbing volume.

For the sample concentrations used (higher than 100 μM) the quantity of molecules in the area under irradiation (a minimum value of 1.22 x 10^{-10}) was always higher than the number of protons formed (a maximum of 4 x 10^{-11} mol). Assuming that the volume of irradiated sample is 1.22 x 10^{-6} dm^3 (corresponding to a laser pulse diameter of 3.5 mm), if the starting pH (prepulse pH) is 5.3 a post pulse pH of 4.4 is obtained. For a starting pH of 7.3, the post pulse pH is 4.8 (Table 3.1). Those are instantaneously pH variations felt by the samples in the irradiated volume, which tend to dissipate over time.

Table 3.1: Determination of the pH jump magnitude.

Laser Pulse Energy mJ	Number of photons[1] Mol	Fraction of o-NBA molecules that absorb[2]	Number of o-NBA molecules that absorb[3] mol	Number of released protons[4] mol	Additional concentration of protons (ΔH^+)[5] M	pH$_{initial}$	pH$_{after\ laser\ pulse}$[6]
1.0	2.97×10^{-9}	0.0345	1.02×10^{-10}	4.09×10^{-11}	3.35×10^{-5}	5.3	4.41
						7.3	4.47
0.30	8.91×10^{-10}	0.0345	3.07×10^{-11}	1.23×10^{-11}	1.01×10^{-5}	5.3	4.82
						7.3	4.99

[1] Number of photons= E_{laser}/ E_{photon}/ N_A; Energy of one photon calculated as E = hc/λ with h = $6.6260 10^{-34}$ J s^{-1} , c = 3 x10^8 m s^{-1}; λ = 355 nm; N_A = 6.02 x 10^{23} mol^{-1} .

[2] Fraction of o-NBA molecules that absorb = (1-10^{-Abs}); Abs = photoacoustic cell optical path length x absorption (1cm);

[3] Number of o-NBA molecules that absorb = number of photons x fraction of o-NBA molecules that absorb.

[4] Number of released protons = Number of o-NBA molecules that absorb x photodissociation quantum yield (Φ); $\Phi_{o\text{-}NBA}$ = 0.4.

[5] Additional concentration of protons ΔH^+ = number of released protons / $V_{irradiated}$; $V_{irradiated}$ = π x $r_{laser\ pulse}^2$ x cell thickness with $r_{laser\ pulse}$ = 0.175 cm, cell thickness = 0.127 mm; optical path length = 0.254 mm.

[6] pH$_{after\ laser\ pulse}$ = -log (10$^{pH_{initial}}$ + ΔH^+).

43

Chapter 4

Probing the energetics and dynamics of protonation reactions and their contribution to protein folding by photoacoustic calorimetry

4.1 Introduction

Amino acids are the monomeric building blocks of proteins. The linear sequence of amino acids in a protein is known as its primary structure, and it is today generally accepted that the folding of a particular protein and the resulting native structure is autonomously governed and determined by the amino acid sequence of the protein and its natural solvent environment. Protonation of specific amino acid side chains is sometimes sufficient to induce unfolding/folding processes that may occur on the nanosecond to microsecond time scales. Therefore, characterization of the energetics and dynamics of protonation reactions involving amino acids is essential for the understanding of the earliest steps in protein unfolding/folding induced by pH transitions.

Amino acids with ionizable side chains make up, on average, 29 % of the amino acids in proteins (Pace et al. 2009). The acid-base behaviour of such amino acids is an important subject of study due to their role in enzyme catalysis, substrate binding and protein structure. There are many examples of amino acid residues with ionizable side chains in the active sites of proteins that play central roles in protein functions. In particular, the protonation of residues such as aspartic acid (Asp) and glutamic acid (Glu)

accompanies proton pumping by bacteriorhodopsin (Lanyi 1998), electron transfer reactions (Mezzetti et al. 2002) or even Ca^{2+} release from the Ca^{2+} ATPase (Barth & Zscherp 2000). Furthermore, histidine (His) residues are frequently identified as essential for enzymatic activity. As an example, two His residues located at the active site of bovine pancreatic ribonuclease A (RNase A), His-12 and His-119, are involved in the RNA cleavage reaction catalyzed by this protein (Park et al. 2001). Seven of the 20 amino acid side chains contain groups that readily ionize. For example, at high pH (low acidity conditions), the amino acid side chains containing carboxylic acids tend to be negatively charged (deprotonated) while the ones containing amines tend to be uncharged (unprotonated). At low pH (high acidity), the opposite is verified. Thus, for Asp, Glu, tyrosine (Tyr), and cysteine (Cys), the ionizable side chains are uncharged below their pK_a and negatively charged above their pK_a. For histidine (His), lysine (Lys) and arginine (Arg), the side chains are positively charged below their pK_a and uncharged above their pK_a. The average pK_a values for the ionizable side chains as well as the average content of the corresponding amino acids reported for several proteins are given in Table 4.1.

Mapping the early steps in pH-induced conformational changes occurring in proteins and peptides requires the characterization of the protonation/deprotonation reactions involving the amino acid residues with ionizable side chains. In fact, amino acid side chains and their roles in stabilizing protein structure and in catalysing enzymatic reactions have been increasingly investigated at the molecular level by techniques such as infrared spectroscopy and neutron protein crystallography. The latter provides the definitive protonation states of the amino acid residue in a protein because neutron scattering can identify the presence of hydrogen atoms in a molecular structure (Niimura & Bau 2008), while infrared spectroscopy may characterize diverse information on amino acid side chains, like protonation state, charge, accessibility to H-bonding patterns and conformational freedom (Barth, 2000). However, techniques able to assess conformational and dynamic parameters in correlation with the protonation state of amino acid side chains in proteins are still very limited.

In the present work, the sub-millisecond protonation dynamics of several ionizable amino acids were studied after a rapid acidic pH-jump following laser-induced proton release from the caged photolabile compound *o*-nitrobenzaldehyde (*o*-NBA), coupled with time-resolved photoacoustic calorimetry (TR-PAC) detection. In addition to its sensitivity to enthalpic and volume changes, TR-PAC provides nanosecond to microsecond time resolution to those measurements. Previously published results have

been obtained using laser-induced pH jumps coupled with TR-PAC to explore pH-induced conformational changes in proteins and polypeptides such as apomyoglobin (Abbruzzetti, Crema, et al. 2000; Miksovská & Larsen 2003), poly-L-lisine (Viappiani et al. 1998) and poly-L-glutamic acid (Abbruzzetti, Viappiani, et al. 2000). One interesting result from previous work revealed that neutralization of Glu induces a volume expansion due to the disappearance of two charges, corresponding to proton and charged amino acid moiety, with an apparent bimolecular rate on the order of 10^{10} M^{-1} s^{-1} (Abbruzzetti, Viappiani, et al. 2000).

Table 4.1: Summary of the average pK_a values of the ionizable amino acid side chains and the average content of ionizable amino acid residues tabulated from 78 proteins (adapted from Pace et al. 2009). The pKa values of the ionizable side chains for capped amino acid derivatives of Asp, Glu and His, and the pK_a of imidazole are also shown.

Amino acid	pK_a value (side chain)	Content (%)
Asp	3.5	5.2
Glu	4.2	6.5
His	6.6	2.2
Cys	6.8	1.2
Tyr	10.3	3.2
Lys	10.5	5.9
Arg	12.3[a]	5.1
C-terminus	2.4	
N-terminus	6.8	
Ac-Glu-NH$_2$	4.50[b]	
Ac-Asp-NH$_2$	4.08[b,c]	
Ac-His-NHMe	6.38[c,d]	
Imidazole	6.95	

[a] pK_a value obtained in alanine pentapeptides.
[b] Data from Yasuhiko Nozaki & Charles Tanford 1967.
[c] Data from Marti 2005.
[d] Data from Tanokura et al. 1976.

Before performing TR-PAC studies using biological systems exhibiting high-level of complexity, our primary purpose is to fully understand, at the molecular level, fundamental events occurring during the protonation/deprotonation of individual amino

acids. It is worth to note that the pK_a of ionizable side chains in isolated amino acids are likely to be shifted by the neighboring negative and positive charges of its C and N termini, respectively (Nozaki & Tanford 1967; Tanokura et al. 1976). Moreover, in a protein the amino acid's termini are involved in peptide bonds with the neighbouring amino acids. Being so, model compounds are frequently used and should be as similar as possible to an amino acid residue in a protein. Here, three model compounds have been used to characterize the protonation reactions involving Glu, Asp and His. Figure 4.1 presents the structure of such model compounds, namely acetyl-L-isoglutamine (Ac-Glu-NH$_2$), acetyl-L-isoasparagine (Ac-Asp-NH$_2$) and acetyl-L-histidine methylamide (Ac-His-NHMe). Several studies using these amino acid derivatives as model compounds have shown that the imidazole group of Ac-His-NHMe and the carboxylate groups in both Ac-Glu-NH$_2$ and Ac-Asp-NH$_2$ present intrinsic (or unperturbed) pK_a values similar to those typically found in proteins or peptides (Tanokura et al. 1976; Perutz et al. 1985; Marti 2005).

This chapter describes the structural volume changes, enthalpies and dynamics resulting from the protonation in aqueous solutions of isolated amino acid model compounds and their mixtures at different concentration ratios, promoted by an ultrafast laser-induced pH jump and using TR-PAC detection. These protonation reactions are the initial events occurring in pH-induced protein or peptide folding/unfolding processes, and new methodologies able to distinguish protonation of ionizable groups from the subsequent folding/unfolding of a polypeptide chain are essential to fully characterize the contribution of such amino acids in protein folding. Moreover, new clues about the thermodynamics and kinetics of protonation reactions involving ionizable amino acids may help to further clarify their roles in stabilizing protein structure and in catalysing enzymatic reactions.
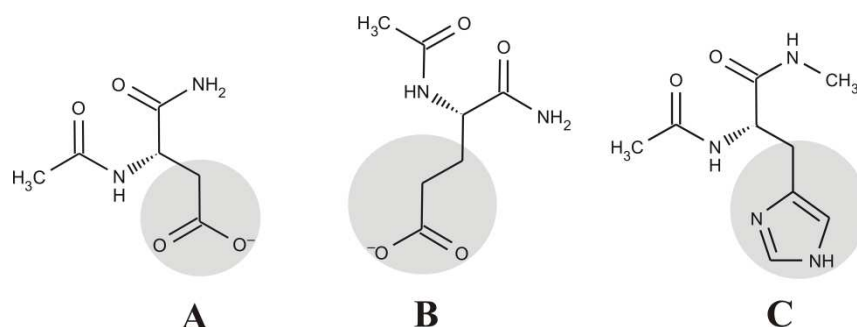
Figure 4.1: Structure of amino acid model compounds (A) acetyl-L-isoasparagine (Ac-Asp-NH$_2$), (B) acetyl-L-isoglutamine (Ac-Glu-NH$_2$) and (C) acetyl-L-histidine methylamide (Ac-His-NHMe). Amino acid derivatives substituted at the N-terminal by a group Acetyl (Ac), and at the C-terminal by an amine ($-$NH$_2$) or N-methylamine ($-$NHMe). The grey circles highlight the ionizable side chains, namely the negatively charged carboxylic acids in both Ac-Glu-NH$_2$ and Ac-Asp-NH$_2$, and the imidazole ring in Ac-His-NHMe.

4.2 Materials and Methods

4.2.1 Sample Preparation

The amino acid model compounds acetyl-L-isoglutamine (Ac-Glu-NH$_2$), acetyl-L-isoasparagine (Ac-Asp-NH$_2$) and acetyl-L-histidine methylamide (Ac-His-NHMe) were purchase from Bachem (Bubendorf, Switzerland). Bromocresol purple (BP), o-nitrobenzaldehyde (o-NBA) and imidazole were obtained from Sigma-Aldrich Chemical Company, St. Louis, USA.

Sample solutions for photoacoustic measurements were prepared by dissolving the amino acid model compounds Ac-Glu-NH$_2$, Ac-Asp-NH$_2$, Ac-His-NHMe and imidazole into an aqueous solution with sufficient o-NBA to produce a final optical absorption of 0.6 in a 1.0 cm path length cell, at 355 nm. Concentrations of amino acid model compounds and imidazole varied between 200 μM and 2.0 mM. In addition, sample solutions containing mixtures of both Ac-Glu-NH$_2$ and Ac-His-NHMe at different concentration ratios were also prepared. Bromocresol purple (BP) was used as the photocalorimetric reference compound and it was dissolved in an aqueous solution and its optical absportion was adjusted to match that of the sample solutions at 355 nm. The pH of sample and reference solutions was adjusted by addition of concentrated HCl or NaOH and measured using a glass microelectrode. The pH of BP solutions was adjusted to 9.0, in

order to avoid instability in optical absorption at the excitation wavelength (Abbruzzetti et al. 1999). Sample solutions of Ac-Glu-NH$_2$ and Ac-Asp-NH$_2$ were prepared at approximately pH 5.3, while sample solutions of Ac-His-NHMe and imidazole were prepared at approximately pH 7.3 and 7.8, respectively. To evaluate the effect of ionic strength on the rate of protonation reactions, photoacoustic measurements were also performed using both sample and BP solutions prepared in aqueous solutions containing 100 mM NaCl. All experiments were repeated at least three times.

4.2.2 Time-resolved Photoacoustic Calorimetry

Experiments of laser-induced pH jump coupled with photoacoustic detection were performed using a time-resolved photoacoustic calorimetry flow cell developed in-house that follow the front-face irradiation design described by Arnaut et al. (Arnaut et al. 1992), connected to systems for temperature control and automatic injection (Kloehn syringe pump). In Chapter 3, a detailed description of the experimental setup is presented. The light source, operated at 355 nm, was the third harmonic of a nanosecond Q-switched Nd:YAG laser (Ekspla NL301G). The laser pulse width was approximately 6 ns, and the pulse repetition rate was 10 Hz. Before initiating each experiment, the maximum laser pulse energy was verified and adjusted to approximately 1 mJ/pulse. Furthermore, each solution analyzed (sample, BP and solvent) was excited with four different intensities corresponding to 25, 50, 75 and 100 % of the full laser intensity by employing neutral density filters. The PAC signals were measured between 1.8 ºC and 20.0 ºC, and the temperature variation during an experiment was less than 0.5 ºC. The sample data were analyzed by comparison with those for the photocalorimetric reference compound, which releases all the energy absorbed upon photoexcitation as heat with a quantum efficiency of 1.0. The photoacoustic pressure waves were detected with a 2.25 MHz Panametrics transducer (model A106S). The PAC signals from 200 shots were average, pre-amplified with a Panametrics ultrasonic preamplifier (model 5676) and then recorded using a digital oscilloscope (Tektronix DPO7254).

The principles of deconvolution of photoacoustic waveforms are described in detail in Chapter 3. Briefly, the energy fractions and lifetimes of a sample $E(t)$ can be

obtained by the convolution of the instrumental response, or reference waveform $T(t)$, with the time-dependent function of the decay process $H(t)$.

$$E(t) = T(t) \otimes H(t) \qquad\qquad (4.1)$$

Experimentally, the function $T(t)$ can be obtained using a photocalorimetric reference compound such as BP, that releases nonradiatively (only heat deposition) all the radiative energy absorbed, in a time faster than the transducer resolution.

The function $H(t)$ represents the overall time-dependent volume change is written as the summation of sequential single exponential terms:

$$H(t) = \sum_i \frac{\phi_i}{\tau_i} e^{-(t/\tau_i)} \qquad\qquad (4.2)$$

where ϕ_i and τ_i are the respective energy fraction and decay time for the ith component in the sum of the exponentials. The *CPAC* software developed in our laboratory was used to obtain ϕ_i and τ_i parameters (Schaberle et al. 2010). This software provide an analytical description for the instrumental response photoacoustic wave $T(t)$, and the analytical solution for the convolution between $T(t)$ and the heat function $H(t)$. The ϕ_i and τ_i parameters are varied until the calculated $E(t)$ fits the experimental wave $E(t)$. The kinetics of processes occurring faster than roughly 10 ns cannot be resolved, but the integrated enthalpy and volume changes can be quantified from the amplitude of the acoustic wave.

Structural volume changes as a function of the concentration of amino acid model compound or the concentration ratios of the mixtures under study were determined using a two-temperature method (Gensch & Braslavsky 1997). The sample waveforms were acquired at the temperature $T_{\beta=0}$, for which the thermal expansion coefficient of the solution, β, is zero. The value of $T_{\beta=0}$ can be determined experimentally by measuring the temperature at which the signal for the reference compound vanishes. The temperature obtained for $T_{\beta=0}$ in an aqueous solution was 3.0 ºC, while in the presence of 100 mM NaCl we found $T_{\beta=0} = 1.8$ ºC. The reference waveforms were measured at a higher temperature, $T_{\beta\neq0} = 6.0$ ºC. Signals measured at $T_{\beta=0}$ originate solely from the structural volume changes in the solution and include no enthalpic contributions. The extend of the

observed structural volume change ΔV_i (estimated as milliliters per mole of absorbed photons) is calculated from ϕ_i as:

$$\Delta V_i = \phi_i E_\lambda \left(\frac{\beta}{C_p \rho} \right)_{\beta \neq 0} \qquad (4.3)$$

where E_λ is the energy of one mole of photons at the excitation wavelength and $(\beta/C_p\rho)_{\beta\neq0}$ is the thermoelastic parameter of the solution at $T_{\beta\neq0}$. The two-temperature method also allowed the determination of the rate constants of protonation for each amino acid model compound, using τ_i values obtained from the fitting procedure.

Experiments conducted at multiple temperatures have been used to determine for each transient the heat release, the structural volume change and, from the temperature dependence of the rate constants, the activation energy (Callis et al. 1972; Peters & Snyder 1988; Braslavsky & Heibel 1992). Deconvolution was performed at several temperatures, and the pre-exponential factors ϕ_i were used to determine the energy content, $E_\lambda \phi_i$ of the transient at each temperature. This parameter was then plotted versus the ratio $(C_p\rho/\beta)_{\beta\neq0}$. From the linear relation:

$$\phi_i E_\lambda = Q_i + \Delta V_i \left(\frac{C_p \rho}{\beta} \right) \qquad (4.4)$$

it is possible to determine the heat release after excitation per mole of photons absorbed Q_i (from the intercept) and the structural volume change per mole of photons absorbed ΔV_i (from the slope) for each ith process.

In both methods, two-temperature and multiple-temperature, the volume changes can be converted in molar reaction volume (expressed as milliliters per mole of photons released) dividing ΔV_i by the deprotonation quantum yield of o-NBA, $\Phi_{H+} = 0.4$, (George & Scaiano 1980). The heat released Q_i obtained using the multiple-temperature method can be converted in enthalpy change using the same assumption.

The temperature dependence of the rate constants can be analyzed by the following relationships:

$$k = k_0 e^{-E_a / RT} \qquad\qquad\qquad (4.5)$$

$$\ln k = \ln k_0 - \frac{E_a}{RT} \qquad\qquad\qquad (4.6)$$

where $k = 1/\tau$. The activation energy (E_a) and the pre-exponential factor k_0 could then be derived from a linear plot of $\ln k$ vs $1/T$ (Arrhenius Plot).

4.3 Results

The principle of photoacoustic calorimetry is relatively simple. Basically, in TR-PAC one monitors the pressure wave caused by the volume change generated in the system on a time scale of tens of nanoseconds to several microseconds. The pressure wave arises from the volume changes that are produced by radiationless relaxation (heat deposition) and structural rearrangements at the molecular level, initiated by a laser pulse. This pressure wave is propagated through the solution and can be detected by piezoelectric transducers located in the cell plane parallel to the laser beam direction and recorded by a digital oscilloscope. Here, laser irradiation at 355 nm, in the presence of o-NBA, promotes an ultrafast pH jump due to the rapid release of protons following photolysis of o-NBA. Subsequent to the laser-induced generation of protons, the photoacoustic waves of the ionizable compounds under study were collected. A detailed description of the well studied proton cage o-NBA and its proton photo release mechanism is presented in Chapter 3. Briefly, the release of protons by o-NBA, both in the absence and in the presence of proton-accepting groups, is accompanied by a fast subresolution contraction (lifetime below a few nanoseconds), at pH around and below neutrality.

In this chapter, the main subject of study is the protonation reactions involving the amino acid models presented in Figure 1.1, which represent two classes of ionizable amino acids. Above their pK_a values, both Ac-Asp-NH$_2$ and Ac-Glu-NH$_2$ exhibit side chains with carboxylate groups negatively charged. In Ac-His-NHMe the side chain is the imidazole ring that is uncharged above its pK_a. The pH before laser irradiation (prepulse pH) was adjusted to approximately one unit lower than the pK_a. At the prepulse pH only few molecules are protonated and after laser irradiation and o-NBA photolysis a high

percentage are protonated due to the fast pH jump. Although the protonation of the imidazole group has not been explored by laser-induced pH jump techniques, compounds such as acetate and glutamic acid (Glu) have already been studied (Abbruzzetti, Viappiani, et al. 2000). Previously published results have shown that the structural volume change expected for the protonation of carboxylates ranges between 6 ml mol^{-1} and 17 ml mol^{-1}, depending on the nature of the group attached to the carboxylate (Abbruzzetti, Viappiani, et al. 2000; Borsarelli & Braslavsky 1998). Two-temperature and multiple-temperature experimental procedures for photoacoustic measurements in aqueous solutions, were performed and the rate constants, reaction enthalpies, volume changes and activation energies were derived by analyzing the time profile of the acoustic wave generated by he heat and volume changes associated with the protonation reactions.

4.3.1 Concentration Dependence of Proton-accepting Groups: Two-Temperature Method Experiments

The overall photoacoustic signal is generally composed by a thermal component related with the release of heat, and a structural part due to the reaction volume variation of the photo initiated reactions. In aqueous solutions, these thermal and volumetric contributions can be separated by performing measurements at two different temperatures (the so called two-temperature method, previously described in section 4.2.2). Although enthalpies cannot be determined, the rate constants for protonation and the structural volume changes can be assessed performing experiments at $T_{\beta=0}$ and using different proton acceptor concentrations.

Figure 4.2 show examples of the photoacoustic waves obtained for Ac-Asp-NH$_2$, Ac-His-NHMe and o-NBA measured at 3.0 ℃, along with the bromocresol purple (BP) photoacoustic wave acquired at 6.0 ℃. As other photocalorimetric reference compounds, BP releases nonradiatively (only heat deposition) all the radiative energy absorbed in a time faster than the transducer resolution, producing a photoacoustic signal that is characteristic of a fast volume expansion. The signals obtained for o-NBA in an aqueous solution are inverted when compared with the waveform of BP, at both pH values of 5.3 and 7.3. This behaviour is in agreement with previously published work and reflects the volume contraction typically observed for o-NBA photolysis due to solvation of the photo released protons and nitrobenzoate anions (Bonetti et al. 1997a).

The experiments using the two-temperature method have been performed using several concentrations of proton-accepting groups. Figure 4.2(A) shows the photoacoustic waves for increasing concentrations of Ac-Asp-NH$_2$ in presence of o-NBA, at pH around 5. The waveforms exhibit significant differences in amplitude, as well as, in phase when compared with the ones acquired for o-NBA in similar solvent conditions. Qualitatively, our results suggest that besides the fast release of protons by o-NBA there is a second process occurring that produces an additional photoacoustic wave due to the protonation of the side chain of Ac-Asp-NH$_2$ containing a negatively charged carboxylate group at pH 5. Moreover, our results evidence that the protonation reaction is concentration-dependent because the photoacoustic waves acquired were found to be progressively shifted in phase and the amplitude diminished upon increasing concentrations of proton-accepting groups. Since the increase in concentration promotes a decrease in amplitude, our results also show that the additional process observed is opposite in shape to that detected for o-NBA and thus should correspond to a volume expansion. The profile of the photoacoustic waves obtained for Ac-Glu-NH$_2$ is nearly identical to that described above for Ac-Asp-NH$_2$, and is presented Figure A.1 of the Appendix.

Examples of photoacoustic waves acquired for Ac-His-NHMe upon photolysis of o-NBA are shown in Figure 4.2(B). Although the waveforms collected at several concentrations do not show a significant shift in phase as reported for Ac-Asp-NH$_2$ and Ac-Glu-NH$_2$, the amplitude changes upon increasing concentrations of Ac-His-NHMe. Contrary to the results obtained with protonation of carboxylates groups, the amplitude is much more reduced in the presence of lower concentrations of Ac-His-NHMe (200 μM) than with higher concentrations (2 mM). Hence, our results indicate that there is an additional process related with the protonation of the uncharged imidazole group. Just comparing with the typical photoacoustic wave of o-NBA it is difficult to predict the structural volume change occurring. The waveforms acquired in the presence of Ac-His-NHMe are lower in amplitude when compared with the ones obtained for o-NBA. The same behaviour was observed for Ac-Glu-NH$_2$ and Ac-Asp-NH$_2$. However, it is worth to note that increasing concentrations of Ac-His-NHMe promote an increase in amplitudes. This concentration-dependent profile is contrary to that observed for carboxylate groups protonation. Being so, instead of the volume expansion observed when the carboxylate groups are protonated, qualitatively our results suggest that the protonation of imidazole ring may be accompanied by a slow volume contraction.
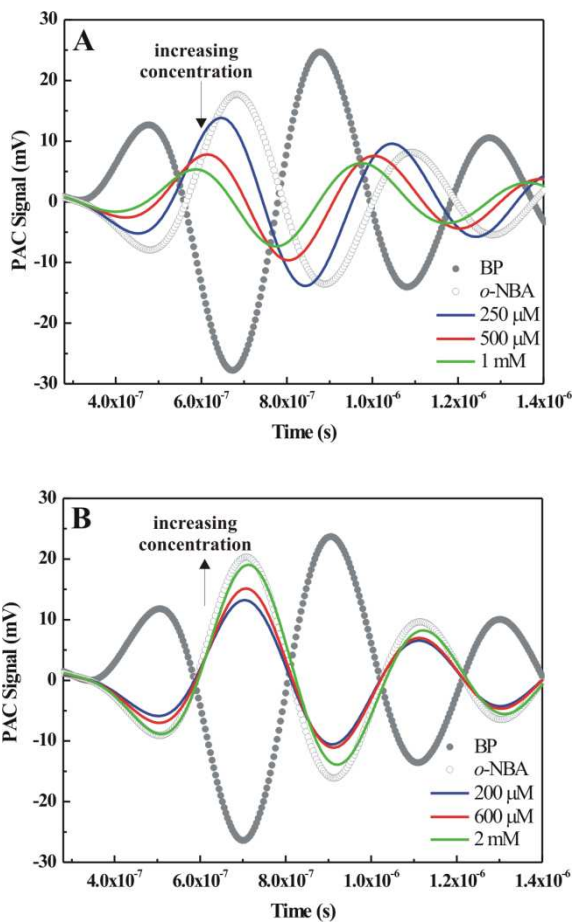
Figure 4.2: Photoacoustic waves generated after laser irradiation, obtained using the two-temperature method. The signals from BP and *o*-NBA are represented by closed circles and open circles, respectively. The signals of the amino acid model compounds Ac-Asp-NH$_2$ (A) and Ac-His-NHMe (B), at different concentrations and in an aqueous solution containing *o*-NBA, are shown as solid lines. The BP signal was measured at T$_{\beta \neq 0}$ = 6.0 ºC, while the signals from *o*-NBA and amino acid model compounds were measured at T$_{\beta = 0}$ = 3.0 ºC. The value of the prepulse pH used for solutions of Ac-Asp-NH$_2$ was 5.3, while for solutions of Ac-His-NHMe was 7.3. Noise reduction was achieved by FFT Low Pass Filter processing, using the software package *OriginPro7* (OriginLab Corporation, USA).

The PAC signals were deconvoluted using the software *CPAC* developed in our laboratory (Schaberle et al. 2010) and available online (http://cpac.qui.uc.pt/). The photoacoustic waves for the amino acid models were well fitted by a function involving two sequential exponential decays. Each decay is characterized by a lifetime τ_i and an amplitude that can be correlated with ϕ_i parameter. The two components derived from the fitting procedure represent two events, the *o*-NBA photolysis and the subsequence

protonation reaction. Figure 4.3 shows examples of the simulated waves for Ac-Asp-NH$_2$ and Ac-His-NHMe obtained from the results of the deconvolution, together with the two component waves associated with: *(i)* the release of protons from *o*-NBA and *(ii)* the respective protonation reaction. The first component corresponds to the reaction of photolysis of *o*-NBA (in green), which in the presence of either Ac-Asp-NH$_2$ or Ac-His-NHMe exhibit negative amplitude that is characteristic of a volume contraction. On the contrary, the simulated wave relative to the protonation of carboxylate group in Ac-Asp-NH$_2$ (Figure 4.3(A)) displays positive amplitude and is shifted to the right when compared with the BP waveform. Being so, the protonation of negatively charged carboxylate groups is associated with a volume expansion. As expected, similar behaviour was detected for Ac-Glu-NH$_2$ protonation (see appendix Figure A.2). Deconvolution of the signal obtained for Ac-His-NHMe allowed the identification of a second component much slower than the first component. As shown in Figure 4.3(B) by the blue line, the protonation of imidazole ring produces a photoacoustic wave that is negative in amplitude and strongly shifted to the right. This very elongated photoacoustic signal is characteristic of very slow volume contractions. Hence, the waveforms obtained at lower Ac-His-NHMe concentrations decrease in amplitude when compared with the signal of *o*-NBA mainly because the protonation leads to photoacoustic signals that are extremely shifted to the right. If the protonation reaction occurred though a faster kinetics, the sample photoacoustic signals should be higher in amplitude than those found for *o*-NBA (see Figure A.3).
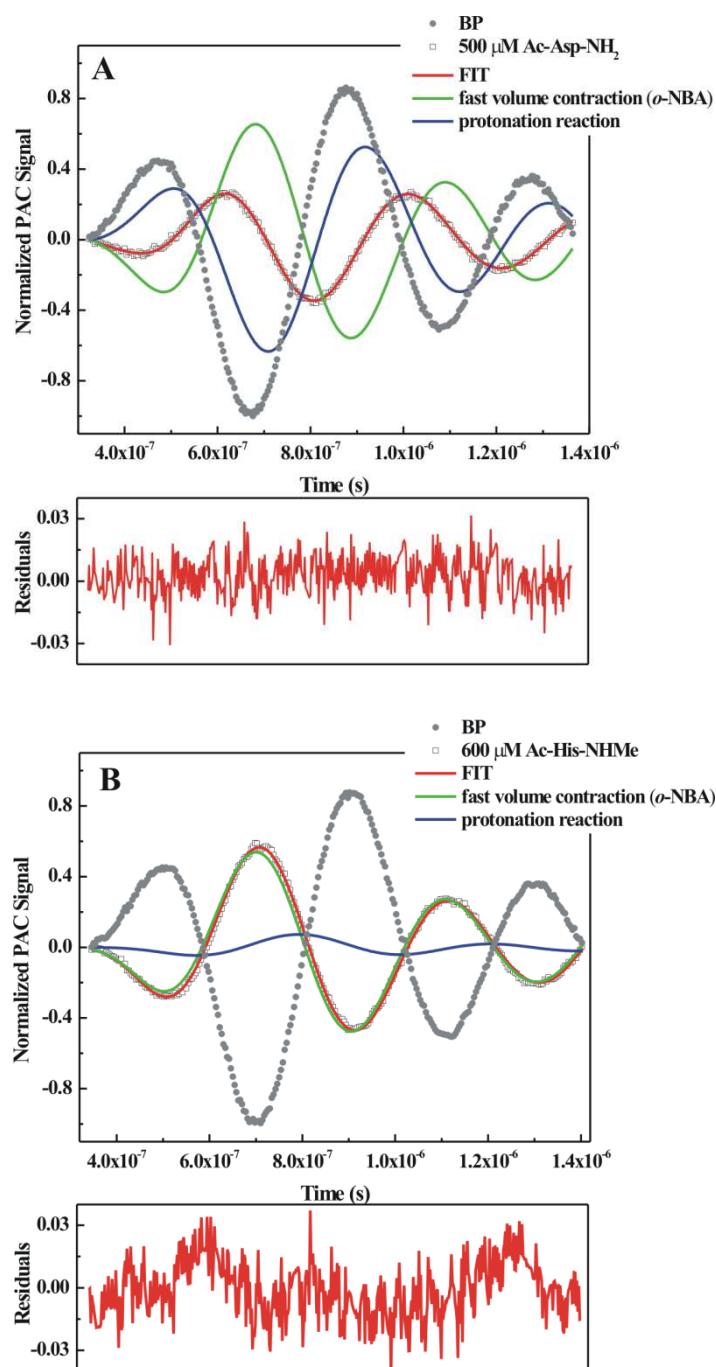
Figure 4.3: The photoacoustic wave generated by laser irradiation of 500 μM Ac-Asp-NH$_2$ (A) and 600 μM Ac-His-NHMe (B) in an aqueous solution containing *o*-NBA, at prepulse pH around 5 and 7, respectively. The BP signals are represented by filled circles. The signals from the amino acid model compounds are represented by open squares. The fit derived from the results of the deconvolution is represented by the red lines. Both red lines correspond to the summation of two component waves that are associated with the fast contraction of *o*-NBA and the protonation reaction, that are represented by green and blue lines, respectively.

The structural volume changes can be determined using the amplitude values derived from the fitting procedure and applying Equation 4.3. For solutions containing only o-NBA, upon laser irradiation at 355 nm, occur an average contraction of approximately -4.5 ± 1 ml mol^{-1} at pH 5.3 and -4.5 ± 0.6 ml mol^{-1} at pH 7.3 (see Chapter 3). The first amplitude decay measure in the present experiments, ϕ_1, refers to this fast volume contraction with a τ_1 shorter than 10 ns. Our results show that this subresolution component does not change significantly with increasing concentrations of different compounds in solution. However, the values of ϕ_1 may slightly depend on the nature of the proton-accepting groups if the presence of the protonable solutes influences specific interactions between o-NBA or its photoproducts and the solvent (Borsarelli & Braslavsky 1998; Abbruzzetti, Viappiani, et al. 2000). Average values of the structural volume change, ΔV_1, resulting from photolysis of o-NBA are shown in Table 4.2. As expected, under pH conditions near neutrality and in the presence of proton-accepting groups, such as carboxylate and imidazole, the values obtained for the fast volume contraction are very similar to those measured for o-NBA solutions, varying between -4.4 and -5.2 ml mol^{-1} (see Table 4.2).

The amplitude decays of the second component, ϕ_2, are concentration-dependent and are associated with the protonation reactions under study. Although under our experimental conditions the proton-accepting groups are in excess when comparing with photo released protons, not all the protons bind to the protonable groups. Only a large excess of proton-accepting molecules allows a close to complete protonation reaction. Thus, as the concentration of proton-accepting groups increases, the number of non-binding protons decreases and eventually become negligible. Figure 4.4 shows the dependence of the observed ΔV_2^{exp} (volume change per mole of added protons) on the concentration of proton-accepting groups. At high concentrations of proton-accepting groups the fraction of unreacted protons is very small and ΔV_2^{exp} reaches a plateau value, ΔV_2. As shown in Figure 4.4 (A) the values of ΔV_2^{exp} reaches a plateau when the concentrations of both Ac-Glu-NH$_2$ and Ac-Asp-NH$_2$ are greater than 500 μM. For Ac-His-NHMe the plateau of ΔV_2^{exp} was only obtained for concentrations greater than 1 mM (Figure 4.4(B)). This observation is in agreement with our qualitative analysis of the photoacoustic signals collected for Ac-His-NHMe, suggesting that the protonation of the imidazole ring is a slow process. In addition, a higher concentration of Ac-His-NHMe is

needed to assure that most of the released protons react by protonating the imidazole ring. Experiments were also performed using imidazole to investigate if the blocking groups in Ac-His-NHMe produce any significant effect on structural volume changes and rate constants upon protonation of the imidazole ring. As previously observed for Ac-His-NHMe, our results also show that the protonation of imidazole is associated with a slow volume contraction. Table 4.2 shows the values of ΔV_2 obtained in the plateau region for each molecule under study.
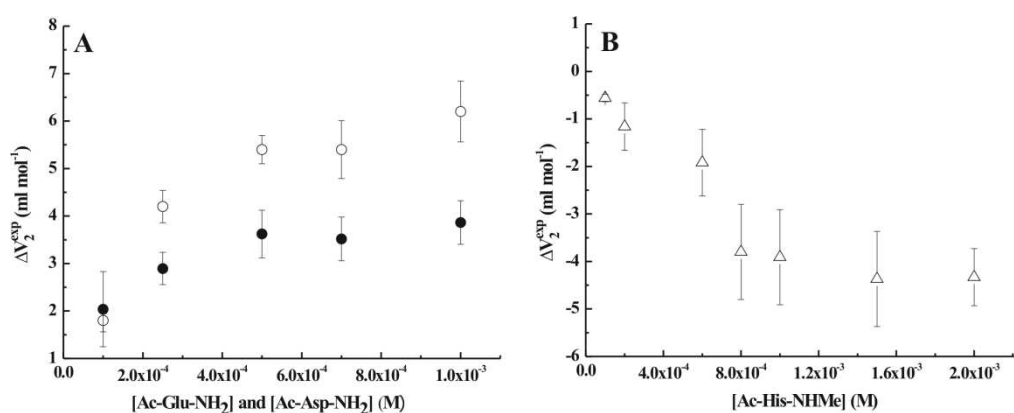
Figure 4.4: Dependence of ΔV_2^{exp} on the concentration of different proton-accepting groups: Ac-Glu-NH$_2$ and Ac-Asp-NH$_2$ (A) and Ac-His-NHMe (B). The protonation of negatively charged carboxylate groups are represented by Ac-Glu-NH$_2$ (filled circles) and Ac-Asp-NH$_2$ (open circles), and the prepulse pH used was approximately 5. The protonation reaction involving the uncharged imidazole group is represented by the use of Ac-His-NHMe (triangles), at prepulse pH around 7. The reaction volumes (ΔV_2) estimated for the protonation of each proton-accepting molecule are reported in Table 4.2.

Table 4.2: Structural volume changes (ΔV) and protonation rate constants (k_b) determined using the PAC two-temperature method.

Proton-accepting groups	Compounds	ΔV_1 $ml\ mol^{-1}$	ΔV_2 $ml\ mol^{-1}$	k_b $10^{10} M^{-1} s^{-1}$
Negatively charged carboxylate group	Ac-Glu-NH$_2$	-4.6 ± 1	3.7 ± 0.3	2.4 ± 0.1
	Ac-Asp-NH$_2$	-5.2 ± 1	6.2 ± 0.5	2.8 ± 0.1
Uncharged imidazole ring	Ac-His-NHMe	-4.5 ± 1	-4.4 ± 0.2	0.14 ± 0.03
	Imidazole	-4.4 ± 0.3	-4.8 ± 0.4^a	0.18^b

[a] Average of the structural volume changes calculated for high concentrations of Imidazole (1 mM, 1.5 mM and 2 mM).
[b] Average value of k_b obtained at 2 mM. For 2 mM Ac-His-NHMe the average value obtained for τ_2 was 275 ns.

In the experimental conditions used, the studied protonation reactions can be treated as pseudo-first order reactions, because the concentration of the proton-accepting groups is always in large excess when compared with the concentration of the proton-releasing photoacid o-NBA. Moreover, the lifetimes τ_2 corresponding to the protonation reactions show an inversely proportional linear dependence on the concentration of the proton-accepting groups which is indicative of pseudo-first order reactions. As shown in Figure 4.5, from the slope of the plot of rate constant ($k_2 = 1/\tau_2$) as a function of the concentration of proton-accepting groups, the bimolecular rate constants were obtained, k_b. The values of k_b are reported in Table 4.2 and revealed that protonation of negatively charged carboxylate groups in the amino acid models Ac-Glu-NH$_2$ and Ac-Asp-NH$_2$ yield values of 2.4 x 10^{10} M^{-1}s^{-1} and 2.8 x 10^{10} M^{-1}s^{-1}, respectively. These values indicate that the protonation reactions involving carboxylate groups are diffusion-controlled. For the protonation of the uncharged imidazole ring in Ac-His-NHMe the bimolecular rate constant observed is approximately 20 times lower than the ones determined for the carboxylate groups.
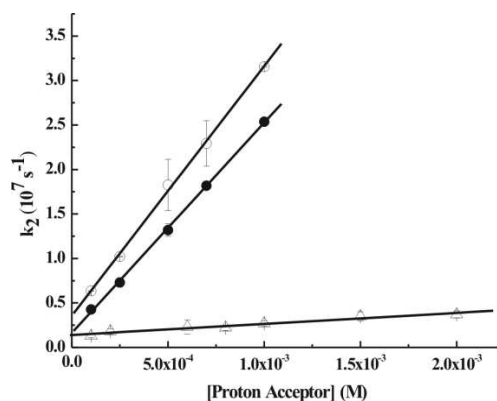
Figure 4.5: Dependence of the rate constants ($k_2 = 1/\tau_2$) on the concentration of the proton accepting groups from Ac-Asp-NH$_2$ (open circles), Ac-Glu-NH$_2$ (filled circles) and Ac-His-NHMe (triangles), using the two-temperature method. Bimolecular rate constants were derived from the slope of the linear relationship (solid lines) of the rate constants as a function of proton acceptor concentration and are reported as k_b in Table 4.2.

**4.3.2 Temperature Dependence Experiments: Multiple-Temperature Method**

The multiple-temperature method allows the determination of volume and enthalpy changes (Equation 4.4) and activation energies (Equation 4.6) for the protonation of the proton-accepting groups under study. At all investigated temperatures the photoacoustic signals were well described by two sequential exponential decays. The fast, time-unresolved decay is due to o-NBA photo-induced proton release. The slower component corresponds to temperature-dependent rate constants, which reflects proton transfer reactions to the acceptors present in solution. In the multiple-temperature method, the concentration of proton-acceptor groups is held fixed.

We have examined the protonation reactions of the negatively charged carboxylate group and the uncharged imidazole ring over a narrow temperature range and using concentrations where ΔV_2^{exp} reaches a plateau, as determined by the two-temperature method (see Figure 4.4). Examples of temperature-dependent acoustic signals recorded between 6.0 °C and 20.0 °C are shown in Figure 4.6.

The data at multiple temperatures enables a plot of $\phi_i E_\lambda$ vs $C_p \rho / \beta$ (Equation 4.4), from which the volume change accompanying each process can be obtained from its slope and the heat released from the solution from its yy intercept (Figure 4.7). The enthalpy (ΔH_1) of the reaction for the first process is calculated from the heat released (Q_1), where $\Delta H_1 = (E_\lambda - Q_1)/\Phi$ and $\Phi = 0.4$ corresponds to the quantum yield for the release of protons by o-NBA. The subsequent kinetic processes are described by an enthalpy change calculated as $\Delta H_i = -Q_i/\Phi$. Figure 4.7(A) shows the results for Ac-Asp-NH$_2$ and Ac-Glu-NH$_2$, while in Figure 4.7(B) the results obtained for Ac-His-NHMe and imidazole are shown. In all experiments, the fast component decay exhibit a volume contraction (negative slope) of approximately -5 ml mol^{-1} and the corresponding enthalpy change is approximately -50 kcal mol^{-1}. The values of volume contraction obtained using the multiple-temperature method are slightly higher than those obtained by the two-temperature method, in spite of being within experimental error (Table 4.2 and 4.3). Clearly, the fast process represents the photolysis of o-NBA: the volume change for this component decay is negative as previously observed. The fast process is followed by a slower reaction. These slower processes correspond to either protonation of charged carboxylic acids through reactions with Ac-Glu-NH$_2$ and Ac-Asp-NH$_2$, or protonation of the uncharged imidazole ring in Ac-His-NHMe and imidazole. The protonation reaction

involving the carboxylic groups under study induces a volume expansion (positive slope) that ranges between 4.4 and 5.0 ml mol^{-1}, and the enthalpy changes obtained were -9.6 kcal mol^{-1} for Ac-Glu-NH$_2$ and -16.5 kcal mol^{-1} for Ac-Asp-NH$_2$. The protonation of the imidazole ring is associated with a volume contraction of approximately -3 ml mol^{-1} in both Ac-His-NHMe and Imidazole. The enthalpy changes varies between the negative value of +4.0 kcal mol^{-1} obtained for Ac-His-NHMe and the slightly positive value of -0.5 kcal mol^{-1} determined for imidazole.
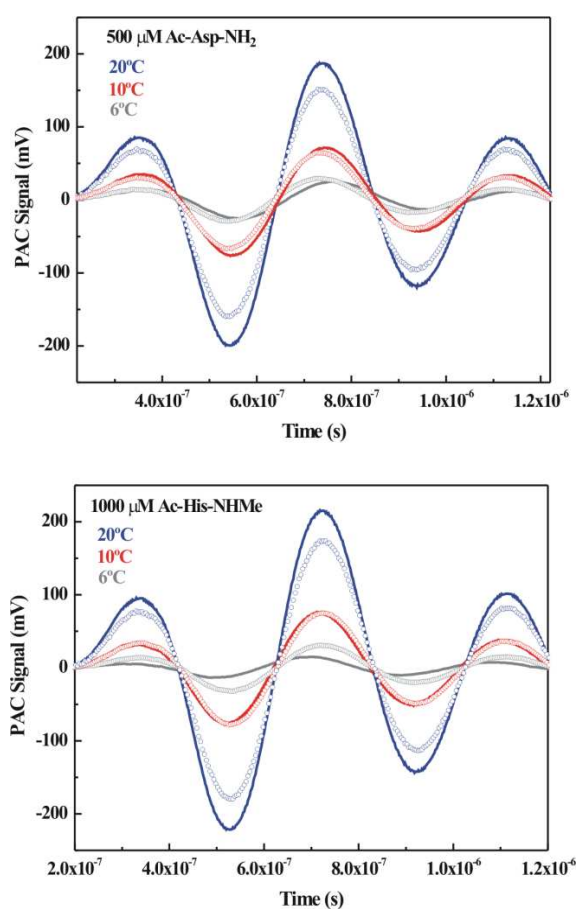
Figure 4.6: Examples of the photoacoustic waves generated after laser irradiation of the photocalorimetric reference BP (open circles) and the sample solutions containing Ac-Asp-NH$_2$ and Ac-His-NHMe (solid lines), at 6.0 ℃ (in gray), 10.0 ℃ (in red) and 20.0 ℃ (in blue).
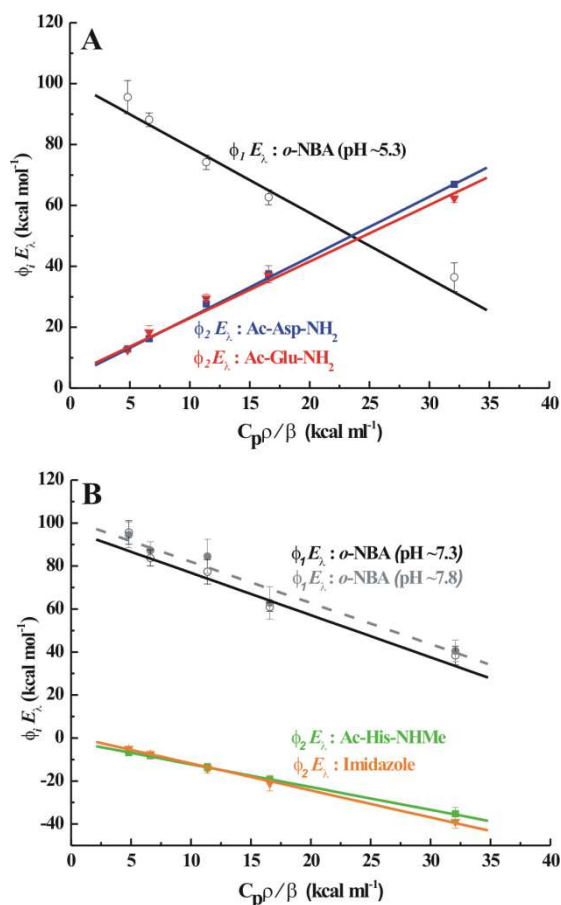
Figure 4.7: Plots of the energy content for the photo-dissociation of o-NBA ($\phi_1 E_\lambda$) and for the binding of the photo-released protons in water ($\phi_2 E_\lambda$) to the amino acid model compounds Ac-Asp-NH$_2$ (in blue), Ac-Glu-NH$_2$ (in red), Ac-His-NHMe (in green) and Imidazole (in orange), as a function of the parameter $C_p\rho/\beta$. $C_p\rho/\beta$ was changed by varying the temperature between 6 and 20.0 ºC. The Ac-Asp-NH$_2$ and Ac-Glu-NH$_2$ concentrations were 500 μM, at pH 5.3. The concentration of Ac-His-NHMe and Imidazole were 1500 μM, at pH 7.3 and pH 7.8, respectively. The volume changes and heat releases were obtained from the linear fits represented by the solid lines, and based on Equation 4.4. The results are reported in Table 4.3.

Activation energies (E_a) of the protonation reactions were also calculated from the temperature dependence of the rate constant associated with the slow component decay ($k_2 = 1/\tau_2$), according to Equation 4.6. The plots of ln k_2 versus 1/T (Arrhenius Plot) are shown in Figure 4.8 and the values of E_a and frequency factors are presented in Table 4.3. As shown, activation energies are higher for the protonation of the imidazole ring than for the protonation of carboxylic acids, which is in line with the bimolecular rate constants values obtained using the two-temperature method (Table 4.2). The Arrhenius Plot obtained for imidazole is presented in the appendix (Figure A.4).
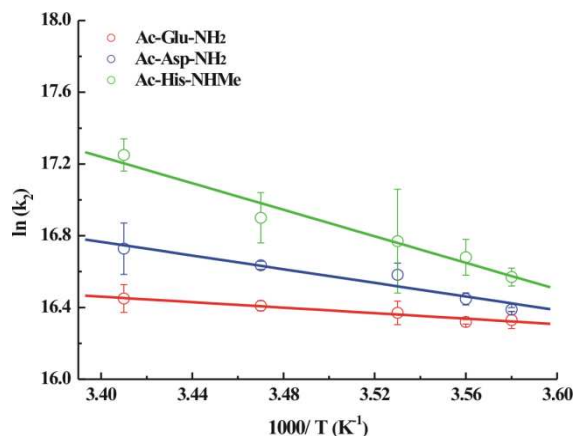
Figure 4.8: Arrhenius plots for the protonation reactions involving negatively charged carboxylic side chains of Ac-Glu-NH$_2$ and Ac-Asp-NH$_2$, and the uncharged imidazole ring of Ac-His-NHMe. The activation energy (E_a) and frequency factors for each reaction were derived from the linear relationship (solid lines) of the rate constants as a function of 1/T (see Equation 4.6) and are reported in Table 4.3.

Table 4.3: Structural volume changes (ΔV_i) and heat released (Q_i), for the deprotonation of *o*-NBA and the protonation reactions involving negatively charged carboxylic side chains (Ac-Glu-NH$_2$ and Ac-Asp-NH$_2$), and the uncharged imidazole ring (Ac-His-NHMe and imidazole), determined using the multiple-temperature method. The activation energy (E_a) and frequency factors for the protonation reactions were determined using Arrhenius plots.

Proton-accepting groups	Compounds	ΔV_1 *ml mol^{-1}*	Q_1 *kcal mol^{-1}*	ΔV_2 *ml mol^{-1}*	Q_2 *kcal mol^{-1}*	E_a *kcal mol^{-1}*	Frequency factor $\ln(1/\tau_2)$
Negatively charged carboxylate group	Ac-Glu-NH$_2$	-5.4 ± 0.4	102.4 ± 2	4.4 ± 0.1	6.6 ± 1	3.8 ± 3	19.1 ± 2
	Ac-Asp-NH$_2$	-5.1 ± 0.1	100.0 ± 2	5.0 ± 0.05	3.9 ± 1	6.3 ± 3	23.3 ± 2
Uncharged imidazole ring	Ac-His-NHMe	-5.0 ± 0.5	99.7 ± 4	-2.6 ± 0.2	-1.6 ± 0.5	16.7 ± 0.5	28.5 ± 0.3
	Imidazole	-5.0 ± 0.6	102.5 ± 4	-3.1 ± 0.3	0.2 ± 0.5	13.5 ± 5	25.8 ± 4

4.3.3 Effect of Ionic Strength

Photoacoustic measurements were performed in aqueous solutions containing 100 mM NaCl and compared with measurements in the absence of NaCl to evaluate the effect of ionic strength on the protonation of the amino acid model compounds having the negative charged carboxylic group (Ac-Glu-NH$_2$) or the uncharged imidazole ring (Ac-His-NHMe). In aqueous solutions, the ratio $C_p\rho/\beta$ strongly depends on the temperature, mainly due to the changes in β. As shown in the previous sections, monitoring photoacoustic waves at $T_{\beta=0}$ allows the straightforward assessment of the structural volume changes because no signal is detected due to heat release. However, for aqueous solutions containing salts or other additives at mM concentrations or higher, $(C_p\rho/\beta)_T$ and $T_{\beta=0}$ must be determined by comparison of the signal obtained for a calorimetric reference in the solvent of interest and in water (Braslavsky & Heibel 1992; Gensch & Cristiano Viappiani 2003). Figure 4.9 shows examples of photoacoustic waves obtained in the absence an in the presence of 100 mM NaCl. As can be observed, the waveforms acquired in the presence of 100 mM NaCl are dephased relatively to the ones detected in water. In fact, previous studies have shown that the presence of dissolved salts in aqueous solutions produces an increase in the sound speed (Sigrist 1986). Thus, the acoustic waves measured in the presence of salts should present slightly different arrival times. Our results are in good agreement with these studies because the photoacoustic waves produced in the presence of 100 mM NaCl are detected by the transducer earlier than the ones recorded in the absence of salt. Moreover, our results evidence differences in amplitude of the BP waveforms, because the ratio $C_p\rho/\beta$ increases approximately 20% in the presence of 100 mM NaCl, and the heat released by BP produces no photoacoustic signal at a lower temperature ($T_{\beta=0}$ = 1.8 °C). Interestingly, the variation in amplitude between BP and sample signals in the presence of NaCl is different from the one observed in aqueous solutions (see Figure 4.9), which suggests that the measured parameters, such as structural volume changes, may differ.
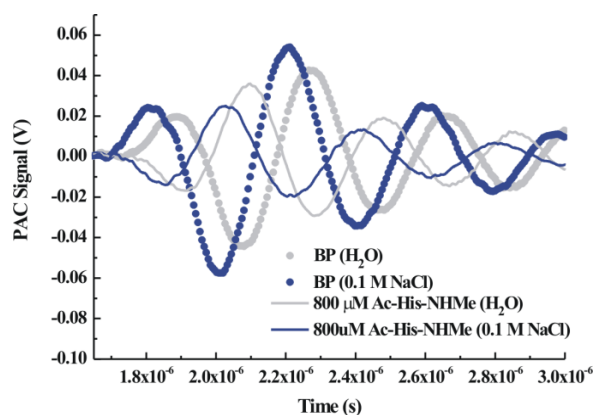
Figure 4.9: Examples of photoacoustic waves generated after laser irradiation of the photocalorimetric reference BP (filled circles) and Ac-His-NHMe (solid lines), in the absence (gray) and in the presence of 100 mM NaCl (blue).

Both methods, two-temperature and multiple-temperature, have been used to determine the structural volume changes, protonation rates and activation energies involved in the protonation of Ac-Glu-NH$_2$ and Ac-His-NHMe in 100 mM NaCl. Figure 4.10 shows plots of the energy content for the binding of the photo-released protons ($\phi_2 E_\lambda$) to the amino acid model compounds as a function of the parameter $C_p \rho / \beta$. As shown in Table 4.4, the values of structural volume changes, as well as the rates of protonation, decrease in experiments conducted with aqueous solutions containing 100 mM NaCl. In particular, the ionic strength dependence of the photolysis of o-NBA has already been examined by TR-PAC revealing that the addition of NaCl to aqueous solutions reduces the extent of structural volume changes and the protonation rate for water formation, which results from the reaction of photo-released protons with hydroxide ions in solution (Viappiani et al. 1998). These findings are in good agreement with the data in the literature and correctly reproduce the expected dependence on ionic strength (Viappiani et al. 1998). Our results show that the structural volume changes occurring due to protonation of the negatively charged carboxylic acid of Ac-Glu-NH$_2$ and the uncharged imidazole ring of Ac-His-NHMe slightly decreases. The protonation rates in the presence of NaCl were determined using the two-temperature method and are reduced in magnitude when compared with the ones obtained in water. On the contrary, the activation energies (E_a) (determined by the Arrhenius Plot) are increased by the presence of NaCl, which is in concordance with the decrease observed in the protonation rates.
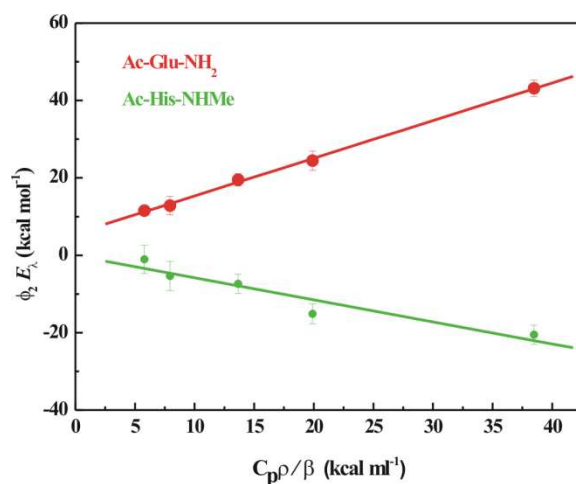
Figure 4.10: Plots of the energy content for the binding of the photo-released protons ($\phi_2 E_\lambda$) to the amino acid model compounds Ac-Glu-NH$_2$ (in red) and Ac-His-NHMe (in green) in an aqueous solution containing 100 mM NaCl, as a function of the parameter $C_p\rho/\beta$. $C_p\rho/\beta$ was changed by varying the temperature between 6.0 and 20.0 °C. The Ac-Glu-NH$_2$ concentration was 500 μM, at pH 5.3. The concentration of Ac-His-NHMe was 1500 μM, at pH 7.3. The volume change and heat releases were obtained from the linear fits represented by solid lines, and based on Equation 4.4. The results are reported in Table 4.4.

Table 4.4: Structural volume changes, protonation rate constants, enthalpy changes and activation energies for the protonation of Ac-His-NHMe and Ac-Glu-NH$_2$ in the presence of 100 mM NaCl, determined using the two-temperature method and the multiple-temperature method.

	Proton Acceptors	
	Ac-Glu-NH$_2$	**Ac-His-NHMe**
Two-temperature Method		
ΔV_1 (*ml mol^{-1}*)	-3.4 ± 0.4	-3.2 ± 0.4
ΔV_2 (*ml mol^{-1}*)	3.9 ± 0.3	-3.7 ± 0.2
k_b (*M^{-1} s^{-1}*)	9.5 ± 0.2 x 10^9	8.3 ± 0.1 x 10^8
Multiple-Temperature Method		
ΔV_1 (*ml mol^{-1}*)	-3.3 ± 0.2	-2.8 ± 0.6
Q_1 (*kcal mol^{-1}*)	101.3 ± 1	96.9 ± 6
ΔV_2 (*ml mol^{-1}*)	2.4 ± 0.3	-1.4 ± 0.4
Q_2 (*kcal mol^{-1}*)	5.6 ± 1	-0.12 ± 4
E_a (*kcal mol^{-1}*)	11.0 ± 6	26 ± 9

4.3.4 Mixtures of Amino Acid Model Compounds

Primary sequences of proteins and peptides are composed by several types of amino acids with ionizable side chains that are likely to be involved in protonation reactions. Thus, mixtures of amino acid compounds at different concentration ratios were investigated to decipher if our experimental setup of TR-PAC could resolve different protonation reactions involving for example carboxylic acids and imidazole groups. The prepulse pH was adjusted to 7 in order to protonate both the carboxylic group in Ac-Glu-NH_2 and the imidazole ring in Ac-His-NHMe. Under our experimental conditions, when the laser irradiation is performed at pH 7 occurs a fast pH jump decreasing the pH of the solution to approximately 4.8. Table 4.5 shows the structural volume changes obtained when the fitting procedure is carried out assuming only two sequential exponential decays, at prepulse pH 7. As can be observed, when the amino acid models are studied individually the fast volume expansion (lifetime < 10 ns) is followed by a volume contraction if the proton acceptor is Ac-His-NHMe or by a volume expansion if Ac-Glu-NH_2 molecules are present in solution. When the mixtures of amino acid models in the concentration ratio 1:1 and 2:1 (Ac-His-NHMe:Ac-Glu-NH_2) are analyzed by fitting the photoacoustic waves to two sequential exponential decays the subsequence process after fast release of protons from *o*-NBA is characterized by a volume expansion of approximately 2 ml mol^{-1} with a lifetime around 40 ns. It is worth to note that the volume expansion is lower than the one determined for 500 μM Ac-Glu-NH_2. We thus conclude that the observed volume expansion probably corresponds to the protonation of both amino acid models, not time resolved as separated processes. Hence, since the two protonation processes could not be resolved using two sequential exponential decays and our previous studies have shown that the lifetimes associated with the protonation of imidazole from Ac-His-NHMe is much slower than the protonation of carboxylic groups, the deconvolution of the photoacoustic waves was also performed assuming three processes.

Table 4.5: Structural volume changes and lifetimes obtained in the absence and in the presence of the amino acid model mixtures, at prepulse pH approximately 7 and using the two-temperature method. The parameters listed were obtained by fitting the photoacoustic waves using two sequential exponential decays.

Ac-His-NHMe	Ac-Glu-NH$_2$	Concentration ratio	ΔV_1	ΔV_2^{exp}	τ_2
mM	*mM*		*ml mol^{-1}*	*ml mol^{-1}*	*ns*
-	0.5	-	-3.8	3.5	74
1	-	-	-4.5	-3.0	389
1	1	1:1	-4.4	2.1	49
1	0.5	2:1	-3.8	1.9	40

The photoacoustic waves of the mixtures studied were fitted using a function included in the *CPAC* software that involves three sequential exponential decays (Schaberle et al. 2010). Figure 4.11 presents the fits obtained using two and three exponential decays. As can be observed, there is a further improvement in the residuals when the deconvolution of the photoacoustic waves of the mixture Ac-His-NHMe and Ac-Glu-NH$_2$ (concentration ratio 7:1) is performed assuming three different processes. In all the concentration ratios analysed, the photoacoustic waves of the mixture were well fitted using three exponential decays and thus three processes could be clearly distinguished.

Figure 4.12 shows an example of the photoacoustic wave obtained for the mixture of Ac-Glu-NH$_2$ and Ac-His-NHMe at a concentration ratio of 5, the result of the fitting to the function involving three exponential decays and the simulated waves for each process. The global fit (in red) can be separated in three component decays: photolysis of *o*-NBA (in green) and the subsequent protonation of Ac-Glu-NH$_2$ (in blue) and Ac-His-NHMe (in orange). As expected, the simulated waves for *o*-NBA photolysis and Ac-His-NHMe protonation are inverted when compared with the BP waveform reflecting the volume contractions previously observed. On the contrary, the simulated wave for Ac-Glu-NH$_2$ exhibit positive amplitude which is associated with the volume expansion occurring due to protonation of carboxylic groups. Both simulated waves for Ac-Glu-NH$_2$ and Ac-His-NHMe are shifted relatively to the BP signal which suggests that the protonation is slower than the heat deposition due to laser irradiation of BP. In fact, the determined lifetimes indicate that, in the mixtures, the protonation of Ac-Glu-NH$_2$ typically occurs in less than 100 ns, while the protonation of Ac-His-NHMe it is associated with slower lifetimes for all the concentrations observed.
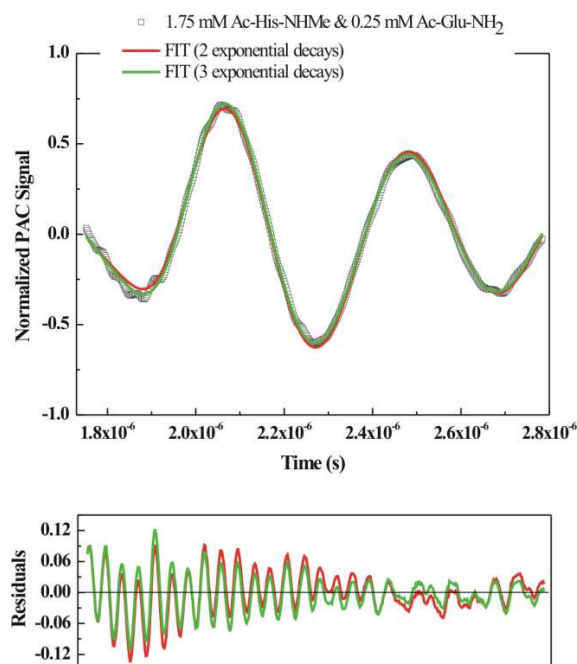
Figure 4.11: Comparison of the fitting procedure using two exponential decays (in red) and three exponential decays (in green). The experimental photoacoustic wave of the mixture of 1.75 mM Ac-His-NHMe and 0.25 mM Ac-Glu-NH$_2$ (concentration ratio 7:1) obtained at 100 % laser energy, 3.0 °C and prepulse pH 7, is represented by open squares.
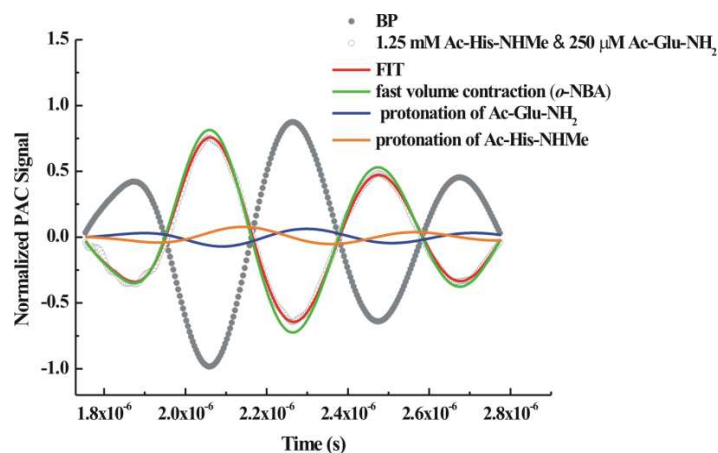
Figure 4.12: The photoacoustic wave generated by laser irradiation of the mixture of 1.25 mM Ac-His-NHMe and 250 μM Ac-Glu-NH$_2$ in an aqueous solution containing o-NBA, at prepulse pH around 7. The signals from the amino acid model compounds are represented by open circles. The fit derived from the results of the deconvolution is shown by the red line together with the three deconvolution component waves associated with the fast contraction of o-NBA and the protonation reaction of Ac-Glu-NH$_2$ and Ac-His-NHMe that are represented by green, blue and orange lines, respectively.

Figure 4.13 shows the structural volume changes obtained at different concentration ratios of Ac-His-NHMe and Ac-Glu-NH$_2$ and using a function involving three sequential exponential decays. The fast volume contraction ΔV_1 corresponding to the photo-release of protons by o-NBA presents a similar value in all mixtures, while we propose that ΔV_2 and ΔV_3 corresponds to the protonation of Ac-Glu-NH$_2$ and Ac-His-NHMe, respectively, appear to be concentration ratio-dependent. Interestingly, when the Ac-His-NHMe is 7 times higher than Ac-Glu-NH$_2$ the structural volume change obtained is close to the one obtained for Ac-His-NHMe (see Figure 4.4). Thus, the fraction protons binding to Ac-His-NHMe might be higher due to its large excess. Otherwise, if the excess of Ac-His-NHMe is only two times higher than Ac-Glu-NH$_2$ the structural volume change observed for Ac-His-NHMe is reduced, while the value observed for Ac-Glu-NH$_2$ is similar to the one observed for Ac-Glu-NH$_2$ sample. Table 4.6 shows the lifetimes associated with the protonation of Ac-Glu-NH$_2$ and Ac-His-NHMe.
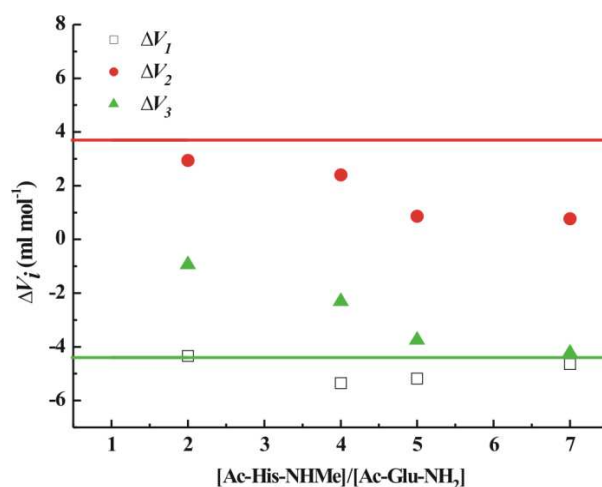
Figure 4.13: Structural volume changes obtained at different concentration ratios of Ac-His-NHMe and Ac-Glu-NH$_2$, using the two-temperature method and prepulse around pH 7. The values of ΔV_1 correspond to the photolysis of o-NBA. The protonation of negatively charged carboxylate groups is represented by Ac-Glu-NH$_2$ (triangles) and correspond to ΔV_2. The protonation reaction involving the uncharged imidazole group is represented by Ac-His-NHMe (circles) and corresponds to ΔV_3. The solid lines represent the expected values for the volume expansion due to Ac-Glu-NH$_2$ protonation (in red) and for volume contraction upon protonation of Ac-His-NHMe (in green).

Table 4.6: Lifetimes obtained with mixtures of amino acid models at different concentration ratios and prepulse pH approximately 7, and using the two-temperature method. The parameters listed were obtained by fitting the photoacoustic waves to three sequential exponential decays.

Ac-His-NHMe	Ac-Glu-NH$_2$	Concentration Ratio	τ_2	τ_3
mM	*mM*		*ns*	*ns*
1	0.5	2	49	405
1	0.25	4	98	118
1.25	0.25	5	112	321
1.75	0.25	7	70	208

4.4 Discussion

Amino acids are found in all naturally occurring proteins or peptides, which play a vital role in nearly all chemical and biological processes. The structure, stability, solubility and function of proteins depend on their net charge and on the ionization state of the individual amino acids that constitute those proteins (Pace et al. 2009). Thus, it is of critical importance to fully understand the contribution of protonation reactions involving ionizable amino acids in protein folding. In the present work, the amino acid model compounds Ac-Glu-NH$_2$, Ac-Asp-NH$_2$ and Ac-His-NHMe represent two types of ionizable side chains. While in Ac-His-NHMe the proton-accepting group is the uncharged imidazole ring, in Ac-Asp-NH$_2$ and Ac-Glu-NH$_2$ the protonation occur on the negatively charged carboxylic groups. Experiments using laser-induced pH jump coupled with TR-PAC detection were performed to monitor the structural volume changes, enthalpy changes and protonation rates. The effect of ionic strength on protonation has been evaluated by performing experiments in the presence of 100 mM NaCl. Moreover, the photoacoustic signals of mixtures of Ac-Asp-NH$_2$ and Ac-His-NHMe at different concentration ratios have been measured to predict the signals when both ionizable amino acids are present and protonated in a polypeptide chain.

Volume changes due to protonation of Ac-Glu-NH$_2$ and Ac-Asp-NH$_2$

In general the volume changes upon protonation may be considered as a sum of an intrinsic volume change and a solvational volume change, with the intrinsic part arising from the net motion of the nuclei of the reacting species (changes in bond lengths and angles) and the solvation component representing volume changes associated with electrostriction, changes in polarity, and dipole interactions (Van Eldik et al. 1989).

The neutralization of the amino acid models such as Ac-Glu-NH$_2$ and Ac-Asp-NH$_2$ involves the disappearance of two charges: the negative charge on the carboxylate group and the proton positive charge. Prior to protonation both ions are solvated by water molecules. Upon protonation, the rearrangement of the solvent must occur because the protons released due to *o*-NBA photolysis react with the negatively charged side chains of both amino acid models. As the concentration of protonated Ac-Glu-NH$_2$ or Ac-Asp-NH$_2$ increases, the number of solvation waters around the charged carboxylate group and proton is reduced. These water molecules become free in solution to form their preferential hydrogen bonds with its immediate neighbours (Gutman & Nachliel 1990). Thus, it is expected a volume expansion because the protonation of the COO$^-$ on Ac-Glu-NH$_2$ and Ac-Asp-NH$_2$ neutralizes two net charges, releasing the water molecules constrained in solvation shells.

Studies on simple molecules demonstrate that volume increases between 6 and 17 ml mol^{-1} occur upon protonation of carboxylate groups, depending on the nature of R, attached to COO$^-$ (Kauzmann et al. 1962; Van Eldik et al. 1989). For instance, the volume change for neutralization of formic acid in water at 25 °C is 6 ml mol^{-1}. However, it increases to 11.5 ml mol^{-1} for acetic acid, 13.2 ml mol^{-1} for *i-Pr*COOH, and 17 ml mol^{-1} for *t-Bu*COOH (Van Eldik et al. 1989). If positively charged groups exist close to the carboxylate then the volume increase is only 6 or 7 ml mol^{-1} (Van Eldik et al. 1989). Additionally, the structural volume changes upon protonation of Glu and and acetate have been examined using TR-PAC by Abbruzzetti et al. (Abbruzzetti, Viappiani, et al. 2000). Using the two-temperature method, Abbruzzetti and collaborators observed that the protonation of Glu induces a volume expansion of 6.4 ml mol^{-1}, while a volume change of 8.9 ml mol^{-1} is observed for acetate. When applying the multiple-temperature method the authors obtained 5.8 and 4.5 ml mol^{-1} for acetate and Glu, respectively. In proteins, protonation of Glu or Asp leads generally to volume changes of about 11 ml mol^{-1}, but in

some cases smaller values can be observed, possibly related to the proximity of positively charged residues such as histidine, lysine or arginine residues (Kauzmann et al. 1962).

Despite the equivalence of the multiple-temperature and two-temperature methodologies in the determination of reaction volumes, the values obtained are slightly different (Table 4.2 and 4.3). However, the differences fall within the estimated uncertainties. The volume expansion obtained for Ac-Glu-NH$_2$ varied between 3.7 ml mol^{-1} (~6 Å^3) and 4.4 ml mol^{-1} (~7 Å^3) using the two-temperature and the multiple-temperature method, respectively. The protonation involving Ac-Asp-NH$_2$ promotes a volume expansion of 6.2 ml mol^{-1} (~10 Å^3) or 5.0 ml mol^{-1} (~8 Å^3) using the multiple-temperature method.

Values of volume change obtained for Ac-Glu-NH$_2$ are systematically lower than those determined for Ac-Asp-NH$_2$. The difference observed between both amino acid models may be due the length of the side chain. In fact, previous studies using Glu and acetate found that the volume change accompanying the protonation of acetate is higher than that observed for Glu. Thus, in both cases the molecule with longer length chains attached to the COO$^-$ group presents a smaller volume expansion upon protonation.

Moreover, the amino acid models present slight differences in the pK_a values of approximately 0.4, being the pK_a of Ac-Asp-NH$_2$ the lowest (Table 4.1). Since in both experiments the prepulse pH was similar (pH 5.3) the final pH value should be around 4.4. Thus, under these conditions of pH jump the percentage of protonated molecules of Ac-Asp-NH$_2$ can be lower than molecules of Ac-Glu-NH$_2$ ($pK_a = 4.50$). However, this difference does not seem to explain the higher volume change observed for Ac-Asp-NH$_2$.

Volume changes due to protonation of Ac-His-NHMe

In the amino acid model Ac-His-NHMe, the proton-accepting group is the uncharged imidazole ring. As mentioned before, upon photolysis of *o*-NBA a volume contraction is observed, associated with the solvation of both photoreleased proton and nitrosobenzoate anion. Using our experimental setup of TR-PAC and laser pH jump a further volume contraction is observed upon protonation of Ac-His-NHMe. It seems that the water molecules are more organized around the formed Ac-His-NHMe cation than around the the uncharged imidazole group in Ac-His-NHMe. In addition, photoacoustic measurements have also been performed using imidazole in order to evaluate if the extent

of the volume contraction depends on the attached group to the imidazole ring and to check if the observed volume contraction has its origin in the imidazole ring. The differences observed in terms of volume changes and kinetics between the protonation of Ac-His-NHMe and imidazole are negligible. Being so, the attached group to the imidazole ring does not seem to have a significant effect on the volume changes and kinetics upon protonation.

Our results indicate that there is a decrease of volume when the proton reacts with the uncharged imidazole ring. The relevant molecular structures in solution are the proton, the uncharged imidazole group as reagents and the protonated imidazole group as a product. The high density of positive charge on the proton promotes the organization of the surrounding water molecules, while the lower density charge of the uncharged imidazole should induce the formation of less organized hydration shells. As the product is formed, the presence of a localized charge on the imidazole ring contributes to an increase on the organization of the water molecules surrounding the ion. Thus, our observations show that the net volume balance between the hydrated proton and uncharged imidazole ring *versus* the solvated protonated product is a volume contraction (see Figure 4.14). Using the two-temperature method, the volume changes calculated were approximately -4.4 ($\sim$7 Å^3) and -4.8 ml mol^{-1} ($\sim$8 Å^3) for Ac-His-NHMe and imidazole at high concentrations, respectively. Lower values were determined applying the multiple-temperature method: -3.1 ml mol^{-1} ($\sim$5 Å^3) for imidazole and -2.6 ml mol^{-1} ($\sim$4 Å^3) to Ac-His-NHMe.
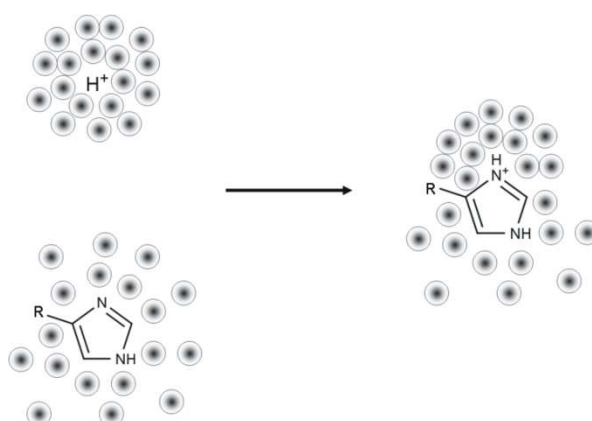
Figure 4.14: Schematic representation of the net volume balance upon protonation of the uncharged imidazole group. The circles represent water molecules.

Previously, volume changes for ionization processes in water were calculated from the partial molar volume data obtained from differential flow microcalorimetry or by dilatometry (Katz & Miller 1971; Riedl & Jolicoeur 1984; Kitamura & Itoh 1987). Volume changes of 0.8 and 1.8 ml mol^{-1} were obtained for 4-methylimidazole and imidazole dissociation, respectively. Experiments of high pressure one-dimensional HR-NMR spectroscopy have shown that the negative reaction volume of protonation of L-histidine (His) and Ac-His-NHMe is -2 ml mol^{-1} at atmospheric pressure (dilatometry) and remains unchanged up to 150 MPa (Hauer et al. 1981). Moreover, several authors consider the reaction volumes reviewed by Van Eldik et al., which refers that the protonation of the imidazole ring of His free in solution is accompanied by a small contraction of -1 ml mol^{-1} (Van Eldik et al. 1989). Thus, our results obtained through the apparatus of a new methodology are in agreement with the previous ones, revealing a relatively small volume contraction upon protonation of Ac-His-NHMe and imidazole.

On a quantitative point of view, it is possible to explain the volume contraction observed upon protonation of Ac-His-NHMe and imidazole using Equation 4.7. Assuming that the ions are incompressible, the electrostatic volume change (ΔV_{sol}) can be described as the derivative of the electrostatic Gibbs free energy of solvation an ion (ΔG_{sol}) of a total charge e and with radius r, in a medium of dielectric constant ε, as represented by the following Equation 4.7 (Serpa & Arnaut 2000).

$$\Delta V_{sol} = \frac{\partial \Delta G_{sol}}{\partial p} = -\frac{e^2}{2\varepsilon r}\left(\frac{\partial \ln \varepsilon}{\partial p}\right)_T \qquad (4.7)$$

Prior to protonation, the positive charge it is centered in the proton and in aqueous environment characterized by a dielectric constant of 78.3, at 25 °C. Upon protonation, this positive charge becomes central in the N heteroatom of the imidazole ring. Thus, this positive charge changes from a polar aqueous environment to a less polar environment. On the contrary to Ac-Glu-NH$_2$ and Ac-Asp-NH$_2$, there is no decrease of the net number of charges in solution when the imidazole ring is protonated. We assumed that upon Ac-His-NHMe protonation the positive charge is in a much less polar environment. Considering, as an approximation, that the non-polar environment of an imidazole ring is similar to benzene, which is characterized by a dielectric constant of approximately 2.3. The fraction

$(\partial \ln \varepsilon / \partial p)_T$ can be obtained from tabulated values for several solvents (Marcus 1998). In particular, for water this fraction corresponds to 0.59 GPa^{-1} and to benzene is 0.69 GPa^{-1}, at 25 ºC. Qualitatively, since there are large differences between the dielectric constants and they are inversely proportional to the ΔV_{sol}, the volume change due to solvation of an ion in non-polar environment is lower than in aqueous environment. Being so, a volume contraction must occur when a positive charge is transfer from a full aqueous solution to a less polar environment.

Enthalpies Changes

The heat released per mole of photons upon photolysis of *o*-NBA has been previously determined corresponding to approximately 100 kcal mol^{-1} (Abbruzzetti, Viappiani, et al. 2000; Abbruzzetti, Crema, et al. 2000). Using our experimental setup, the heat released per mole of photons varies between 102 and 99 kcal mol^{-1}, which are in agreement with the previously published results. Considering the fraction of energy released as heat in this photochemical process measured by photoacoustic calorimetry and the quantum yield for the release of protons by *o*-NBA (0.4), the enthalpy changes per mole of reacting molecules can be calculated using Equation 3.9a, yielding a value of approximately -50 kcal mol^{-1}. Since the hydrogen abstraction from *o*-NBA involves multiple steps of intramolecular rearrangements (Bonetti et al. 1997), the assignment of the enthalpy observed to the individual steps becomes complex. Nevertheless the overall enthalpy change obtained for *o*-NBA proton release presents a negative value that should be directly related with the enthalpy change upon breaking of a O−H bond in *o*-NBA (average value 110.7 kcal mol^{-1}, (Atkins & Jones 1999)). The enthalpy change due to water reorganization around the formed charged species formed should also have a contribution, namely the hydration enthalpy of the proton that is characterized by a negative value of approximately of -274 kcal mol^{-1} (Mejías & Lago 2000).

The protonation reactions require the formation of bonds between the protons and the proton acceptors in solution, which is associated with a negative enthalpy change. In addition, the formation of O−H (average value -110.7 kcal mol^{-1}, (Atkins & Jones 1999)) and N−H bonds (average value - 92.7 kcal mol^{-1}, (Atkins & Jones 1999)) in the carboxylic group and in the imidazole ring, respectively, is accompanied by energy cost of removing the water molecules around the unprotonated species and the subsequent structural

rearrangements of the solvent. All these factors may contribute for the overall enthalpy change associated with the protonation reaction.

Experiments performed by TR-PAC have also shown that the heat released per mole of photons upon protonation of Glu and acetate were 0.7 and 2.0 kcal mol^{-1}, respectively (Abbruzzetti, Viappiani, et al. 2000). Our results suggested that the heat released per mole of photons upon protonation of carboxylic groups varies between 6.6 kcal mol^{-1} for Ac-Glu-NH$_2$ and 3.9 kcal mol^{-1} for Ac-Asp-NH$_2$. Both values are higher than the communicated by Abbruzzetti and Viappiani. By applying Equation 3.9a, our photoacoustic data revealed negative values of enthalpy change for Ac-Glu-NH$_2$ (-9.6 kcal mol^{-1}), Ac-Asp-NH$_2$ (-16.5 kcal mol^{-1}), a slightly negative value for Ac-His-NHMe (-0.5 kcal mol^{-1}) and a positive value for imidazole (4.0 kcal mol^{-1}). Over the years, the thermodynamic data for ionization reactions of several buffers have been studied using different techniques such as calorimetry, potentiometric titration, among many others (Goldberg et al. 2002). Enthalpy change for the ionization of acetic acid corresponds approximately to -0.19 kcal mol^{-1}. For L-histidine and imidazole, values for enthalpy change due to the ionization reaction were around 7.1 and 8.6 kcal mol^{-1}, respectively. In general, our photoacoustic results suggest that the protonation reactions studied are associated with relatively low enthalpy changes, which is consistent with the thermodynamic data obtained for ionization processes. However, the estimated error in the determination of the heat released per mole of photons for the protonation reactions (Q_2) precludes a more precise comparison with the literature.

Protonation Rates

The diffusion rate constant in water at 3.0 ºC is approximately 3.7 x 10^9 M^{-1} s^{-1} (Equation 4.8). Following our experimental results, the bimolecular rate constant (k_b) associated with the protonation of Ac-Glu-NH$_2$ and Ac-Asp-NH$_2$ is significantly higher than that determined for Ac-His-NHMe. The average value of k_b for protonation of carboxylic group is approximately 2.5 x 10^{10} M^{-1}s^{-1}, while for the protonation of imidazole group k_b is more than one order of magnitude lower, 1.4 x 10^9 M^{-1}s^{-1}. Those results suggest that the protonation reaction involving the negatively charged carboxylic acids and the uncharged imidazole groups may be diffusion controlled reactions.

Chemical reactions controlled by diffusion are characterized by several properties, namely their rates have an inversely relation with the solvent viscosity, the activation energy is relatively lower and the size of the reacting molecules do not affect significantly the diffusion constant. In particular, the diffusion rate constant for reacting molecules with equal molecular radius is described by Equation 4.8, where k_B is the Boltzmann's constant, r is the molecular radius, and η is the solvent viscosity (Formosinho & Arnaut 2003).

$$k_D = \frac{8k_BT}{3\eta} \tag{4.8}$$

Diffusion limited reactions are strongly affected by the presence of charged species in solution. The diffusion rate constant of reactions between two charged species need to include an electrostatic parameter to describe the attractive and repulsive interactions as described by Equation 4.9, where ε is the dielectric constant, T is the temperature, d_{AB} corresponds to the sum of the molecular radius of the two reacting molecules and Ze the charge of the ion (Formosinho & Arnaut 2003).

$$k_D = \frac{8k_BT}{3\eta} \frac{Z_AZ_Be^2}{4\pi\varepsilon k_BTd_{AB}} \tag{4.9}$$

The protonation reaction of carboxylic acids involves the diffusion of two charged species, proton and Ac-Glu-NH$_2$ or Ac-Asp-NH$_2$. On the contrary, the protonation of imidazole is characterized by the diffusion of the uncharged molecules of Ac-His-NHMe and the positively charged protons. It has been shown previously that charged species of opposite charges have diffusion rate constant higher than neutral molecules, due to atractive interactions between ions (Formosinho & Arnaut 2003). Thus, it is expected that reactions involving one charged specie and a neutral molecule, such as the reaction between Ac-His-NHMe and the photo-released protons by o-NBA, may be governed by a lower rate constant than the reaction involving protons and carboxylic acids.

The effect of ionic strength

Our results reveal that the presence of 100 mM NaCl is clearly responsible by slightly decrease in the reaction volume changes as well as in the protonation rates. The rate of protonation of Ac-Glu-NH$_2$ in water is 2.4 higher than in the presence of 100 mM NaCl. The protonation rate of Ac-His-NHMe is decreased 1.7 times in the presence of 100 mM NaCl. An increase of viscosity of the solution η upon addition of 100 mM NaCl may have a contribution to the reduction in the protonation rates. As an example at 25 ℃, the viscosity of pure water is approximately 0.890 mPa s (Kestin et al. 1978), while an aqueous solution containing 100 mM NaCl is characterized by a viscosity of 0.899 mPa s (Out & Los 1980). Moreover, the ionic strength I strongly affects the rate constants. In particular, if the reacting molecules have the opposite charges the rate constants decrease because attractive forces between the two molecules are reduced due to the screening effects of other charges in solution (Formosinho & Arnaut 2003).

The decrease in the reaction volumes can be explained by the differences in the dielectric constants upon addition of NaCl, because the volume change depends on the solvent dielectric constant ε (see Equation 4.7). The presence of 100 mM NaCl induces an increase in the solvent dielectric constant. As a consequence, the volume changes observed decrease due to the inversely relation between dielectric constant and volume change.

Mixtures of Ac-Glu-NH$_2$ and Ac-His-NHMe

Proteins can have more than one protonable exposed amino acid residues. Small natural or synthetic peptides can also have distinct amino acid residues that can be protonable within the same pH range. Although mixtures of amino acid model compounds might not be as complex as having the same amino acid residues within a peptide or protein chain, we studied this model system as a good first approximation.

With an prepulse pH of approximately 7 and the photorelease of 4 x 10^{-11} mol of protons in a volume of 1.22 x 10^{-6} dm^3, a pH decrease to 4.8 should be enough to promote protonation of carboxylic acid ($pK_a \sim 4.2$) and imidazole ($pK_a \sim 6.6$). Our results show that the protonation reaction of those groups is distinct in both kinetics and volume changes. In fact, volume changes of opposite signal were observed upon protonation. The Ac-His-

NHMe protonation reaction is characterized by a rate constant of 1.4×10^9 M^{-1} s^{-1} yielding a -4.4 ml mol^{-1} contraction, while the protonation of Ac-Glu-NH$_2$ has a rate constant of 2.8×10^{10} M^{-1} s^{-1}, associated with a volume expansion of 3.7 ml mol^{-1}.

Assuming that there is no interaction between the amino acid models present in solution, it can be qualitatively predicted that the observed photoacoustic signal will reflect the volume expansion due to Ac-Glu-NH$_2$ protonation and the volume contraction due to protonation of Ac-His-NHMe. In a particular concentration ratio of Ac-Glu-NH$_2$ and Ac-His-NHMe, the positive photoacoustic signal that arises from the Ac-Glu-NH$_2$ would be canceled by the negative photoacoustic signal that is characteristic of Ac-His-NHMe. In such experiment the only observed signal would be the negative arising from the photoacid dissociation.

A precise analysis of the photoacoustic experiment has to take in consideration the following factors: *(i)* the distinct kinetics of the protonatin reactions; *(ii)* the relative quantities of Ac-His-NHMe and Ac-Glu-NH$_2$ present in solution; *(iii)* the opposite signal of the volume changes; *(iv)* the distinct magnitude of the volume changes. When *o*-NBA photolysis occurs in the presence of mixtures of Ac-Glu-NH$_2$ and Ac-His-NHMe the reactions can be described by the following equations:

$$o - NBA + h\nu \longrightarrow H^+ + NBA^- \qquad (4.10)$$

$$H^+ + His \xrightarrow{k_{His}} HisH^+ \qquad (4.11)$$

$$H^+ + Glu^- \xrightarrow{k_{Glu}} GluH \qquad (4.12)$$

$$\frac{d[H^+]}{dt} = -k_{His}[H^+] - k_{Glu}[H^+] = k_T[H]^+ \qquad (4.13)$$

$$\frac{d[His]}{dt} = k_{His}[H^+] \qquad (4.14)$$

$$\frac{d[Glu]}{dt} = k_{Glu}[H^+] \qquad (4.15)$$

$$k_T = k_{His}[His] + k_{Glu}[Glu] \qquad (4.16)$$

Equation 4.10 describes the photorelease of the proton by o-NBA, which is a reaction well characterized in terms of kinetics and volume changes. Equations 4.11 and 4.12 represent the competitive protonation events. The photoreleased proton can either react with Ac-Glu-NH$_2$ or Ac-His-NHMe, both present in solution in excess relative to the protons formed. The quantity of protons present in solution will decrease with a rate that depends on the second order rate constants of protonation of both Ac-Glu-NH$_2$ and Ac-His-NHMe and the concentrations of both amino acid model compounds. The individual rate constants, k_{Glu} and k_{His}, for both processes have already been reported.

Within the limited range of frequencies sensed by the piezoelectric detector, the acoustic waves arising from our experiment can be separated in time resolved elementary processes, corresponding to pressure waves deposited in the solution at distinct time scales. The photoacoustic signal does not follow the disappearance of one single reagent. In a set of competitive reactions, the pressure waves will not depict the disappearance of the protons, but the "individual" volume change processes that contribute to that suppression. In our experiments, it is followed the volume changes occurring upon formation of the protonated species (GluH and HisH$^+$). In fact, if the individual processes occur with distinct time scales and give rise to well defined volume change, photoacoustic calorimetry, using the two temperature method, should be able to resolve both processes. The decrease of protons in solution will be governed by Equation 4.16, but the photoacoustic waves should retain information on both the two competitive processes occurring.

Photoacoustic waves obtained for mixtures of Ac-Glu-NH$_2$ and Ac-His-NHMe with distinct relative concentrations (1:2; 1:4; 1:5; 1:7) were first analyzed using two sequential exponential decays. Although a fast volume contraction that can be associated with the o-NBA photolysis was clearly identified, the second fast volume expansion could not be directly associated with any reactive process. These observations are consistent with the fact that the photoacoustic signal observed is originated from three distinct processes. Using the *CPAC* software was only possible performed fits with three processes assuming three sequential exponential decays occurring within distinct time scales. However, the protonation reactions under study occur competitively, not sequentially.
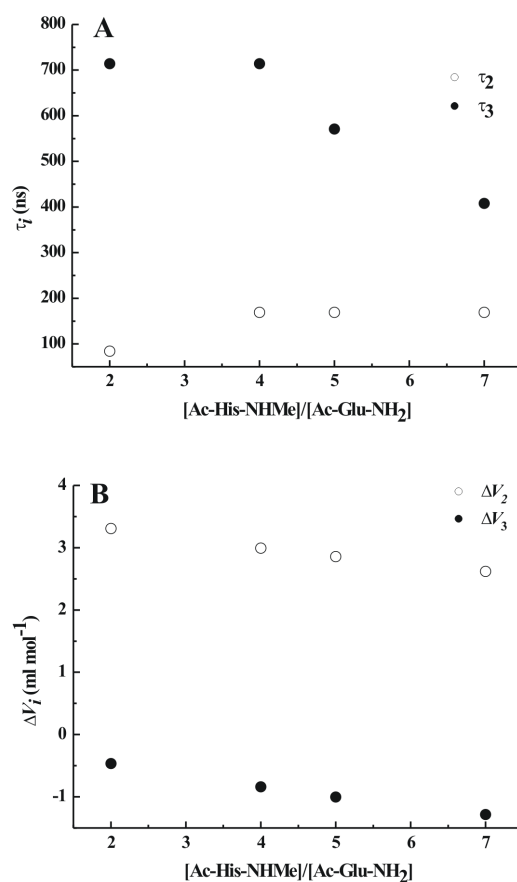
Figure 4.15: Predicted lifetimes (A) and volume changes (B) upon protonation of Ac-Glu-NH$_2$ and Ac-His-NHMe in different concentration ratio mixtures.

Figure 4.15 presents the predicted lifetimes and volume changes, when the protonation reactions are investigated in separate. The volume changes can be predicted from the fraction of protonated molecules of each amino acid model under and the volume change obtained for the isolated amino acid model (Figure 14.5).

Since the two protonation reactions occur at different time scales, our experimental data were fitted using three exponential decays. In fact, it is possible to separate the two opposite signal volume changes due to protonation of Ac-Glu-NH$_2$ (a faster volume expansion) and Ac-His-NHMe (a slower volume contraction). These volume changes clearly follow the predicted trend in Figure 4.15. Quantitatively, the volume changes observed for Ac-His-NHMe are larger than the predicted values and at the concentration ratio of 7:1 the volume change observed is close to the ones obtained for Ac-His-NHMe samples. At lower concentration ratios, the volume changes observed

Ac-Glu-NH$_2$ in mixtures are similar to the predicted value as well as to that observed for Ac-Glu-NH$_2$ samples. For higher concentration ratios the calculation overestimates the observed result.

Our results suggest that it is possible to apply photoacoustic calorimetry to separate the contribution of the volume contraction due to imidazole protonation from the volume expansion arising from the carboxylic acid protonation in Ac-Glu-NH$_2$ and Ac-Asp-NH$_2$ amino acid models. Furthermore, our results indicate that this separation may be possible even when the distinct diffusion effect on the individual protonation rates of carboxylic and imidazole groups does not contribute to the separation, as in a polypeptide chain.

Chapter 5

Role of ionizable amino acid residues on α-helix conformational stability and folding dynamics

5.1 Introduction

Our contemporary understanding of protein folding pathways have been greatly enhanced by the study of single domain peptides (Searle & Ciani 2004; Kubelka et al. 2004; Buchner et al. 2011). Some short peptide fragments excised from proteins can fold autonomously in aqueous solution into native-like conformations (Shoemaker et al. 1987; Blanco et al. 1994; Searle et al. 1995; Mukherjee et al. 2008). These polypeptide fragments may act as a folding nucleus and play a critical role in initiating and driving protein folding (Dill 1990). Moreover, many features of the overall protein folding process have been observed in the folding of these short peptide fragments, including general hydrophobic collapse, close packing of side chains, and the formation of intramolecular hydrogen bonds (Fairman et al. 1990; Shoemaker et al. 1990; Kobayashi et al. 2000; Ciani et al. 2003; Seshasayee et al. 2006; Santiveri et al. 2008). Therefore, due to their small size and the structural simplicity, short peptide fragments that fold into well defined structures are ideal model systems for examining factors governing the mechanisms of formation of the regular secondary structural elements, α-helices (Du et al. 2007; Mukherjee et al. 2008), β-hairpins (Chen et al. 2004; Du et al. 2004; Schrader et al. 2007), and other short

structural motifs (Fierz et al. 2007). Here, we intent to investigate in detail the conformational dynamics and stabilizing factors contributing for the α-helix formation in a short peptide fragment.

α-Helical secondary structures occur widely in proteins and their folding and stability has been a subject of great interest for several years. Moreover, experimental studies have suggested that the stability of native helical conformations in amyloid-forming peptides and proteins, such as amyloid-β peptide (Ito et al. 2011), transthyretin (Palaninathan 2012) and lung surfactant protein C (Kallberg et al. 2001), play a crucial role in the aggregation behaviour of such proteins, reducing their propensity for amyloid fibril formation. As a consequence, examining the energetics and kinetics of α-helix formation is essential not only to understand protein folding but also to provide structural insights into the molecular basis of amyloid formation. A variety of spectroscopic methods have been employed to examine the nanosecond folding dynamics of monomeric α-helices in response to a conformational trigger, such as a temperature jump (T-jump) (Du et al. 2007; Mukherjee et al. 2008; Lin et al. 2011), a pH jump (Abbruzzetti et al. 2000; Causgrove & Dyer 2006), or a photo-triggering event (Bredenbeck et al. 2005). In addition, numerous theoretical and computational studies have also been carried out (Wu & S. Wang 2001; Wei et al. 2005; Morozov & Lin 2006; Khandogin et al. 2006). Because in absence of stabilizing tertiary contacts, isolated protein helical fragments frequently present low conformational stability and/or high tendency to aggregate, these previous studies on the folding dynamics and mechanisms of α-helix formation have focused mainly on alanine-based peptides. This is because alanine has the highest helix-forming propensity (Marqusee et al. 1989). Although studying alanine-rich peptides has provided invaluable information on the kinetics and mechanism of α-helix formation, such sequences are rarely encountered in proteins. Moreover, alanine is not the most abundant residue in native peptides and proteins, and may be unwise to assume that naturally occurring helices would show similar folding rates as those of alanine-rich peptides. In fact, recent studies using laser-induced T-jump relaxation kinetics with infrared spectroscopy detection, were applied to investigate the folding kinetics of the neuroactive peptide Conantokin-T (Con-T) (Du et al. 2007) and the central helix of the ribosomal protein L9:41-79 from the bacterium *Baccilus stearothermophilus* (Mukherjee et al. 2008), and have suggested that individual α-helical segments in proteins may fold on a time scale significantly slower than the folding time of alanine-based peptides. Both these peptides

exhibit unusually high helicity in aqueous solution due to a series of side chain-side chain interactions, most of which are electrostatic in nature. In particular, the sequence of Con-T is rather unique because it contains four γ-carboxiglutamic acid residues which are less commonly found in nature. Taken together, these results have proposed that salt-bridges play an important role in determining the folding rate of α-helical peptides. However, our current understanding of the folding dynamics of the α-helix motif is still mainly based on studies of model peptides with very limited sequence variation. As a consequence, the key factors governing α-helix formation of peptides composed by naturally occurring amino acids need to be further examined.

In the present work, we examine the role of specific interactions, such as salt-bridges and π-stacking interactions, on the folding dynamics and stability of an α-helical model peptide with 13 amino acid residues using time-resolved photoacoustic calorimetry (TR-PAC) experiments triggered by a laser-induced pH-jump. The model protein fragment selected is an analogue of the well studied C-peptide from bovine pancreatic ribonuclease-A (RNase A) (see Figure 5.1 and Table 5.1). C-peptide results from cyanogen bromide cleavage and its sequence corresponds to the 13 N-terminal residues of RNase A. Several nuclear magnetic resonance (NMR) and circular dichroism (CD) studies have shown that C-peptide exhibit high helicity in aqueous solution in the presence of 100 mM NaCl and at pH 5. Moreover, these studies have also revealed a bell-shaped pH profile for the total helix content with a maximum near pH 5 (Shoemaker 1985; Shoemaker et al. 1987; Fairman et al. 1990; Shoemaker et al. 1990). Therefore, C-peptide and some analogues sequences have been classified as the shortest amino acid sequences that display pH-dependent α-helix formation in aqueous solution. Thus, these amino acid sequences represent an excellent model system for examining unfolding/folding dynamics and energetics of α-helix formation using a laser-induced pH-jump technique.

Amino acid substitution studies have been exhaustively performed to investigate α-helix formation in analogues of the C-peptide. In Table 1.1 are listed the amino acid sequences of eight C-peptide analogues that were previously studied. Most of these peptides are frequently designed with the N-terminal and C-terminal blocked to avoid destabilizing interactions between the α-NH$_3^+$ and α-COO$^-$ groups and the α-helix macrodipole. These studies have provided strong evidence that specific side chain interactions including salt-bridge formation and aromatic interactions must stabilize the α-helical conformation at pH 5.
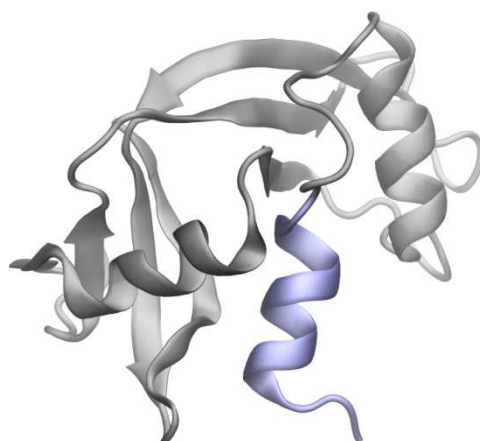
Figure 5.1: Ribbon diagram of the three-dimensional structure of RNase A (PDB entry 3DH5). The C-peptide α-helix comprising the 13 N-terminal residues of RNase A is represented in blue.

Table 5.1: Amino acid sequences of C-peptide analogues.

Peptide	Sequence
C-peptide	**K E T A A A K F E R Q H – homoserine lactone**
RN21	Acetyl- A E T A A A K F L R A H A -NH$_2$
RN23	Acetyl- A A T A A A K F L R A H A -NH$_2$
RN24	Succinyl- A E T A A A K F L R A H A -NH$_2$
RN25	Acetyl- A R T A A A K F L E A H A -NH$_2$
RN26	Acetyl- A D T A A A K F L R A H A -NH$_2$
RN54	Acetyl- A A T A A A K F L A A H A -NH$_2$
RN77	Acetyl- A R T A A A K A L E A A A -NH2
RN80	**Acetyl-A E T A A A K Y L R A H A-NH$_2$**

Initially, it was hypothesized that there was a stabilizing salt-bridge formed between the side chains of Glu-9 and His-12 (Bierzynski 1982). However, subsequent studies disproved this hypothesis (Shoemaker 1985). It appears instead that the stabilizing ionized groups are the side chains of Glu-2 and His-12, both located at opposite ends of the α-helix, which suggests the existence of a favorable interaction with the α-helix macrodipole (Shoemaker 1985; Shoemaker et al. 1987). Moreover, a salt-bridge between Glu-2 and Arg-10 has been detected in the crystal structure of RNase A (Wlodawer & Sjölin 1983) as well as in C-peptide in aqueous solution (Shoemaker et al. 1987; Osterhout et al. 1989; Fairman et al. 1990; Khandogin et al. 2006). Synthetic peptides in which either

Glu-2 or Arg-10 was replaced by Ala have provided support for the importance of this interaction in stabilizing the α-helical conformation. In addition to interacting favorably with the α-helix macrodipole, His-12 might also form a π-stacking interaction with Phe-8 (Shoemaker et al. 1987; Osterhout et al. 1989; Shoemaker et al. 1990; Khandogin et al. 2006). Experimental and computational evidences suggest that this interaction is stronger for the protonated than for the nonoprotonated form of His-12.

Herein, the C-peptide analogue investigated was RN80 (see Table 5.1) because tyrosine absorbance allows accurate determination of peptide concentration. Moreover, previous studies have shown that replacement of Phe-8 by Tyr-8 produces only a small effect on the interaction with His-12 maintaining the helical content (Shoemaker et al. 1990). Destabilization on site-specific regions of this α-helical peptide model was achieved by protonation of individual amino acid residues in the peptide sequence, using a laser-induced pH-jump method. Conformational and dynamics parameters, such as volume changes, enthalpy and kinetics on the nanosecond to microsecond time scales were obtained using TR-PAC. In addition, CD and NMR were used to characterize structural details at different pH conditions.

5.2 Materials and Methods

5.2.1 Sample Preparation

The RN80 analogue of the C-peptide was custom-synthesized by GenScript Corporation, at a purity of >95 % by HPLC analysis. The C-peptide analogue has the sequence: AETAAAKYLRAHA, with the N-terminal group modified by acetylation and the C-terminal group modified by amidation. Peptide solutions were prepared by dissolving the lyophilized peptide samples in the appropriate solvent for each different experiment. The final peptide concentrations were checked optically on a Spectronic Unicam UV-500 spectrometer by tyrosine absorbance at 280 nm, using $\varepsilon_{280} = 1490 \text{ M}^{-1}\text{cm}^{-1}$ (Creighton 1997).

Deuterium oxide (D_2O, 99.9 atom % in D), bromocresol purple (BP) and o-nitrobenzaldehyde (o-NBA) were purchase from Sigma-Aldrich Chemical Company, St. Louis, USA. Sodium deuteroxide (NaOD, 99.5 % in D) was obtained from Cambridge

Isotope Laboratories, Inc., USA. Deuterium chloride (DCl, 99.7 % in D) was obtained from Isotec, Inc., USA.

5.2.2 Circular Dichroism Spectroscopy

Circular dichroism (CD) spectra were recorded on an Olis DSM-20 CD spectrophotometer with a temperature-controlled cell holder. The C-peptide analogue was dissolved in an aqueous solution with 100 mM NaCl, and the pH of the samples was adjusted using HCl and NaOH. Final peptide concentrations were approximately 1 and 9 mg/ml for far-UV and near-UV CD experiments, respectively. Far-UV measurements were recorded between 190 nm and 260 nm, using a 0.2 mm path length cell, at 3.0 ℃ and 20.0 ℃. The near-UV data were collected in the wavelength range of 250 to 340 nm with a 2.0 mm path length cell, at 3.0 ℃. CD spectra were run with a step-resolution of 1 nm, an integration time of 5 s, and using a bandwidth of 0.6 nm. The spectra were averaged over at least three scans and corrected by subtraction of the buffer signal.

The results are expressed as the mean residue ellipticity $[\Theta]_{MRW}$, defined as $[\Theta]_{MRW} = \Theta_{obs}(0.1MRW)/(lc)$, where Θ_{obs} is the observed ellipiticity in millidegrees, MRW is the mean residue weight, c is the concentration in milligrams per mililitre, and l is the length of the light path in centimeters. Noise reduction was achieved by adjacent-averaging smooth processing using the software package *OriginPro7* (OriginLab Corporation, USA). Secondary structure was estimated by analysis of the far-UV CD spectra between 190 and 240 nm, using the program CONTIN (Provencher 1982).

5.2.3 Nuclear Magnetic Resonance Spectroscopy

Peptide samples for NMR were dissolved in 100 mM NaCl containing 10 % (v/v) D_2O to a final concentration of approximately 3 mM. Spectra of the RN80 C-peptide analogue were obtained at four different pH values (2.8, 5.6, 7.1, 8.7). The pH of the solution was adjusted by addition of appropriate amounts of either DCl or NaOD. The pH was measured by using a glass microelectrode and was not corrected for the isotope effect.

NMR measurements were performed on a Bruker Avance III 400 spectrometer operating at a proton frequency of 400.133 MHz, and at a temperature of 3.0 ℃. The

sample temperature was calibrated against a methanol standard. One-dimensional NMR spectra and a set of typical homonuclear two-dimensional spectra were recorded: double quantum filtered correlated spectroscopy (DQF-COSY) (Derome & Williamson 1990), total correlated spectroscopy (TOCSY) (Shaka et al. 1988), and rotating-frame overhauser effect spectroscopy (ROESY) (Bax & Davis 1985). In all two-dimensional spectra, the sign of the frequency in the indirect dimension was discriminated using the States-TPPI method (Marion et al. 1989). Typically, one-dimensional spectra were collected with 16 scans and 16k data points in the time domain, with a spectral width of 4424 Hz. Two-dimensional spectra were collected with 512 increments (8 scans each) in t1 and 2k data points in t2, using a spectral width of 4424 Hz in both dimensions. The water signal was suppressed by excitation sculpting with z-gradients (Hwang & Shaka 1995). TOCSY experiments were performed with a mixing time of 60 and 80 ms using homonuclear Hartman-Hahn transfer using the DIPSI2 sequence for mixing (Shaka et al. 1988). ROESY experiments were collected with mixing times of 200, 300 and 400 ms. One-dimensional free induction decays (FIDs) were apodized with a 2 Hz line broadening function and zero filled to 32k data points prior to Fourier transformation. TOCSY and ROESY FID's were apodized by QSINE window functions in both dimensions, whereas DQF-COSY were apodized by a 0º phase shifted squared sine-bell window function in t2 and a 0º phase shifted bell function in t1. Baselines were typically corrected using a fourth order polynomial function in both dimensions. A FLATT baseline correction algorithm was further applied to the t2 dimension in TOCSY experiments (Güntert & Wüthrich 1992). The NMR data was processed using the program Topsin v2.1 and the cross-peak intensities were determined by volume integration. The $^3J_{HNH\alpha}$ coupling constants were measured from both one-dimensional and DQF-COSY spectra.

Saturation Transfer Difference (STD) NMR spectra (Mayer & Meyer 1999) were acquired at 3.0 ºC, with a standard pulse sequence from the Bruker library with a spin-lock (T1ρ) filter for protein background suppression and water suppression with excitation sculpting using z-gradients. The spectra were collected with 256 increments in a matrix of 32 k data points in t2 using a spectral window of 6410 Hz centered at 1877.8 Hz. A 2 kHz spin lock filter with a length of 15 ms was used. For the *on-resonance* spectra (I_{SAT}), selective saturation of peptide resonances was performed by irradiating at 526 Hz using a series of Eburp2.1000 shaped 90º pulses (50 ms, 1 ms delay between pulses) for a total saturation time of 2.5 s. For the *off-resonance* spectra (I_0), irradiation was performed at 10000 Hz. All data was processed using the program Topspin v2.1 and the STD spectra

were obtained after subtraction of the *on-resonance* spectra from the *off-resonance* spectra ($I_{STD} = I_0 - I_{SAT}$). Control STD-NMR experiments were performed using an identical experimental setup and the same ligand concentration but in the absence of the peptide.

5.2.4 Time-Resolved Photoacoustic Calorimetry

Sample solutions for photoacoustic measurements were prepared by dissolving the lyophilized peptide samples into an aqueous solution containing 100 mM NaCl and sufficient *o*-NBA to produce a final optical absorption of 0.6 in a 1.0 cm path length cell, at 355 nm. Peptide concentrations varied between 200 μM and 2.0 mM. Bromocresol purple (BP) was used as the photocalorimetric reference compound. BP was dissolved in an aqueous solution containing 100 mM NaCl and its optical absorption was adjusted to match that of the sample solution at 355 nm. The pH of the sample and reference solutions was adjusted by addition of concentrated HCl or NaOH and measured using a glass microelectrode. The pH of BP solutions was adjusted to 9.0, in order to avoid instability in optical absorption at the excitation wavelength. All experiments were repeated at least three times.

Experiments of laser-induced pH jump coupled with photoacoustic detection were performed using an home-made time-resolved photoacoustic calorimetry flow cell with temperature control and automatic injection (Kloehn syringe pump). In Chapter 3 is presented a detailed description of the experimental setup. As light source, operated at 355 nm, was used the third harmonic of a nanosecond Q-switched Nd:YAG laser (Ekspla NL301G). The laser pulse width was approximately 6 ns, and the repetition rate was 10 Hz. The typical maximum power per pulse used in the experiments was 1.0 mJ. Furthermore, each solution analyzed (sample, BP and solvent) was excited with four laser intensities corresponding to 25, 50, 75 and 100 % of the full laser intensity by employing neutral density filters. The PAC signals were measured between 1.8 ℃ and 20.0 ℃, and the temperature variation during an experiment was around 0.5 ℃. The sample data were analyzed by comparison with those for the calorimetric reference compound, which releases all the energy absorbed upon photoexcitation as heat with a quantum efficiency of 1.0. The photoacoustic pressure waves were detected using 2.25 MHz and 0.5 MHz frequency microphones (Olympus Panametrics, USA). The PAC signals from 200 shots were averaged, amplified by a preamplifier and then recorded using a digital oscilloscope.

The principles of deconvolution of photoacoustic waveforms are described in detail in Chapter 3. Briefly, the observed time-dependent acoustic signal $E(t)$ is produced by the convolution of the time-dependent function of the decay process $H(t)$ with an instrument response function, or reference waveform, $T(t)$.

$$E(t) = T(t) \otimes H(t) \hspace{4cm} (5.1)$$

The instrument response function, essential to deconvolution, was obtained by recording the signal from the reference BP. Because the heat release of the reference compound is much faster than the instrument response time, the signal for the reference compound was used as the instrument response function $T(t)$.

The function $H(t)$ represents the overall time-dependent volume change is written as the summation of sequential single exponential terms:

$$H(t) = \sum_i \frac{\phi_i}{\tau_i} e^{-(t/\tau_i)} \hspace{4cm} (5.2)$$

where ϕ_i and τ_i are the respective amplitude and decay time for the ith component in the sum of the exponentials. The *CPAC* software developed in our laboratory was used to obtain the ϕ_i and τ_i parameters (Schaberle et al. 2010). This software provide an analytical description for the instrumental response photoacoustic wave $T(t)$, and the analytical solution for the convolution between $T(t)$ and the heat function $H(t)$. The ϕ_i and τ_i parameters are varied until the calculated $E(t)$ fits the experimental wave $E(t)$. The kinetics of processes occurring faster than roughly 10 ns cannot be resolved, but the integrated enthalpy and volume changes can be quantified from the amplitude of the acoustic wave.

Structural volume changes as a function of the solution pH and the peptide concentration were determined using a two-temperature method (Gensch & Braslavsky 1997). The sample waveforms were acquired at the temperature $T_{\beta=0}$, for which the thermal expansion coefficient of the solution, β, is zero. The value of $T_{\beta=0}$ can be determined experimentally by measuring the temperature at which the signal for the reference compound vanishes. The thermoelastic parameter ($C_p\rho/\beta$) of 100 mM NaCl as a function of temperature was determined by using BP as a reference compound in pure water compared to 100 mM NaCl. Under our experimental conditions (100 mM NaCl) we

found $T_{\beta=0}$ = 1.8 ℃. The reference waveforms were measured at a slightly higher temperature, $T_{\beta\neq0}$ = 6.0 ℃. Signals measured at $T_{\beta=0}$ originate solely from the structural volume changes in the solution and include no enthalpic contributions. The extent of the observed structural volume change ΔV_i (estimated as milliliters per mole of absorbed photons) is calculated from ϕ_i as:

$$\Delta V_i = \phi_i E_\lambda \left(\frac{\beta}{C_p \rho} \right)_{\beta\neq0} \qquad (5.3)$$

where E_λ is the energy of one mole of photons at the excitation wavelength and $(\beta/C_p\rho)_{\beta\neq0}$ is the thermoelastic parameter of the solution at $T_{\beta\neq0}$.

Experiments conducted at multiple temperatures have been used to determine for each transient the heat release, the structural volume change and, from the temperature dependence of the rate constants, the activation energy (Callis et al. 1972; Peters & Snyder 1988; Braslavsky & Heibel 1992). Deconvolution was performed at several temperatures, and the pre-exponential factors ϕ_i were used to determine the energy content, $E_\lambda\phi_i$, of the transient at each temperature. This parameter was then plotted versus the thermoelastic parameter of the solution, $(C_p\rho/\beta)_{\beta\neq0}$. From the linear relation:

$$\phi_i E_\lambda = Q_i + \Delta V_i \left(\frac{C_p \rho}{\beta} \right) \qquad (5.4)$$

it is possible to determine the heat release after excitation per mole of photons absorbed Q_i (from the intercept) and the structural volume change per mole of photons absorbed ΔV_i (from the slope) for each ith process.

In both methods, two-temperature and multi-temperature, the volume changes can be converted into molar reaction volume (expressed as milliliters per mole of molecules) dividing ΔV_i by the deprotonation quantum yield of o-NBA, Φ_{H+} = 0.4, (George & Scaiano 1980). The heat release per mole of photons Q_i, obtained using the multiple-temperature method, can be converted in enthalpy change taking in consideration the quantum yield of o-NBA.

The temperature dependence of the rate constants could be analyzed by the following relationships:

$$k = k_0 e^{-E_a / RT} \qquad\qquad\qquad (5.5)$$

$$\ln k = \ln k_0 - \frac{E_a}{RT} \qquad\qquad\qquad (5.6)$$

where $k = 1/\tau$. The activation energy (E_a) and the pre-exponential factor k_0 could then be derived from a linear plot of ln k vs 1/T (Arrhenius Plot).

5.3 Results

5.3.1 Evidence for RN80 α-Helical Structure at pH 5.0

The currently available information on C-peptide analogues structure were obtained mainly from far-UV CD and one dimensional ^{1}H-NMR and have shown that these peptides, constructed with specific side-chain interactions, are folded in a stable α-helical conformation in an aqueous solution with 100 mM NaCl, at pH 5. In particular, C-peptide analogue RN24 (see Table 5.1) has been a subject of great interest and several studies using CD, NMR and computational approaches have been performed (Osterhout et al. 1989; Khandogin et al. 2006). Moreover, it is the only analogue whose structure has been examined in detail using a set of two-dimensional ^{1}H-NMR experiments (Osterhout et al. 1989). The assignments have been deposited at the Biological Magnetic Resonance Data Bank (BMRB) with accession number 302. Here we studied the C-peptide analogue RN80 (see Table 5.1), which is a 13 amino acid residue peptide with two basic, one acid and one aromatic residue, and C-terminus and N-terminus blocked. Only a few studies have been conducted with the analogue RN80. Thus, the structural features of this peptide were first examined using the standard experimental conditions (100 mM NaCl and pH 5) by NMR and CD in order to demonstrate that RN80 present similar properties to those previously observe in the well studied C-peptide analogues.

Far-UV CD spectra were used to monitor the helicity of RN80 in 100 mM NaCl, at pH 5. As shown in Figure 5.2, the far-UV CD spectrum of the peptide at pH 5 and 3.0 ºC exhibits the characteristic double minima of α-helices at 222 nm and 208 nm,

indicating that the helical conformation is significantly populated under these experimental conditions. The fraction of helical content was quantitatively estimated using the program CONTIN. At pH 5 and 3.0 ℃, the helical content was estimated to be approximately 55 %, i.e., about 8 amino acid residues are in α-helix conformation. Moreover, in Figure 5.2 is also shown that increasing the temperature from 3.0 ℃ to 20.0 ℃ results in an increase in the random coil population from 45 % to 70 %. As expected, the degree of helicity of the RN80 analogue is temperature dependent and decreases with increasing temperature. This behaviour is consistent with previous studies performed with others C-peptide analogues.
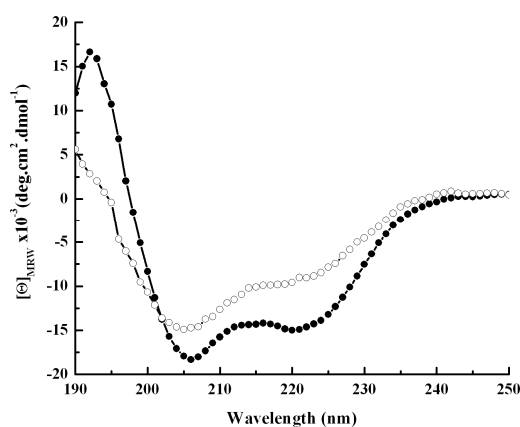
Figure 5.2: Far-UV CD spectra of RN80 in 100 mM NaCl and pH 5, at 3.0 ℃ (filled circles) and 20.0 ℃ (open circles). The double negative peak at approximately 208 and 222 nm is typical of α-helix secondary structure.

Moreover, the structure of the peptide RN80 was also investigated using a set of two-dimensional ^{1}H-NMR experiments, and it was possible to identify the complete spin systems of most of the 13 amino acid residues for this C-peptide analogue. The atom identifier used throughout this chapter, as well as any NMR related nomenclature, follow the guidelines previously described (Markley et al. 1998) (see Figure B.1).

Figure 5.3 shows the ^{1}H^N-^{1}H$^\alpha$ fingerprint region of DQF-COSY and TOCSY experiments of the RN80 analogue in 100 mM NaCl, at pH 5.6 and 3.0 ℃. Only 11 spin systems were assigned unambiguously, because residues Ala-1 and Ala-5 present identical H^N and H$^\alpha$ chemical shifts which can explain the difficulty to assign these residues at pH 5. However, experiments performed at different pH conditions helped to discriminate both

spin systems allowing the assignment of Ala-1 and Ala-5. Therefore, all expected correlations for a 13 residue peptide were obtained. Moreover, expansion of the NH-aliphatic region of TOCSY spectrum show the amide to alpha and amide to side chain spin systems for each assigned residue (see Figure B.2). The identified spin systems at pH 5.6 are characterized in Table B.1 of the appendix.
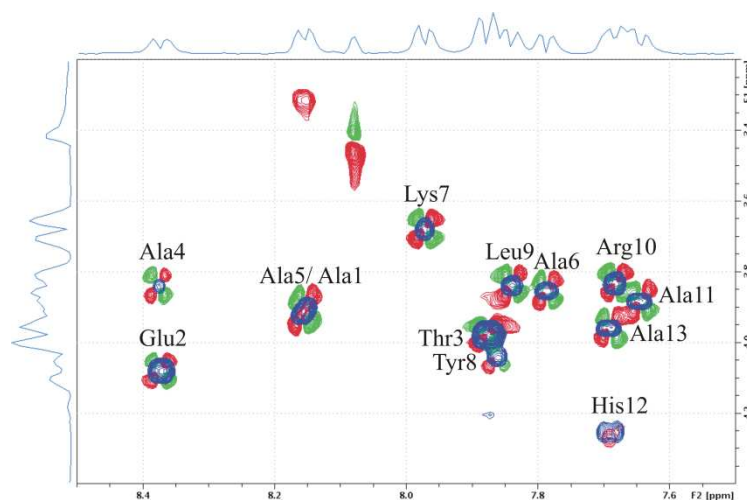
Figure 5.3: Superimposition of the $^1H^N - ^1H^\alpha$ fingerprint region of the DQF-COSY (in red and green) and TOCSY spectra (in blue) of RN80 in 90 % H_2O/ 10 % D_2O containing 100 mM NaCl, at pH 5.6 and 3.0 ℃. The cross peaks are labeled by the three-letter amino acid code and the residue number.

The sequential assignment of the peptide resonances relies on the observation of a series of inter-residue NOEs, namely $H^N(i)$-$H^N(i+1)$, $H^\alpha(i)$-$H^N(i+1)$ and $H^\beta(i)$-$H^N(i+1)$ (Wüthrich 1986). Figure 5.4 presents a survey of the experimental data used for the secondary structure determination of RN80 in 100 mM NaCl, at pH 5.6 and 3.0 ℃. Connectivities between sequential H^N or H^α protons were observed along the peptide sequence from Ala-1 to Ala-11. The connectivities were lost due to identical H^N chemical shifts between residues i, $i + 1$ with $i = 11, 12$. Furthermore, some connectivities $H^\beta(i)$-$H^N(i+1)$ were also observed. It can also be seen that, in addition to sequential NOEs extending along the molecule, there are a considerable number of $H^\alpha(i)$-$H^N(i+3)$ and $H^\alpha(i)$-$H^\beta(i+3)$ NOEs, which are characteristic of a helical structure (Wüthrich 1986). This

NOE pattern suggests that the peptide RN80 is an α-helix over most of its length at pH 5.6 and 3.0 °C.

$^1H^N$-$^1H^\alpha$ vicinal spin-spin coupling constants ($^3J_{HNH\alpha}$) can provide further conformational information. These coupling constants are related to the torsional angle ϕ by the Karplus equation (Karplus 1959). $^3J_{HNH\alpha}$ coupling constants were measured from both one-dimensional and DQF-COSY spectra. The observed values are indicated in Figure 5.4 and in Table B.4 of appendix. It is observed that at pH 5.6 most of these ^3J coupling constants are smaller than 6 Hz, consistent with the existence of a helical structure for most of the molecule. Values higher than 6 Hz observed for Glu-2, Thr-3 and Ala-13 may reflect some end effects, either partial unwinding of the helix or distortion of its geometry. These results are in agreement with the far-UV CD results showing that around 8 amino acid residues are in α-helix conformation.

In addition, H^α chemical shift data available from our experiments were used to perform a qualitative secondary structure estimate according to the chemical shift index (CSI) strategy (Wishart et al. 1991; Wishart et al. 1992; Wishart et al. 1995). Briefly, since the chemical shift is sensitive to the environment, it should also contain structural information. Wishart et al. (1991) have demonstrated that ^1H-NMR chemical shifts are strongly dependent on the character and nature of protein secondary structure. The chemical shift index method relies on calculation of chemical shift deviations for $^1H^\alpha$ (or $^{13}C^\alpha$) in all amino acid residues, when random coil chemical shifts are used as references. Consecutive deviations large enough to be meaningful indicate either helical structures or β-strands, depending on the sign of the deviation. Negative deviations to H^α chemical shifts correspond to local α-helical structures, whereas the opposite is true for local β-sheet structures. In this way, the location of helix and strand segments may be identified. Figure 5.4 shows the CSI behaviour for the C-peptide analogue under study in 100 mM NaCl, at pH 5.6 and 3.0 °C. The $^1H^\alpha$ chemical shifts observed are consistently smaller than the random coil values (CSI = -1) suggesting the presence of an α-helix motif. Hence, the overall analysis of Figure 5.4 clearly demonstrates that the C-peptide analogue adopts an α-helical structure in 100 mM NaCl, at pH 5.6 and 3.0 °C.
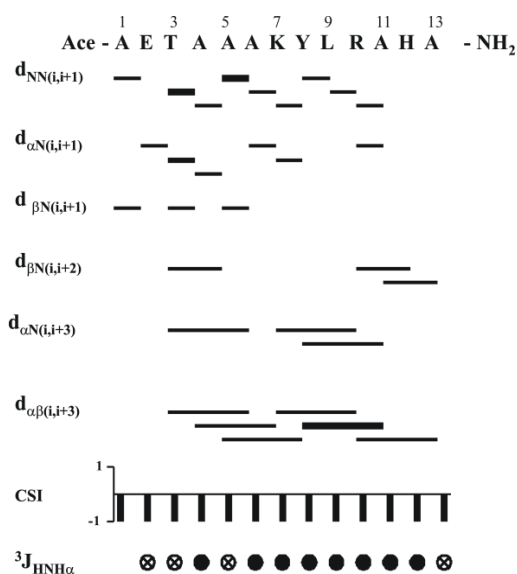
Figure 5.4: Summary of the NMR data used to establish the secondary structure of RN80 in 100 mM NaCl, at pH 5.6 and 3.0 ℃. Sequential and medium-range NOEs, chemical shift index (CSI) of $^1H^\alpha$ and $^3J_{HNH\alpha}$ coupling constants are presented, along with the amino acid sequence. The height of the bars for NOE connectivities indicates the NOE intensity. Values of $^3J_{HNH\alpha}$ are indicated by filled ($^3J_{HNH\alpha} < 6$ Hz) and crossed ($6 \leq {}^3J_{HNH\alpha} \leq 8$ Hz) circles.

5.3.2 Examining the pH-dependent Structural Changes of RN80 α-Helix by CD and NMR Spectroscopy

Previous studies with several C-peptide analogues have shown that there are a number of potentially favorable short-range and medium-range interactions along the peptide sequence which contribute to the unusually large helical content. In order to examine the relative importance of these interactions we have undertaken a detailed study of the effect of pH on the helical content, using both CD and NMR spectroscopy. Furthermore, to understand the pH dependence of α-helix formation is essential to decipher the ideal experimental conditions to employ in the laser-induced pH jump technique.

CD analysis of the peptide RN80 was carried out in the far- and near-UV regions, in different pH conditions. The former (shorter wavelengths) reflects the secondary structure, whereas the latter (longer wavelengths) reflects the tertiary structure of the protein. Figure 5.5 (A) shows that the α-helical conformation of the peptide is strongly pH

dependent. Table 5.2 presents the α-helix contents of RN80 peptide, determined using the program CONTIN, in different pH conditions. As expected, the α-helix content of RN80 reaches its maximum, 58 %, around pH 5.8. Although the low-pH forms of the peptide show a typical far-UV CD curve for α-helix, the random coil conformations predominate and it was obtained an estimated value of 65 % for unordered structure. In high pH conditions, the degree of helical content is even further diminished and the estimated value for random coil is around 70 – 80 %. This decrease in the helical peptide population is not only revealed by a significant reduction in the mean residue ellipticity at 222 nm, but also by the blue shift of the minimum at 208 nm in the far-UV CD spectra. Therefore, in general, alkaline pH conditions seem to induce a larger decrease in the helical content of the peptide than acid pH conditions.
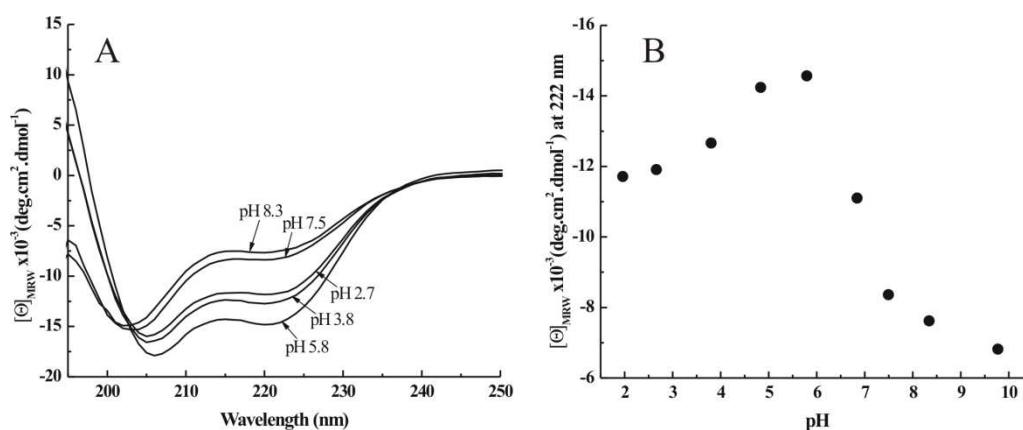
Figure 5.5: (A) Far-UV CD spectra of RN80 in 100 mM NaCl, in different pH values and at 3.0 ºC. Far-UV CD spectra were fit to a linear combination of three contributions (α-helix, β-sheet and unordered structure) to estimate the α-helix content in different pH conditions, using the program CONTIN (see Table 5.2). (B) Mean residue ellipticity of RN80 at 222 nm as a function of pH.

Figure 5.5(B) shows the pH profile of the α-helix content for RN80. As observed in other C-peptide analogues, the pH-dependent curve of helix formation (as measured by $[\Theta]_{222nm}$) is bell shaped with a maximum close to pH 5, at 3.0 ºC. The apparent pK values observed are approximately 4.2 and 6.5, suggesting that charged amino acid side chains are critical for α-helix stability. A significant sharp decrease in peptide α-helix content is observed between pH 5 and pH 8. The only group in the peptide sequence titrating

between pH 5 and pH 8 is the side chain of His-12. Glu-2 is identified as the residue responsible for the decrease in the CD signal between pH 5 and pH 2. However, protonation of Glu-2 only slightly reduces the α-helix content. Thus, this bell-shaped pH profile indicates that the α-helix content may be governed by two pairs of side chain-side chain interactions, Glu-2:Arg-10 and Tyr-8:His-12. The highest α-helix content is observed at approximately pH 5.5, where both Glu-2 and His-12 residues are ionized. Moreover, since the positive pole of the α-helix macrodipole is near the N-terminus and the negative pole is near the C-terminus, interactions with the helix macrodipole should be favorable at pH 5.5 because Glu-2 is negatively charged and it is close to the N-terminus while His-12 is positively charged and it is close to the C-terminus.

Table 5.2: Estimation of the RN80 peptide secondary structure from far-UV CD data, using the program CONTIN.

pH	% Helical Structure	% Non-Helical Structures
2.0	35 ± 1.4	65 ± 0.85
2.7	37 ± 1.6	63 ± 1.0
3.8	46 ± 1.6	54 ± 1.5
4.8	55 ± 2.1	45 ± 1.9
5.8	58 ± 2.3	42 ± 2.1
6.8	33 ± 1.4	67 ± 0.90
7.5	24 ± 0.80	77 ± 0.80
8.3	22 ± 1.2	78 ± 0.70
9.8	17 ± 1.1	83 ± 1.3

The CD signal in the near-UV spectral region (250 - 350 nm) has been reported to be sensitive to local tertiary structure around aromatic residues (tryptophan, tyrosine and phenylalanine) and disulphide bonds. In fact, the near-UV CD spectra generate an effective fingerprint of the chiral environment around those residues, providing a tool to monitor structural changes in proteins and peptides. Near-UV CD bands from individual residues in a protein or peptide may be either positive or negative and vary dramatically in intensity. Each of the aromatic amino acid residues tend to have a characteristic CD

profile: tryptophan with a peak close to 290 nm and with fine structure between 290 and 305 nm; tyrosine with a peak between 275 and 282 nm, whose fine structure at longer wavelengths may be obscured by that from tryptophan; phenylalanine with sharp fine structure between 255 and 270 nm. The near-UV absorption of the disulphide bond occurs near 260 nm and is generally quite weak. Moreover, aromatic residues immobilized and/or interacting strongly with neighboring residues produce the strongest signals. Figure 5.6 shows the near-UV CD spectra of RN80 in different pH conditions, in aqueous solution with 100 mM NaCl and at 3.0 ℃. A single negative band was observed in the wavelength range between 270 nm and 285 nm due to the contribution of Tyr-8. Upon different pH conditions, significant changes are observed in this wavelength region, indicating changes in the environment of Tyr-8. As expected, the negative CD band is more intense at pH 5. Concomitantly with the decrease of secondary structure content at pH 3 and pH 8, the near-UV CD spectra show less intense signals. Hence, as previously reported for other C-peptide analogues the interaction between Tyr-8 and His-12 seems to be perturbed with pH changes. A significant decrease in the CD signal occurs at pH 8 because the π-stacking interaction between Tyr-8 and His-12 is not favored due to the deprotonation of histidine. These near-UV CD data are consistent with previously obtained results from amino acid substitution experiments, which revealed that the π-stacking interaction between aromatic residues in position 8 and histidine in position 12 of the C-peptide analogues play a crucial role in folding and their proximity is a key factor for α-helix formation.
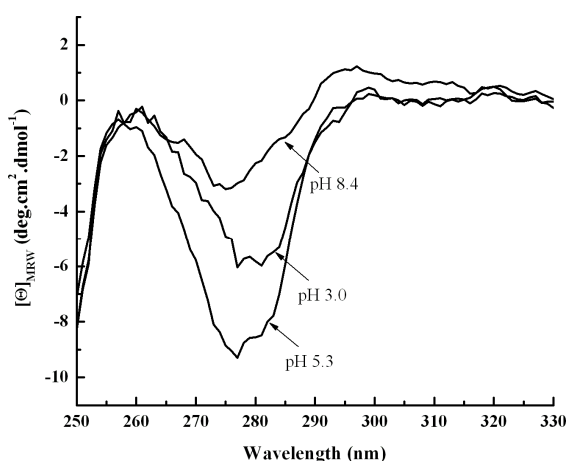
Figure 5.6: Near-UV CD spectra of RN80 in 100 mM NaCl, in different pH values and at 3.0 ℃. CD signals in the region between 275 and 285 nm are characteristic of tyrosine residues.

The structure of RN80 was also assessed by ^{1}H-NMR in different pH conditions, namely at pH around 3 and 8. Even without resonance assignments, the resonance dispersion observed in a one-dimensional spectrum can be used as a crude estimate of the presence of ordered structures. The chemical shifts for protons in the 20 common amino acid residues in random coil polypeptides have been extensively studied and well characterized (Wishart et al. 1995). If the polypeptide is unstructured, resonances from the amide (random-coil shifts 8.5 - 8.0 ppm) and α-carbon protons (random-coil shifts 4.4 - 4.1 ppm) fall within a small range of chemical shifts, with reduced chemical shift dispersion. However, folded polypeptides will exhibit a much broader range of well defined chemical shifts (Cavanagh et al. 1995). One-dimensional ^{1}H-NMR spectra in different pH conditions indicate that RN80 may present the higher conformationally ordered state at pH 5.6 (see Figure B.3). Furthermore, at pH 8 the ^{1}H-NMR spectrum exhibits broader peaks indicating exchange process among different conformational states. Thus, the peptide in alkaline pH conditions, such as pH 8, must be in a less regular secondary structure conformation. The assigned proton resonances for RN80 at pH 3 and pH 8, are detailed on tables B.2 and B.3 of the Appendix, respectively.

Figure 5.7 summarizes the inter-residue NOEs observed for RN80, at approximately pH 2.8 and 3.0 ºC. Several gaps in the sequential connectivities are observed. Along with sequential NOEs, there are also some $H^{\alpha}(i)$-$H^{N}(i+3)$ and $H^{\alpha}(i)$-$H^{\beta}(i+3)$ NOEs, characteristic of helical structure. The CSI pattern indicates propensity for the existence of an α-helical region extending from Thr-3 to Ala-13. However, only three $^3J_{NHH\alpha}$ coupling constants are less than 6 Hz (see Table B.4). Thus, these NMR data seem to indicate a structure more closely to helical structure with α-helical propensity but with higher conformational flexibility, agreeing with the CD data which indicate a lower α-helical content. This may in fact be a consequence of conformational dyamics.
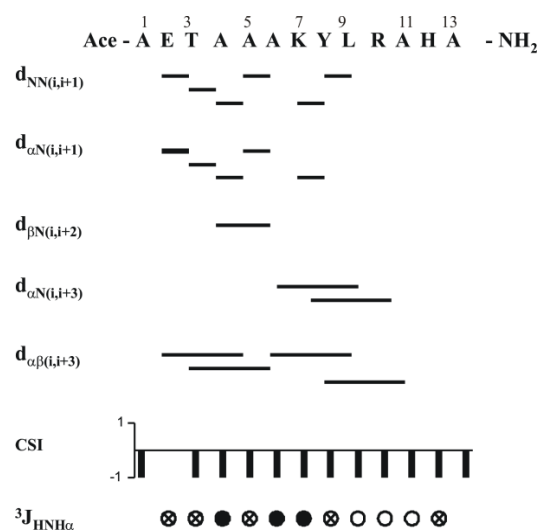
Figure 5.7: Summary of the NMR data used to establish the secondary structure of RN80 in 100 mM NaCl, at pH 2.8 and 3.0 °C. Sequential and medium-range NOEs, chemical shift index of $^1H^\alpha$ and $^3J_{HNH\alpha}$ coupling constants are presented, along with the amino acid sequence. The height of the bars for NOE connectivities indicates the NOE intensity. Values of $^3J_{HNH\alpha}$ are indicated by filled ($^3J_{HNH\alpha} < 6$ Hz), crossed ($6 \leq {}^3J_{HNH\alpha} \leq 8$ Hz) and open ($^3J_{HNH\alpha} > 8$ Hz) circles.

Figure 5.8 illustrates the distribution of inter-residue NOEs along the RN80 sequence in an aqueous solution with 100 mM NaCl, at pH 8.7 and 3.0 °C. A significant loss in sequential connectivites is observed when compared with the sequential NOEs pattern obtained at pH 5.6. Most residues have average coupling constants ($6 \leq {}^3J_{HNH\alpha} \leq 8$ Hz) and there are several residues along the peptide sequence that exhibit ^3J couplings higher than 8 Hz (see Table B.4), providing strong evidence that α-helical conformation is not present under these experimental conditions. This finding is supported by CSI analysis because no consecutive negative deviations in the H^α chemical shifts are observed. Moreover, no $H^\alpha(i)$-$H^N(i+3)$ or $H^\beta(i)$-$H^N(i+3)$ NOEs are observed. Therefore, NMR data indicate that C-peptide analogue RN80 is in a random coil conformation at pH 8.7.

Ace - A E T A A A K Y L R A H A - NH$_2$
(positions: 1, 3, 5, 7, 9, 11, 13)

$d_{NN(i,i+1)}$

$d_{\alpha N(i,i+1)}$

$d_{\beta N(i,i+1)}$

$d_{\beta N(i,i+2)}$

$d_{\alpha N(i,i+2)}$

CSI
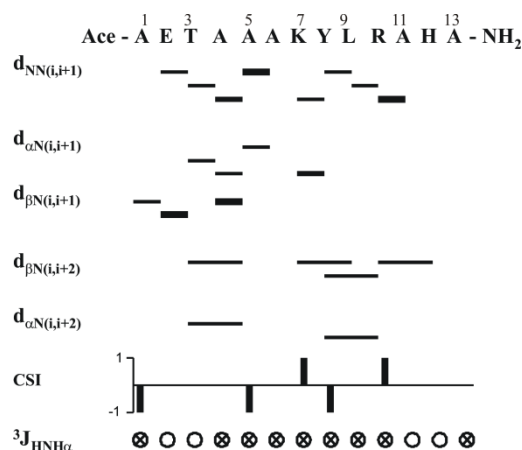
$^3J_{HNH\alpha}$

Figure 5.8: Summary of the NMR data used to establish the secondary structure of RN80 in 100 mM NaCl, at pH 8.7 and 3.0 °C. Sequential and medium-range NOEs, chemical shift index of $^1H^\alpha$ and $^3J_{HNH\alpha}$ coupling constants are presented, along with the amino acid sequence. The height of the bars for NOE connectivities indicates the NOE intensity. Values of $^3J_{HNH\alpha}$ are indicated by crossed ($6 \leq {}^3J_{HNH\alpha} \leq 8$ Hz) and open ($^3J_{HNH\alpha} > 8$ Hz) circles.

Apart from the patterns of short-range NOEs at each pH that allowed the characterization of secondary structure, relevant medium-range NOEs were also observed. Figure 5.9 shows an expansion of the aromatic region of the ROESY spectrum of RN80, at pH 5.6. The cross-peak corresponding to close proton–proton contacts between the rings of Tyr-8 and His-12 (depicted by dashed lines) is highlighted in the spectrum. A clear correlation between the signal for the aromatic protons of Tyr-8 at $\delta = 6.34$ ppm and the signal for protons from His-12 ring at $\delta = 8.15$ is observed. The presence of this medium-range NOE suggests that the side chains of these two amino acid residues are involved in a π-stacking interaction, at pH around 5. The π-stacking interaction between Tyr-8 and His-12 may be favored at pH 5, because this NOE is less intense in the ROESY spectra collected at pH 3 while at pH 8 is not observed. Thus, these results together with near-UV CD data provide strong evidence that the aromatic contact between Tyr-8 and the charged His-12 contributes for the increased α-helix stability at pH 5.
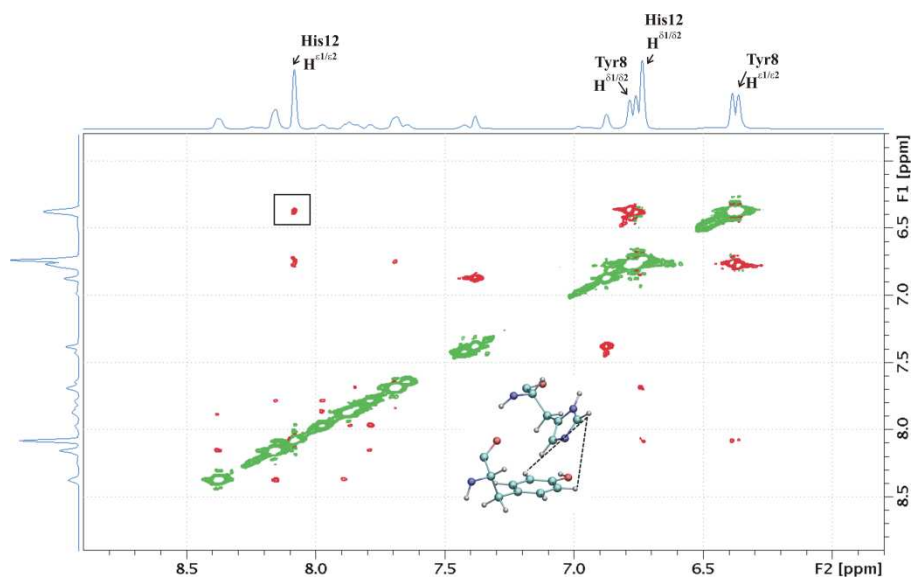
Figure 5.9: ROESY-NMR spectrum of the aromatic region of RN80 acquired with a mixing time of 200 ms, at pH 5.6 and 3.0 ºC. The cross-peak highlighted in a rectangular box is related with the π-stacking interaction between protons in the rings of Tyr-8 ($H^{\varepsilon 1/\varepsilon 2}$) and His-12 ($H^{\varepsilon 1/\varepsilon 2}$). A hypothetical perspective of the π-stacked rings is displayed and the proton contacts observed (< 5 Å) are represented by dashed lines.

5.3.3 Deciphering the Optimal Experimental Conditions for Laser-induced pH Jump Experiments

To trigger conformational changes in proteins or peptides using a laser-induced pH jump method is essential to understand how different pH conditions affect their structural stability. In the previous sections, we demonstrate that the C-peptide analogue RN80 seems to be an excellent peptide model for examining folding dynamics and energetics of α-helix formation with a pH jump methodology. The extensive studies carried out using ^{1}H-NMR and CD have shown that alkaline pH conditions cause a significant loss of α-helix content and the amino acids in the RN80 sequence controlling the pH-induced conformational changes were identified. Most of these experiments have been performed at low temperature because the peptide presents higher helical content (~ 50 %). Using the two-temperature method, the measurements of photoacoustic signals from the peptide samples need to be collected at low temperature, namely 1.8 ºC, where the peptide contains a larger number of residues in α-helical conformation.

Figure 5.10 represents a schematic view of how different pH conditions affect the α-helical content of the RN80 peptide. Briefly, the pH-dependence curve of RN80 α-helix content is bell-shaped with a maximum near pH 5.5 and the main forces stabilizing this structure are the salt-bridge formed between Glu-2 and Arg-10 and the π-stacking interaction involving His-12 and Tyr-8. Thus, protonation of Glu-2 promotes partial unfolding of the RN80 α-helix (Figure 5.10). Moreover, His-12 protonation promotes the folding of the α-helix from highly unfolded conformations (Figure 5.10). These experimental findings were used to select the ideal initial pH conditions to employ in the laser-induced pH jump experiments. In the present work, peptide samples were prepared in the presence of *o*-NBA, a well studied photo-triggered proton generator, at different initial conditions namely near pH 5 and pH 7. Upon laser irradiation at 355 nm, *o*-NBA molecules deprotonate promoting a pH-jump. Thus, we propose to selectively protonate Glu-2 and His-12 and evaluate their contribution on folding dynamics using TR-PAC measurements.

Before performing laser-induced pH jump experiments, we have investigated any relevant interactions occurring between *o*-NBA and RN80 that could perturb the α-helix structure.
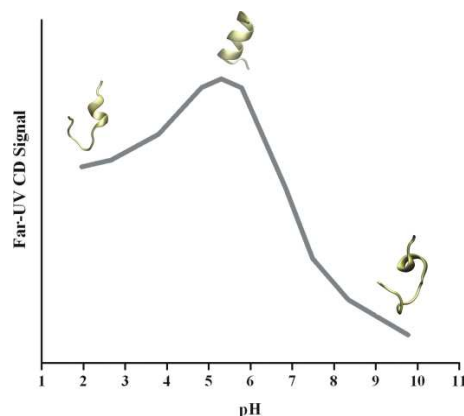
Figure 5.10: Schematic diagram showing the pH effect on RN80 α-helical structure.

5.3.4 Effect of *o*-NBA on the RN80 α-Helix Structure

Because in the laser-induced pH jump procedure it is essential to prepare peptide solutions in the presence of *o*-NBA, it was critical to investigate if the photoacid produce any effect in the RN80 structure. Figure 5.11 depicts the far-UV CD spectra of RN80 in the presence and in the absence of *o*-NBA. One can see that the two spectra are very similar. Both display strong negative bands at 207 and 222 nm. Hence, the presence of *o*-NBA in the sample solutions for photoacoustic measurements has a negligible effect on the secondary structure of the C-peptide analogue under study.
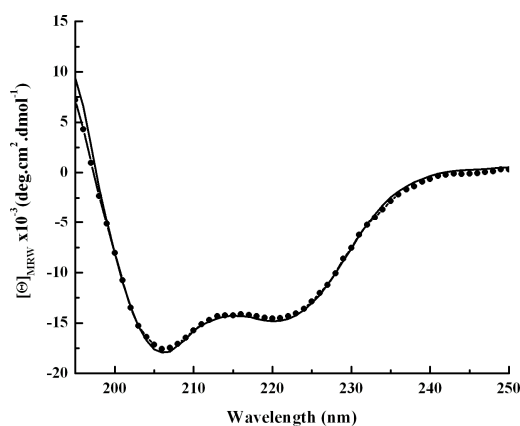
Figure 5.11: Comparison of the far-UV CD spectra of RN80 in the absence (line) and in the presence of 2 mM *o*-NBA (circles), in an aqueous solution with 100 mM NaCl, at pH 5 and 3.0 °C.

Saturation-transfer difference NMR (STD-NMR) experiments were also performed to detect if *o*-NBA molecules were interacting with the peptide under study. The STD-NMR experiment (Mayer & Meyer 1999; Meyer & T. Peters 2003; Viegas et al. 2011) can be used not only for screening ligands with dissociation constants K_d ranging from 10^{-8} to 10^{-3} M but also to provide insight on parts of the ligand that are most directly involved in binding, since it is expected that the regions of the ligand having the closest contact with the protein will show the most intense STD NMR signals (Viegas et al. 2011). During the experiment, resonances of the receptor are selectively saturated and intramolecular NOEs are developed within the receptor and, in addition, they give rise to intermolecular NOE effects in a bound ligand. These NOE effects may be observed as

enhancements in the difference (STD-NMR) spectrum resulting from subtraction of this spectrum from a reference spectrum in which the receptor protein is not saturated. Enhancements are observed for the ligand resonances of protons in close contact with the receptor (≤ 5 Å).

The STD-NMR spectra obtained for the mixture of *o*-NBA and RN80 at pH 5 and pH 8, and the reference spectrum for the mixture under study are presented in Figure 5.12. At both pH conditions, the proton signals of *o*-NBA present similar intensity on the *on-resonance* and *off-resonance* spectra. As a consequence, after subtraction no proton signals appear in the difference spectrum. The absence of signals in the STD-NMR spectra of *o*-NBA suggests that this compound does not interact with the RN80 peptide. These STD-NMR results are in agreement with the far-UV CD experiments that show no significant changes on the secondary structure of RN80 in the presence of *o*-NBA.
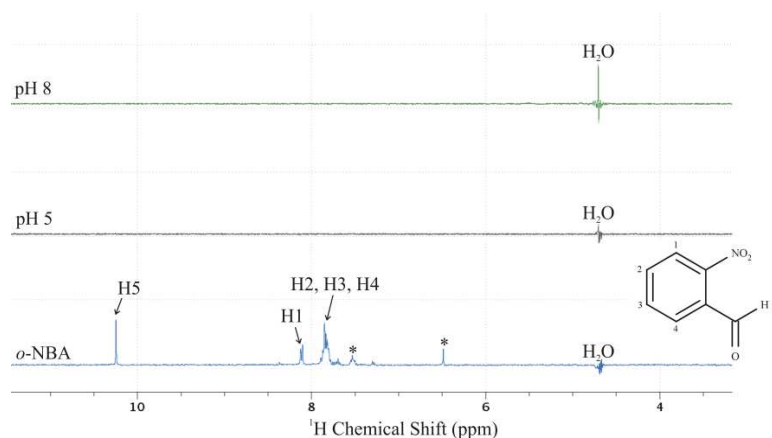
Figure 5.12: STD-NMR spectra of RN80 (500 μM) in the presence of 2 mM *o*-NBA, in an aqueous solution 90 % H_2O / 10 % D_2O with 100 mM NaCl, in different pH conditions and 3.0 °C (2.0 s of saturation time). The bottom spectrum is the ^{1}H-NMR reference spectrum of *o*-NBA with the corresponding spectral assignments. The asterisk indicates impurities present in the sample. Note that the signals of the impurities are not present in STD-NMR spectra.

## 5.3.5 Structural Volume Changes and Folding Dynamics Monitored by TR-PAC

Although TR-PAC has been widely used to study photoinitiated nonradiative processes in solution, the application of this method to protein folding is quite new. The principle of TR-PAC is relatively simple. The molecule under study absorbs a photon, and

the light absorption triggers a chemical event that leads to heat release and possibly to a conformational event. Expansion or contraction of the solvent induced by the heat of the reaction and/or the volume change associated with the conformational event generates a pressure wave, which is propagated through the solution to a piezoelectric transducer for acoustic detection. Here, upon laser irradiation a photoacid produces a pH jump which is responsible for the protonation of ionizable amino acid residues and any subsequent protein or peptide conformational change.

Since the primary sequence of the RN80 peptide includes one glutamic acid (Glu) and one histidine (His), mixtures in the ratio 1:1 of the amino acid models Ac-His-NHMe and Ac-Glu-NH$_2$ were analyzed at different initial pHs and at the same solution conditions needed for the stability of the RN80 α-helix (aqueous solutions containing 100 mM NaCl). Figure 5.13 shows the photoacoustic wave of the *o*-NBA (prepulse pH ~5) and the photoacoustic waves from the mixture 1:1, at prepulse pH of 5.3 and 7.3, along with the BP photoacoustic wave.

Using the *CPAC* software and at first assuming two sequential exponential decays, the amplitude ϕ_i and lifetime τ_i of each process were obtained. Under both prepulse pH conditions, it is observed that the first process corresponds to a volume contraction with a very short lifetime (less than 10 ns), while the second process is characterized by a volume expansion with a lifetime around 60 ns. The structural volume changes (ΔV_1 and ΔV_2^{exp}) were calculated using Equation 5.3 (see Table 5.3). The first process, ΔV_1 is characterized by a volume contraction of ~-3.6 ml mol^{-1}, which is probably related with the volume change previously described for the photo-release of protons by *o*-NBA. When the initial pH is adjusted to 5.3, the pH jump protonates mainly the Ac-Glu-NH$_2$ molecules and ΔV_2^{exp} is associated with the slower process corresponding to a volume expansion of 3.8 ml mol^{-1} (lifetime ~ 65 ns). If the prepulse pH is 7.3, the protons may react with either Ac-Glu-NH$_2$ or Ac-His-NHMe molecules. In fact, the structural volume change ΔV_2^{exp} observed at pH 7.3 corresponds to a volume expansion of approximately 2.4 ml mol^{-1} (lifetime ~ 59 ns). Being so, the observed volume expansion at pH 7.3 is smaller than at pH 5.3. It is worth to note that the protonation of Ac-His-NHMe is characterized by a volume contraction (see Chapter 4). As previously described in Chapter 4, when a mixture Ac-His-NHMe and Ac-Glu-NH$_2$ are present in solution and the prepulse pH is 7.3, both amino acid models can be protonated inducing a volume expansion, instead of the volume contraction typically observed when only the imidazole group is protonated.

At both start pH conditions we considered the fitting of the experimental PAC waves with an additional third decay. At pH 5.3 most of the Ac-His-NHMe molecules must be already protonated. In fact, photoacoustic waves of the 1:1 mixture measured at pH 5.3 were not well fitted when we tried to use three exponential decays because the third process was characterized by ϕ_3 with no physical meaning and lifetimes τ_3 that could not be time resolved using the 2.25 MHz transducer. However, when the prepulse pH is 7.3, it is possible to distinguish three processes using three exponential decays. As previously, the first decay is described by a volume contraction of approximately ~-3.6 ml mol^{-1}. The second decay is characterized by a volume expansion of ~3.1 ml mol^{-1} (lifetime ~100 ns) and the third corresponds to a volume contraction of ~-1.2 ml mol^{-1} that occurs within 120 ns. While the volume expansion corresponds to the protonation of Ac-Glu-NH$_2$, the volume contraction it is observed during the protonation of the imidazole group from Ac-His-NHMe.
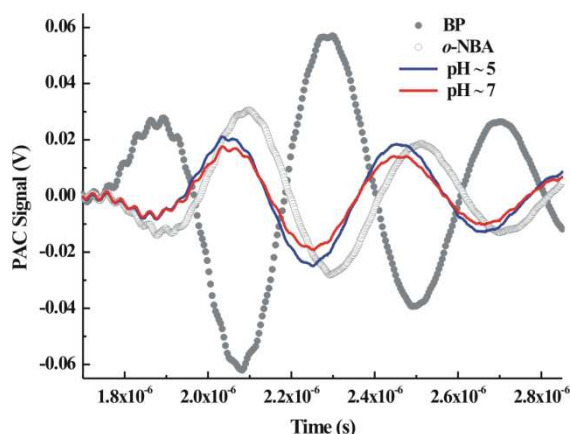
Figure 5.13: Photoacoustic waves of the 1:1 mixture of the amino acid models Ac-His-NHMe/ Ac-Glu-NH$_2$ (500 μM) in different prepulse pH conditions, obtained by the two-temperature method. The signals from BP and *o*-NBA are represented by closed circles and open circles, respectively. The signals of the mixture of amino acid models in aqueous solution containing 100 mM NaCl are represented by solid lines. The BP signal was measured at T$_{\beta\neq0}$ = 6.0 ºC, while the signals from both *o*-NBA and the mixture were measured at T$_{\beta=0}$ = 1.8 ºC.

The kinetics, enthalpic and volume changes resulting from the pH-dependent folding/unfolding events of the RN80 peptide were investigated using TR-PAC experiments by performing the two-temperature and multiple-temperature methods and at different pH conditions, namely near pH 5 and pH 7.

Figure 5.14 shows the photoacoustic signals of the peptide RN80 after the photo-release of protons by *o*-NBA in different prepulse pH conditions. As can be observed, using both prepulse pHs the results are identical and there is no significant dependence on the peptide concentration when compared to the waveforms observed for the amino acid model compounds (see Chapter 4). Moreover, the signal obtained for *o*-NBA is inverted when compared with the waveform of BP. After deconvolution, the amplitude ϕ_i and lifetime τ_i of each process were obtained using the *CPAC* software. Although a third conformational process is likely to occur following the protonation reaction, photoacoustic data were first analyzed assuming only two sequential processes. The lifetime corresponding to a very short time (less than 10 ns) can be associated with the volume contraction observed for *o*-NBA photolysis.

The second process corresponds to a volume expansion, which is in good agreement with the studies performed with the mixture of amino acid models in the ratio 1:1 described in Chapter 4. This process occurs immediately after photolysis of the photoacid, and may be associated to the protonation of Glu-2 and/or His-12. When the prepulse pH was adjusted to pH 5.3, only the Glu-2 residue is protonated. However, if the prepulse pH is 7.3 either His-12 or Glu-2 residues may be protonated.

Structural volume changes were calculated using the amplitude values derived from the fitting procedure and applying Equation 5.3. The average value obtained for the structural volume change ΔV_1, resulting from photolysis of *o*-NBA in the presence of different concentrations of RN80, was approximately -4.0 ml mol^{-1} (see Table 5.3). This value is in good agreement with previous results obtained for the fast volume contraction, under pH conditions near neutrality and in the presence of 100 mM NaCl (see Chapter 4).

Figure 5.15(A) shows the dependence of the calculated structural volume changes for the second process (ΔV_2^{exp}) on the concentration of RN80 peptide. Although there is no high dependence on the peptide concentration, the values of ΔV_2^{exp} reach a plateau when the concentration is greater than 1.2 mM using either pH 7.3 or pH 5.3 as initial conditions. In the plateau the estimated value for the structural volume change accompanying the protonation of RN80 (ΔV_2) corresponds to a volume expansion of approximately 3.0 ml mol^{-1} and 2.2 ml mol^{-1}, when the prepulse pH is 5.3 and 7.3, respectively. As in the case of the 1:1 mixture of amino acid models, the volume expansion observed at higher pH is slightly smaller in magnitude.
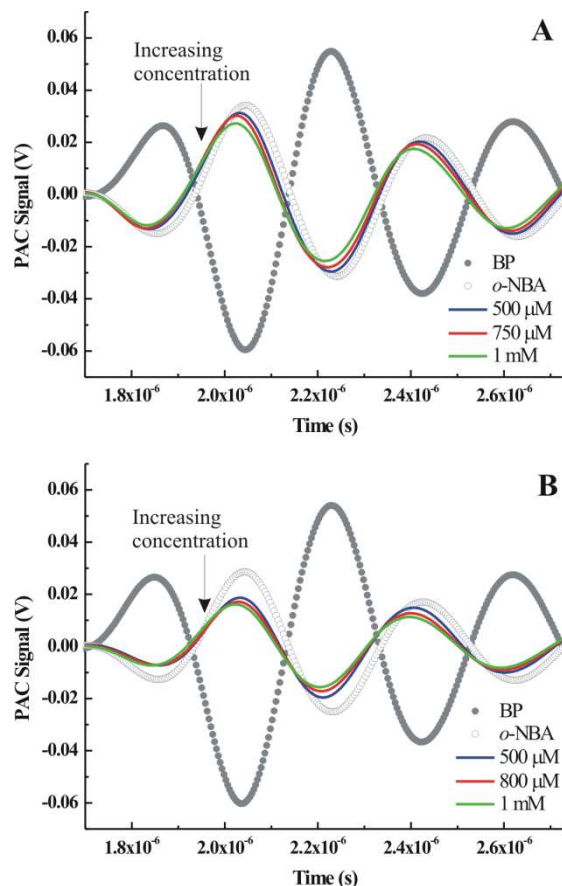
Figure 5.14: Photoacoustic waves generated after laser irradiation, obtained using the two-temperature method, at different prepulse pH conditions, 5.3 (A) and 7.3 (B). The signals from BP and *o*-NBA are represented by closed and open circles, respectively. The signals of the RN80 peptide at different concentrations, and in an aqueous solution containing 100 mM NaCl and *o*-NBA are shown as solid lines. The BP signal was measured at $T_{\beta \neq 0}$ = 6.0 ºC, while the signals from both *o*-NBA and peptide were measured at $T_{\beta = 0}$ = 1.8 ºC. Noise reduction was achieved by FFT Low Pass Filter processing, using the software package *OriginPro7* (OriginLab Corporation, USA).

The rate constants ($k_2 = 1/\tau_2$) for this volumetric expansion increase linearly with RN80 concentration, as shown in Figure 5.15(B). From the slope of the plot of rate constants as a function of the peptide concentration, the bimolecular rate constant k_b can be determined. At pH 5.3, the protonation of Glu-2 in RN80 yields a k_b value of 1.3 x 10^{10} M^{-1}s^{-1}. When the prepulse pH is 7.3, and therefore His-12 is also protonated, the value of k_b is 2.3 x 10^{10} M^{-1}s^{-1}.
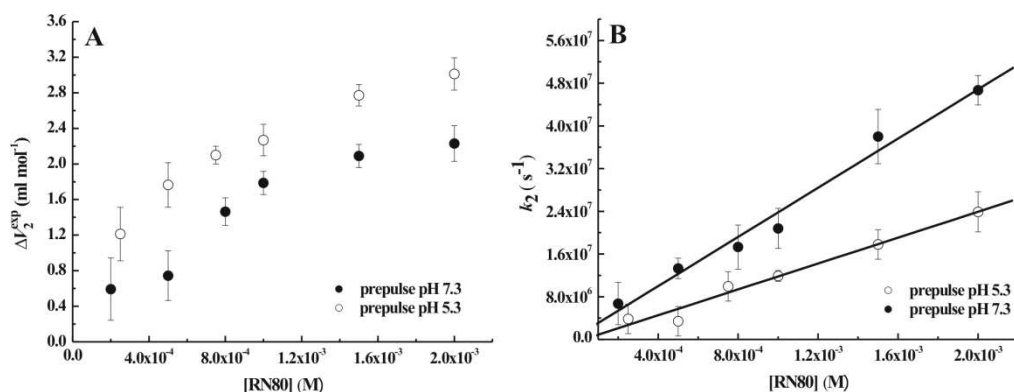
Figure 5.15: (A) Dependence of ΔV_2^{exp} on the concentration of RN80 peptide at different prepulse pH conditions. The reaction volumes (ΔV_2) estimated for the protonation of RN80 peptide are reported in Table 5.3. (B) Dependence of the rate constants ($k_2 = 1/\tau_2$) on the concentration of RN80 peptide at prepulse pH of 5.3 (open circles) and 7.3 (filled circles), using the two-temperature method. Bimolecular rate constants were derived from the slope of the linear relationship (solid lines) of the rate constants as a function of RN80 concentration, and are reported as k_b in Table 5.3.

Table 5.3: Parameters from the TR-PAC experiments obtained using the two temperature and the multiple-temperature methods, and fitting the experimental PAC waves with two exponential decays.

	Two-temperature Method		
	ΔV_1 *(ml mol^{-1})*	ΔV_2 *(ml mol^{-1})*	k_b *($10^{10}M^{-1}s^{-1}$)*
Prepulse pH ~5.3	-3.5 ± 0.5	3.0 ± 0.2	1.3 ± 0.1
Prepulse pH ~7.3	-4.5 ± 1	2.2 ± 0.5	2.3 ± 0.5

	Multiple-temperature Method					
	ΔV_1 *(ml mol^{-1})*	Q_1 *(kcal mol^{-1})*	ΔV_2 *(ml mol^{-1})*	Q_2 *(kcal mol^{-1})*	E_a *(kcal mol^{-1})*	Frequency factor
Prepulse pH ~5.3	-4.0 ± 0.3	101.9 ± 4	1.2 ± 0.2	6.0 ± 1	15.4 ± 6.1	26.2 ± 5.0
Prepulse pH ~7.3	-2.3 ± 0.7	104.7 ± 3	1.0 ± 0.3	1.8 ± 1	8.6 ± 2	22.6 ± 1.2

In addition, we have also examined the protonation of RN80 using the multiple-temperature method. The temperature-dependence of the photoacoustic signals recorded between 6.0 ºC and 20.0 ºC allowed plot $\phi_i E_\lambda$ vs $C_p \rho/\beta$, from which the volume change accompanying each process could be determined from the slope, and the heat released from the solution determined from the intercept, according to Equation 5.4 (Figure 5.16(A)). The enthalpy change (ΔH_1) of the fast process is calculated from the heat released (Q_1), where $\Delta H_1 = (E_\lambda - Q_1)/\Phi$ and $\Phi = 0.4$ corresponds to the quantum yield for the release of protons by o-NBA. The enthalpy change of the subsequent kinetic processes is calculated assuming that $\Delta H_i = -Q_i/\Phi$. The temperature dependence of the lifetime also provides information on the activation energy for each process with rate constant within the experimental resolution range.

Assuming two sequential exponential decays, the photoacoustic signals can be described by a fast subresolution process due to the photolysis reaction of o-NBA and solvation of photo-dissociated ions followed by a slower decay. This slower process, with a temperature-dependent rate constant, reflects the proton transfer reactions with either Glu-2 or His-12 from RN80. The fast decay exhibit a volume contraction (negative slope) and the corresponding enthalpy change is approximately -55 kcal mol^{-1}. The protonation of RN80 induces a volume expansion (positive slope) of approximately 1.2 ml mol^{-1} at pH 5.3 and 1.0 ml mol^{-1} at pH 7.3. The enthalpy changes obtained for the second process were -15.0 kcal mol^{-1} and -4.5 kcal mol^{-1} at pH 5.3 and pH 7.3, respectively.

Figure 5.16(B) shows the Arrhenius plot for the rate of proton binding ($k_2 = 1/\tau_2$) to RN80 in different pH conditions. The activation energy (E_a) and frequency factor obtained from Arrhenius analysis of multiple-temperature data are include in Table 5.3.

The interpretation of laser-induced acoustic waves and its time-resolved analysis must be complemented with other tecnhiques to obtain details on the mechanism of processes such as protein or peptide folding. Being so, the interpretation of TR-PAC data is frequently supported by the results obtained using tecnhiques such as CD and NMR. As reported in the previous sections, the peptide RN80 presents pH-dependent conformational transitions. Under our experimental conditions, when the laser irradiation of o-NBA is performed at pH 5.3, a fast pH jump of approximately one pH unit occur. According to the far-UV CD spectra, this change in pH induces a loss of 10 % in helical content most probably due to the disruption of the salt-bridge between Glu-2 and Arg-10. On the other hand, if the prepulse pH is 7.3 the photo-release of protons decrease the pH of the solution

to a final pH o approximately 4.8. This reduction of pH promotes the protonation of His-12, favoring the π-stacking interaction between His-12 and Tyr-8, which leads to an increase of approximately 30 %. Thus, since the protonation of either Glu-2 or His-12 induces a conformational change in the peptide, it seems to be reasonable to try an experimental data fit using three sequential exponential decays. As previously mentioned, the first and the fastest process results from the *o*-NBA photolysis, and the second process can be associated with the protonation of the negatively charged side chain of Glu-2 and/or the protonation of the uncharged imidazole group of His-12. The third process can be attributed to a unimolecular conformational event due to folding/unfolding of the α-helical peptide RN80 upon protonation of Glu-2 or His-12.
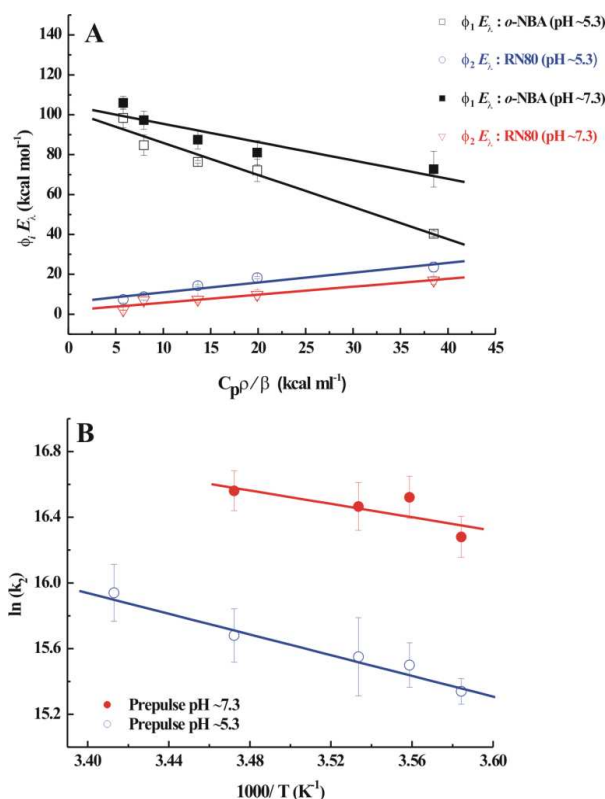
Figure 5.16: (A) Plots of the energy content for the photo-dissociation of o-NBA ($\phi_1 E_\lambda$) and for the binding of the photo-released protons ($\phi_2 E_\lambda$) to the RN80 peptide in different prepulse pH conditions, as a function of the parameter $C_p\rho/\beta$. $C_p\rho/\beta$ was changed by varying the temperature between 6.0 and 20.0 ºC. The concentration of RN80 was 500 μM. The volume changes and heat releases were obtained from the linear fits represented by solid lines, and based on Equation 5.4. The results are reported in Table 5.3. (B) Arrhenius plots for the protonation reaction of RN80 in different pH conditions. The activation energy (E_a) and frequency factors for each reaction were derived from the linear relationship (solid lines) of the rate constants as a function of 1/T (Equation 5.6) and are reported in Table 5.3.

The photoacoustic data collected at pH 7.3 could not be fitted using three sequential exponential decays. Not only because the third component did not add any improvement on the fit, but also because the third process was not-resolved in time (its lifetime is redundant with the previous temporal parameters). On the contrary, the results obtained when the prepulse pH is 5.3 were well fitted using three sequential exponential decays and three processes can be clearly distinguished. Figure 5.17 presents the fits resulting from both analysis. As can be observed in Figure 5.17, there is no clear improvement in the residuals when the fit is performed assuming three exponential decays. However, our previous results using structural detecting techniques indicate that it is physically reasonable to consider that an unfolding event may occur upon protonation of Glu-2.

Additionaly, the third component is clearly distinguishable from the previous in terms of the temporal parameters obtained. All the fits were performed without any constraint, this is, without fixing any of the six parameters. Another important factor to judge the adequacy of the three exponentials fit is to check if it evaluates correctly known values. In this regard, the PAC experiments performed with the photoacid and with the amino acid model compounds give valuable insight. In the present case, the fit would have to exponentially yield, both in terms of amplitude and time. Furthermore, the two first decays are consistent with *(i)* the photo release of the proton from the photoacid and *(ii)* the protonation of a charged carboxylic acid.
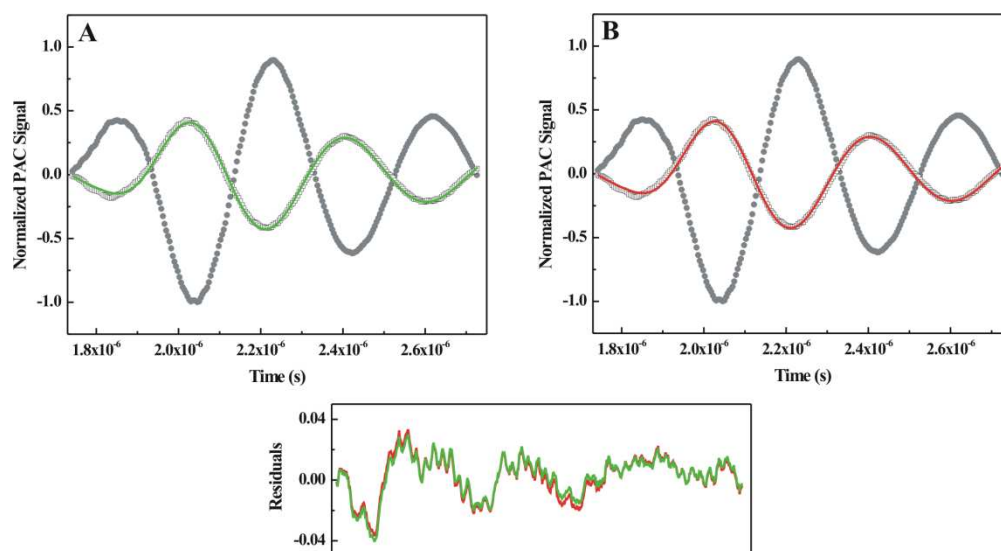
Figure 5.17: Comparison of the fitting procedure using two sequential exponential decays (A, in green) and three sequential exponential decays (B, in red). The signals from BP and RN80 (1000 μM) are represented by closed circles and open squares, respectively. The fit derived from the deconvolution is represented by green and red solid lines. (C) Residuals obtained from the fitting with the *CPAC* software.

Figure 5.18(A) presents the structural volume changes obtained for the RN80 peptide at the prepulse pH 5.3, and using three sequential exponential decays. Basically, it is observed a fast volume contraction followed by two volume expansions. The volume contraction of -4.0 ± 0.2 ml mol^{-1} with a lifetime shorter than 10 ns can be assigned to the *o*-NBA photolysis. The volume changes as well as the lifetimes of the second exponential

decay are dependent on the RN80 concentration. This behaviuor is consistent with the previous results for protonation reactions obtained using the amino acid models. In particular, it is expected that the protonation of the negatively charged carboxylic side chain of Glu produce a volume expansion. The bimolecular rate constant (k_b) for the protonation of Glu-2 of RN80 is approximatelly 6.8×10^9 $M^{-1}s^{-1}$, which is lower than that determined by fitting the TR-PAC with two exponential decays. However, this value is in better aggrement with the ones determined for the protonation of amino acid models in the presence of 100 mM NaCl (see Chapter 4). In fact, the increase in ionic strength produces a reduction of the rates of protonation and the k_b calculated for the amino acid models. The third process corresponds to a slower volume expansion of 0.77 ml mol^{-1} that seems to be concentration-independent. The rate constants ($k_3 = 1/\tau_3$) do not increase linearly with the peptide concentration (Figure 5.18(B)), suggesting that this slower decay corresponds to a unimolecular process, as expected for conformational changes due to folding/unfolding events.
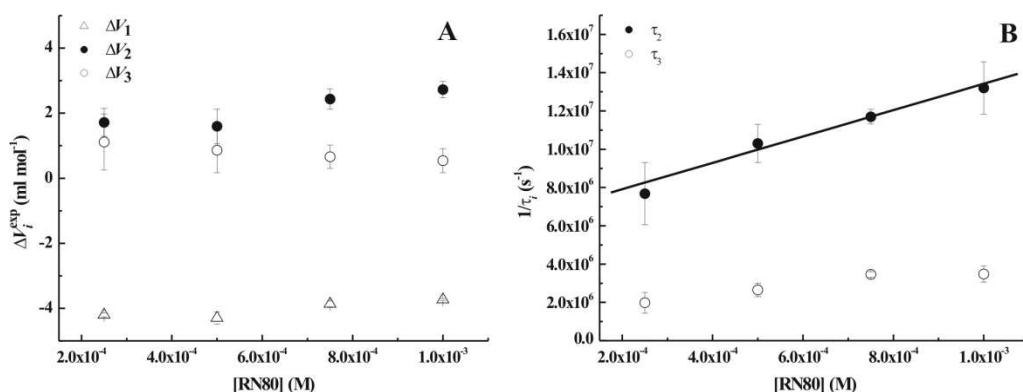
Figure 5.18: (A) Dependence of the structural volume changes (ΔV_i^{exp}) on the concentration of RN80 peptide obtained by fitting the photoacoustic waves to three sequential exponential decays. (B) Dependence of the rate constants ($k_2 = 1/\tau_2$) on the concentration of RN80 peptide.

Table 5.4: Parameters obtained by fitting the photoacoustic waves to three sequential exponential decays, using the two-temperature method and prepulse pH 5.3.

	Two-temperature Method					
	ΔV_1 (ml mol^{-1})	ΔV_2 (ml mol^{-1})	ΔV_3 (ml mol^{-1})	τ_l (ns)	k_b (10^9 M^{-1} s^{-1})	τ_3 (ns)
Prepulse pH ~5.3	-4.0 ± 0.2	3.0 ± 0.2	0.77 ± 0.3	< 10	6.8 ± 2	369 ± 57

The photoacoustic waves obtained at different temperatures were also well-fitted using three sequential exponential decays and Figure 5.19 shows plots of $\phi_i E_\lambda$ vs $C_p\rho/\beta$. The volume change accompanying the events associated with each decay and the heat release to the solution were determined according to Equation 5.4. The fast process exhibited a volume expansion of -3.6 ± 0.5 ml mol^{-1} and the corresponding enthalpy change was approximately -40 kcal mol^{-1}. The fast process was followed by two slower reactions that induce volume expansions of 0.30 ± 0.1 and 0.42 ± 0.3 ml mol^{-1}, respectively. In addition both processes present a similar enthalpy change of -11 kcal mol^{-1}. Assuming that the second process corresponds to the protonation of Glu-2 from the folded RN80 peptide, the third process can be attributed to the unfolding event. Since the multiple temperature experiments were not performed using a peptide concentration at the plateau region, a smaller ΔV_2 than the one calculated using the two-temperature method is observed. The third process is associated with a small volume change similar to those determined using the two-temperature method.
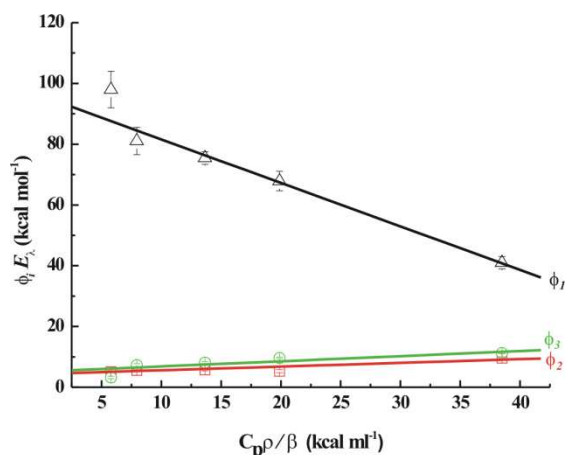
Figure 5.19: Plots of the energy content for the photo-dissociation of *o*-NBA ($\phi_1 E_\lambda$), for the binding of the photo-released protons to Glu-2 residues($\phi_2 E_\lambda$), and for the subsequent peptide unfolding event ($\phi_3 E_\lambda$) at a prepulse pH of 5.3, as a function of the parameter $C_p\rho/\beta$. $C_p\rho/\beta$ was changed by varying the temperature between 6.0 and 20.0 ºC. The concentration of RN80 was 500 µM. The volume change and heat releases were obtained from the linear fits represented by solid lines, and based on Equation 5.4. The results are reported in Table 5.5.

Tabela 5.5: Multiple-temperature parameters obtained by fitting the photoacoustic waves to three sequential exponential decays.

	Multiple-temperature Method					
	ΔV_1 (*ml mol^{-1}*)	ΔV_2 (*ml mol^{-1}*)	ΔV_3 (*ml mol^{-1}*)	Q_1 (*kcal mol^{-1}*)	Q_2 (*kcal mol^{-1}*)	Q_3 (*kcal mol^{-1}*)
Prepulse pH ~5.3	-3.6 ± 0.5	0.30 ± 0.1	0.42 ± 0.3	95.9 ± 4	4.4 ± 1	5.2 ± 1

In order to explore any slow folding event occuring when the prepulse pH is 7.3, experiments of TR-PAC have been performed using the 0.5 MHz transducer that is able to detect processes whitin the microsecond time scale. Figure 5.20(A) shows examples of the photoacoustic waves obtained for the phoacoustic reference BP at 6.0 ºC and for the RN80 peptide at 800 µM and using the prepulse pH 7.3. Best fits were obtained using only two sequential exponential decays. In fact, when the fitting is performed using three exponential decays, the third process is associated with ϕ_3 and τ_3 parameters that do not have physical meaning. Tipically the lifetime parameters obtained are much longer than the allowed to detect by the 0.5 MHz transducer resolution. Figure 5.20(B) shows the fits

obtained for the T wave (BP) and for E wave (800 μM RN80 peptide). The first process (component wave in blue) can be characterized by the summation of two processes: *o*-NBA photolysis and protonation of Glu-2 and His-12 residues. While the proton release by *o*-NBA corresponds to a volume contraction and thus a negative ϕ value, the protonation of both amino acid residues corresponds to a small expansion as previously observed in the 1:1 mixtures of amino acid models. As a result this first process corresponds to a small contraction associated with an average ϕ_1 value of -0.1, which is related with a volume change of approximatelly -0.78 ml mol^{-1} with a lifetime not time resolved (<100 ns). The second process corresponds to a much slower corresponding to a lifetime of 1.5 and 2 μs and an average ϕ_2 value of -0.76 that represents a volume contraction of -6.0 ml mol^{-1}. Being so, the folding of the RN80 peptide may be characterized by a much slower event than the unfolding occuring within 369 ns.
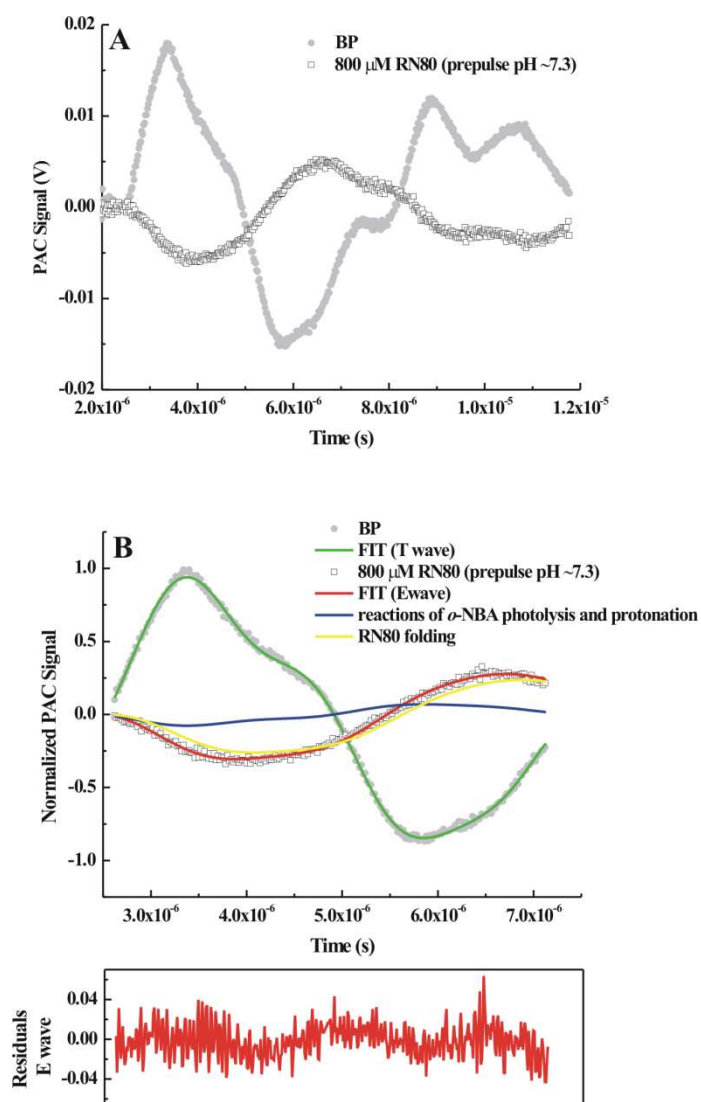
Figure 5.20: (A) Photoacoustic waves generated after laser irradiation, obtained using 0.5 MHz transducer and applying the two-temperature method. The BP signal (in filled circles) was measured at $T_{\beta \neq 0} = 6.0$ °C, while the signal of the RN80 peptide (in open squares) was measured at $T_{\beta=0} = 1.8$ °C. The value of prepulse pH used for solutions of the RN80 peptide was 7.3. (B) Fits obtained using the *CPAC* software. Solid lines represent the fit obtained for the photoacoustic reference BP (T wave, in green) and for 800 μM RN80 (E wave, in red) using the prepulse pH 7.3. The global fit (in red) corresponds to the summation of two component waves that are associated with the fast contraction due to *o*-NBA photolysis and protonation reaction (in blue), and the RN80 folding (in yelow).

5.4 Discussion

An important goal of protein folding is to quantitavely predict the contributions of amino acid sequence, pH, temperature, and salt concentration to kinetics and thermodynamics of the protein folding process. To achieve this goal, detailed knowledge of the structural and thermodynamic properties of the different states populated during folding and the kinetics involved in going from one state to another is required. Peptides ranging from 12 to 30 residues have been studied to understand the interplay between side chain interactions, the helix dipole, and the intrinsic helix-forming ability of each amino acid. In the present work, the folding kinetics of the shortest peptide sequence known forming an α-helix in aqueous solution has been the subject of study. RN80 is a 13 amino acid synthetic peptide analogue of the C-peptide from the protein RNase A. NMR and CD spectra indicate that RN80 adopts an α-helical structure and undergoes pH-dependent transitions upon protonation of Glu-2 and His-12. Furthermore, these techniques reveal that the pH-dependence curve of α-helix formation by RN80 is bell-shaped with a maximum near pH 5. The main forces stabilizing this short peptide in α-helical conformation are the salt-bridge formed between Glu-2 and Arg-10 and the π-stacking interaction involving His-12 and Tyr-8 (Figure 5.21). The protonation of His-12 is the main responsible for the increase of RN80 helicity, because the π-stacking interaction between His-12 and Tyr-8 is stronger when the imidazole is charged, as shown by the near-UV and NMR experiments (Figures 5.6 and 5.9). On the other hand, the protonation of Glu-2 induces α-helix partial unfolding due to the disruption of the salt-bridge between Glu-2 and Arg-10. Thus, the two ionizable amino acid residues of RN80 that seem to play a fundamental role on α-helix formation and their protonation correspond to the earliest event occuring in pH-dependent conformational transitions.
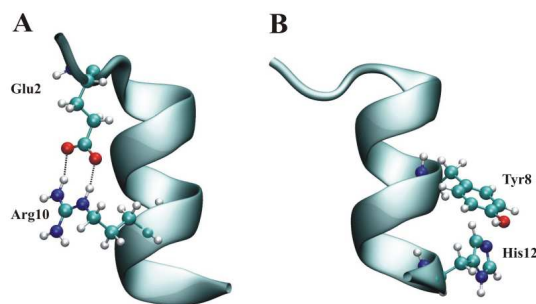
Figure 5.21: Ribbon diagram of the three-dimensional structure of the RN80 peptide showing the salt-bridge formed between Glu-2 and Arg-10 (A) and the π-stacking interaction involving His-12 and Tyr-8 (B).

Compared to the widely studied alanine-based α-helical peptides and other peptides such as Con-T and the central helix of the ribosomal protein L9 (residues 41 to 79), the distinct feature of RN80 is that it corresponds to the shortest polypeptide amino acid sequence that folds into an α-helical structure in aqueous solution. Because the helicity of RN80 depends on the pH, a laser-triggered pH jump allows, via an appropiate detection method, the measurement of conformational changes associated with rapid pH changes, and thus obtain information regarding its folding and unfolding kinetics.

An appropriate analysis of photocoustic data need to be supported by structural and mechanistic suplementar information about the system under study. Although structural studies clearly show that the protonation of either Glu-2 or His-12 does perturb the RN80 helicity, and three sequential processes should be detected including the *o*-NBA photolysis, the protonation reaction and subsequent folding/unfolding event, we followed a cautious analysis approach. Therefore, the photoacoustic waves were first analyzed assuming only two sequential processes. The second process describes the event immediately after photolysis of the photoacid, which is the protonation of Glu-2 and/or His-12. When the prepulse pH was adjusted to pH 5.3, only the Glu-2 residue is protonated with the pH jump, promoting a volume expansion of 3.0 ml mol^{-1} (~5.0 Å^3) (two-temperature method). The volume expansion accompanying neutralization of carboxylic acids has been previously described in Chapter 4. However, if the prepulse pH is 7.3 both His-12 and Glu-2 residues may be protonated and a smaller volume expansion of 2.2 ml mol^{-1} (~3.6 Å^3) is observed (two-temperature method). This volume expansion observed at prepulse pH 7.3 is in good agreement with the studies performed with the mixture of amino acid models Ac-Glu-NH$_2$ and Ac-His-NHMe at a concentration ratio of

1:1, in the presence of 100 mM NaCl. The rate constants of the second process depend on peptide concentration, with the bimolecular rates (k_b) at both initial pH conditions around 10^{10} $M^{-1}s^{-1}$. These values of k_b are higher than those determined for the amino acid models in the presence of 100 mM NaCl, in particular, the value of k_b for Ac-Glu-NH$_2$ is 9.5 x 10^9 $M^{-1}s^{-1}$, and for Ac-His-NHMe is 8.3 x 10^8 $M^{-1}s^{-1}$.

Since the protonation of either Glu-2 or His-12 induces conformational changes in peptide, the photoacoustic waves were also fitted using three sequential exponential decays. The experimental data recorded at pH 5.3 were well fitted using this model. The protonation of Glu-2 corresponds to the second process observed, which is characterized by a volume expansion that is concentration-dependent. The rate constants of protonation depend linearly on the peptide concentration and k_b has a value of approximatelly 7 x 10^9 $M^{-1}s^{-1}$. This behaviour is consistent with the protonation of carboxylic acids and the value of k_b is in good agreement with the result obtained for the protonation of Ac-Glu-NH$_2$ in the presence of 100 mM NaCl (see Chapter 4). The third process corresponds to a concentration-independent volume expansion of 0.77 ml mol^{-1} (~1.3 Å^3) and can be associated with an unimolecular processes such as peptide unfolding following the protonation of Glu-2. In addition, the rate constants ($k_3 = 1/\tau_3$) do not increase linearly with RN80 concentration, which is an additional evidence that the process may correspond to an unimolecular reaction.

When the *o*-NBA photolysis was initiated at pH 7.3 in the presence of the RN80 peptide, our aim was to perturb the π-stacking interaction between His-12 and Tyr-8. Photoacoustic experiments performed with the faster 2.25 MHz transducer do not allowed the detection of any conformational change following the protonation of His-12. Our studies with the RN80 peptide clearly confirmed that the protonation of mixtures of Ac-Glu-NH$_2$ and Ac-His-NHMe (concentration ratio 1:1 and prepulse pH 7.3) is accompanied by a volume expansion and both amino acid models are protonated. If only Ac-His-NHMe molecules were protonated the photoacoustic data should reveal a volume contraction as described in the previous Chapter 4.

Although from the structural studies by CD and NMR there is an increase in helicity from pH 7.3 to pH 5.5, it was not possible to resolve a third process associated with conformational changes by fitting the photoacoustic waves to three sequential exponential decays, even when the photoacoustic measurements were performed with the 0.5 MHz transducer. Using this transducer was not possible to separate the photo-induced proton release by *o*-NBA from the protonation reaction. The second process was assigned

to the (slow) component of the fit that may be related to the pH-induced conformational change of the RN80 peptide. Photoacoustic measurements acquired using the 0.5 MHz transducer suggest that when the photolysis of *o*-NBA occurs at pH 7.3, in the presence of the RN80 peptide, occurs a slow folding event accompanied by a volume contraction of approximately -6.0 ml mol^{-1} (~-10 Å^3).

Although an isolated α-helix is one of the simplest structural motifs in proteins, its folding dynamics are nevertheless complex. Some α-helical proteins and polypeptides have been investigated using different techniques. Polypeptides that fold into α-helix structures, such as poly-L-glutamic Acid (PLG; n = 82) and poly-L-lysine (PLL; n = 165), were used as model systems to investigate the early events in acid-induced protein unfolding/folding processes. In particular, PLL is an α-helical structure at pH 12 that completely unfolds into a random coil at neutral pH (Viappiani et al. 1998). The unfolding process is due to the strong electrostatic repulsive forces between the protonated ε-amino groups. The acid-induced local disruption of the helical structure of PLL is associated with a contraction of ~ -17 ml mol^{-1} and lifetime of 250 ns (Abbruzzetti, Viappiani, et al. 2000). On the contrary, PLG is unfolded at neutral pH but protonation of γ-carboxylates reduces the intramolecular electrostatic repulsive forces occurring local formation of secondary structure. The coil to helix transition in PLG induced by pH jump and studied by PAC revealed an expansion of ~7 ml mol^{-1} with a lifetime of 100 ns. Moreover, the unfolding rate of ConT-T, a 21-residue helical peptide whose native conformation is largely stabilized by salt-bridges, is approximately 722 ns at 28 ºC.

Our results reveal that the unfolding promoted by the disruption of a single salt-bridge in the RN80 peptide occurs within approximately 369 ns. In longer polypeptide chains it is expected a volume contraction upon α-helix disruption due to the polypeptide chain collapse. However, the sign of volume change associated with the unfolding event due to protonation of Glu-2 of RN80 is positive corresponding to a small expansion of 0.77 ml mol^{-1}. It is likely that the volume change measured is representative of local conformational changes in short peptides. In particular, since His-12 and Tyr-8 are residues closed to the C-terminal seems to be occurring a local partial unfolding of the RN80 α-helix. In fact, our near-UV CD results show that the π-stacking interaction is maintained at pH ~3 (Figure 5.6), thus the disruption of the salt-bridge induces only partial unfolding of the α-helix. Being so, due to the short length of RN80 the volume contraction typically observed upon α-helix unfolding and collapse may not occur, and our results

reveal a local early unfolding event. Figure 5.22 illustrates a schematic representation of the folding and unfolding events detected using photoacoustic measurements. Upon protonation of Glu-2, the salt-bridge formed between Arg-10 and Glu-2 is disrupted leading to partial unfolding, which is characterized by a small volume expansion.
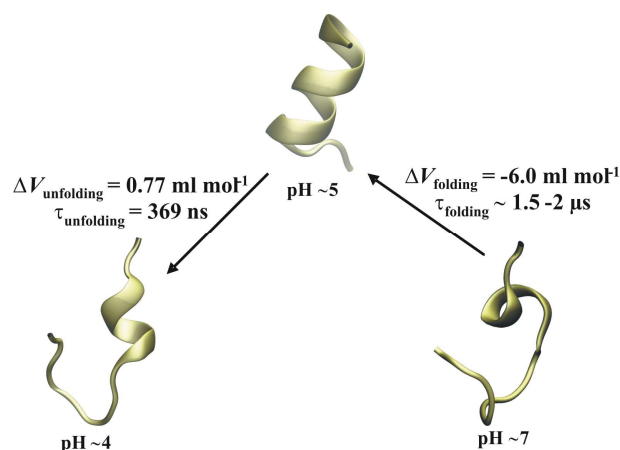
Figure 3.22: Schematic representation of the RN80 folding and unfolding. Protonation of Glu-2 promotes RN80 partial unfolding due to the disruption of the salt-bridge between Glu-2 and Arg-10, while the protonation of His-12 stabilizes the π-staking interaction between His-12 and Tyr-8 leading to RN80 folding.

On the contrary, preliminary results using the 0.5 MHz transducer suggest that a slow volume contraction may be occurring during the RN80 folding. The transition between unfolded conformations at pH 7.3 and folded conformation at pH approximately 5 is accompanied by a volume contraction of -6 ml mol^{-1} and a lifetime within 1.5 and 2 µs. In addition to the photoacoustic measurements, DOSY experiments have been performed to determine the hydrodynamic radius of the RN80 peptide in different pH conditions (data not shown). These experiments are typically used to measure the diffusion coefficients (Jones et al. 1997). The diffusion coefficient, D, characteristic of the RN80 α-helix at pH 5.5 is 1.54 m^2 s^{-1}, while the unfolded α-helix of the RN80 at pH 7.5 is defined by diffusion coefficient of 1.41 m^2 s^{-1}. The diffusion coefficient of a spherical body at a temperature T is given by the Stokes-Einstein equation (Equation 5.7), where r is the hydrodynamic radius of the body, k_B is the Boltzamn constant, η is the viscosity of an aqueous solution containing 100 mM NaCl. Using this equation it is possible estimate the

hydrodynamic radius r of the unfolded (at pH 7.5) and folded (at pH 5.5) peptide conformations.

$$D = \frac{k_B T}{6\pi\eta r}$$ (5.7)

The hydrodynamic radius of the unfolded α-helix corresponds to 8.9 Å, while the folded α-helix is characterized by an hydrodynamic radius of 8.2 Å. Hence, the radius of the RN80 peptide at pH 5.5 is smaller, which is in agreement with our photoacoustic measurements that suggest a volume contraction upon the RN80 folding. Although the folding of proteins is characterized by a volume expansion, our results suggest that the folding of short-length α-helical peptides may result in a volume contraction. In short peptides such as RN80 peptide, composed by only 13 amino acid residues, the unfolded species may not be as compact as in proteins. As a result, the volume occupied by the unfolded conformations is higher than the folded conformations. Furthermore, in the future, computational studies using molecular dynamics simulations of RN80 at constant pH may also reveal the degree of compactness of folded and unfolded conformations in different pH conditions.

Chapter 6

Bovine serum albumin conformational dynamics triggered by fast pH-jump events

6.1 Introduction

One of the major challenges in the field of biophysical chemistry is the understanding of protein folding, i.e., the acquisition of the three-dimensional native structure of a protein. Defects in protein folding are the molecular basis for a wide range of human disorders, among them are rare neurodegenerative pathologies such as Alzheimer's and Parkinson's diseases (Thomas et al. 1995). Misfolding processes and partially unfolded states may occur in competition with the normal folding process (Dobson 2004). Thus, substantial attention has been devoted to characterize partially unfolded states in the protein folding pathways. The intermediate states formed during unfolding and refolding pathways can be studied by different techniques using kinetic and thermodynamic approaches (Dill & Shortle 1991). Here, we apply a methodology based on a laser-induced pH jump combined with time-resolved photoacoustic detection (TR-PAC) to explore pH-induced unfolding processes, using the protein bovine serum albumin (BSA) as a model.

Serum albumin is the most abundant protein in the circulatory system and plays a key role in the transport of a large number of metabolites, endogenous ligands, fatty acids, bilirubin, hormones, anesthetics, and commonly used drugs, which may be delivered to the appropriate cellular targets (Bhattacharya et al. 2000; Ghuman et al. 2005). In particular,

BSA is frequently used as a model protein in different academic research areas, such as in the development of pharmaceutical formulations (Kragh-Hansen 1981; Umrethia et al. 2010), for developing new analytical methods (Xia et al. 2010) or even to study aggregation of proteins (Brahma et al. 2005). At neutral pH, the crystal structure of the 66 kD protein reveals a heart-shaped molecule organized into three similar structural domains, each subdivided into two subdomains (see Figure 6.1). The domains are predominantly α-helical and include loops and a large number (17) of disulfide bonds. The sequence of BSA is 76% identical to that of human serum albumin (HSA). (Peters 1985; Carter & Ho 1994).
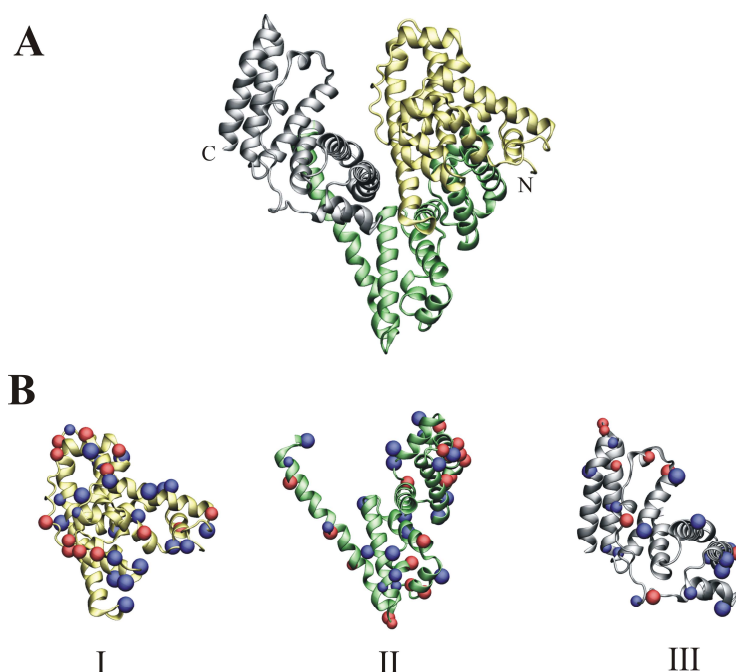
Figure 6.1: (A) Ribbon diagram of the three-dimensional structure of bovine serum albumin (BSA) (PDB entry 3V03). Each structural domain of BSA is represented in a different colour (domain I in yellow, domain II in green, domain III in gray). N- and C- termini are marked as N and C, respectively. (B) The location of glutamic acid and aspartic acid residues in each structural domain of BSA is represented by the blue and red beads, respectively.

The ability of albumins to undergo a major reversible conformational modification, induced by decreasing pH in the 7–2 range, was described several decades ago by Foster (Forster 1960) and has been documented by a wide range of methods (Suzukida et al. 1983; Sadler & Tucker 1993; Dockal 2000; El Kadi et al. 2006). At neutral pH, the conformation of BSA in its common physiological state is referred as the N form. An abrupt transition occurs at a pH value of 4.3, changing the N form to the so-called fast migrating F form, and when the pH reaches 2.7, an additional transition takes place from the F form to the extended E form. Furthermore, when the pH increases from neutral to 8, the N conformation changes to the basic B form, and at a pH above 10 the structure changes to the A form. These conformational transitions can be summarized by the following scheme: $E \xleftrightarrow[2.7]{} F \xleftrightarrow[4.3]{} N \xleftrightarrow[8]{} B \xleftrightarrow[10]{} A$.

Interestingly, the N to F conformational transition has been found to be highly conserved among different species (Bertucci & Domenici 2002). Such conservation has led to the belief that the F conformation occurs when the albumin molecule binds to the membrane surfaces of several tissues under physiological conditions at a lower pH value (Wilting et al. 1982). Here, our aim is to explore the early events related to the partial unfolding of BSA occurring due to the conformational transition N to F, induced by a pH jump at pH 5.3 and monitoring the processes using TR-PAC. Previously, circular dichroism (CD) and saturation transfer difference (STD) NMR studies have been performed to obtained structural details of the BSA α-helical content in different pHs and the potential interaction between o-NBA and BSA, respectively.

6.2 Materials and Methods

6.2.1 Sample Preparation

The protein bovine serum albumin (BSA) was purchase from Sigma-Aldrich Chemical Company, St. Louis, USA, as lyophilized powder and used without further purification. BSA solutions were prepared by dissolving the lyophilized protein samples in the appropriate solvent for each different experiment. The final protein concentrations

were checked optically on a Spectronic Unicam UV-500 spectrometer, using $\varepsilon_{280} = 43600 \ M^{-1} cm^{-1}$ (Cardamone & Puri 1992).

Bromocresol purple (BP) and *o*-nitrobenzaldehyde (*o*-NBA) were obtained from Sigma-Aldrich Chemical Company, St. Louis, USA.

6.2.2 Circular Dichroism Spectroscopy

Circular dichroism (CD) spectra were recorded on an Olis DSM-20 CD spectrophotometer with a temperature-controlled cell holder. BSA was dissolved in water, and the pH of the samples was adjusted using HCl or NaOH. Final protein concentrations were approximately 1 mg ml^{-1}. Far-UV measurements were recorded between 190 nm and 260 nm, using a 0.2 mm path length cell, at 3.0 °C. CD spectra were run with a step-resolution of 1 nm, an integration time of 5 s, and using a bandwidth of 0.6 nm. The spectra were averaged over at least three scans and corrected by subtraction of the buffer signal.

The results are expressed as the mean residue ellipticity [Θ]$_{MRW}$, defined as [Θ]$_{MRW}$ = Θ_{obs}(0.1MRW)/(lc), where Θ_{obs} is the observed ellipiticity in millidegrees, MRW is the mean residue weight, c is the concentration in milligrams per mililitre, and l is the length of the light path in centimeters. Secondary structure was estimated by analysis of the far-UV CD spectra between 190 and 240 nm, using the program CONTIN (Provencher 1982). Noise reduction was achieved by adjacent-averaging smooth processing using the software package *OriginPro7* (OriginLab Corporation, USA).

The *pK$_a$* of the transition between native and unfolded state can be calculated using Equation 6.1 (Abbruzzetti et al. 2000; Abbruzzetti et al. 2006), which describes an ionic equilibrium monitored by the physically observable property *a* (mean residue ellipticity at 222 nm).

$$a = a_{\min} + \left(a_{\max} - a_{\min}\right)\frac{10^{n\left(pH - pK_a\right)}}{1 + 10^{n\left(pH - pK_a\right)}} \qquad (6.1)$$

The limits $a_{\min}$ and $a_{\max}$ represent observable values at pH far above and below pK_a, respectively. The *n* parameter represents an empirical Hill coeficient ($n > 1$ positive

cooperativity, $n < 1$ negative cooperativity; $n = 1$ Equation 6.1 reduces to the Henderson-Hasselbalch Equation).

6.2.3 Saturation Transfer Difference (STD) NMR

BSA samples for NMR were prepared by dissolving the lyophilized powder in an aqueous solution containing 10 % (v/v) D_2O and sufficient o-NBA to give a final optical absorption of 0.6 at 355 nm (~ 2 mM o-NBA) in a 1.0 cm path length cell. The final protein concentration was 20 μM. The pH of the solution was adjusted by addition of appropriate amounts of either DCl or NaOD. The pH was measured by using a glass microelectrode and was not corrected for the isotope effect.

NMR measurements were performed on a Bruker Avance III 400 spectrometer operating at a proton frequency of 400.133 MHz, at a temperature of 3.0 ℃. The sample temperature was calibrated against a methanol standard. The Saturation Transfer Difference (STD) NMR spectra (Mayer & Meyer 1999) were acquired with a standard pulse sequence from the Bruker library with a spin-lock (T1ρ) filter for protein background suppression and water suppression with excitation sculpting using z gradients. The spectra were collected with 256 increments and 32 k data points in t2 using a spectral window of 6410 Hz centered at 1882.5 Hz. A 2 kHz spin lock filter of 15 ms was used. For the *on-resonance* spectra (I_{SAT}), selective saturation of protein resonances was performed by irradiating at 526 Hz using a series of Eburp2.1000 shaped 90º pulses (50 ms presaturation and 1 ms delay between pulses) for a saturation time varying between 0.5 and 4.0 s. For the *off-resonance* spectra (I_0), irradiation was performed at 10000 Hz. All data was processed using the program Topspin v2.1 and the STD spectra were obtained after subtraction of the *on-resonance* spectra from the *off-resonance* spectra ($I_{STD} = I_0 - I_{SAT}$). Control STD-NMR experiments were performed using an identical experimental setup and the same ligand concentration but in the absence of the protein.

6.2.4 Time-resolved Photoacoustic Calorimetry

Sample solutions for photoacoustic measurements were prepared by dissolving the protein lyophilized samples into an aqueous solution containing sufficient o-NBA to

give a final optical absorption of 0.6 in a 1.0 cm path length cell, at 355 nm. Protein concentrations varied between 20 μM and 120 μM. Bromocresol purple (BP) was used as photocalorimetric reference compound. It was used dissolved in water and its optical absorption was adjusted to match that of the sample solution at 355 nm. The pH sample and reference solutions was adjusted by addition of concentrated HCl or NaOH and measured using a glass microelectrode. The pH of BP solutions was adjusted to 9.0, in order to avoid instability in optical absorption at the excitation wavelength (Stefania Abbruzzetti et al. 1999). The pH of the sample solutions (mixtures of BSA and *o*-NBA) were adjusted to pH 5.3. All experiments were repeated at least three times.

Experiments of laser-induced pH jump coupled with photoacoustic detection were performed using a time-resolved photoacoustic calorimetry flow cell developed in-house that follow the front-face irradiation design described by Arnaut et al. (Arnaut et al. 1992), connected to systems for temperature control and automatic injection (Kloehn syringe pump). In Chapter 3, a detailed description of the experimental setup is presented. The light source, operated at 355 nm, was the third harmonic of a nanosecond Q-switched Nd:YAG laser (Ekspla NL301G). The laser pulse width was approximately 6 ns, and the pulse repetition rate was 10 Hz. Before initiating each experiment, the maximum laser pulse energy was verified and adjusted to approximately 1 mJ/pulse. Furthermore, each solution analyzed (sample, BP and solvent) was excited with four different intensities corresponding to 25, 50, 75 and 100% of the full laser intensity by employing neutral density filters. The PAC signals were measured between 3.0 ºC and 20.0 ºC, and the temperature variation during an experiment was less than 0.5 ºC. The photoacoustic pressure waves were detected using 2.25 MHz (model A106S) and 0.5 MHz (model V101-RB) Panametrics transducers. The PAC signals from 200 shots were average, pre-amplified with a Panametrics ultrasonic preamplifier (model 5676) and then recorded using a digital oscilloscope (Tektronix DPO7254).

The principles of deconvolution of photoacoustic waveforms are described in detail in Chapter 3. Briefly, the energy fractions and lifetimes of a sample *E(t)* can be obtained by the convolution of the instrumental response, or reference waveform *T(t)*, with the time-dependent function of the decay process *H(t)*.

$E(t) = T(t) \otimes H(t)$ *(6.2)*

Experimentally, the function *T(t)* can be obtained using a photocalorimetric reference compound such as BP, that releases nonradiatively (only heat deposition) all the radiative energy absorbed, in a time faster than the transducer resolution.

The function *H(t)* represents the overall time-dependent volume change and can be written as the summation of sequential single exponential terms:

$$H(t) = \sum_i \frac{\phi_i}{\tau_i} e^{-(t/\tau_i)} \qquad (6.3)$$

where ϕ_i and τ_i are the respective energy fraction and decay time for the *i*th component in the sum of the exponentials. The *CPAC* software developed in our laboratory was used to obtain ϕ_i and τ_i parameters (Schaberle et al. 2010).This software provide an analytical description for the instrumental response photoacoustic wave *T(t)*, and the analytical solution for the convolution between *T(t)* and the heat function *H(t)*. The ϕ_i and τ_i parameters are varied until the calculated *E(t)* fits the experimental wave *E(t)*. The kinetics of processes occurring faster than roughly 10 ns could not be resolved, but the integrated enthalpy and volume changes can be quantified from the amplitude of the acoustic wave.

Structural volume changes as a function of the concentration of BSA can be determined using a two-temperature method (Gensch & Braslavsky 1997). The sample waveforms were acquired at the temperature $T_{\beta=0}$, for which the thermal expansion coefficient of the solution, β, is zero. The value of $T_{\beta=0}$ can be determined experimentally by measuring the temperature at which the signal for the reference compound vanishes. The temperature obtained for $T_{\beta=0}$ in an aqueous solution was 3.0 ºC. The reference waveforms were measured at a slightly higher temperature, $T_{\beta\neq0} = 6.0$ ºC. Signals measured at $T_{\beta=0}$ originate solely from the structural volume changes in the solution and include no enthalpic contributions. The extent of the observed structural volume change ΔV_i (estimated as milliliters per mole of absorbed photons) is calculated from ϕ_i as:

$$\Delta V_i = \phi_i E_\lambda \left(\frac{\beta}{C_p \rho} \right)_{\beta\neq0} \qquad (6.4)$$

where E_λ is the energy of one mole of photons at the excitation wavelength (355 nm, $E_\lambda = 80.54$ kcal mol^{-1}) and $(\beta/C_p\rho)_{\beta\neq0}$ is the thermoelastic parameter of the solution at $T_{\beta\neq0}$.

The two-temperature method also allowed the determination of the rate constants, using τ_i values obtained from the fitting procedure.

Experiments conducted at multiple temperatures have been used to determine for each transient the heat release, the structural volume change and, from the temperature dependence of the rate constants, the activation energy (Callis et al. 1972; Peters & Snyder 1988; Braslavsky & Heibel 1992). Deconvolution was performed at several temperatures, and the pre-exponential factors ϕ_i were used to determine the energy content, $E_\lambda \phi_i$, of the transient at each temperature. This parameter was then plotted versus the ratio $(C_p \rho / \beta)_{\beta \neq 0}$. From the linear relation:

$$\phi_i E_\lambda = Q_i + \Delta V_i \left(\frac{C_p \rho}{\beta} \right) \tag{6.5}$$

it is possible to determine the heat release after excitation per mole of photons absorbed Qi (from the intercept) and the structural volume change per mole of photons absorbed ΔV_i (from the slope) for each ith process.

In both methods, two-temperature and multiple-temperature, the volume changes can be converted into molar reaction volume (expressed as milliliters per mole of photons released) dividing ΔV_i by the deprotonation quantum yield of o-NBA, $\Phi_{H+} = 0.4$ (George & Scaiano 1980). The heat released Q_i obtained using the multiple-temperature method can be converted in molar enthalpy changetaking in consideration the quantum yield of o-NBA.

The temperature dependence of the rate constants can be analyzed by the following relationships:

$$k = k_0 e^{-E_a / RT} \tag{6.6}$$

$$\ln k = \ln k_0 - \frac{E_a}{RT} \tag{6.7}$$

where $k = 1/\tau$. The activation energy (E_a) and the pre-exponential factor k_0 could then be derived from a linear plot of $\ln k$ vs $1/T$ (Arrhenius Plot).

6.3 Results

In the previous Chapter we have explored the volume changes and kinetics governing α-helix folding/unfolding in peptides. Here, our main goal is to apply the same methodology to explore partially unfolding events in BSA induced by pH changes. In particular, we intend to study the unfolding events associated with the protonation of both glutamic acid (Glu) and aspartic acid (Asp) residues occurring within the nanosecond to microsecond time scale. The prepulse pH was adjusted to approximately 5.3, one unit higher than the typical pK_a of Asp and Glu residues. BSA is known to undergo a pH induced conformational transition at pH 4.3 ($N \leftrightarrow F$) accompanied by loss in α-helix content. Brahma and co-workers proposed that the conformer at pH 4.3, presumably close to the F state, could attain a dimeric structure (Brahma et al. 2005). As evidenced in Figure 6.1(B), BSA has a large number of Asp an Glu residues. Being so, when inducing a pH jump from 5.3 to lower pH we expect to protonate the most solvent-exposed Asp and Glu amino acid residues, and promote the partially unfolding of BSA associated with the conformational transition N to F. Firstly, the secondary structure content has been evaluated in different pH conditions using far-UV CD measurements. Secondly, since the BSA binds different types of ligands, STD-NMR experiments have been performed to examine the possible interaction between BSA and the photoacid responsible for the pH jump. Finally, using TR-PAC and a laser-induced pH jump at pH 5.3, one can estimate the rate of protonation of BSA, as well as, estimate enthalpy and volume changes associated with the partial unfolding of the protein.

6.3.1 Conformational Transition of BSA at Acidic pH Monitored by CD Spectroscopy

Far-UV CD experiments were used to monitor the secondary structure content of BSA in different pH conditions and 3.0 ℃, the temperature used for most of the experiments reported in the present work. Figure 6.2(A) shows the far-UV CD spectra of BSA at pH conditions between 6.9 and 2.3. The spectra exhibit the characteristic double minima of α-helices at 222 nm and 208 nm. The fraction of helical content was

quantitatively estimated using the program CONTIN. At 3.0 ℃ and pH values between 7 and 5.5, the helical content was estimated to be approximately 80 %. Recently the crystal structure of BSA has been determined and the helical content reported to be 78 % (PDB entry: 3V03) (Majorek et al. 2012), which is in good agreement with the value we obtained at pH around 7. When the pH is reduced to 2.3 an estimated helical content value of 55 % is obtained.

Figure 6.2(B) reports changes in the mean residue ellipticity at 222 nm ($[\Theta]_{222nm}$) as a function of pH, at 3.0 ℃. The titration of BSA with HCl reveals only marginal changes in the secondary structure of BSA between pH 6.9 and 4.5 as judged from both spectra and the ellipticities at 222 nm. In fact, the helical content is reduced around 6 % when the pH is 4.5. Then $[\Theta]_{222nm}$ becomes less negative with decreasing pH from about -17500 deg cm^2 dmol^{-1} at pH 4.5, to -12000 deg cm^2 dmol^{-1} at pH 2.3. These values of ellipticities at different pH conditions are in good agreement with the literature (Muzammil et al. 1999; El Kadi et al. 2006). Fitting the data of $[\Theta]_{222nm}$ to Equation 6.1, we estimated a pK_a of 3.6 ± 0.1, at 3.0 ℃, with a Hill coefficient of 1.1 ± 0.2. The titration is fully reversible and no suggestion of aggregation was evident in any of our experiments.
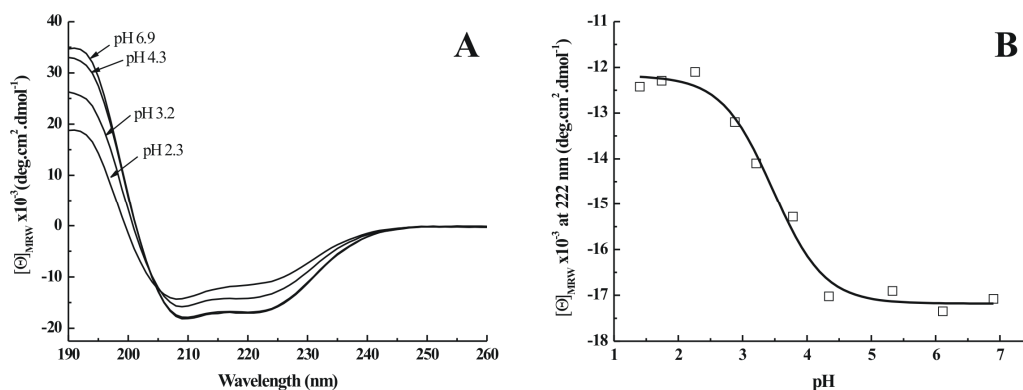
Figure 6.2: Far-UV CD of an aqueous solution of BSA at different pH values, at 3.0 ℃. The secondary structure of BSA displays few changes in a range of pH values between 6.9 and 4.3. Below the isoelectric point of the protein (pI 4.8), the ellipticity measured at 222 nm decreases markedly to a minimum value at around pH 2. In our experimental conditions, the estimated pK_a for the formation of the acid-unfolded state at pH 2 is 3.6 ± 0.1, with a Hill coefficient of 1.1 ± 0.2, as determined using Equation 6.1.

6.3.2 Potential Interaction Between BSA and *o*-NBA

STD-NMR experiments were performed to examine if the photoacid used to produce the pH jump, *o*-NBA, interacts with the protein of interest. As mentioned in Chapter 5, STD-NMR is a powerful method for studying protein-ligand interactions in solution. Ligand protons that are in close contact with the receptor protein receive a higher degree of saturation, and as a result stronger STD-NMR signals can be observed. Protons that are either less or not involved in the binding process reveal no STD-NMR signals. This technique can be used to study ligand binding with association constants K_a between 10^7 and 10^3 M^{-1}, being also capable of identifying the binding epitope of a ligand when bound to its receptor protein (Viegas et al. 2011).

STD-NMR results obtained for the mixture of *o*-NBA and BSA, in an aqueous solution at pH 5.3 and 3.0 ºC, as well as, the ^{1}H-NMR spectrum of *o*-NBA in the same conditions are presented in Figure 6.3. Figure 6.3(B) shows that STD signals were observed for the mixture *o*-NBA and BSA, thus the photoacid interacts with the protein, and considering the relative intensities of the proton signals (1 – 5) it seems that all have similar qualitatively contributions for the protein - ligand interaction. The association constant K_a has been determined using data from fluorescence emission spectra of BSA upon addition of different *o*-NBA concentrations and applying the Stern-Volmer formalism (data not shown). The observed K_a values are in the range of 10^3 M^{-1}, which indicates a weak interaction between BSA and *o*-NBA. Moreover, the stoichiometry of the association is 1:1.

These results suggest that in the experimental conditions used in the TR-PAC experiments some molecules of *o*-NBA bind to BSA. However, since the photoacid is in large excess relative to the protein concentration (20 μM - 120 μM) we assume that this protein-photoacid interaction does not have a significant effect in the pH jump efficiency.
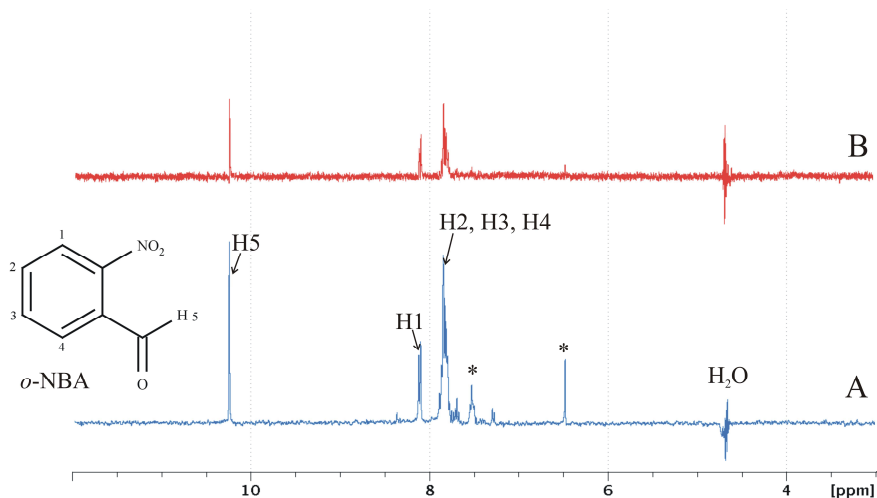
Figure 6.3: (A) ^{1}H-NMR spectrum of free *o*-NBA in aqueous solution at pH 5.3, and respective spectral assignments. (B) ^{1}H STD-NMR spectrum of a mixture containing *o*-NBA (2 mM) and BSA (20 μM) in an aqueous solution at pH 5.3 (3.0 s of saturation time). The experiments were performed in 90% H_2O /10% D_2O, at 3.0 ℃. The on-resonance irradiation of the protein was performed at 1.32 ppm, using saturation times between 0.5 and 4.0 s. The asterisk indicates impurities present in the samples.

6.3.3 Protonation of BSA Monitored by TR-PAC

To resolve processes occurring in less than 1 μs, TR-PAC measurements were performed using the 2.25 MHz transducer. Firstly, the two-temperature method was applied to investigate the processes occurring upon protonation of BSA and determine the structural volume changes and rates associated with each process identified.

Figure 6.4(A) shows examples of the photoacoustic waves obtained for *o*-NBA in presence of BSA at three different concentrations and *o*-NBA alone measured at 3.0 ℃, along with the BP photoacoustic wave acquired at 6.0 ℃. As previously described in Chapter 4, in an aqueous solution at pH 5.3, the signal obtained for *o*-NBA is inverted when compared with the waveform of BP, because its photolysis is accompanied by a prompt (lifetime below a few nanoseconds) volume contraction. Furthermore, Figure 6.4(A) also evidences differences in amplitude, as well as, in phase for the mixture of BSA/*o*-NBA when compared with the one acquired for *o*-NBA alone. Hence, our data suggest that the fast *o*-NBA photolysis is followed by an additional process or processes that produce an additional photoacoustic signal. Qualitatively, our results indicate that the

BSA photoacoustic signals are concentration-dependent. It is worth to note that the profile of the photoacoustic waves obtained for BSA is nearly identical to that described for both Ac-Asp-NH$_2$ and Ac-Glu-NH$_2$ presented in the previous Chapter 4.
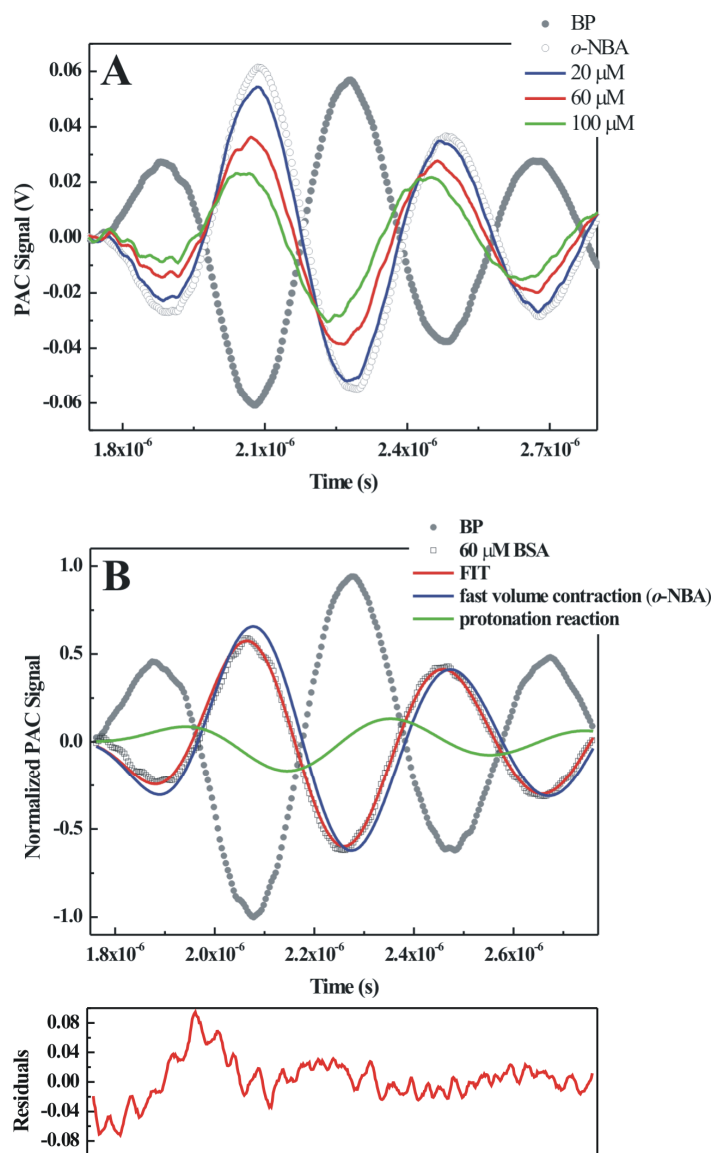
Figure 6.4: (A) Photoacoustic waves generated after laser irradiation, obtained using a 2.25 MHz transducer and applying the two-temperature method. The BP signal was measured at T$_{\beta\neq0}$ = 6.0 °C, while the signals from *o*-NBA and BSA were measured at T$_{\beta=0}$ = 3.0 °C. The value of prepulse pH used for solutions of BSA and *o*-NBA was 5.3. (B) Example of a result obtained from the fitting procedure using the *CPAC* software. The fit derived from the deconvolution is shown by the red line. The overall fit correspond to the sum of the two deconvoluted component waves, which are associated with the fast contraction of *o*-NBA and the protonation reaction that are represented by blue and green lines, respectively.

PAC signals were resolved using the software *CPAC*. The photoacoustic waves of BSA at different concentrations were well-fitted by a function involving two sequential exponential decays. Fitting with three exponential decays did not improve the fit. In fact, ϕ_3 values with no physical meaning and lifetimes i_3 much higher than the transducer resolution were obtained. Each component decay is characterized by a lifetime, τ_1 and τ_2, and an amplitude change proportional to the volume change, ϕ_1 and ϕ_2. Figure 6.4(B) shows an example of the fit obtained from the deconvolution of the signal for BSA at 60 μM, together with the two component waves. The first component wave (in blue) clearly can be associated with the reaction of photolysis of *o*-NBA exhibiting negative amplitude and a time profile that is characteristic of a fast volume contraction. The second component wave (in green) displays positive amplitude and is shifted to the right when comparing with the BP waveform. This second process seems to correspond to the protonation of the negatively charged side chains of Asp and Glu from BSA, typically characterized by volume expansion as shown in Chapter 4.

Structural volume changes were calculated using the amplitude values derived from the fitting procedure and applying Equation 6.4. The average value obtained for the structural volume change ΔV_1, resulting from photolysis of *o*-NBA in the presence of different concentrations of BSA, was -4.7 ± 0.9 ml mol^{-1} (see Table 6.1). This value is in good agreement with previous results for the fast volume contraction, under pH conditions near neutrality and in the presence of others proton-accepting groups such as the previously studied amino acid models (see Chapter 4).

Figure 6.5(A) shows the dependence of the calculated structural volume change for the second process (ΔV_2^{exp}) on the concentration of BSA. As shown, the values of ΔV_2^{exp} reach a plateau when the concentration is greater than 80 μM. In the plateau the estimated value for the structural volume change ΔV_2 accompanying the protonation of BSA corresponds to a volume expansion of approximately 3.8 ml mol^{-1}. The rate constants for this volumetric expansion, $k_2 = 1/\tau_2$, increase linearly with BSA concentration, as shown in Figure 6.5(B). From the slope of the plot of rate constants as a function of the BSA concentration, the bimolecular rate constant k_b can be determined. The value of k_b revealed that protonation of Asp and Glu residues from BSA yielded a value of approximately 1.3×10^{11} M^{-1}s^{-1}. This value is higher than the diffusion limited rate constant between a charged proton and a large molecule (BSA) in water. One possible

reason for this observation could be the formation of a ground state complex between the photoacid and BSA. However, our STD-NMR experiments suggest a weak binding interaction between BSA and *o*-NBA.
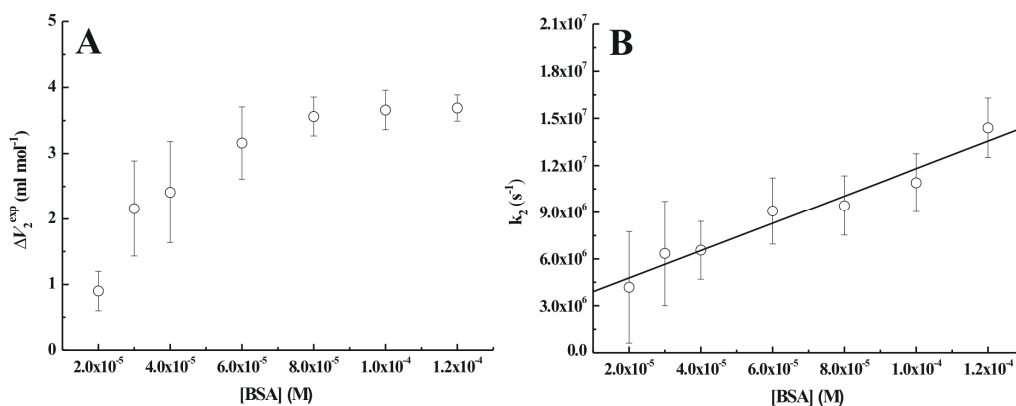
Figure 6.5: (A) Dependence of ΔV_2^{exp} on the concentration of proton-accepting groups, namely solvent exposed residues of Glu and Asp in BSA. The reaction volumes (ΔV_2) estimated for the protonation of BSA is reported in Table 6.1. (B) Dependence of the rate constant ($k_2 = 1/\tau_2$) on the concentration of BSA. The bimolecular rate constant was derived from the slope of the linear relationship (solid line) of the experimental rate constants as a function of BSA concentration and is reported as k_b in Table 6.1.

Table 6.1: Parameters from the TR-PAC experiments obtained using a 2.25 MHz transducer and applying the two-temperature and the multiple-temperature methods.

Two-Temperature Method	
ΔV_1 (*ml mol^{-1}*)	-4.7 ± 0.9
ΔV_2 (*ml mol^{-1}*)	3.8 ± 0.3
k_b (*$10^{11} M^{-1} s^{-1}$*)	1.3 ± 0.5
Multiple-Temperature Method	
ΔV_1 (*ml mol^{-1}*)	-4.5 ± 0.4
Q_1 (*kcal mol^{-1}*)	94.7 ± 2
ΔV_2 (*ml mol^{-1}*)	3.9 ± 0.9
Q_2 (*kcal mol^{-1}*)	5.4 ± 3
E_a (*kcal mol^{-1}*)	4.7 ± 1
Frequency factor $\ln(1/\tau_2)$	20.8 ± 2

In addition, we have also examined the protonation of BSA using the multiple-temperature method, at a protein concentration where $\Delta V_2^{\mathrm{exp}}$ reaches a plateau, as determined by the two-temperature method (see Figure 6.5(A)). The temperature-dependent acoustic signals recorded between 6.0 and 20.0 ºC enabled a plot of $\phi_i E_\lambda$ *versus* $C_\mathrm{p}\rho/\beta$, from which the volume change accompanying each process can be obtained from the slope and the heat released from the solution from the yy intercept, according Equation 6.5 (Figure 6.6). Also the temperature dependence of the lifetime provides information on the activation energy for each process whose rate constant falls within the experimental resolution range.

At all studied temperatures the photoacoustic signals were well described by two sequential exponential decays with the fast, sub-resolution process related to the *o*-NBA photolysis and a slower decay, with a temperature-dependent rate constant reflecting proton transfer reactions with the acceptors present in solution, namely the Glu and Asp residues from the protein BSA. The fast component decay exhibit a volume contraction (negative slope) of approximately -4.5 ml mol^{-1} and the corresponding enthalpy change is approximately -36 kcal mol^{-1}. The protonation of BSA induces a volume expansion (positive slope) of approximately 3.8 ml mol^{-1}, and the enthalpy changes obtained was -12.8 kcal mol^{-1}.

Figure 6.6(B) shows the Arrhenius plot for the rate of proton binding ($k_2 = 1/\tau_2$) to BSA at pH 5.3. The activation energy (E_a) and frequency factor obtained from Arrhenius analysis of the multiple-temperature data are included in Table 6.1.
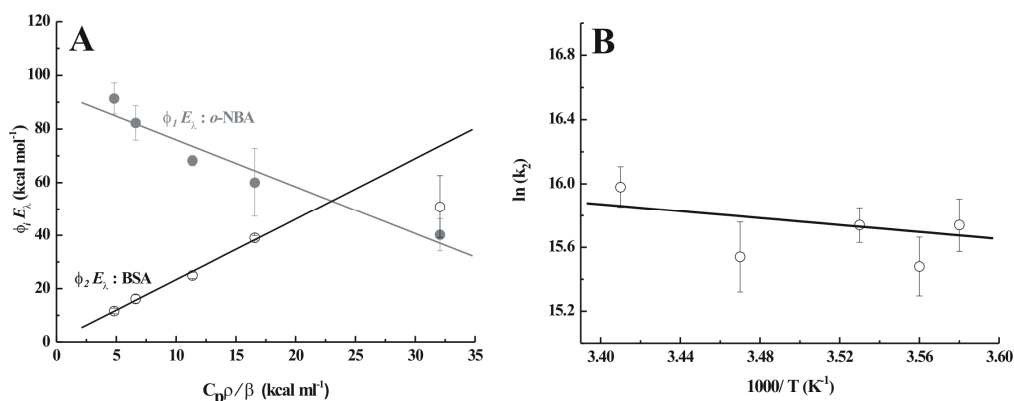
Figure 6.6: (A) Plots of the energy content for the photo-dissociation of *o*-NBA ($\phi_1 E_\lambda$) and for the binding of the photo-released protons to BSA ($\phi_2 E_\lambda$), as a function of the parameter $C_p\rho/\beta$. $C_p\rho/\beta$ was changed by varying the temperature between 6.0 and 20.0 °C. The BSA concentration was 80 µM, at pH 5.3. The volume change and heat releases were obtained from the linear fits represented by solid lines, and based on Equation 6.5. (B) Arrhenius plot for the protonation of BSA, at pH 5.3. The activation energy (E_a) and frequency factors were derived from the linear relationship (solid line) of the rate constants as a function of 1/T (see Equation 6.7). The results are reported in Table 6.1.

As just described the photoacoustic measurements performed with the 2.25 MHz transducer only allowed the identification of two sequential processes, namely *o*-NBA photolysis and the protonation reaction involving the Asp and Glu amino acid residues from the protein BSA. In fact, this transducer is limited to a time resolution of approximately 800 ns. As a consequence, any slower conformational change of BSA due to its protonation would not be detected. Thus, TR-PAC experiments were also performed using the 0.5 MHz transducer in order to investigate any early unfolding event occurring on a slower time scale following the protonation of carboxylic acids. In particular, if there is a volumetric change occurring on a time scale between 800 ns and 2 µs, this transducer should be able to detect and resolve it.

Figure 6.7(A) shows the photoacoustic waves of *o*-NBA and bromocresol purple (BP) acquired with the 0.5 MHz transducer. As can be observed, the *o*-NBA waveform acquired at 3.0 °C is inverted when compared with the BP waveform at 6.0 °C. As expected, this behaviour is similar to that observed using the 2.25 MHz transducer and it can be associated with a fast volume contraction. The photoacoustic signal is well-fitted using a single exponential decay. Whereas the lifetimes τ_1 were not resolved in time, ϕ_1 values were obtained from the fitting procedure at different laser intensities. The volume change associated with the *o*-NBA photolysis is -4.7 ± 0.4 ml mol^{-1}, which is in good

agreement with the volume contraction previously observed with the 2.25 MHz transducer (Table 6.1). Figure 6.7(B) shows examples of the BSA photoacoustic waves obtained at two different protein concentrations. At low concentration (30 μM) the photoacoustic signal is inverted when compared with the BP waveform, but exhibits a significant difference in amplitude and shape from that observed for the photoacid. Our results also show that the increase in protein concentration progressively promotes an increase in the amplitude of the signal. Based on the results with the 2.25 MHz transducer, we observed a kinetic constant k_b of approximately 1.3 x10^{11} M^{-1} s^{-1}. Being so, we expected to observe a protonation reaction with an apparent time of more than two hundred nanoseconds ($\tau_2 \sim$ 265 ns) for the lower BSA concentration. Moreover, higher concentrations, close to 400 μM, should be characterized by a protonation lifetime of 20 ns as estimated from the relation $1/\tau_2 = k_b$[BSA]. While lifetimes of approximately two hundred nanoseconds are within the time resolution of the 0.5 MHz transducer and it is possible to resolve the respective acoustic wave, the latter lifetime of 20 ns is in the lower limit of resolution of the detector. Using the 0.5 MHz transducer, was not possible to resolve lifetimes < 100 ns. Although the photoacoustic wave is detected, it would not be separated from the o-NBA photolysis.
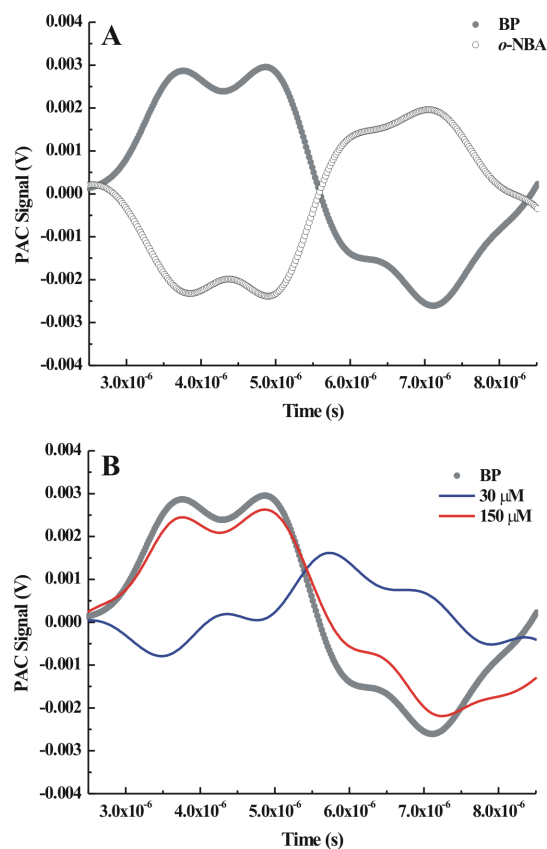
Figure 6.7: Photoacoustic waves generated after laser irradiation, obtained using a 0.5 MHz transducer and applying the two-temperature method. (A) Photoacoustic waves of BP and o-NBA. (B) Photoacoustic waves from BP and BSA at different concentrations. The BP signal was measured at $T_{\beta \neq 0} = 6.0$ ºC, while the signals from *o*-NBA and BSA were measured at $T_{\beta = 0} = 3.0$ ºC. The value of prepulse pH used for solutions of BSA and *o*-NBA was 5.3. Noise reduction was achieved by FFT Low Pass Filter processing, using the software package *OriginPro7* (OriginLab Corporation, USA).

Figure 6.8(A) for data obtained with the 0.5 MHz transducer shows the fit obtained for the photoacoustic reference bromocresol purple (in green), as well as, the fit to the photoacoustic wave of 30 μM BSA (in red). At low protein concentration (30 μM) the photoacoustic signal of BSA is only well-fitted using three sequential exponential decays. Actually, a two exponential decay is unable to fit the experimental wave. Figure 6.8(B) shows the component waves derived from the fitting procedure. A sub-resolution acoustic wave (Figure 6.8(B), in yelow) corresponds to the release of protons by *o*-NBA and it is characterized by a volume change of approximately -4.1 ml mol^{-1}. The second component wave derived from the global fit is related with the protonation reaction

involving the negatively charged carboxylic acids and it is represented by an average lifetime of 306 ns and an average volume change of 3.3 ml mol^{-1} (Figure 6.8(B), in blue). It is worth to note that the BSA concentration used (30 μM) is below the plateau defined in Figure 6.5(A). Therefore, the value does not correspond to the ΔV_2, but to the ΔV_2^{exp} observed at 30 μM. The third component wave can be associated with the early unfolding of BSA due to protonation and although the associated lifetime should not depend on the protein concentration because it is a unimolecular reaction, the correspondent volume change is not absolute because the protonation yield is not unitary at the experimental BSA concentration. Preliminary results reveal that this early unfolding event corresponds to a volume expansion of approximately 1.6 ml mol^{-1} and a lifetime of approximately 1 μs (Figure 6.8(B), in orange).

At high BSA concentrations, such as 400 μM, we would expect that the proton release and the BSA protonation should appear as a single unresolved event. In fact, the photoacoustic signal is well-defined by two sequential exponential decays, being the second event associated with the unfolding event (data not shown). In particular, the volume change associated with the o-NBA photolysis and protonation reactions corresponds to approximately 4.1 ml mol^{-1}, while the BSA partial unfolding is well characterized by a volume expansion of approximately 2.3 ml mol^{-1} and a lifetime of approximately 1.5 μs.
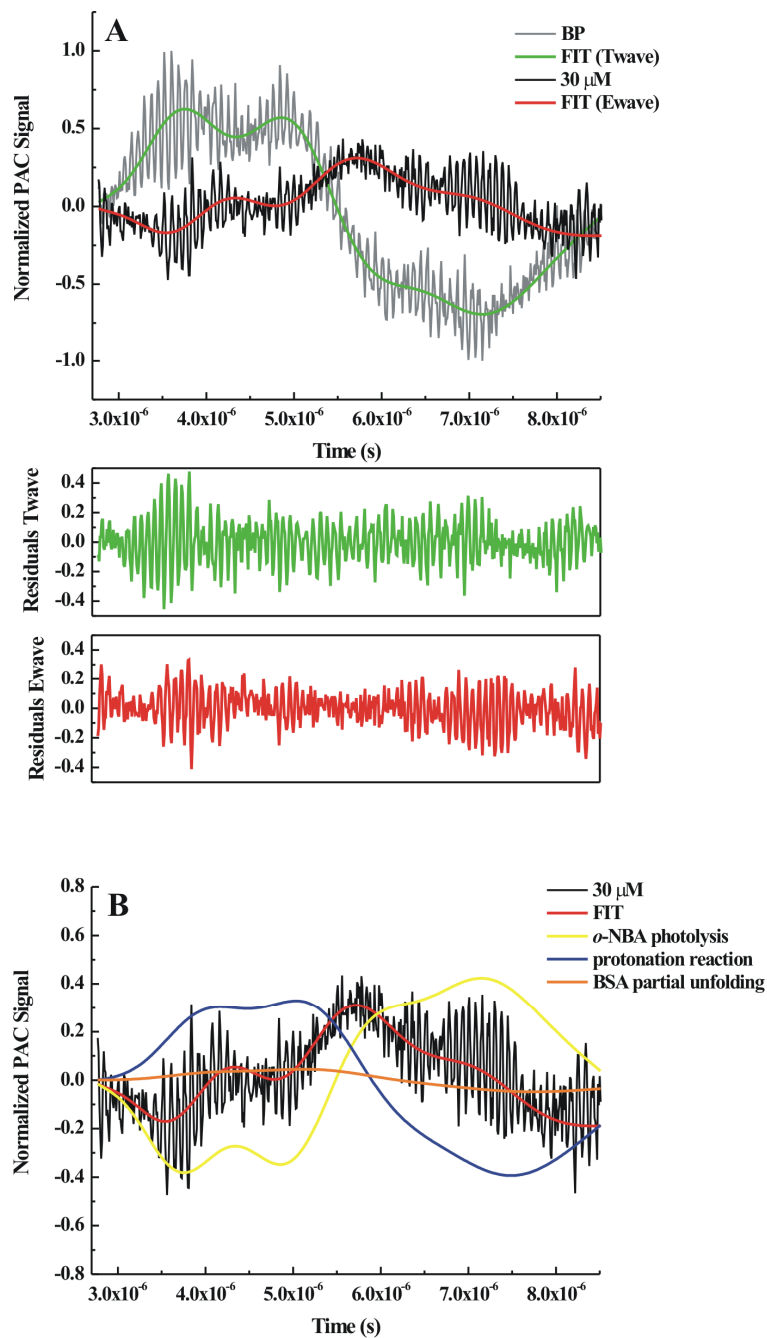
Figure 6.8: (A) Photoacoustic waves generated after laser irradiation of bromocresol purple (BP, in grey) and 30 μM BSA (in black) in an aqueous solution containing *o*-NBA, using a 0.5 MHz transducer. Solid lines represent the fit obtained for the photoacoustic reference BP (T wave, in green) and for 30 μM BSA (E wave, in red) using the prepulse pH 5.3. (B) Component waves derived from the fitting procedure. The global fit (in red) corresponds to the summation of three component waves that are associated with the fast contraction due to *o*-NBA photolysis (in yelow), the volume expansion due to protonation of carboxylic acids (in blue) and the BSA partial unfolding (in orange).

153

6.4 Discussion

The stability, structure, and function of proteins are dependent on the pH of their environment (Matthew et al. 1985). Several proteins undergo partial or complete unfolding, due to protonation of selected amino acid side chains. During the acid unfolding of BSA a conformational transition between the *N* and *F* states occurs, with a pH midpoint of approximately 4.3. From previous studies, it is known that in the pH region of the *N* to *F* transition (pH 5.0 – 3.5) a drastic structural change takes place primarily in domain III and domain II which convert to a molten-globule like state, whereas domain I undergoes a structural rearrangement with minor changes in secondary structure (Qiu et al. 2006). Furthermore, the conformer at pH 4.3, presumably close to the *F* state, seem to attain a dimeric structure (Brahma et al. 2005). In all our TR-PAC experiments, the prepulse pH used was 5.3 and the *o*-NBA photolysis reduces the solution pH to approximately 4.4. According to the far-UV CD measurements described here, at low temperature (3.0 ºC) the conformational transition between pH 5 and 4 is associated with a loss of approximately 6% of the BSA helical content. Moreover, although BSA weakly binds the *o*-NBA as determined by fluorescence and STD-NMR, this weak binding may reduce the number of photoacid molecules free in solution.

Our results of TR-PAC using the two-temperature and multiple-temperature methods and the 2.25 MHz transducer suggest the presence of two processes with distinct volume changes occurring after the pH jump. The observed fast volume expansion of approximately -4.5 ml mol^{-1} represents the volume change due to photolysis of *o*-NBA. It has been shown previously that the proton release from *o*-NBA is accompanied by a negative volume change of approximately -5 ml mol^{-1} (Viappiani et al. 1998). In BSA, the amino acid residues having appropriate pK_a to be protonated bellow 5.3 are the carboxylic groups of Glu and Asp amino acid residues. Protonation of negatively charged carboxyl groups is expected to lead to a positive volume change due to the decrease of the net number of charges in solution (Van Eldik et al. 1989). The magnitude of the volume change is influenced by the nature of the groups attached to the carboxylic group. Following the results of Rasper and Kauzmann, in proteins the protonation of a carboxylic group causes a volume increase of approximately 11 ml per mole of protons reacting and this value may be smaller if there is a positive charge in the vicinity of the carboxylic group (Rasper & Kauzmann 1962). Under our experimental conditions we observed that

the neutralization of Asp and Glu residues in BSA at pH 5.3 (~3.8 ml mol^{-1}) is slightly lower than the values reported for proteins such as ovalbumin, ribonuclease, lysozyme and BSA, at 30 ℃ and 150 mM NaCl (Kauzmann et al. 1962) using Carlsberg dilatometers. Maybe a larger volume change would be expected considering that BSA is a highly charged protein with more than 180 charges at pH 7, among them 39 aspartic acids and 59 glutamic acids (see Figure 6.1(B)). However, only a fraction of carboxylic acid side chains would have the pK_a between pH 5.3 and 4.4 and thus could be protonated after the pH jump. In addition, only a fraction of carboxylic acids are on the protein surface and solvent exposed, and thus available for protonation. In fact, the volume change obtained is nearly identical to the ones obtained for the amino acid models Ac-Glu-NH$_2$ and Ac-Asp-NH$_2$ described in Chapter 4. It is worth to note that in a polypeptide chain the vicinity of other amino acids to Glu and Asp greatly influences the chemical environment of the carboxylic groups relative to the isolated amino acid models Ac-Glu-NH$_2$ and Ac-Asp-NH$_2$ previously studied.

The rate constants obtained for the protonation of Glu and Asp amino acid residues can be compared to values reported by Gutman in different proteins: 2.5 x 10^{10} M^{-1} s^{-1} for BSA and RNase, and 1.2 x 10^{10} M^{-1} s^{-1} for lysozyme (Gutman & Nachliel 1990). Table 6.1 presents the value of k_b measured from a linear plot of the apparent rate constant k_2 versus the concentration of BSA, rather than versus the concentration of protonable sites. At neutrality the total number of Asp and Glu residues per molecule of BSA is 98. If we assume for the bimolecular rate an average value of k_{av} 2.5 x 10^{10} M^{-1} s^{-1} from the results obtained for the neutralization of the amino acid models Ac-Asp-NH$_2$ and Ac-Glu-NH$_2$ (in Chapter 4), it is possible to estimate the average number of reacting carboxylates as the ratio between k_b and k_{av} values. Thus, the effective number of Asp and Glu residues protonated per molecule of BSA would be 5, when the pH jump is promoted at pH 5.3. Among other kinetic assumptions, this reasoning considers that the diffusion in water of charged model compounds and the large BSA molecule is characterized by similar coefficients. This is an approximation and thus the number of Glu and Asp residues protonated per BSA molecule should be considered as a minimum value. In addition, the ratio between Ac-Glu-NH$_2$ and Ac-Asp-NH$_2$ concentration (~500 μM) and BSA concentration (~80 μM) needed to reach the plateau region of the plot ΔV_2 *versus* protein/amino acid concentration can also be used to estimate the average number of reacting carboxylates. This concentration is related with the number of molecules needed to "saturate" the protons released from the photoacid. As the number of protons released

on both experiments is the same, the relation between the saturation concentrations should be associated with the number of protonable sites. Using this approximation, one can estimate that the number of Asp or Glu residues protonated per BSA molecule is approximately 6.

To complement our results, calculations of solvent accessible surface area (SASA) have been performed to evaluate the extent of an amino acid exposure to the solvent (Ooi et al. 1987). SASA calculations are a geometric measure that can be applied to assess this exposure. It is usually calculated for the entire protein, but when calculated for each individual amino acid residue, provides a greater level of detail on the individual contributions of the different amino acids residues of a protein for the folding or unfolding processes. Relative solvent accessible surface area (RSASA) of an amino acid X can be defined as the ratio of the solvent accessible surface area of that residue in the three-dimensional structure of a protein to that observed in the tripeptide Gly-X-Gly in an extended conformation (Equation 6.8).

$$RSASA_X(t) = \frac{SASA_X(t)}{SASA_{Gly-X-Gly}} \times 100 \qquad (6.8)$$

The value of RSASA lies between 0% and 100%, with 0% corresponding to a fully buried amino acid residue and 100% to a fully exposed solvent amino acid residues. RSASA of each of the 98 Asp and Glu amino acid residues of BSA was computed with the program GETAREA (Fraczkiewicz & Braun 1998) using a spherical probe of 1.4 Å radius, mimicking a water molecule.

Figure 6.9 depicts the RSASA of the Asp and Glu amino acid residues in BSA (PDB entry 3V03). As can be observed, several Asp and Glu amino acid residues are highly exposed to the solvent (RSASA ≥ 90%), namely 38 Glu and 25 Asp. Only a small fraction is partially buried or buried (RSASA ≤ 50%), including 3 Asp and 2 Glu amino acid residues. Although some of these protonable residues are located in random coil regions, such as Asp-111, Glu-299 and Glu-293, other amino acid residues including Asp-279, Asp-268, Glu-226 are in α-helical regions. Most likely the protonation of the amino acid residues located in α-helical regions may perturb the helical content of the protein and contribute to the protein pH-dependent unfolding. Based on the secondary structure content, it can be observed that around 83% of the Asp and Glu amino acid

residues located in domain III are in α-helical conformation. In domain II, 85% of the Glu and Asp amino acid residues are present in α-helices. On the other hand in domain I, only approximately 65% of the Asp and Glu amino acid residues belong to α-helices. Thus, RSASA calculations suggest that the highest percentage of Asp and Glu amino acid residues in α-helical conformation are located in domain III and II. The protonation of these residues may play a critical role in BSA partial unfolding because they may contribute for destabilization of salt-bridges and/or electrostatic interactions which might partially disrupt α-helices. In fact, previous studies have shown that the *N* to *F* transition is the result of conformational changes occurring mainly in domain III and II, whereas the secondary structure of domain I is only slightly rearranged (Qiu et al. 2006).
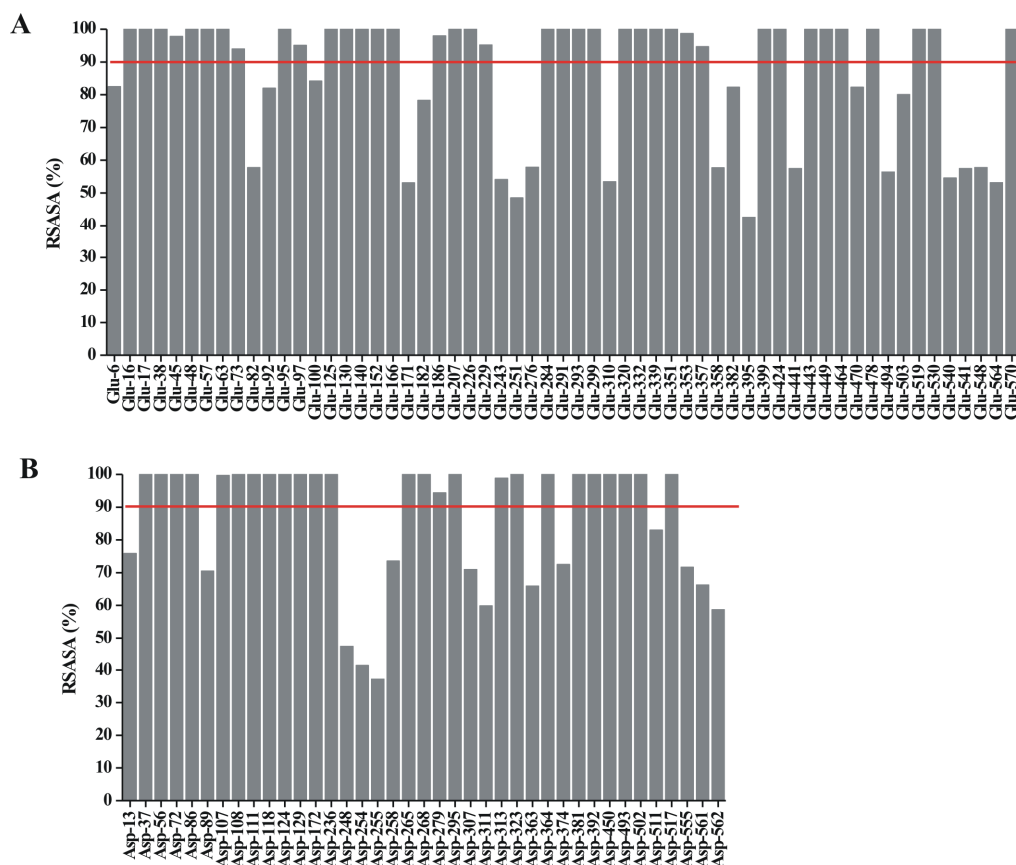
Figure 6.9: Relative solvent accessible surface area (RSASA) of the Glu (A) and Asp (B) amino acid residues of BSA. RSASA varies between 0% and 100%, with 0% corresponding to a fully buried amino acid residue and 100% to a fully solvent exposed amino acid residues.

Since a significant number of Asp and Glu amino acid residues are located in α-helical regions it is possible that their protonation perturb the BSA α-helical content. According to our results less than 10 Asp or Glu residues are protonated under our experimental conditions. The protonation of such residues produces an unfolding event measurable on the microsecond time scale as suggested by photoacoustic measurements performed using the 0.5 MHz transducer. In fact, preliminary results obtained with the 0.5 MHz transducer reveal that the protonation of Asp and Glu residues may contribute to this BSA partial unfolding which can be characterized by a small volume expansion of approximately 2.3 ml mol^{-1} and a lifetime between 1 and 1.6 μs.

Some α-helical proteins and polypeptides have been investigated using different techniques. In particular, laser-induced pH jump with TR-PAC detection has been applied to examine the structural volume changes accompanying the early events leading to the formation of the compact acid intermediate of a 17 kDa protein, apomyoglobin (ApoMb), in the presence of 200 mM guanidinium hydrochloride (GuHCl) (Abbruzzetti, Crema, et al. 2000), and in the absence of denaturant (Miksovská & Larsen 2003). The protonation of histidine residues (His 24 and His 119) were proposed to be involved in the partial unfolding of this protein. A large contraction of ~ -82 ml mol^{-1} with a lifetime of ~2.4 μs was assigned to structural changes taking place during the ApoMb unfolding. In the absence of denaturant, Miksovská and collaborators observed a smaller volume decrease of about -22 ml mol^{-1} with a lifetime of 620 ns. Furthermore, the acid-induced disruption of the helical structure of poly-L-Lysine acid (PLL) (n = 165) is associated with a contraction of approximately -17 ml mol^{-1} and lifetime of 250 ns. The coil to helix transition in poly-L-glutamic (PLG) (n = 82) induced by pH jump and studied by PAC shows an expansion of approximately 7 ml mol^{-1} with a lifetime of 100 ns.

Although a significant loss of helical content is typically characterized by a considerable volume contraction, under our experimental conditions the protonation of BSA seems to promote a small volume expansion of 2.3 ml mol^{-1} (3.8 Å^3). Previous studies on volume changes of BSA using ultrasound measurements have shown that as the binding of protons to BSA proceeds with decreasing pH from about 5 to 2 a progressive decrease of volume is observed (El Kadi et al. 2006). The variation of volume is originated from at least two phenomena. First, the partial unfolding process of the BSA helices leads to a progressive exposure of the protein surface to the acid aqueous environment, leading to increased hydration. At the same time protein voids and cavities, which in the native

protein contribute substantially to the compressibility and to the partial specific volume are collapsing. Hence, if sufficiently number of Asp and Glu residues are protonated the volume expansion due to protonation of these residues should be followed by a slow volume contraction as reported for other α-helical proteins undergoing complete unfolding.

Our results indicate that a reduced number of Asp and Glu amino acid residues are protonated under our experimental conditions. As a consequence, only a minor partial unfolding of the BSA may be occurring and it is not possible to identify the location of the Asp and Glu amino acid residues being protonated. The small expansion of 2.3 ml mol^{-1} could be associated with an early local partial unfolding event, which has previously been observed upon unfolding of the RN80 peptide (in Chapter 5). One can suggest that this partial unfolding event may be occurring on domains II or III because there are several Asp and Glu residues highly solvent-exposed located in α-helical regions in these domains. Although in the RN80 an unfolding lifetime around 369 ns is observed, for BSA a longer lifetime around 1 to 1.6 μs is detected, which may be explained taking in consideration that α-helices in a protein are not isolated fragments and there are several stabilizing interactions that need to be perturbed upon partial unfolding.

Chapter 7

Transsthyretin folding kinetics:

Does slower refolding imply enhanced amyloidogenicity?

7.1 Introduction

Research concerning the stability and folding and unfolding pathways for oligomeric proteins, mainly dimers and tetramers, has not been as extensive as with the monomeric counterparts. Significant insights have been gained from monomeric folding systems regarding the intramolecular forces responsible for the formation and stabilization of secondary and tertiary structures. However, it is not yet clear how these insights apply to the intermolecular association reactions that stabilize the quaternary structure of oligomeric proteins. Further knowledge into the folding of oligomeric proteins is essential, especially since the majority of proteins found in nature are ''multiple subunit'' type structures, which offer evolutionary advantages, such as increased thermostability relative to monomers and exquisite regulation through allostery and cooperativity in ligand binding. The folding of oligomeric proteins requires that the protein folding code direct the formation of intramolecular secondary and tertiary structure as well as the quaternary interactions necessary for biological function. A lack of reversibility, often resulting from aggregation, is a complication in the folding of many proteins, and particularly oligomeric systems (Jaenicke & Lilie 2000). *In vivo*, this competition between folding and aggregation is often offset by the assistance of chaperones (Jaenicke & Lilie 2000).

The present work describes not only the investigation into the folding pathway of the tetrameric protein transthyretin (TTR), which is one of several proteins known to be involved in human amyloid diseases, but also how the single point mutation V30M affects the TTR folding rate and how this may affect its amyloid fibril-forming propensity.

Human TTR is a homotetrameric protein with a total molar mass of 55 kDa found in the plasma and cerebrospinal fluid (see Figure 7.1). It is synthesized mainly in the liver, choroid plexus, and retina (Brito et al. 2003; Soprano et al. 1985; Stauder et al. 1986) and its main known functions are the transport of thyroxine and retinol, the later in association with the retinol-binding protein (RBP). The concentration of TTR in serum ranges from 170 and 420 µg/ml, and in the cerebrospinal fluid varies between 5 and 20 µg/ml (Vatassery et al. 1991). The three-dimensional structures of wild-type TTR (WT-TTR) and several of its variants have been solved to high-resolution by X-ray crystallography. In general, the crystal structures of the TTR variants are similar to that of the wild-type protein (Hörnberg et al. 2000; Palaninathan 2012). The main structural element of each TTR subunit is a *β*-sandwich consisting of two *β*-sheets with four *β*-strands each (Figure 7.1). The association of the four subunits in the native tetramer forms a central channel with two thyroxine-binding sites (Blake et al. 1978). More than 80 mutations of TTR have been reported, most of them amyloidogenic.

Abnormal protein aggregation into highly structured oligomers and insoluble fibrils, known as amyloid, is the hallmark of several neurodegenerative diseases, such as Alzheimer's disease, Parkinson's disease, Familial Amyloidotic Polyneuropathy (FAP), Senile Systemic Amyloidosis (SSA) among many others (Chiti et al. 1999). The neurodegenerative amyloid pathology FAP is a peripheral neuropathy with a high mortality rate which is characterized by extracellular deposition of amyloid fibrils mostly constituted by variants of TTR. Amongst TTR variants, V30M is the most prevalent amyloidogenic variant and L55P yields the most aggressive symptoms. In SSA the fibrils are essentially formed by wild-type TTR and its proteolytic fragments. In contrast to SSA, that predominantly affects patients over 80 years of age, FAP is an autosomal dominant lethal disease that may affect individuals from their twenties (Saraiva et al. 1984; Saraiva 1996). It is known today that amyloid formation by TTR is preceded by tetramer dissociation and partial unfolding of the resulting low stability monomers. Thus, multiple physico-chemical factors, chief among them, tetramer dissociation kinetics, monomer conformational stability, and aggregation kinetics do play a critical role in TTR amyloidogenesis (Brito et al. 2003). Accordingly, the characterization of potential

differences in the folding kinetics of WT-TTR and some of its variants may provide important clues for the understanding of how different TTR variants have different amyloidogenic potentials and target different tissues.
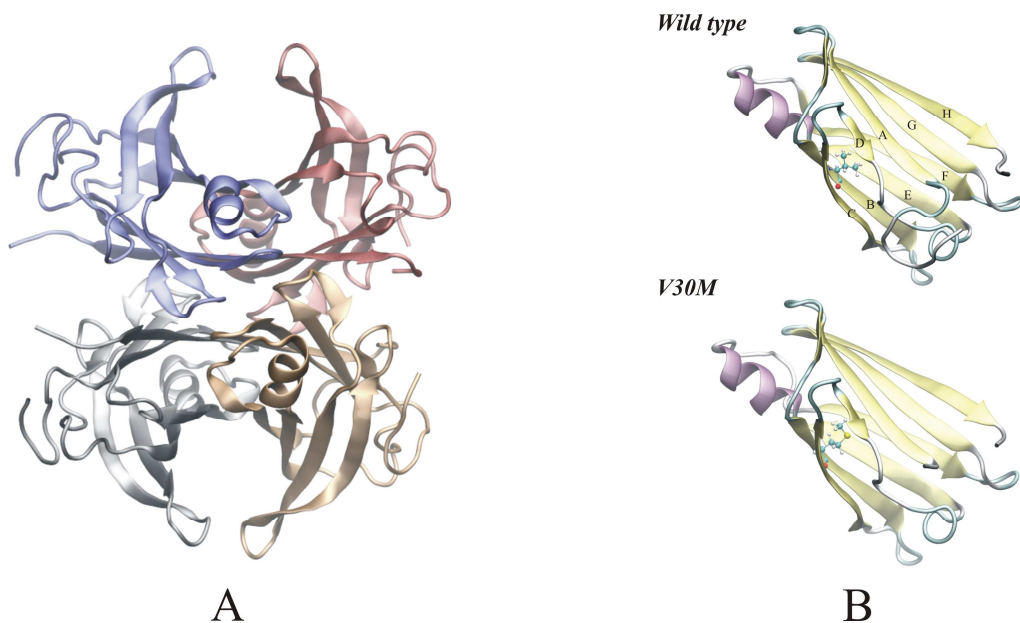
Figure 7.1: (A) Ribbon diagram of the three-dimensional structure of human transthyretin. (B) Schematic representation of the X-ray crystal structures of wild type and V30M subunits of human TTR (PDB entries 1TTA and 3KGT, respectively). TTR subunits are composed by eight β-strands (in yellow) labeled with letters A to H and a small α-helix (in purple). Residue 30, located in β-strand B, is represented in balls-and-sticks.

Several studies have investigated the correlation between the structural stability and aggregation propensity of TTR variants, using either experimental or computational approaches. Previously published results on TTR tetramer stability have shown that WT-, V30M-, L55P-, and the non-amyloidogenic T119M-TTR are highly stable to thermal unfolding (Shnyrov et al. 2000). The tetrameric forms of the amyloidogenic variants present only slightly lower thermodynamic stabilities than the non-amyloidogenic ones. In addition, a number of studies showed that the kinetics of TTR tetramer dissociation do not fully correlate with the amyloidogenic potential of all known TTR variants (Quintas et al. 2001; Hammarström et al. 2002; Brito et al. 2003). In fact, complex tetramer dissociation pathways may also contribute to increase the rate of partitioning of TTR into aggregation

pathways (Babbes et al. 2008). One interesting result from previous work revealed that amyloidogenic TTR variants produce large amounts of partially unfolded monomeric species in solution as a consequence of the low conformational stability of the non-native monomers formed upon TTR dissociation and/or due to high rates of tetramer dissociation (Quintas et al. 1997; Quintas et al. 2001; Babbes et al. 2008). Analysis of molecular dynamics unfolding simulations of WT- and L55P-TTR revealed that the subunits of the amyloidogenic TTR variant does present a much higher probability of forming transient conformations compatible with aggregation and amyloid formation (Rodrigues et al. 2010).

Previous studies on WT-TTR refolding kinetics by Kelly and collaborators (Wiseman et al. 2005) were performed over a relatively wide range of protein concentrations and an unusual 3-step refolding mechanism was proposed. In the present work, protein concentrations within the range observed in physiological conditions were used in order to compare the refolding kinetics of WT- and its amyloidogenic variant V30M-TTR and study how folding rates may affect the TTR amyloidogenic potential.

7.2 Materials and Methods

7.2.1 Protein Sample Preparation

Recombinant WT- and V30M-transthyretin were produced in an *Escherichia coli* expression system (Furuya et al. 1991) and purified as described previously (M. R. Almeida et al. 1997). Protein concentrations were determined spectrophotometrically at 280 nm, using an extinction coefficient of $7.76 \times 10^4 \ M^{-1} \ cm^{-1}$, based on a molecular mass of 55 kDa for TTR $[\varepsilon_{280}(1 \ \%) = 14.1 \ mg^{-1} \ ml \ cm^{-1}]$ (Raz & Goodman 1969). Protein samples were prepared in 20 mM sodium phosphate buffer, 150 mM sodium chloride, at pH 7.0. Guanidinium thiocyanide (GdmSCN), urea, thyroxine (T_4) and all other chemicals were of the highest purity commercially available and were purchased from Sigma-Aldrich Chemical Company, St. Louis, USA.

7.2.2 TTR Denaturation

In order to avoid long exposure times (> 24 hours) to high urea concentrations required for TTR unfolding that may lead to chemical modification of the protein, chemically-induced unfolding of TTR was accomplished in two steps. Protein samples were incubated in 2 M GdmSCN for 12 hours, followed by dialysis against 6 M urea during 10 hours. Once tetramer dissociation and unfolding is achieved by the action of GdmSCN, urea is able to maintain the denatured state. Denaturant solutions were prepared in 20 mM sodium phosphate buffer, 150 mM sodium chloride, at pH 7.0. Stock solutions of GdmSCN were prepared at an approximate concentration of 5.8 M. Freshly prepared 6 M urea stock solutions were employed in all experiments. The concentration of stock solutions of GdmSCN and urea were checked by their refractive index (Pace & Scholtz 1997). These measurements were performed on Automatic Refractometer from Rudolph Research.

7.2.3 Refolding Experiments

WT- and V30M-TTR, denatured as described above, were refolded by dilution into 20 mM sodium phosphate buffer, 150 mM sodium chloride, pH 7.0, to the desired urea and protein concentrations, at 25 ºC. The refolding reaction was allowed to proceed for 12 hours and was monitored by intrinsic fluorescence. Protein refolding experiments were carried out at several urea and protein concentrations. Final concentrations of urea varied between 1.8 - 2.6 M (for WT-TTR experiments) and 0.4 - 1.2 M (for V30M-TTR experiments). To analyse the dependence of refolding kinetics on protein concentration, refolding experiments were performed by using final protein concentrations that varied between 1.0 and 0.1 μM. Fluorescence measurements were performed on a Varian Eclipse spectrofluorometer equipped with a thermostated cell compartment at 25°C, with continuous stirring. Spectra of intrinsic fluorescence of TTR were recorded in the wavelength range of 300 to 420 nm upon excitation at 280 nm. The kinetic traces were collected at 380 nm with excitation at 290 nm, using 10 and 5 nm slit widths for emission and excitation, respectively. A 1.0 cm path length rectangular cell was used for these studies. The refolding experiments were repeated several times and found to be reproducible within experimental errors.

7.2.4 Far-UV Circular Dichroism

Circular dichroism (CD) experiments were performed to monitor the structural transitions that occur during the unfolding and refolding of WT- and V30M-TTR. Far-UV CD spectra were recorded on an OLIS DSM 20 CD spectrophotometer in the wavelength range of 190 to 260 nm, and using a 0.2 mm path length cell. CD spectra of WT- and V30M-TTR were run with a step-resolution of 1 nm, an integration time of 6 s, and using a bandwidth of 0.6 nm. The spectra were averaged over two scans and corrected by subtraction of the corresponding buffer signal. Since solutions containing high concentration of GdmSCN absorb too strongly in the far-UV region, the CD spectra of TTR samples incubated in this denaturant were not recorded. The absorption of urea in the far-UV also restricts the wavelength range of the CD measurements and consequently reliable CD spectra in presence of urea were only collected at wavelengths above 205 nm.

The results are expressed as the mean residue ellipticity $[\Theta]_{MRW}$, defined as $[\Theta]_{MRW} = \Theta_{obs} (0.1MRW)/(lc)$, where Θ_{obs} is the observed ellipticity in millidegrees, MRW is the mean residue weight, c is the concentration in milligrams per millilitre and l is the light path length in centimeters. Final spectra were smoothed using a Savitsky-Golay filter (*OriginPro7* software).

7.2.5 Gel Filtration Chromatography

Refolded species of TTR were characterized by gel filtration chromatography performed on an Amersham Pharmacia Biotech FPLC Superdex-75 HR column, coupled to a Pharmacia P-500 pump and a Gilson UV detector. The column was allowed to equilibrate with 5 column volumes of chromatography buffer (20 mM sodium phosphate, 150 mM sodium chloride, pH 7.0). Final chromatography runs were performed at a flow rate of 0.4 ml/min. Apparent molecular masses were calculated by interpolation on an elution volume *versus* log(molecular mass) calibration curve of four protein standards: bovine serum albumin (66 kDa), carbonic anhydrase (29 kDa), cytochrome *C* (12.4 kDa), and aprotinin (6.5 kDa).

7.2.6 Thyroxine Binding Assays

The native-like behavior of the refolded TTR samples was evaluated by monitoring the ability to bind the natural ligand thyroxine (T_4). Thyroxine binding assays were performed taking advantage of the quenching of the intrinsic protein fluorescence upon thyroxine binding. Stock solutions of T_4 were prepared in 20 mM sodium phosphate buffer, 150 mM sodium chloride, pH 7.0. Concentrations of T_4 solutions were determined spectrophotometrically at 325 nm, using an extinction coefficient of 6.18 x 10^3 M^{-1} cm^{-1} (Edelhoch 1962). Refolded protein samples were dialyzed against 20 mM sodium phosphate buffer, 150 mM sodium chloride, pH 7.0, before the binding assay. Binding assays were performed by adding aliquots of freshly prepared stock solutions of T_4 to the refolded tetramer of TTR, at approximately 1 μM concentration. The final concentrations of T_4 varied between 0.19 and 6.0 μM. Fluorescence measurements were performed on a Varian Eclipse spectrofluorometer with continuous stirring, at 25 ºC. Intrinsic fluorescence of TTR was recorded in the wavelength range of 300 to 420 nm, upon excitation at 280 nm, using 5 and 10 nm slit widths for excitation and emission, respectively. A 0.5 cm path length rectangular cell was used for these studies. The emission fluorescence data at 350 nm were analyzed by nonlinear least-squares fitting, using the software package *OriginPro7* (OriginLab Corporation, USA). Experimental binding curves were fitted using Equation 7.1:

$$y = \Delta F_{max}\left(\frac{1 + K_a[L]_0 + nK_a[C]_0 - \sqrt{\left(-4K_a^2[C]_0[L]_0 + (-1 - K_a[L]_0 - nK_a[C]_0)^2\right)}}{2nK_a[C]_0}\right) \quad (7.1)$$

where ΔF_{max} is the maximum variation in fluorescence intensity, n is the number of equivalent binding sites, K_a is the association constant, and $[C]_0$ and $[L]_0$ are the total protein concentration and the total ligand concentration after each ligand addition, respectively (Wyman & Gill 1990; Klotz 1997).

7.2.7 Refolding Data Analysis

Refolding kinetics curves were constructed using the variation in emission fluorescence upon TTR refolding, at 380 nm. Several refolding kinetic schemes were tested for compatibility with the experimental data. The simplest best-fitting and more likely kinetic model for the refolding and assembly of the TTR tetramer was found to be a simple 2-step mechanism:

$$2M_{Denatured} \xrightarrow{k_1} D \tag{7.2}$$

$$2D \xrightarrow{k_2} T_{Native} \tag{7.3}$$

where M, D and T correspond to monomer, dimer and tetramer, respectively. The system of differential equations associated with this mechanism is:

$$\frac{d[M]}{dt} = -2k_1[M]^2 \tag{7.4}$$

$$\frac{d[D]}{dt} = k_1[M]^2 - 2k_2[D]^2 \tag{7.5}$$

$$\frac{d[T]}{dt} = k_2[D]^2 \tag{7.6}$$

where the brackets indicate the molar concentration of the enclosed species and t is the time in seconds. Conservation of mass dictates that $C = 4[T] + 2[D] + [M]$, where C is the total concentration of protein subunits. Since we are concerned with homotetramer assembly starting from a pool of unfolded monomers, the initial conditions are $[M]_{t=0} = C$ and $[D]_{t=0} = [T]_{t=0} = 0$. Assuming these considerations, the differential equations were solved using the program *Mathematica 4*.2 (Wolfram Research, Inc., USA) to obtain the concentrations of *M*, *D* and *T* over time, which were used in Equation 7.7. The time course of fluorescence change was described by the equation:

$$I_f = f_M[M] + f_D[D] + f_T[T] \tag{7.7}$$

where $I_f(t)$ is the observed fluorescence intensity at time t, and f_T, f_D and f_M are the specific fluorescence intensities of T, D and M, respectively. The equations to obtain the numerical solutions of the differential equations associated with the 2-step folding mechanism described above are presented in Appendix C. The rate constants k_1 and k_2 were obtained by fitting Equation 7.7 to the data, using nonlinear least-squares analysis, and the software package *OriginPro7* (OriginLab Corporation, USA). The final values of k_1 and k_2 were refined until no further significant improvement of the fit was observed, and judged by the distribution of the residuals.

The dependence on urea concentration of the refolding rate constants k_1 and k_2 was fitted to Equation 7.8:

$$\ln k_r = \ln k_r{}^0 + m_r \left[urea \right] \tag{7.8}$$

where k_r is the rate constant for refolding obtained at different urea concentrations, $k_r{}^0$ is the apparent refolding rate constant in the absence of denaturant, and m_r is the refolding rate dependence on urea concentration.

7.3 Results

Previously published results have shown that amyloidogenic and non-amyloidogenic TTR variants dissociate to non-native monomers, with the amyloidogenic variants producing larger amounts of partially unfolded monomeric species as a consequence of the marginal conformational stability of the non-native monomeric state (Quintas et al. 1997; Quintas et al. 1999; Quintas et al. 2001). In this work, we study the refolding kinetics of WT-TTR and its amyloidogenic variant V30M-TTR to investigate if differences in folding rates also play a crucial role in aggregate formation and potentially in amyloidosis.

7.3.1 Examining TTR Conformational Changes upon Denaturation and Refolding

Tetrameric TTR is highly stable and difficult to denature even at high urea concentrations (Hammarström et al. 2001). Thus, to avoid long exposures to urea which may lead to chemical modification of the protein, chemically-induced unfolding of TTR was accomplished by incubating the protein in 2 M GdmSCN for 12 hours. However, preliminary refolding experiments from 2 M GdmSCN showed that complete unfolding and refolding of TTR occurs in a very narrow GdmSCN concentration range (data not shown). In order to study refolding kinetics in a wider range of denaturant concentrations and a larger range of apparent rate constants, protein unfolding was performed in two steps as described in the Materials and Methods section. TTR was first incubated in 2 M GdmSCN for 12 hours, followed by dialysis against 6 M urea during 10 hours. Then, protein refolding experiments were performed by sample dilution to the desired final urea and protein concentrations. To evaluate and optimize the denaturing and refolding conditions, intrinsic tryptophan fluorescence and far-UV CD experiments were used, providing information about changes in tertiary and secondary protein structure, respectively.

Intrinsic protein fluorescence, using tryptophan (Trp) as a reporter, provides a sensitive measure of protein tertiary structure changes and is widely used in protein folding studies. Most proteins, however, possess multiple Trp residues and the overall protein emission, naturally, yields only average information on the protein structure. In these cases, to extract and evaluate the contribution of each reporter, and thereby track the conformational changes occurring in different parts of the macromolecule might be difficult. In particular, TTR has two tryptophan residues in each of its four identical subunits at positions 41 and 79. Trp-79 is located in the single α-helix of the protein positioned between strands E and F, while Trp-41 is located in the loop proximal to the beginning of strand C (see Figure 7.2). Previous studies showed that in the tetrameric form, while Trp-41 has a solvent exposure of 34.1 %, Trp-79 is almost totally buried in the protein interior presenting a solvent exposure of only 1.0 % (Quintas et al. 1999). Moreover, it is also shown that the intrinsic fluorescence exhibited by TTR at pH 7 is mainly due to Trp-41 (Lai et al. 1996; Quintas et al. 1999).
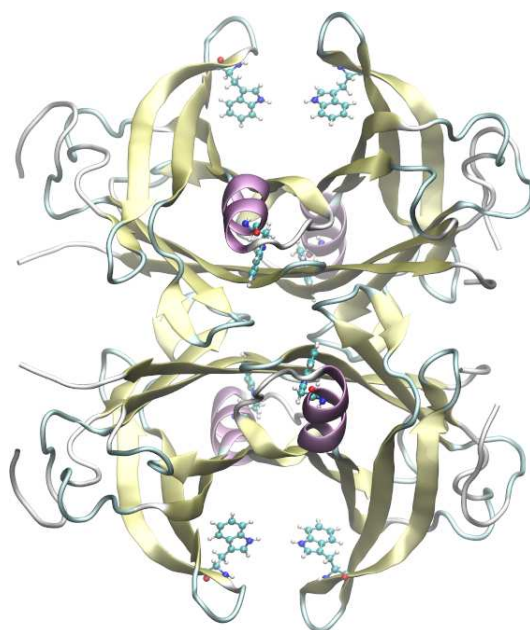
Figure 7.2: Representation of the X-ray crystal structure of wild type human TTR (PDB entry 1TTA) showing the position of the two tryptophan residues in each protein subunit.

Analysis of the intrinsic tryptophan fluorescence spectra in Figure 7.3 revealed that the native tetramers of WT- and V30M-TTR have very similar emission maxima, at approximately 340 nm, characteristic of partially buried tryptophans which in TTR corresponds to Trp-41. A large red-shift in the emission maximum occurs upon TTR unfolding in 2 M GdmSCN (Figure 7.3), due to an increase in solvent exposure of both tryptophans and consequently a less hydrophobic environment around the tryptophan residues in the denatured state. As shown in Figure 7.3, the fluorescence spectrum of both TTR variants incubated in 2 M GdmSCN virtually overlaps the spectrum taken after dialysis against 6 M urea, indicating that urea is able to maintain the GdmSCN-induced denatured state. The fluorescence spectra also show that the refolded species of WT- and V30M-TTR have emission spectra very similar to those of the native tetramers, with emission maxima of approximately 340 nm, indicating that protein refolding was achieved upon urea dilution. These results suggest that the tryptophan residues completely recover their native state of solvent exposure upon refolding, which suggests that both TTR variants regain their native tertiary conformation.
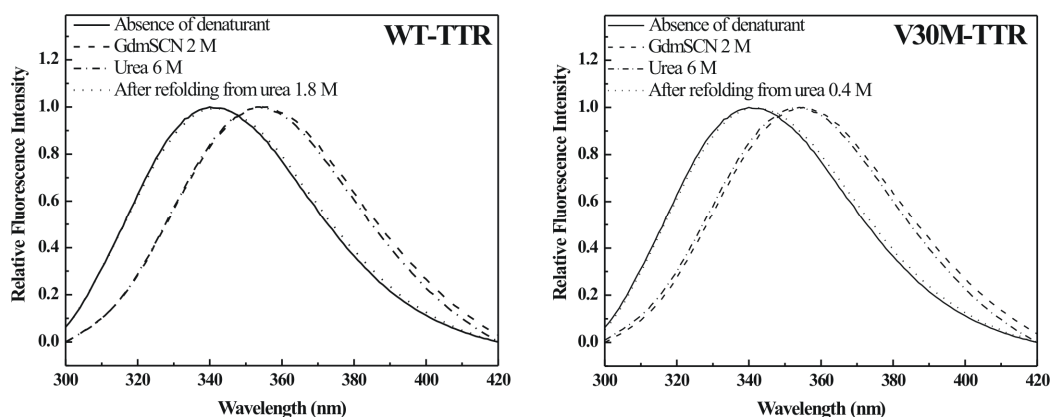
Figure 7.3: Changes in intrinsic tryptophan fluorescence of WT and V30M-TTR in denaturing conditions (2 M GdmSCN and 6 M urea) and after the refolding reaction induced by urea dilution, at pH 7.0 and 25 ℃.

The changes in secondary structure exhibited by WT- and V30M-TTR upon unfolding and refolding in urea were monitored by far-UV CD. As shown in Figure 7.4, both native TTR variants present a CD profile typical of mainly β-sheet proteins, with a single negative band, at approximately 215 nm, and a positive band between 190 - 200 nm. Under urea denaturing conditions, the CD spectra of WT- and V30M-TTR show the appearance of negative peak of greater magnitude around 200 nm accompanied by a significant decrease in intensity at 215 nm, due to the loss of β-sheet structure (Figure 7.4). However, the absorption of urea in the far-UV region restricts the wavelength range of the CD measurements, and thus CD spectra were only collected at wavelengths above 205 nm. Nevertheless, upon dilution of the samples denatured in 6 M urea, the far-UV CD spectra of the refolded WT- and V30M-TTR virtually overlap with the spectra of the native proteins with a single negative band at 215 nm, indicating that after dilution the residual concentration of urea has a negligible effect on the secondary structure of the proteins (Figure 7.4). These results demonstrate that prior to dilution, both TTR variants are largely unfolded in 6 M urea, but the native-like secondary structure of WT- and V30M-TTR is completely recovered upon refolding from urea.
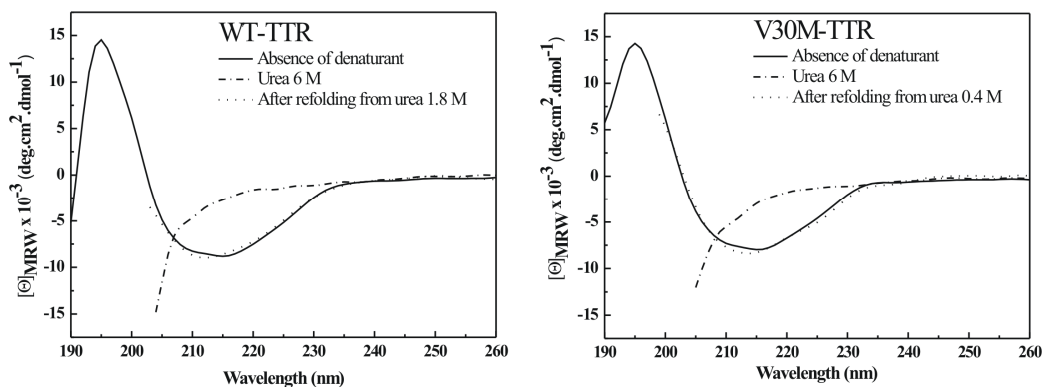
Figure 7.4: Changes in secondary structure of WT and V30M-TTR variants monitored by far-UV CD, in the presence and absence of urea, at pH 7.0 and 25 °C.

7.3.2 Characterization of the TTR Refolded Species

In addition to intrinsic tryptophan fluorescence and far-UV CD, refolded species of WT- and V30M-TTR were characterized by size exclusion chromatography and thyroxine binding assays. Figure 7.5 show size exclusion chromatograms of WT- and V30M-TTR after refolding from urea. The chromatograms show the presence of one major peak (> 95 %), with an elution volume of approximately 22 ml and an apparent molecular mass of 60 kDa, clearly showing the tetrameric nature of the refolded species of WT- and V30M-TTR. Furthermore, the absence in the chromatogram of other molecular species, in any significant amount, indicates that both TTR variants refold to the tetrameric form with a very high yield.
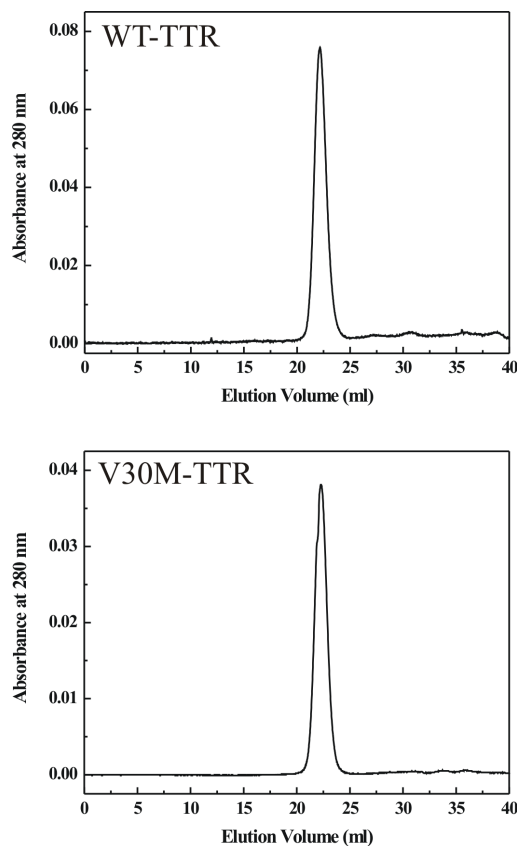
Figure 7.5: Size exclusion chromatograms of WT-TTR and V30M-TTR after protein refolding from 6 M urea, respectively.

Thyroxine binding assays were performed to assess if the refolded tetramers of WT- and V30M-TTR displayed native-like binding properties. Values for the affinity of transthyretins of different species to thyroid hormones have been reported (Chang et al. 1999). The dissociation/association constants for thyroxine binding to TTR have been determined using different pH and temperature conditions and several methods have been applied, such as equilibrium dialysis, fluorescence quenching, gel filtration, immunoadsorption, among many others. Although TTR has two binding sites for thyroxine that sit in a central channel in the interface between the two dimers, it is worth of note that the values obtained by most of these methods report only the affinity of a single strong binding site (Nilsson & Peterson 1971; Chang et al. 1999). As mentioned in the literature, due to the negative cooperativity exhibited by TTR for thyroxine binding, the second binding site present weaker affinity and escaped to detection using these methods that are well suited for reactions of high affinity. On the other hand, it is difficult

to distinguish between two association constants presenting low difference in magnitude. Hence, most of the values published in the literature are apparent association or dissociation constants and it is observed that their values vary greatly both within and between species (Chang et al. 1999). In particular, for the binding of thyroxine to human transthyretin the values of K_d range from 0.3 to 128 nM.

Herein, the measurements of thyroxine binding to TTR were performed by taking advantage of the quenching of TTR intrinsic fluorescence by the ligand. Since the absorption maximum for thyroxine, around 326 nm, overlaps the emission spectrum of tryptphan in TTR, quenching of the tryptophan fluorescence would be expected when trypophan and thyroxine are within less than 50 Å from each other. However, the quenching of the intrinsic fluorescence of TTR is most likely due to deactivation of the TTR fluorophores excited state by the iodine atoms of thyroxine. Several synthetic TTR ligands lacking halogen atoms do not quench the TTR fluorescence upon binding (data not shown), which evidences the role of the iodine atoms in the mechanism of fluorescence quenching (Quintas et al. 1999). Because no shifts in the fluorescence emission maxima are observed, no major conformational changes are expected to occur in TTR upon thyroxine binding, which is also evident from the analysis of the crystal structures of TTR in the absence and presence of thyroxine (Wojtczak et al. 1996). Figure 7.6 shows the isothermal binding curves of thyroxine to WT- and V30M-TTR after the refolding reaction, obtained by plotting the variation of TTR intrinsic fluorescence intensity as a function of thyroxine concentration. The stepwise addition of thyroxine to TTR caused a progressive quenching of tryptophan fluorescence in the protein (inset graphics in Figure 7.6). The apparent association constants (K_a) for T_4 binding were determined by fitting Equation 7.1 to the experimental data (Table 7.1). Previous fluorescence quenching measurements to obtain the affinity of thyroxine for human TTR have reported values raging from 7.8×10^6 M^{-1} to 3.1×10^8 M^{-1} (Nilsson & Peterson 1971; Nilsson et al. 1975; Cheng et al. 1977; Chang et al. 1999). Under our experimental conditions (pH 7.0 and 25 ºC), T_4 binds to WT- and V30M-TTR with apparent association constants of $1.6 \pm 0.2 \times 10^6$ M^{-1} and $1.5 \pm 0.4 \times 10^6$ M^{-1}, respectively (Table 7.1). As shown in Table 7.1, the mean apparent K_a value for both TTR variants was slightly but not significantly reduced upon refolding. Thus, the similarity between the T_4 apparent association constants for native and refolded TTR indicates that both WT- and V30M-TTR refold to the active tetrameric form.
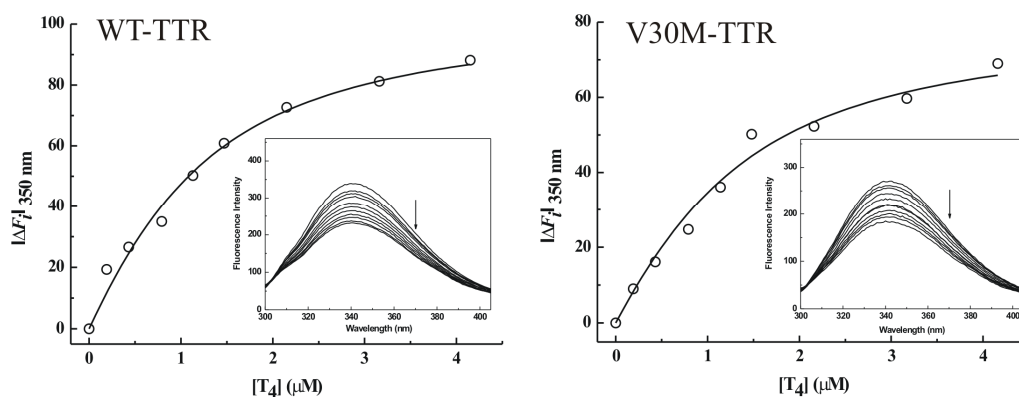
Figure 7.6: Isothermal binding curves of thyroxine to refolded WT- and V30M-TTR monitored by the variation of fluorescence emission at 350 nm. The graphs inset show the intrinsic emission spectra of the protein TTR in the presence of increasing T_4 concentrations.

Table 7.1: The apparent association constant (K_a) of T_4 binding to native and refolded TTR, at pH 7.0 and 25 °C.

	K_a x 10^6 (M^{-1})	
TTR variants	*Native*	*Refolded from 6M urea*
WT	1.6 ± 0.2	1.5 ± 0.3
V30M	1.5 ± 0.4	1.3 ± 0.4

7.3.3 TTR Refolding Kinetics

TTR refolding under urea denaturing conditions is associated with a significant change in the tryptophan residues environment, as revealed by a large blue-shift of approximately 15 nm in the emission maximum (Figure 7.3). Since TTR tryptophan residues are located at the inter-monomer and inter-dimer interface, monitoring the intrinsic tryptophan fluorescence changes seems to be an appropriate methodology to measure folding and assembly kinetics of the native tetramer (Figure 7.2). Refolding kinetics of WT- and V30M-TTR was followed by changes in intrinsic fluorescence at 380 nm upon tryptophan excitation at 290 nm. TTR refolding was initiated by dilution of solutions of unfolded TTR, containing 6 M urea, to the desired final urea and protein concentrations. Figure 7.7 shows typical examples of fluorescence refolding decays for WT- and V30M-TTR. Several kinetic models were tested, such as a single exponential

decay simulating a single-step *(4M → T)* refolding mechanism, but the fits were of poor quality and were discarded. The simplest best fitting kinetic model was found to be a simple 2-step mechanism with one folding intermediate, as represented by Equations 7.2 to 7.7 in the Materials and Methods section. As shown in Figure 7.7, the residuals exhibit random distribution and small dispersion, indicating that the chosen kinetic model is appropriate to describe the refolding mechanism for the TTR variants under analysis. The apparent refolding rate constants for WT- and V30M-TTR, at different final urea concentrations, are shown in Table 7.2. In all experiments, the faster kinetic constant (k_1) is at least one order of magnitude larger than the second kinetic constant (k_2).
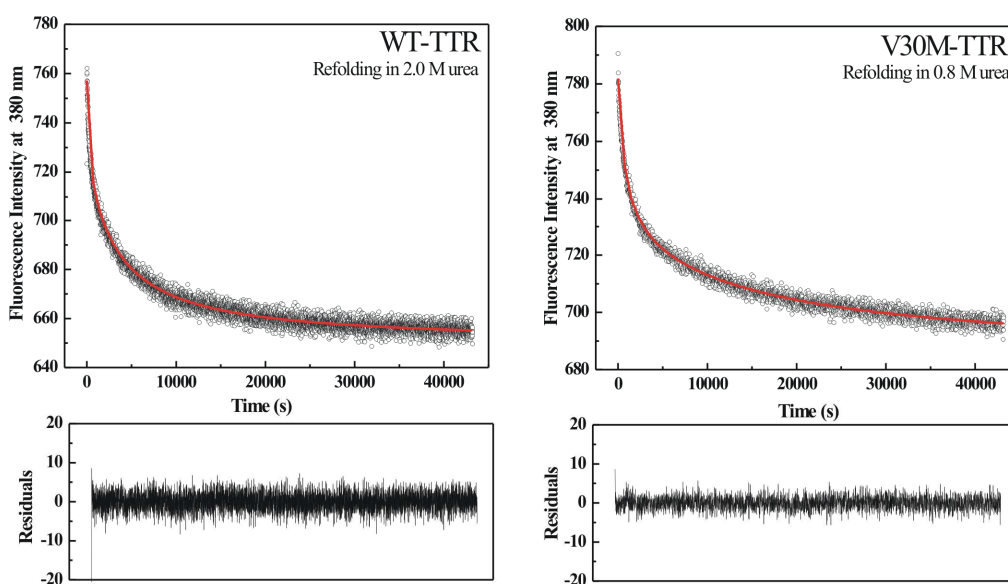
Figure 7.7: Representative kinetic traces of WT- and V30M-TTR refolding monitored by intrinsic fluorescence emission, at different urea concentrations, pH 7.0 and 25 °C. The best fitting curves (solid lines) to the experimental data points were obtained using a 2-step model. These refolding assays were performed at a constant protein concentration of 1 µM. The lower panels show the residuals (the difference between the experimental data and the fitted data for each point).

177

Table 7.2: Refolding rate constants of WT-TTR and its amyloidogenic variant V30M-TTR at a protein concentration of 1 μM (calculated as tetramer).

Dependence of the refolding kinetics on urea concentration[a]			
	Urea Concentration[b] M	$k_1{}^c$ x10^3 $M^{-1}s^{-1}$	$k_2{}^d$ x10^1 $M^{-1}s^{-1}$
WT-TTR	0.4	1.7 ± 0.01	5.7 ± 0.4
	0.6	0.52 ± 0.04	4.0 ± 0.8
	0.8	0.34 ± 0.04	2.8 ± 0.08
	1.0	0.25 ± 0.01	1.7 ± 0.05
	1.2	0.16 ± 0.01	8.0 ± 0.04
V30M-TTR	1.8	3.6 ± 0.02	13.0 ± 0.75
	2.0	0.55 ± 0.01	5.8 ± 0.14
	2.2	0.17 ± 0.01	2.5 ± 0.08
	2.4	0.10 ± 0.01	1.5 ± 0.07
	2.6	0.03 ± 0.004	0.75 ± 0.02
Extrapolation to the absence of denaturant[e]			
		$k_1{}^0$ $M^{-1}s^{-1}$	$k_2{}^0$ $M^{-1}s^{-1}$
WT-TTR		2.2×10^6	8.1×10^3
V30M-TTR		1.8×10^3	1.9×10^2

[a] The refolding rate constants were obtained by fitting Equations 7.4 to 7.7 to the experimental data, at different urea concentrations;
[b] Final urea concentration in the refolding mixture;
[c] k_1 is the rate constant for the initial step of the two-step refolding mechanism, corresponding to the formation of a folding intermediate;
[d] k_2 is the rate constant for the slower step of the refolding mechanism, corresponding to the formation of the native TTR homotetramer;
[e] Apparent refolding rate constants of both TTR variants in the absence of denaturant were obtained by extrapolation of the refolding rates at different urea concentrations and using Equation 7.8 (see Figure 7.9).

The extrapolation of the experimentally determined apparent rate constants for conditions of absence of urea, allows the direct comparison of the folding rates of WT- and V30M-TTR. Plots of the apparent rate constants k_1 and k_2 as a function of urea concentration are shown in Figure 7.8. Each data point is an average of at least three independent measurements, and a linear least-square fit of Equation 7.8 to the data yields

the kinetic constants in the absence of urea (Table 7.2). The rate constants for V30M-TTR refolding in the absence of urea are significantly lower than those for WT-TTR: k_1 is three orders of magnitude lower, and k_2 is 40-fold smaller. In both cases, the kinetic constants k_1 and k_2 show similar dependence on urea concentration, suggesting that both kinetic phases might correspond to reactions analogous in nature, for example hiding of hydrophobic surfaces. In addition, there are no experimental evidences to suggest that the TTR refolding pathway may include rate-limiting processes such as proline isomerization (Bodenreider et al. 2002), because in general these kinetic steps present weaker or even no dependence on denaturant concentration.
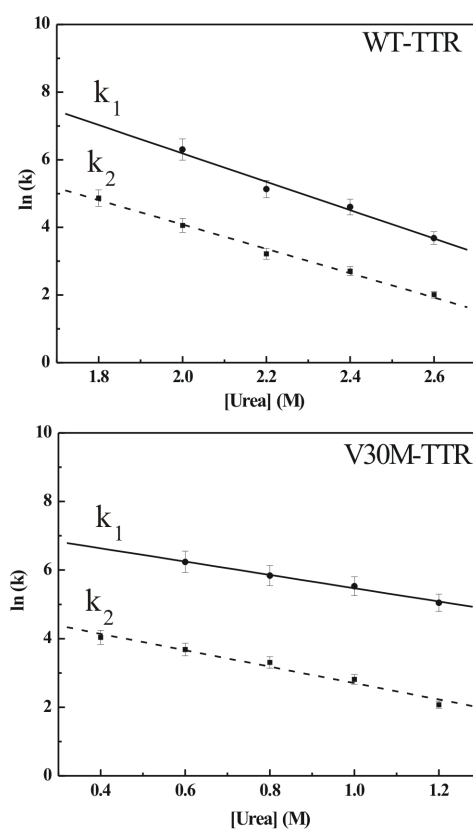
Figure 7.8: Urea dependence of the refolding rate constants WT-TTR and V30M-TTR, measured by intrinsic fluorescence at 380 nm, pH 7.0 and 25 ºC. The plotted rate constants are an average of at least three independent experiments. The symbols (●) and (■) represent the values of k_1 and k_2 for each urea concentration, respectively. The solid and dashed lines are the linear least-squares fits for k_1 and k_2, respectively.

7.4 Discussion

Most amyloid diseases are caused by extracellular cytotoxic protein aggregates produced by non-native protein conformations. Thus, issues like protein conformational stability, and protein unfolding and refolding kinetics which determine the ensemble of non-native partial unfolded conformations accessible to a protein, may be crucial for amyloidogenesis (Brito et al. 2003). In the case of TTR, a tetrameric protein, additional factors like tetramer dissociation kinetics (Hammarström et al. 2002) and subunit conformational stability (Quintas et al. 2001; Rodrigues et al. 2010) have been shown to play a role.

Herein, we compare the refolding kinetics of the tetrameric protein transthyretin WT-TTR and one of its most common amyloidogenic mutants V30M-TTR. The experiments were carried out at relatively low protein concentrations, within the observed physiological levels, which range between 3.6 μM in the plasma and 0.31 μM in the cerebral spinal fluid (Vatassery et al. 1991). Since TTR has two tryptophan residues per subunit and they are located at the interfaces monomer-monomer and dimer-dimer, the changes in intrinsic fluorescence may report not only the folding but also the assembly of the TTR tetramer. Thus, we monitored protein refolding following intrinsic fluorescence changes, a direct method, to measure the disappearance of the unfolded monomers in solution. The kinetic results obtained suggest that the simplest and most likely model for folding and assembly of both TTR variants is consistent with the pathway *4M → 2D → T*. This model can be justified based on the following observations: *(i)* the refolding kinetics obtained for both TTR variants fit well to a 2-step process, indicating the presence of a single folding intermediate (Figure 7.7); *(ii)* Similar dependence on denaturant concentration was observed for both kinetic steps which indicate that these two phases may be describing processes of similar nature like for example the progressive hiding of hydrophobic surfaces (Figure 7.8); *(iii)* At the denaturing conditions used, both TTR variants completely unfold as shown by changes in the TTR intrinsic fluorescence and far-UV CD (Figure 7.4); *(iv)* The native TTR tetramer is the main product of refolding, as revealed by its spectroscopic and binding properties (fluorescence, far-UV CD, molecular mass and thyroxine binding) (Figure 7.3, Figure 7.4 and Figure 7.5). In addition to the intrinsic tryptophan fluorescence refolding experiments, the refolding profiles of both TTR variants were analyzed by transverse urea gradient gel electrophoresis (Jesus et al. 2013).

This technique provides useful information about the kinetics of the refolding transition as well as the presence of any folding intermediate state in this transition (Goldenberg 1997; Goldenberg & Creighton 1984; Creighton 1986; Siddiqui & Francisci 2007). Briefly, the urea gradient gel electrophoresis refolding patterns have shown that a single unfolded state is preferred at the higher urea concentrations as well as the single band with constant electrophoretic mobility detected at low urea concentrations is consistence with the presence of a single main product of refolding, which corresponds to the TTR tetramer. These refolding patterns also suggest both TTR variants refold through a 2-step mechanism, thus an intermediate may be involved. Thus, the urea gel electrophoresis results are in very good agreement with the data obtained from protein intrinsic fluorescence, chromatography and far-UV CD and further corroborate the previous observations *(i), (iii) and (iv)*. The proposed TTR refolding model is consistent with all the results described above (Figure 7.9).
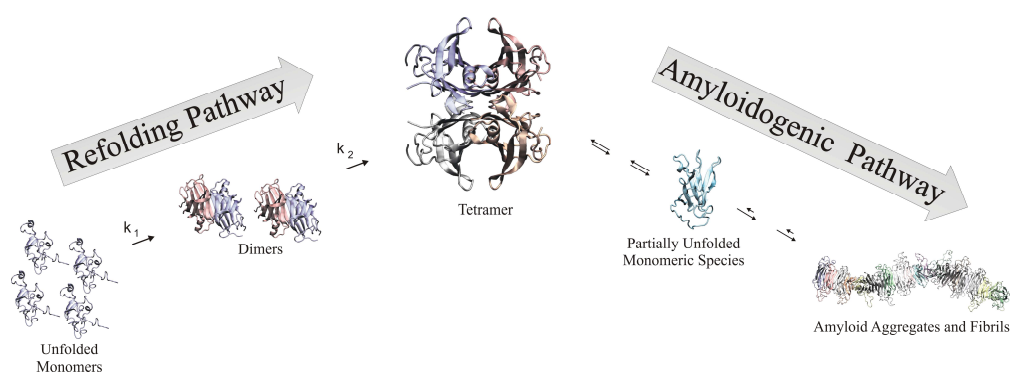
Figure 7.9: Schematic representation of transthyretin folding and amyloidogenesis. In denaturing conditions, native tetrameric TTR dissociates and unfolds to unfolded monomers. At physiologically relevant protein concentrations, we show that the simplest best-fitting refolding model involves the presence of a dimeric intermediate. TTR may alternatively present amyloidogenic behavior, characterized by the dissociation of the native tetramer to non-native monomers, which in turn depending on their conformational stability may undergo partial unfolding leading to aggregate formation and eventually amyloid assembly.

The folding mechanisms of a number of other homotetrameric proteins have been studied by several authors and in all cases, folding and assembly were postulated to occur *via* a Monomer (M) - Dimer (D) - Tetramer (T) pathway (MDT mechanism). Among these, are dihydrofolate reductase (Bodenreider et al. 2002), the potassium channel Kv1.3

(Tu & Deutsch 1999), p53 (Mateu et al. 1999), β-galactosidase (Nichtl et al. 1998), pyruvate oxidase (Risse et al. 1992), glyceraldehyde-3-phosphate dehydrogenase (Rehaber & Jaenicke 1992), human platelet factor 4 (Chen & Mayo 1991), phosphofructokinase (Le Bras et al. 1989), phosphoglycerate mutase (Hermann et al. 1983; Hermann et al. 1985), and lactate dehydrogenase (Bernhardt et al. 1981; Hermann et al. 1981). Kelly and collaborators have previously performed refolding kinetic studies of WT-TTR following tetramer assembly through binding of a fluorescent compound and using a wide TTR concentration range (0.72 – 36 μM in monomer) (Wiseman et al. 2005). To fit the data over such a wide protein concentration range, the authors postulated a more complex folding mechanism involving a Monomer (M) - Dimer (D) - Trimer (R) - Tetramer (T) pathway (MDRT mechanism). However, the authors suggested that at low protein concentrations, the simpler and more common MDT mechanism could occur (Wiseman et al. 2005). Furthermore, it has been pointed out that while for the MDT mechanism the tetramer is inevitably the end product, this is not necessarily true for the MDRT mechanism, since the protein may be trapped in intermediate oligomeric states (Powers & Powers 2003). Our kinetic data fits extremely well (with very low residuals) the conventional MDT mechanism, in accordance with what has been postulated for many other homotetrameric proteins. Thus, it can be affirmed that the refolding mechanism of WT- and V30M-TTR, at physiologically relevant protein concentrations, comprises a single oligomeric intermediate, dimeric in nature. The formation of this intermediate corresponds to the initial fast step represented by the kinetic constant k_1. This fast process is followed by a slower step which probably corresponds to the final assembly of the homotetramer, and it is represented by the kinetic constant k_2. Moreover, the refolding patterns obtained in urea gradient gel electrophoresis for WT and V30M-TTR are also consistent with the presence of only one folding intermediate (Jesus et al. 2013). If any additional steps exist, such as dimer or tetramer conformational rearrangements before the native state is reached, they should be either very rapid and hence appear coupled to the association process, or be spectroscopically silent.

Despite the common refolding mechanism that WT- and V30M-TTR share, refolding of the WT protein is significantly faster. Extrapolation of the refolding constants to 0 M urea (Table 7.2) shows that the first step in the refolding mechanism is 3 orders of magnitude faster for WT-TTR, and the second step is more than 40-fold faster. In particular, the WT-TTR the refolding the rate of the first step (Table 7.2) is comparable to that of other tetrameric proteins forming a dimeric intermediate (Mateu et al. 1999; Mehl

et al. 2012).The differences in refolding rate constants observed between TTR variants translate in very significant differences in refolding half-lives of approximately 113 ms for WT-TTR and 132 s for its amyloidogenic variant V30M-TTR, at 1μM. Furthermore, on a qualitative basis, the results of urea gradient gels electrophoresis experiments also support this conclusion since the refolding transition of V30M-TTR observed in our study appears to be slower than WT-TTR on the time scale of the electrophoresis (Jesus et al. 2013). The observed difference in refolding kinetics between the two proteins is probably directly coupled with the reduced conformational stability of the V30M-TTR monomeric subunits, as previously reported (Quintas et al. 2001). This is also suggested by the urea concentration dependence of the refolding assays where complete refolding is observed for WT-TTR at a higher urea concentration range than for V30M-TTR (Table 7.2). Knowing that in most amyloidoses, amyloid deposition occurs extracellularly, and might be a consequence of unfolding - misfolding events, the much slower refolding times presented by the amyloidogenic variant V30M-TTR might be of critical importance for amyloid formation *in vivo*. The slower rate at which tetramer assembly occurs for the amyloidogenic variant, might facilitate the accumulation of monomers in the extracellular environment, which could result in preferential kinetic partition into aggregation pathways instead of native refolding.

In conclusion, here we showed that, at physiologically relevant protein concentrations, the refolding pathway of WT-TTR, and of the amyloidogenic variant V30M-TTR, follow a common mechanism observed among tetrameric proteins: 4 Monomers → 2 Dimers → Tetramer. We also show the assembly of the native homotetramer is kinetically much more favourable for the WT protein than for the amyloidogenic variant, despite their high three-dimensional structural similarity. Since, *in vivo,* amyloidogenesis might be viewed as a question of protein stability and protein unfolding followed by kinetic partition between refolding and aggregation, the longer refolding times observed for V30M-TTR might increase the probability of formation of non-native intermediate monomeric species prone to aggregation, which in turn would decrease the extent of native refolding. The different refolding times together with different protein concentrations in distinct physiological states may be an important factor to explain the selective formation of TTR amyloid fibrils, in different tissues by different TTR variants.

7.5 Future Work

In the present work, we have investigated the effect of the amyloidogenic single point mutation V30M on the rate of TTR folding. Interestingly, the significant differences observed on the folding rates of both TTR variants appear to be of critical importance and seem to be correlated with their propensity for amyloid formation. Nevertheless, a wider range of protein concentrations need to be investigated in order to obtain evidences of the dependence between rate constants and protein concentration and further clarify the presence of intermediates on the refolding pathway.

Clearly, specific mutations, such as V30M, play an important role and hamper the TTR refolding reaction, but the link between this and the type or location of different mutations needs further clarification. Careful comparison of refolding pathways of multiple variants, such as the aggressive L55P- variant, the highly amyloidogenic mutation Y78P- located in the α-helix, the variant V122I- which produces strong cardiomyopathy effects or even the T119M- mutation that is a very stable and non-amyloidogenic variant, may help in the future to clarify the relation between protein folding and amyloid formation.

Chapter 8

General Discussion & Conclusions

The detailed knowledge of the molecular mechanisms driving protein folding and unfolding is essential to understand problems as diverse as the development of amyloid diseases, protein function or protein structure prediction from gene sequences. The search and identification of factors governing the acquisition of the functional three-dimensional structure of a protein from its linear sequence of amino acids is one of the central challenges in the field of biophysical chemistry. An important goal of protein folding is to quantitavely predict the contributions of amino acid sequence, pH, temperature, and salt concentration to kinetics and thermodynamics of the protein folding/unfolding process. To achieve this goal it is of critical importance the development of new methodologies and instrumentation. In the last decades, a new generation of kinetic experiments has emerged to investigate the mechanisms of protein folding on the previously inaccessible sub-millisecond time scale. As a result, the earliest conformational events related to folding, such as β-hairpin and α-helix formation, occurring within microseconds or less may be now measured experimentally and interpreted. In this work, we proposed to use a pH-jump methodology to trigger the folding/unfolding events, coupled with TR-PAC to monitor the energetics and kinetics of pH-dependent folding/unfolding of peptides and proteins. Since the protonation of amino acid residues in a polypeptide chain is the earliest event in pH-dependent unfolding/folding process, we first characterized in detail the protonation of amino acid models. In a second stage, pH-dependent conformational changes of a small α-helix peptide were studied and in a latter stage the studies of TR-PAC were applied to investigate the partial unfolding of a mainly α-helical protein.

Amino acids are found in all naturally occurring proteins or peptides, which play a vital role in nearly all chemical and biological processes. The structure, stability, solubility and function of proteins depend on their net charge and on the ionization state of the

individual amino acids that constitute those proteins. Thus, it is of critical importance fully understand the contribution of protonation reactions involving ionizable amino acids in protein folding. In the present work, the amino acid model compounds studied were Ac-Glu-NH_2, Ac-Asp-NH_2 and Ac-His-NHMe, which represent two types of ionizable side chains. While in Ac-His-NHMe the proton-accepting group is the uncharged imidazole ring, in Ac-Asp-NH_2 and Ac-Glu-NH_2 the protonation occur on the negatively charged carboxylic groups. The neutralization of amino acid models, such as Ac-Glu-NH_2 and Ac-Asp-NH_2, involves the disappearance of two charges that is accompanied by a volume expansion of 3.7 ml mol^{-1} (~6 $Å^3$) for Ac-Glu-NH_2 and 6.2 ml mol^{-1} (~10 $Å^3$) for Ac-Asp-NH_2, as determined by the two-temperature method in TR-PAC experiments. On the contrary, protonation of the imidazole ring of Ac-His-NHMe involves a volume contraction of approximately -4.4 ml mol^{-1} (~7 $Å^3$) (two-temperature method). Slight differences in the volume changes were observed when applying the multiple-temperature method. The bimolecular protonation rates of carboxylic acids (~2.5 x 10^{10} $M^{-1}s^{-1}$) and imidazole (1.4 x 10^9 $M^{-1}s^{-1}$) are significantly different, being the protonation of imidazole a slower reaction. In addition, our results have shown that the presence of 100 mM NaCl contributes for the reduction in the reaction volume changes as well as in the protonation rates due to an increase in the ionic strength of the solution. Since the polypeptide chains of proteins or peptides are formed by different ionizable amino acid residues, mixtures of Ac-Glu-NH_2 and Ac-His-NHMe at different concentration ratios were also studied. The photoacoustic waves were analyzed using three processes to distinguish the *o*-NBA photolysis and the subsequent protonation reactions of Ac-Glu-NH_2 and Ac-His-NHMe. Although the protonation of amino acid models should be best characterized assuming parallel reactions because the protons released by *o*-NBA can bind to either Ac-Glu-NH_2 or Ac-His-NHMe, using the *CPAC* software and fitting to three sequential exponential processes it was possible to distinguish the protonation of each amino acid model because their kinetics are significantly different. In the future, we intend to further examine other ionizable amino acids. Two other common ionizable amino acids are lysine (Lys) and arginine (Arg), using the laser-induced pH jump coupled to TR-PAC to determine the parameters associated with their protonation such as volume changes, enthalpy and kinetics. Another interesting ionizable amino acid is cysteine (Cys), which is capable to react with other cysteine in the protein polymer, thus forming a disulfide bridge that provides enhanced stability to the three-dimensional structure of a protein.

Since the discovery of significant helicity in the 13 amino acid C-peptide from RNase A, there has been a considerable amount of research on helicity of *de novo* peptides. Peptides ranging from 12 to 30 residues have been studied to understand the interplay between side chain interactions, the helix dipole, and the intrinsic helix-forming ability of each amino acid. In the present work, the folding kinetics of the shortest peptide sequence forming a α-helix in an aqueous solution has been a subject of study. RN80 is a 13 amino acid synthetic peptide analogue of the C-peptide from the protein RNase A. Our NMR and CD results indicate that RN80 adopts an α-helical structure and undergoes pH-dependent transitions upon protonation of Glu-2 and His-12. Furthermore, these techniques reveal that the pH-dependence curve of RN80 α-helix formation is bell-shaped with a maximum near pH 5 and the main forces stabilizing this short peptide are the salt-bridge formed between Glu-2 and Arg-10 and the π-stacking interaction involving His-12 and Tyr-8. The protonation of His-12 is the main factor contributing for the increase of RN80 helicity, because the π-stacking interaction between His-12 and Tyr-8 is stronger when the imidazole is charged. On the other hand, the protonation of Glu-2 induces α-helix partial unfolding due to the disruption of the salt bridge between Glu-2 and Arg-10. Thus, RN80 peptide contains two ionizable amino acid residues that seem to play a fundamental role on α-helix formation, namely Glu-2 and His-12 and their protonation correspond to the earliest event occuring in pH-dependent conformational transitions.

Although using the prepulse pH 7.3, it was not possible to identify a folding event following the protonation of His-2 occuring on the nanosecond time scale, the photoacoustic waves recorded at pH 5.3 were well fitted using three sequential exponential processes. When the prepulse pH is 5.3, the photolysis of *o*-NBA is followed by the protonation of Glu-2 residues, which is characterized by a volume expansion of 3.0 ml mol^{-1} (~5 Å^3) and the bimolecular constant (k_b) yield a value of approximatelly 7×10^9 M^{-1}s^{-1}. This second process is concentration-dependent which is consistent with protonation reactions and the value of k_b is similar to that observed for carboxylic acids in amino acid models such as Ac-Glu-NH$_2$, in the presence of 100 mM NaCl. The third process corresponds to a concentration-independent volume expansion of 0.77 ml mol^{-1} (~ 1.3 Å^3) and a lifetime of approximately 369 ns, representing an unimolecular process related to the α-helix unfolding due to disruption of the salt bridge between Glu-2 and Arg-10. The sign of volume change associated with the unfolding event due to protonation of Glu-2 of RN80 is positive corresponding thus to a volume expansion. It is likely that the

volume change measured is representative of a conformational change in short peptides. Preliminary photoacoustic measurements performed using a 0.5 MHz transducer allowed the characterization of the RN80 folding upon protonation of His-12. Our results suggest that the folding of RN80 peptide is accompanied by a volume contraction of approximately 6 ml mol^{-1} (~10 Å^3) and occurs within 1.5 and 2 μs. In the future, photoacoustic studies of other secondary structure elements, such as β-harpins, may be of particular interest to investigate the effect of protonation of ionizable amino acid residues on the folding and stability of β-structures.

Bovine serum albumin (BSA) is a mainly α-helical protein that was selected as a system model to explore α-helix unfolding in proteins upon protonation of ionizable amino acid residues. BSA is a highly charged protein with more than 180 charges at pH 7, among them 39 aspartic acids and 59 glutamic acids and undergoes pH-dependent conformational transitions upon a decrease in pH. However, only a fraction of carboxylic acid side chains are solvent exposed and have the pK_a between pH 5 and 4. Using the two-temperature method and a 2.25 MHz transducer, our results suggest that at least 6 Asp or Glu residues are protonated. Although no unfolding event measurable within the nanosecond time scale was detected, preliminary TR-PAC results on the microsecond time scale allowed the identification of a slow unfolding event characterized by a lifetime within 1 to 1.6 μs that leads to a volume expansion of 2.3 ml mol^{-1} (3.8 Å^3). Interestingly, our results have shown that the protonation of Asp and/or Glu residues induce unfolding events that are characterized by a volume expansion not only in the protein BSA, but also in the RN80 peptide. In the future, other proteins with smaller polypeptide lengths exhibiting a pH-dependent folding/unfolding profile will be selected to explore the kinetics and volume changes upon protonation of Asp and Glu residues. As an example, human interleukin-4 (IL-4) undergoes a partial unfolding transition at low pH, losing a small fraction of α-helical content (Redfield et al. 1994).

Abnormal protein aggregation into highly structured oligomers and insoluble fibrils, known as amyloid, is the hallmark of several neurodegenerative diseases, such as Alzheimer's disease, and Parkinson's disease. The neurodegenerative amyloid pathology Familial Amyloidotic Polyneuropathy (FAP) is a peripheral neuropathy with a high mortality rate which is characterized by extracellular deposition of amyloid fibrils mostly constituted by variants of transthyretin (TTR). Amongst TTR variants, V30M is the most prevalent amyloidogenic variant and L55P yields the most aggressive symptoms. It is known today that amyloid formation by TTR is preceded by tetramer dissociation and

partial unfolding of the resulting low stability monomers. Thus, multiple physico-chemical factors, chief among them, tetramer dissociation kinetics, monomer conformational stability, and aggregation kinetics do play a critical role in TTR amyloidogenesis. Accordingly, the characterization of potential differences in the folding kinetics of WT-TTR and some of its variants may provide important clues for the understanding of how different TTR variants have different amyloidogenic potentials and target different tissues. In the present work, low protein concentrations, within the range observed in physiological conditions, were used in order to compare the refolding kinetics of WT- and its amyloidogenic variant V30M-TTR and understand how folding rates may affect the TTR amyloidogenic potential. Here we showed that, at physiologically relevant protein concentrations, the refolding pathway of WT-TTR, and of the amyloidogenic variant V30M-TTR, follow a common mechanism observed among tetrameric proteins: 4 Monomer → 2 Dimers → Tetramer. We also showed that the assembly of the native homotetramer is kinetically much more favourable for the WT protein than for the amyloidogenic variant, despite their high three-dimensional structural similarity. Interestingly, the significant differences observed on the folding rates of both TTR variants appear to be of critical importance and seem to be correlated with their propensity for amyloid formation. V30M-TTR monomers seem to have a significantly lower tendency to refold and thus aggregation-prone monomeric conformations may be favoured.

References

Abbruzzetti, S., Crema, E., Masino L., Vecli, A., Viappiani, C., Small, J. R., Libertini, L. J., Small, E. W., 2000. Fast events in protein folding: structural volume changes accompanying the early events in the N-->I transition of apomyoglobin induced by ultrafast pH jump. *Biophysical Journal*, 78(1), pp.405–415.

Abbruzzetti, S., Sottini, S., Viappiani, C., Corrie, J. E. T., 2006. Acid-induced unfolding of myoglobin triggered by a laser pH jump method. *Photochemical & Photobiological Sciences*, 5(6), pp.621–628.

Abbruzzetti, S., Viappiani C., Murgida, D. H., Erra-Balsells, R., Bilmes, G. M., 1999. Non-toxic, water-soluble photocalorimetric reference compounds for UV and visible excitation. *Chemical Physics Letters*, 304(3-4), pp.167–172.

Abbruzzetti, S., Viappiani, C., Small, J. R., Libertini, L. J., Small, E. W., 2000. Kinetics of local helix formation in poly-L-glutamic acid studied by time-resolved photoacoustics: neutralization reactions of carboxylates in aqueous solutions and their relevance to the problem of protein folding. *Biophysical Journal*, 79(5), pp.2714–2721.

Almeida, M. R., Damas, A. M., Lans, M. C., Brouwer, A., Saraiva, M. J., 1997. Thyroxine binding to transthyretin Met 119. Comparative studies of different heterozygotic carriers and structural analysis. *Endocrine*, 6(3), pp.309–315.

Anfinsen, C. B., 1973. Principles that govern the folding of protein chains. *Science*, 181(4096), pp.223–230.

Arata, H. & Parson, W. W., 1981. Delayed fluorescence from Rhodopseudomonas sphaeroides reaction centers. Enthalpy and free energy changes accompanying electron transfer from P-870 to quinones. *Biochimica et Biophysica Acta (BBA) - Bioenergetics*, 638(2), pp.201–209.

Arnaut, L. G. & Pineiro, M., 2003. Two-photon photoacoustic calorimetry and the absolute measurement of molar absorption coefficients of transient species in solution. *Photochemical & Photobiological Sciences*, 2(7), pp.749–753.

Arnaut, L. G. Caldwell, R. A., Elbert, J. E., Melton, L. A., 1992. Recent advances in photoacoustic calorimetry: Theoretical basis and improvements in experimental design. *Review of Scientific Instruments*, 63(11), pp.5381–5389.

Atkins, P. & Jones, L., 1999. *Chemical Principles: the quest for insight*, W. H. Freeman and Company.

Baldwin, R. L., 1989. How does protein folding get started? *Trends in Biochemical Sciences*, 14(7), pp.291–294.

Barth, A. & Zscherp, C., 2000. Substrate binding and enzyme function investigated by infrared spectroscopy. *FEBS Letters*, 477(3), pp.151–156.

Barth, A., 2000. The infrared absorption of amino acid side chains. *Progress in Biophysics and Molecular Biology*, 74(3-5), pp.141–173.

Bartlett, A. I. & Radford, S. E., 2009. An expanding arsenal of experimental methods yields an explosion of insights into protein folding mechanisms. *Nature Structural & Molecular Biology*, 16(6), pp.582–588.

Bax, A. & Davis, D.G., 1985. Practical aspects of two-dimensional transverse NOE spectroscopy. *Journal of Magnetic Resonance (1969)*, 63(1), pp.207–213.

Bell, A.G., 1881. The Production of Sound by Radiant Energy. *Science*, 2(49), pp.242–253.

Bernhardt, G., Rudolph, R. & Jaenicke, R., Reassociation of lactic dehydrogenase from pig heart studied by cross-linking with glutaraldehyde. *Zeitschrift für Naturforschung. Section C: Biosciences*, 36(9-10), pp.772–777.

Bertucci, C. & Domenici, E., 2002. Reversible and covalent binding of drugs to human serum albumin: methodological approaches and physiological relevance. *Current Medicinal Chemistry*, 9(15), pp.1463–1481.

Bhattacharya, A. A., Curry, S. & Franks, N. P., 2000. Binding of the general anesthetics propofol and halothane to human serum albumin. High resolution crystal structures. *The Journal of Biological Chemistry*, 275(49), pp.38731–38738.

Bierzynski, A., 1982. A Salt Bridge Stabilizes the Helix Formed by Isolated C-Peptide of RNase A. *Proceedings of the National Academy of Sciences*, 79(8), pp.2470–2474.

Blake, C. C., Geisow, M. J., Oatley, S. J., Rérat, B., Rérat, C., 1978. Structure of prealbumin: secondary, tertiary and quaternary interactions determined by Fourier refinement at 1.8 Å. *Journal of Molecular Biology*, 121(3), pp.339–356.

Blanco, F. J., Rivas, G. & Serrano, L., 1994. A short linear peptide that folds into a native stable beta-hairpin in aqueous solution. *Nature Structural Biology*, 1(9), pp.584–590.

Bodenreider, C., Kellershohn, N., Goldberg, M. E., Méjean, A., 2002. Kinetic analysis of R67 dihydrofolate reductase folding: from the unfolded monomer to the native tetramer. *Biochemistry*, 41(50), pp.14988–14999.

Bonetti, G., Vecli, A. & Viappiani, C., 1997. Reaction volume of water formation detected by time-resolved photoacoustics: photoinduced proton transfer between o-nitrobenzaldehyde and hydroxyls in water. *Chemical Physics Letters*, 269(3-4), pp.268–273.

Borsarelli, C. D. & Braslavsky, S. E., 1998. Volume Changes Correlate with Enthalpy Changes during the Photoinduced Formation of the 3MLCT State of Ruthenium(II) Bipyridine Cyano Complexes in the Presence of Salts. A Case of the Entropy–Enthalpy Compensation Effect. *The Journal of Physical Chemistry B*, 102(32), pp.6231–6238.

Brahma, A., Mandal, C. & Bhattacharyya, D., 2005. Characterization of a dimeric unfolding intermediate of bovine serum albumin under mildly acidic condition. *Biochimica et Biophysica Acta*, 1751(2), pp.159–169.

Braslavsky, S. E. & Heibel, G. E., 1992. Time-resolved photothermal and photoacoustic methods applied to photoinduced processes in solution. *Chemical Reviews*, 92(6), pp.1381–1410.

Bredenbeck, J., Helbing, J., Kumita, J. R., Woolley, G. A., Hamm, P., 2005. Alpha-helix formation in a photoswitchable peptide tracked from picoseconds to microseconds by time-resolved IR spectroscopy. *Proceedings of the National Academy of Sciences of the United States of America*, 102(7), pp.2379–2384.

Brito, R. M. M., Damas, A. M. & Saraiva, M. J., 2003. Amyloid Formation by Transthyretin: From Protein Stability to Protein Aggregation. *Current Medicinal Chemistry - Immunology, Endocrine & Metabolic Agents*, 3(4), pp.349–360.

Brockwell, D. J. & Radford, S. E., 2007. Intermediates: ubiquitous species on folding energy landscapes? *Current Opinion in Structural Biology*, 17(1), pp.30–37.

Brockwell, D. J., Smith, D. A. & Radford, S. E., 2000. Protein folding mechanisms: new methods and emerging ideas. *Current opinion in structural biology*, 10(1), pp.16–25.

Buchner, G. S., Murphy, R. D., Buchete, N-V., Kubelka, J., 2011. Dynamics of protein folding: probing the kinetic network of folding-unfolding transitions with experiment and theory. *Biochimica et Biophysica Acta (BBA)*, 1814(8), pp.1001–1020.

Callis, J. B., Parson, W. W. & Gouterman, M., 1972. Fast changes of enthalpy and volume on flash excitation of Chromatium chromatophores. *Biochimica et Biophysica Acta (BBA) - Bioenergetics*, 267(2), pp.348–362.

Cardamone, M. & Puri, N. K., 1992. Spectrofluorimetric assessment of the surface hydrophobicity of proteins. *The Biochemical Journal*, 282, pp.589–593.

Carter, D. C. & Ho, J. X., 1994. Structure of serum albumin. *Advances in Protein Chemistry*, 45, pp.153–203.

Carvalho, C. P., Uzunova, V. D., Da Silva, J. P, Nau, W. M., Pischel, U., 2011. A photoinduced pH jump applied to drug release from cucurbit[7]uril. *Chemical Communications*, 47(31), pp.8793–8795.

Causgrove, T. P. & Dyer, R. B., 2006. Nonequilibrium protein folding dynamics: laser-induced pH-jump studies of the helix–coil transition. *Chemical Physics*, 323(1), pp.2–10.

Cavanagh, J., Fairbrother, W. J., Palmer, A. G., Skelton, N. J., 1995. *Protein NMR Spectroscopy: Principles and Practice*, Academic Press.

Chakrabarty, A., Purkayastha, P. & Chattopadhyay, N., 2008. Laser induced optoacoustic spectroscopy of benzil: evaluation of structural volume change upon photoisomerization. *Journal of Photochemistry and Photobiology A: Chemistry*, 198(1–2), pp.256–261.

Chang, L. Munro, S. L., Richardson, S. J., Schreiber, G., 1999. Evolution of thyroid hormone binding by transthyretins in birds and mammals. *European Journal of Biochemistry*, 259(1-2), pp.534–542.

Chen, H. Sun, L., Li, G., Zhang, S. Y., Chen, H. L., 2004. Laser-induced time-resolved photoacoustic calorimetry study on photo-dissociation of human and bovine oxyhemoglobin. *Biochemical and Biophysical Research Communications*, 319(1), pp.157–162.

Chen, H.-L. Hsu, J.C.-C., Viet, M. H., Li, M. S., Hu, C.-K., Liu, C.-H., Luh, F. Y., Chen, S. S.-W., Chang, E. S.-H., Wang, A. H.-J., et al., 2010. Studying submicrosecond protein folding kinetics using a photolabile caging strategy and time-resolved photoacoustic calorimetry. *Proteins*, 78(14), pp.2973–2983.

Chen, M. J. & Mayo, K. H., 1991. Human platelet factor 4 subunit association/dissociation thermodynamics and kinetics. *Biochemistry*, 30(26), pp.6402–6411.

Chen, R.P.-Y., Huang ,J. J.-T., Chen, H.-L., Jan, H., Velusamy, M., Lee, C.-T., Fann, W., Larsen, R. W., Chan, S. I., 2004. Measuring the refolding of beta-sheets with different turn sequences on a nanosecond time scale. *Proceedings of the National Academy of Sciences of the United States of America*, 101(19), pp.7305–7310.

Cheng, S.-Y., Pages, R. A., Saroff, H. A., Edelhoch, H., Robbins, J., 1977. Analysis of thyroid hormone binding to human serum prealbumin by 8-anilinonaphthalene-1-sulfonate fluorescence. *Biochemistry*, 16(16), pp.3707–3713.

Chiti, F. & Dobson, C. M., 2006. Protein misfolding, functional amyloid, and human disease. *Annual Review of Biochemistry*, 75, pp.333–66.

Chiti, F., Webster, P., Taddei, N., Clark, A., Stefani, M., Ramponi, G., Dobson, C. M., 1999. Designing conditions for in vitro formation of amyloid protofilaments and fibrils. *Proceedings of the National Academy of Sciences of the United States of America*, 96(7), pp.3590–3594.

Ciamician, G. & Silber, P., 1901. Chemische Lichtwirkungen. *Berichte der Deutschen Chemischen Gesellschaft*, 34(2), pp.2040–2046.

Ciani, B., Jourdan, M. & Searle, M. S., 2003. Stabilization of beta-hairpin peptides by salt bridges: role of preorganization in the energetic contribution of weak interactions. *Journal of the American Chemical Society*, 125(30), pp.9038–9047.

Correia, C. F., Guedes, R. C., Borges dos Santos, R. M., Costa Cabral, B. J., Martinho Simões, J. A., 2004. O-H Bond dissociation enthalpies in hydroxyphenols. A time-resolved photoacoustic calorimetry and quantum chemistry. *Physical Chemistry Chemical Physics*, 6(9), pp.2109–2118.

Creighton, T. E., 1986. Detection of folding intermediates using urea-gradient electrophoresis. *Methods in Enzymology*, 131, pp.156–172.

Creighton, T. E., 1997. *Protein structure: a practical approach* 2nd ed. T. E. Creighton, ed., Oxford; New York: IRL Press at Oxford University Press.

Derome, A. E. & Williamson, M. P., 1990. Rapid-pulsing artifacts in double-quantum-filtered COSY. *Journal of Magnetic Resonance (1969)*, 88(1), pp.177–185.

Dill, K. A. & Chan, H. S., 1997. From Levinthal to pathways to funnels. *Nature Structural Biology*, 4(1), pp.10–19.

Dill, K. A. & MacCallum, J. L., 2012. The protein-folding problem, 50 years on. *Science*, 338(6110), pp.1042–1046.

Dill, K. A. & Shortle, D., 1991. Denatured states of proteins. *Annual Review of Biochemistry*, 60, pp.795–825.

Dill, K. A., 1985. Theory for the folding and stability of globular proteins. *Biochemistry*, 24(6), pp.1501–1509.

Dill, K. A., 1990. Dominant forces in protein folding. *Biochemistry*, 29(31), pp.7133–7155.

Dill, K. A., Ozkan, S. B., Shell, M. S., Weikl, T. R., 2008. The protein folding problem. *Annual Review of Biophysics*, 37, pp.289–316.

Dill, K. A., Ozkan, S. B., Weikl, T. R., Chodera, J. D., Voelz, V. A., 2007. The protein folding problem: when will it be solved? *Current Opinion in Structural Biology*, 17(3), pp.342–346.

Dobson, C. M., 2004. Experimental investigation of protein folding and misfolding. *Methods*, 34(1), pp.4–14.

Dobson, C. M., 2004. Principles of protein folding, misfolding and aggregation. *Seminars in Cell & Developmental Biology*, 15(1), pp.3–16.

Dockal, M., 2000. Conformational Transitions of the Three Recombinant Domains of Human Serum Albumin Depending on pH. *Journal of Biological Chemistry*, 275(5), pp.3042–3050.

Donten, M. L., Hamm, P. & VandeVondele, J., 2011. A consistent picture of the proton release mechanism of oNBA in water by ultrafast spectroscopy and ab initio molecular dynamics. *The Journal of Physical Chemistry. B*, 115(5), pp.1075–1083.

Du, D., Bunagan, M. R. & Gai, F., 2007. The effect of charge-charge interactions on the kinetics of alpha-helix formation. *Biophysical Journal*, 93(11), pp.4076–4082.

Du, D., Zhu, Y., Huang, C.-Y., Gai, F., 2004. Understanding the key factors that control the rate of beta-hairpin folding. *Proceedings of the National Academy of Sciences of the United States of America*, 101(45), pp.15915–15920.

Eaton, W. A., Muñoz, V., Hagen, S. J., Jas, G. S., Lapidus, L. J., Henry, E. R., Hofrichter, J., 2000. Fast kinetics and mechanisms in protein folding. *Annual Review of Biophysics and Biomolecular Structure*, 29, pp.327–359.

Edelhoch, H., 1962. The Properties of Thyroglobulin. VIII. The Iodination of Thyroglobulin. *Journal Biological Chemistry*, 237(9), pp.2778–2787.

El Kadi, N., Taulier, N., Le Huérou, J. Y., Gindre, M., Urbach, W., Nwigwe, I., Kahn, P. C., Waks, M., 2006. Unfolding and refolding of bovine serum albumin at acid pH: ultrasound and structural studies. *Biophysical Journal*, 91(9), pp.3397–3404.

Eliezer, D., Jennings, P. A., Wright, P. E., Doniach, S., Hodgson, K. O., Tsuruta, H., 1995. The radius of gyration of an apomyoglobin folding intermediate. *Science*, 270(5235), pp.487–488.

Fairman, R. Shoemaker, K. R., York, E. J., Stewart, J. M., Baldwin, R. L., 1990. The Glu 2^- ... Arg 10^+ side-chain interaction in the C-peptide helix of ribonuclease A. *Biophysical Chemistry*, 37(1-3), pp.107–119.

Ferguson, N. & Fersht, A. R., 2003. Early events in protein folding. *Current Opinion in Structural Biology*, 13(1), pp.75–81.

Fersht, A. R., 1995. Optimization of rates of protein folding: the nucleation-condensation mechanism and its implications. *Proceedings of the National Academy of Sciences of the United States of America*, 92(24), pp.10869–10873.

Fersht, A. R., 1997. Nucleation mechanisms in protein folding. *Current Opinion in Structural Biology*, 7(1), pp.3–9.

Fierz, B., Satzger, H., Root, C., Gilch, P., Zinth, W., Kiefhaber, T., 2007. Loop formation in unfolded polypeptide chains on the picoseconds to microseconds time scale. *Proceedings of the National Academy of Sciences of the United States of America*, 104(7), pp.2163–2168.

Formosinho, S. J. & Arnaut, L. G., 2003. *Cinética Química: Estrutura Molecular e Reactividade Química*, Imprensa da Universidade de Coimbra.

Forster, J. F., 1960. *The Plasma Proteins* F. W. Putman, ed., Academic Press: New York.

Fraczkiewicz, R. & Braun, W., 1998. Exact and efficient analytical calculation of the accessible surface areas and their gradients for macromolecules. *Journal of Computational Chemistry*, 19(3), pp.319–333.

Frydman, J., 2001. Folding of newly translated proteins in vivo: the role of molecular chaperones. *Annual Review of Biochemistry*, 70, pp.603–647.

Furuya, H., Saraiva, M. J. M., Gawinowicz, M. A., Alves, I. L., Costa, P. P., Sasaki, H., Goto, I., Sakaki, Y. 1991. Production of recombinant human transthyretin with biological activities toward the understanding of the molecular basis of familial amyloidotic polyneuropathy (FAP). *Biochemistry*, 30(9), pp.2415–2421.

Gensch, T. & Braslavsky, S. E., 1997. Volume Changes Related to Triplet Formation of Water-Soluble Porphyrins. A Laser-Induced Optoacoustic Spectroscopy (LIOAS) Study. *The Journal of Physical Chemistry B*, 101(1), pp.101–108.

Gensch, T. & Viappiani, C., 2003. Time-resolved photothermal methods: accessing time-resolved thermodynamics of photoinduced processes in chemistry and biology. *Photochemical & Photobiological sciences*, 2(7), pp.699–721.

George, M. V. & Scaiano, J. C., 1980. Photochemistry of o-nitrobenzaldehyde and related studies. *The Journal of Physical Chemistry*, 84(5), pp.492–495.

Ghuman, J., Zunszain, P. A., Petitpas, I., Bhattacharya, A. A., Otagiri, M., Curry, S., 2005. Structural basis of the drug-binding specificity of human serum albumin. *Journal of Molecular Biology*, 353(1), pp.38–52.

Gilmanshin, R., Williams, S., Callender, R. H., Woodruff, W. H., Dyer, R. B., 1997. Fast events in protein folding: relaxation dynamics of secondary and tertiary structure in native apomyoglobin. *Proceedings of the National Academy of Sciences of the United States of America*, 94(8), pp.3709–3713.

Goldberg, R. N., Kishore, N., Lennen, R. M., 2002. Thermodynamic Quantities for the Ionization Reactions of Buffers. *Journal of Physical and Chemical Reference Data*, 31(2), pp.231–370.

Goldenberg, D. P. & Creighton, T. E., 1984. Gel electrophoresis in studies of protein conformation and folding. *Analytical Biochemistry*, 138(1), pp.1–18.

Goldenberg, D. P., 1997. Analysis of protein conformation by gel electrophoresis. In T. E. Creighton, ed. *Protein Structure: A Practical Approach*. Oxford University Press, pp. 187–218.

Grigoryants, V. M., Veselov, A. V. & Scholes, C. P., 2000. Variable velocity liquid flow EPR applied to submillisecond protein folding. *Biophysical Journal*, 78(5), pp.2702–2708.

Güntert, P. & Wüthrich, K., 1992. FLATT—A new procedure for high-quality baseline correction of multidimensional NMR spectra. *Journal of Magnetic Resonance (1969)*, 96(2), pp.403–407.

Gutman, M. & Nachliel, E., 1990. The dynamic aspects of proton transfer processes. *Biochimica et Biophysica Acta (BBA)-Bioenergetics*, 1015, pp. 391–414.

Hammarström, P., Jiang, X., Deechongkit, S., Kelly, J. W., 2001. Anion shielding of electrostatic repulsions in transthyretin modulates stability and amyloidosis: insight into the chaotrope unfolding dichotomy. *Biochemistry*, 40(38), pp.11453–11459.

Hammarström, P., Jiang, X., Hurshman, A. R., Powers, E. T., Kelly, J. W., 2002. Sequence-dependent denaturation energetics: A major determinant in amyloid disease diversity. *Proceedings of the National Academy of Sciences of the United States of America*, 99 Suppl 4, pp.16427–16432.

Hammes, G. G. & Roberts, P. B., 1969. Dynamics of the helix-coil transition in poly-L-ornithine. *Journal of the American Chemical Society*, 91(7), pp.1812–1816.

Hauer, J., Müller, K., Lüdemann, H. D., Jaenicke, R., 1981. The pressure dependence of the histidine ring protonation constant studied by 1H HR-NMR. *FEBS Letters*, 135(1), pp.135–138.

Heihoff, K. & Braslavsky, S. E., 1986. Triplet lifetime determination by laser-induced optoacoustic spectroscopy. benzophenone/iodide revisited. *Chemical Physics Letters*, 131(3), pp.183–188.

Hermann, R., Jaenicke, R. & Price, N. C., 1985. Evidence for active intermediates during the reconstitution of yeast phosphoglycerate mutase. *Biochemistry*, 24(8), pp.1817–1821.

Hermann, R., Jaenicke, R. & Rudolph, R., 1981. Analysis of the reconstitution of oligomeric enzymes by cross-linking with glutaraldehyde: kinetics of reassociation of lactic dehydrogenase. *Biochemistry*, 20(18), pp.5195–5201.

Hermann, R., Rudolph, R., Jaenicke, R., Price, N. C., Scobbie, A., 1983. The reconstitution of denatured phosphoglycerate mutase. *Journal Biological Chemistry*, 258(18), pp.11014–11019.

Hörnberg, A., Eneqvist, T., Olofsson, A., Lundgren, E., Sauer-Eriksson, A. E., 2000. A comparative analysis of 23 structures of the amyloidogenic protein transthyretin. *Journal of Molecular Biology* 302, pp.649–669.

Hurshman Babbes, A. R., Powers, E. T. & Kelly, J. W, 2008. Quantification of the thermodynamically linked quaternary and tertiary structural stabilities of transthyretin and its disease-associated variants: the relationship between stability and amyloidosis. *Biochemistry*, 47(26), pp.6969–6984.

Hwang, T. L. & Shaka, A. J., 1995. Water Suppression That Works. Excitation Sculpting Using Arbitrary Wave-Forms and Pulsed-Field Gradients. *Journal of Magnetic Resonance, Series A*, 112(2), pp.275–279.

Ito, M., Johansson, J., Strömberg, R, Nilsson, L., 2011. Unfolding of the amyloid β-peptide central helix: mechanistic insights from molecular dynamics simulations. *PloS One*, 6(3), p.e17587.

Jabben, M., Garcia, N. A., Braslavsky, S. E., Schaffner, K. , 1986. Photophysical parameters of chlorophylls and b.fluorescence and laser-induced optoacoustic. *Photochemistry and Photobiology*, 43(2), pp.127–131.

Jaenicke, R. & Lilie, H., 2000. Protein folding mechanisms, Elsevier.

Jaenicke, R., 1987. Folding and association of proteins. *Progress in Biophysics and Molecular Biology*, 49(2-3), pp.117–237.

Jaenicke, R., 2000. Stability and stabilization of globular proteins in solution. *Journal of Biotechnology*, 79(3), pp.193–203.

Jennings, P. A. & Wright, P. E., 1993. Formation of a molten globule intermediate early in the kinetic folding pathway of apomyoglobin. *Science*, 262(5135), pp.892–896.

Jesus, C. S. H., De Almeida, Z. L., Vaz, D. C., Saraiva, M. J. M., Brito, R. M. M., 2013. Transthyretin Folding kinetics: Does Slower Refolding Imply Enhanced Amyloidogenicity? (*In Preparation*)

Jones, J. A., Wilkins, D. K., Smith, L. J., Dobson, C. M., 1997. Characterisation of protein unfolding by NMR diffusion measurements. *Journal of Biomolecular NMR*, 10(2), pp.199–203.

Kallberg, Y., Gustafsson, M., Persson, B., Thyberg, J., Johansson, J., 2001. Prediction of amyloid fibril-forming proteins. *The Journal of Biological Chemistry*, 276(16), pp.12945–12950.

Karplus, M. & Weaver, D. L., 1976. Protein-folding dynamics. *Nature*, 260(5550), pp.404–406.

Karplus, M. & Weaver, D. L., 1994. Protein folding dynamics: the diffusion-collision model and experimental data. *Protein Science*, 3(4), pp.650–668.

Karplus, M., 1959. Contact Electron-Spin Coupling of Nuclear Magnetic Moments. *The Journal of Chemical Physics*, 30(1), p.11–15.

Katz, S. & Miller, J. E., 1971. Medium effects of some denaturing agents on volume changes produced by acid-base reactions. *The Journal of Physical Chemistry*, 75(8), pp.1120–1125.

Kauzmann, W., Bodanszky, A. & Rasper, J., 1962. Volume Changes in Protein Reactions. II. Comparison of Ionization Reactions in Proteins and Small Molecules. *Journal of the American Chemical Society*, 84(10), pp.1777–1788.

Kestin, J., Sokolov, M. & Wakeham, W. A., 1978. Viscosity of liquid water in the range −8 °C to 150 °C. *Journal of Physical and Chemical Reference Data*, 7(3), pp.941–948.

Khandogin, J., Chen, J. & Brooks, C. L., 2006. Exploring atomistic details of pH-dependent peptide folding. *Proceedings of the National Academy of Sciences of the United States of America*, 103(49), pp.18546–18550.

Kitamura, Y. & Itoh, T., 1987. Reaction volume of protonic ionization for buffering agents. Prediction of pressure dependence of pH and pOH. *Journal of Solution Chemistry*, 16(9), pp.715–725.

Klotz, I.M., 1997. Ligand-Receptor Energetics: A Guide for the Perplexed, Wiley.

Kobayashi, N., Honda, S., Yoshii, H., Munekata, E., 2000. Role of side-chains in the cooperative beta-hairpin folding of the short C-terminal fragment derived from streptococcal protein G. *Biochemistry*, 39(21), pp.6564–6571.

Komorowski, S. J. & Eyring, E. M., 1987. Pulse shapes of nanosecond photoacoustic signals in liquids detected by piezoelectric foil. *Journal of Applied Physics*, 62(7), p.3066.

Kragh-Hansen, U., 1981. Molecular aspects of ligand binding to serum albumin. *Pharmacological Reviews*, 33(1), pp.17–53.

Krieger, F., Fierz, B., Bieri, O., Drewello, M., Kiefhaber, T., 2003. Dynamics of unfolded polypeptide chains as model for the earliest steps in protein folding. *Journal of Molecular Biology*, 332(1), pp.265–274.

Kubelka, J., Hofrichter, J. & Eaton, W. A., 2004. The protein folding "speed limit". *Current Opinion in Structural Biology*, 14(1), pp.76–88.

Kumar, S. & Nussinov, R., 2002. Close-range electrostatic interactions in proteins. *Chembiochem*, 3(7), pp.604–617.

Kuo, N. N.-W., Huang, J. J.-T., Miksovska, J., Chen, R. P.-Y., Larsen, R. W., Chan, S. I., 2005. Effects of turn stability on the kinetics of refolding of a hairpin in a beta-sheet. *Journal of the American Chemical Society*, 127(48), pp.16945–16954.

Lai, Z., Colón, W. & Kelly, J. W., 1996. The acid-mediated denaturation pathway of transthyretin yields a conformational intermediate that can self-assemble into amyloid. *Biochemistry*, 35(20), pp.6470–6482.

Lanyi, J. K., 1998. Understanding structure and function in the light-driven proton pump bacteriorhodopsin. *Journal of Structural Biology*, 124(2-3), pp.164–178.

Lapidus, L. J., Steinbach, P. J., Eaton, W. A., Szabo, A., Hofrichter, J., 2002. Effects of Chain Stiffness on the Dynamics of Loop Formation in Polypeptides. Appendix: Testing a 1-Dimensional Diffusion Model for Peptide Dynamics. *The Journal of Physical Chemistry B*, 106(44), pp.11628–11640.

Larsen, R.W. & Mikšovská, J., 2007. Time resolved thermodynamics of ligand binding to heme proteins. *Coordination Chemistry Reviews*, 251(9-10), pp.1101–1127.

Larsen, R.W., 2006. Time-resolved thermodynamic profiles for CO photolsysis from the mixed valence form of bovine heart cytochrome c oxidase. *Photochemical & Photobiological Sciences*, 5(6), pp.603–610.

Le Bras, G., Teschner, W., Deville-Bonne, D., Garel, J. R., 1989. Urea-induced inactivation, dissociation and unfolding of the allosteric phosphofructokinase from Escherichia coli. *Biochemistry*, 28(17), pp.6836–6841.

Lednev, I. K., Karnoup, A. S., Sparrow, M. C., Asher, S. A., 1999. α-Helix Peptide Folding and Unfolding Activation Barriers: A Nanosecond UV Resonance Raman Study. *Journal of the American Chemical Society*, 121(35), pp.8074–8086.

Leyva, V., Corral, I., Schmierer, T., Heinz, B., Feixas, F., Migani, A., Blancafort, L., Gilch, P., González, L., 2008. Electronic states of o-nitrobenzaldehyde: a combined experimental and theoretical study. *The Journal of Physical Chemistry. A*, 112(23), pp.5046–5053.

Lin, M. M., Mohammed, O. F., Jas, G. S., Zewail, A. H., 2011. Speed limit of protein folding evidenced in secondary structure dynamics. *Proceedings of the National Academy of Sciences of the United States of America*, 108(40), pp.16622–16627.

Lipfert, J. & Doniach, S., 2007. Small-angle X-ray scattering from RNA, proteins, and protein complexes. *Annual Review of Biophysics and Biomolecular Structure*, 36, pp.307–327.

Majorek, K. A., Porebski, P. J., Dayal, A., Zimmerman, M. D., Jablonska, K., Stewart, A. J., Chruszcz, M., Minor, W., 2012. Structural and immunologic characterization of bovine, horse, and rabbit serum albumins. *Molecular Immunology*, 52(3-4), pp.174–182.

Marcus, Y., 1998. *The Properties of Solvents*, John Wiley & Sons.

Marion, D., Ikura, M., Tschudin, R., Bax, A., 1989. Rapid recording of 2D NMR spectra without phase cycling. Application to the study of hydrogen exchange in proteins. *Journal of Magnetic Resonance (1969)*, 85(2), pp.393–399.

Markley, J. L., Bax, A., Arata, Y., Hilbers, C. W., Kaptein, R., Sykes, B. D., Wright, P. E., Wüthrich, K., 1998. Recommendations for the presentation of NMR structures of proteins and nucleic acids (IUPAC Recommendations 1998). *Pure and Applied Chemistry*, 70(1), pp.117–142.

Marqusee, S., Robbins, V. H. & Baldwin, R. L., 1989. Unusually stable helix formation in short alanine-based peptides. *Proceedings of the National Academy of Sciences of the United States of America*, 86(14), pp.5286–5290.

Marr, K. & Peters, K. S., 1991. Photoacoustic calorimetric study of the conversion of rhodopsin and isorhodopsin to lumirhodopsin. *Biochemistry*, 30(5), pp.1254–1258.

Marti, D. N., 2005. Apparent pKa shifts of titratable residues at high denaturant concentration and the impact on protein stability. *Biophysical Chemistry*, 118(2-3), pp.88–92.

Mateu, M. G., Sánchez, Del Pino, M. M. & Fersht, A. R., 1999. Mechanism of folding and assembly of a small tetrameric protein domain from tumor suppressor p53. *Nature Structural Biology*, 6(2), pp.191–198.

Matthew, J. B., Gurd, F. R., Garcia-Moreno, B., Flanagan, M. A., March, K. L., Shire, S. J., 1985. pH-dependent processes in proteins. *Critical Reviews in Biochemistry*, 18(2), pp.91–197.

Mayer, M. & Meyer, B., 1999. Characterization of Ligand Binding by Saturation Transfer Difference NMR Spectroscopy. *Angewandte Chemie International Edition*, 38(12), pp.1784–1788.

McLean, M. A., Di Primo, C., Deprez, E., Hoa, G. H., Sligar, S. G., 1998. Photoacoustic calorimetry of proteins. *Methods in Enzymology*, 295, pp.316–330.

Mehl, A. F., Okada, K., Dehn, S. M., Kurian, S., 2012. Probing the stability and mechanism for folding of the GrpE1-112 tetrameric deletion mutant of the GrpE protein from E. coli. *Biochemical and Biophysical Research Communications*, 420(3), pp.635–638.

Mejías, J. A. & Lago, S., 2000. Calculation of the absolute hydration enthalpy and free energy of H^+ and OH^-. *The Journal of Chemical Physics*, 113(17), pp.7306–7316.

Melton, L.A., Ni, T. & Lu, Q., 1989. Photoacoustic calorimetry: a new cell design and improved analysis algorithms. *Review of Scientific Instruments*, 60(10), pp.3217–3223.

Meyer, B. & Peters, T., 2003. NMR spectroscopy techniques for screening and identifying ligand binding to protein receptors. *Angewandte Chemie*, 42(8), pp.864–890.

Mezzetti, A., Nabedryk, E., Breton, J., Okamura, M. Y., Paddock, M. L., Giacometti, G., Leibl, W., 2002. Rapid-scan Fourier transform infrared spectroscopy shows coupling of GLu-L212 protonation and electron transfer to QB in Rhodobacter sphaeroides reaction centers. *Biochimica et Biophysica Acta (BBA) - Bioenergetics*, 1553(3), pp.320–330.

Miksovská, J. & Larsen, R.W., 2003. Photothermal studies of pH induced unfolding of apomyoglobin. *Journal of Protein Chemistry*, 22(4), pp.387–394.

Miksovská, J., Horsa, S., Davis, M. F., Franzen, S., 2008. Conformational dynamics associated with photodissociation of CO from dehaloperoxidase studied using photoacoustic calorimetry. *Biochemistry*, 47(44), pp.11510–11517.

Morozov, A. N. & Lin, S. H., 2006. Modeling of folding and unfolding mechanisms in alanine-based alpha-helical polypeptides. *The Journal of Physical Chemistry. B*, 110(41), pp.20555–20561.

Mukherjee, S., Chowdhury, P., Bunagan, M. R., Gai, F., 2008. Folding kinetics of a naturally occurring helical peptide: implication of the folding speed limit of helical proteins. *The Journal of Physical Chemistry. B*, 112(30), pp.9146–9150.

Muñoz, V., Thompson P. A., Hofrichter, J., Eaton, W. A., 1997. Folding dynamics and mechanism of beta-hairpin formation. *Nature*, 390(6656), pp.196–199.

Muralha, V.S.F., Borges dos Santos, R.M. & Martinho Simões, J.A., 2004. Energetics of Alkylbenzyl Radicals: A Time-Resolved Photoacoustic Calorimetry Study. *The Journal of Physical Chemistry A*, 108(6), pp.936–942.

Muzammil, S., Kumar, Y. & Tayyab, S., 1999. Molten globule-like state of human serum albumin at low pH. *European Journal of Biochemistry*, 266(1), pp.26–32.

Nelson, E. D. & Onuchic, J. N., 1998. Proposed mechanism for stability of proteins to evolutionary mutations. *Proceedings of the National Academy of Sciences of the United States of America*, 95(18), pp.10682–10686.

Nichtl, A., Buchner, J., Jaenicke, R., Rudolph, R., Scheibel, T., 1998. Folding and association of beta-Galactosidase. *Journal of Molecular Biology*, 282(5), pp.1083–1091.

Niimura, N. & Bau, R., 2008. Neutron protein crystallography: beyond the folding structure of biological macromolecules. *Acta Crystallographica*, 64, pp.12–22.

Nilsson, S. F. & Peterson, Per A., 1971. Evidence for Multiple Thyroxine-binding Sites in Human Prealbumin. *Journal Biological Chemistry*, 246(19), pp.6098–6105.

Nilsson, S. F., Rask, L. & Peterson, P. A., 1975. Studies on thyroid hormone-binding proteins. II. Binding of thyroid hormones, retinol-binding protein, and fluorescent probes to prealbumin and effects of thyroxine on prealbumin subunit self association. *The Journal of Biological Chemistry*, 250(21), pp.8554–8563.

Norris, C. L. & Peters, K. S., 1993. A photoacoustic calorimetry study of horse carboxymyoglobin on the 10-nanosecond time scale. *Biophysical Journal*, 65(4), pp.1660–1665.

Nozaki, Y. & Tanford, C., 1967. Intrinsic dissociation constants of aspartyl and glutamyl carboxyl groups. *The Journal of Biological Chemistry*, 242(20), pp.4731–4735.

Nunes, P. M., Agapito, F., Costa Cabral, B. J., Borges dos Santos, R. M., Martinho Simões, J. A., 2006. Enthalpy of formation of the cyclopentadienyl radical: photoacoustic calorimetry and ab initio studies. *The Journal of Physical Chemistry. A*, 110(15), pp.5130–5134.

Nunes, P. M., Estácio, S. G., Lopes, G. T., Agapito, F., Santos, R. C., Costa Cabral, B. J., Borges dos Santos, R. M., Martinho Simões, J. A., 2009. Energetics of tert-butoxyl addition reaction to norbornadiene: a method for estimating the pi-bond strength of a carbon-carbon double bond. *The Journal of Physical Chemistry. A*, 113(23), pp.6524–3650.

Onuchic, J. N. & Wolynes, P. G., 2004. Theory of protein folding. *Current Opinion in Structural Biology*, 14(1), pp.70–75.

Ooi, T., Oobatake, M., Nemethy, G., Scheraga, H. A., 1987. Accessible surface areas as a measure of the thermodynamic parameters of hydration of peptides. *Proceedings of the National Academy of Sciences*, 84(10), pp.3086–3090.

Ort, D. R. & Parson, W. W., 1979. Enthalpy changes during the photochemical cycle of bacteriorhodopsin. *Biophysical Journal*, 25, pp.355–364.

Osterhout, J. J., Baldwin, R. L., York, E. J., Stewart, J. M., Dyson, H. J., Wright, P.E. , 1989. Proton NMR studies of the solution conformations of an analog of the C-peptide of ribonuclease A. *Biochemistry*, 28(17), pp.7059–7064.

Out, D. J. P. & Los, J. M., 1980. Viscosity of aqueous solutions of univalent electrolytes from 5 to 95 ºC. *Journal of Solution Chemistry*, 9(1), pp.19–35.

Pace, C. N. & Scholtz, J. M., 1997. Measuring the conformational stability of a protein. In T. E. Creighton, ed. *Protein Structure: A Practical Approach*. Oxford: IRL Press, pp. 299–231.

Pace, C. N., Grimsley, G. R. & Scholtz, J. M., 2009. Protein ionizable groups: pK values and their contribution to protein stability and solubility. *The Journal of Biological Chemistry*, 284(20), pp.13285–13289.

Pace, C. N., Shirley, B. A., McNutt, M., Gajiwala, K., 1996. Forces contributing to the conformational stability of proteins. *FASEB Journal*, 10(1), pp.75–83.

Palaninathan, S.K., 2012. Nearly 200 X-ray crystal structures of transthyretin: what do they tell us about this protein and the design of drugs for TTR amyloidoses? *Current Medicinal Chemistry*, 19(15), pp.2324–2342.

Park, C., Schultz, L. W. & Raines, R. T., 2001. Contribution of the active site histidine residues of ribonuclease A to nucleic acid binding. *Biochemistry*, 40(16), pp.4949–4956.

Patel, C. & Tam, A., 1981. Pulsed optoacoustic spectroscopy of condensed matter. *Reviews of Modern Physics*, 53(3), pp.517–550.

Perutz, M. F., Gronenborn, A. M., Clore, G. M., Fogg, J. H., Shih, D. T., 1985. The pKa values of two histidine residues in human haemoglobin, the Bohr effect, and the dipole moments of alpha-helices. *Journal of Molecular Biology*, 183(3), pp.491–498.

Peters, K. S. & Snyder, G. J., 1988. Time-resolved photoacoustic calorimetry: probing the energetics and dynamics of fast chemical and biochemical reactions. *Science*, 241(4869), pp.1053–1057.

Peters, K. S., 1994. Time-Resolved Photoacoustic Calorimetry: From Carbenes to Proteins. *Angewandte Chemie International*, 33(3), pp.294–302.

Peters, K. S., Watson, T. & Logan, T., 1992. Photoacoustic calorimetry study of human carboxyhemoglobin. *Journal of the American Chemical Society*, 114(11), pp.4276–4278.

Peters, K. S., Watson, T. & Marr, K., 1991. Time-resolved photoacoustic calorimetry: a study of myoglobin and rhodopsin. *Annual Review of Biophysics and Biophysical Chemistry*, 20, pp.343–362.

Peters, T., 1985. Serum albumin. *Advances in Protein Chemistry*, 37, pp.161–245.

Petty, S. A. & Volk, M., 2004. Fast folding dynamics of an α-helical peptide with bulky side chains. *Physical Chemistry Chemical Physics*, 6(5), p.1022–1030.

Plaxco, K. W. & Dobson, C. M., 1996. Time-resolved biophysical methods in the study of protein folding. *Current Opinion in Structural Biology*, 6(5), pp.630–636.

Politi, M. J. & Fendler, J. H., 1984. Laser pH-jump initiated proton transfer on charged micellar surfaces. *Journal of the American Chemical Society*, 106(2), pp.265–273.

Powers, E. T. & Powers, D. L., 2003. A perspective on mechanisms of protein tetramer formation. *Biophysical Journal*, 85(6), pp.3587–3599.

Provencher, S. W., 1982. CONTIN: A general purpose constrained regularization program for inverting noisy linear algebraic and integral equations. *Computer Physics Communications*, 27(3), pp.229–242.

Qiu, W., Zhang, L., Okobiah, O., Yang, Y., Wang, L., Zhong, D., & Zewail, A. H., 2006. Ultrafast solvation dynamics of human serum albumin: correlations with conformational transitions and site-selected recognition. *The Journal of Physical Chemistry. B*, 110(21), pp.10540–10549.

Quintas, A., Saraiva, M. J. & Brito, R. M. M., 1997. The amyloidogenic potential of transthyretin variants correlates with their tendency to aggregate in solution. *FEBS Letters*, 418(3), pp.297–300.

Quintas, A., Saraiva, M. J. & Brito, R. M. M., 1999. The tetrameric protein transthyretin dissociates to a non-native monomer in solution. A novel model for amyloidogenesis. *The Journal of Biological Chemistry*, 274(46), pp.32943–32949.

Quintas, A., Vaz, D. C., Cardoso, I., Saraiva, M. J., Brito, R. M. M. 2001. Tetramer dissociation and monomer partial unfolding precedes protofibril formation in amyloidogenic transthyretin variants. *The Journal of Biological Chemistry*, 276(29), pp.27207–27213.

Rasper, J. & Kauzmann, W., 1962. Volume Changes in Protein Reactions. I. Ionization Reactions of Proteins. *Journal of the American Chemical Society*, 84(10), pp.1771–1777.

Raz, A. & Goodman, DeWitt S., 1969. The Interaction of Thyroxine with Human Plasma Prealbumin and with the Prealbumin-Retinol-binding Protein Complex. *Journal Biological Chemistry*, 244(12), pp.3230–3237.

Redfield, C., Smith, R. A. G. & Dobson, C. M., 1994. Structural characterization of a highly–ordered "molten globule" at low pH. *Nature Structural Biology*, 1(1), pp.23–29.

Rehaber, V. & Jaenicke, R., 1992. Stability and reconstitution of D-glyceraldehyde-3-phosphate dehydrogenase from the hyperthermophilic eubacterium Thermotoga maritima. *The Journal of Biological Chemistry*, 267(16), pp.10999–11006.

Reis, L. A. F., 2011. *Construção de uma célula para Calorimetria Fotoacústica com controlo térmico (Tese de Mestrado)*. University of Coimbra.

Riedl, B. & Jolicoeur, C., 1984. Volume and heat capacity changes upon ionization of water, acetic acid, n-propylamine, and 4-methylimidazole in water and 8 M urea: consequences of ionization on properties of proteins. *The Journal of Physical Chemistry*, 88(15), pp.3348–3356.

Risse, B., Stempfer, G., Rudolph, R., Möllering, H., Jaenicke, R., 1992. Stability and reconstitution of pyruvate oxidase from Lactobacillus plantarum: dissection of the stabilizing effects of coenzyme binding and subunit interaction. *Protein science*, 1(12), pp.1699–1709.

Roder, H. & Shastry, M. R., 1999. Methods for exploring early events in protein folding. *Current Opinion in Structural Biology*, 9(5), pp.620–626.

Rodrigues, J. R., Simões, C. J. V., Silva, C. G., Brito, R. M. M., 2010. Potentially amyloidogenic conformational intermediates populate the unfolding landscape of transthyretin: insights from molecular dynamics simulations. *Protein science*, 19(2), pp.202–219.

Rudzki, J. E., Goodman, J. L. & Peters, K. S., 1985. Simultaneous determination of photoreaction dynamics and energetics using pulsed, time-resolved photoacoustic calorimetry. *Journal of the American Chemical Society*, 107(26), pp.7849–7854.

Sadler, P. J. & Tucker, A., 1993. pH-induced structural transitions of bovine serum albumin. Histidine pKa values and unfolding of the N-terminus during the N to F transition. *European Journal of Biochemistry*, 212(3), pp.811–817.

Santiveri, C. M., León E., Rico, M., Jiménez, M. A., 2008. Context-dependence of the contribution of disulfide bonds to beta-hairpin stability. *Chemistry (Weinheim an der Bergstrasse, Germany)*, 14(2), pp.488–499.

Saraiva, M. J. M., 1996. Molecular genetics of familial amyloidotic polyneuropathy. *Journal of the Peripheral Nervous System*, 1(3), pp.179–188.

Saraiva, M. J., Birken, S., Costa, P. P., Goodman, D. S., 1984. Amyloid fibril protein in familial amyloidotic polyneuropathy, Portuguese type. Definition of molecular abnormality in transthyretin (prealbumin). *The Journal of Clinical Investigation*, 74(1), pp.104–119.

Schaberle, F. A., Nunes, R. M. D., Barroso, M., Serpa, C., Arnaut, L. G., 2010. Analytical solution for time-resolved photoacoustic calorimetry data and applications to two typical photoreactions. *Photochemical & photobiological sciences*, 9(6), pp.812–822.

Schrader, T. E., Schreier, W. J, Cordes, T., Koller, F. O., Babitzki, G., Denschlag, R., Renner, C., Löweneck, M., Dong, S.-L., Moroder, L., et al., 2007. Light-triggered beta-hairpin folding and unfolding. *Proceedings of the National Academy of Sciences of the United States of America*, 104(40), pp.15729–15734.

Schwarz, G., 1965. On the kinetics of the helix-coil transition of polypeptides in solution. *Journal of Molecular Biology*, 11(1), pp.64–77.

Searle, M. S. & Ciani, B., 2004. Design of beta-sheet systems for understanding the thermodynamics and kinetics of protein folding. *Current Opinion in Structural Biology*, 14(4), pp.458–464.

Searle, M. S., Williams, D. H. & Packman, L. C., 1995. A short linear peptide derived from the N-terminal sequence of ubiquitin folds into a water-stable non-native beta-hairpin. *Nature Structural Biology*, 2(11), pp.999–1006.

Serpa, C. & Arnaut, L.G., 2000. Does Molecular Size Matter in Photoinduced Electron Transfer Reactions? *The Journal of Physical Chemistry A*, 104(47), pp.11075–11086.

Serpa, C., Schabauer, J., Piedade, A. P., Monteiro, C. J. P., Pereira, M. M., Douglas, P., Burrows, H. D., Arnaut, L. G., 2008. Photoacoustic measurement of electron injection efficiencies and energies from excited sensitizer dyes into nanocrystalline TiO2 films. *Journal of the American Chemical Society*, 130(28), pp.8876–8877.

Seshasayee, A. S. N., Raghunathan, K., Sivaraman, K., Pennathur, G., 2006. Role of hydrophobic interactions and salt-bridges in beta-hairpin folding. *Journal of Molecular Modeling*, 12(2), pp.197–204.

Shaka, A. J., Lee, C. J. & Pines, A., 1988. Iterative schemes for bilinear operators; application to spin decoupling. *Journal of Magnetic Resonance (1969)*, 77(2), pp.274–293.

Shnyrov, V. L., Villar, E., Zhadan, G. G., Sanchez-Ruiz, J. M., Quintas, A., Saraiva, M. J., Brito, R. M. M., 2000. Comparative calorimetric study of non-amyloidogenic and amyloidogenic variants of the homotetrameric protein transthyretin. *Biophysical Chemistry*, 88(1-3), pp.61–67.

Shoemaker, K. R., 1985. Nature of the Charged-Group Effect on the Stability of the C-Peptide Helix. *Proceedings of the National Academy of Sciences*, 82(8), pp.2349–2353.

Shoemaker, K. R., Fairman, R., Kim, P. S., York, E. J., Stewart, J. M., Baldwin, R. L., 1987. The C-peptide Helix from Ribonuclease A Considered as an Autonomous Folding Unit. *Cold Spring Harbor Symposia on Quantitative Biology*, 52(0), pp.391–398.

Shoemaker, K. R., Fairman, R., Schultz, D. A., Robertson, A. D., York, E. J., Stewart, J. M., Baldwin, R. L., 1990. Side-chain interactions in the C-peptide helix: Phe 8 ... His 12+. *Biopolymers*, 29(1), pp.1–11.

Shum, P., Kim, J.-M. & Thompson, D. H., 2001. Phototriggering of liposomal drug delivery systems. *Advanced Drug Delivery Reviews*, 53(3), pp.273–284.

Siddiqui, K. S. & Francisci, D., 2007. Analysis of unfolding-refolding patterns and stabilities of proteins by transverse urea gradient gel electrophoresis (TUG-GE). In V. Uversky & A. E. Permyakov, eds. Protein Structures. *Methods in Protein Structure and Stability Analysis*. pp. 147–158.

Sigrist, M. W., 1986. Laser generation of acoustic waves in liquids and gases. *Journal of Applied Physics*, 60(7), pp.R83–R121.

Sipe, J. D., Benson, M. D., Buxbaum, J. N., Ikeda, S., Merlini, G., Saraiva, M. J. M., Westermark, P., 2012. Amyloid fibril protein nomenclature: 2012 recommendations from the Nomenclature Committee of the International Society of Amyloidosis. *Amyloid*, 19(4), pp.167–170.

Small, J. R., Libertini, L. J. & Small, E. W., 1992. Analysis of photoacoustic waveforms using the nonlinear least squares method. *Biophysical Chemistry*, 42(1), pp.29–48.

Snow, C. D., Qiu, L., Du, D., Gai, F., Hagen, S. J., Pande, V. S., 2004. Trp zipper folding kinetics by molecular dynamics and temperature-jump spectroscopy. *Proceedings of the National Academy of Sciences of the United States of America*, 101(12), pp.4077–4082.

Soprano, D. R., Herbert, J., Soprano, K. J., Schon, E. A., Goodman, D. S., 1985. Demonstration of transthyretin mRNA in the brain and other extrahepatic tissues in the rat. *The Journal of Biological Chemistry*, 260(21), pp.11793–11798.

Stauder, A. J., Dickson, P. W., Aldred, A. R., Schreiber, G., Mendelsohn, F. A., Hudson, P., 1986. Synthesis of transthyretin (pre-albumin) mRNA in choroid plexus epithelial cells, localized by in situ hybridization in rat brain. *The Journal of Histochemistry and Cytochemistry*, 34(7), pp.949–952.

Suzukida, M., Le, H. P., Shahid, F., McPherson, R. A., Birnbaum, E. R., Darnall, D. W., 1983. Resonance energy transfer between cysteine-34 and tryptophan-214 in human serum albumin. Distance measurements as a function of pH. *Biochemistry*, 22(10), pp.2415–2420.

Tam, A., 1986. Applications of photoacoustic sensing techniques. *Reviews of Modern Physics*, 58(2), pp.381–431.

Tanokura, M., Tasumi, M. & Miyazawa, T., 1976. 1H nuclear magnetic resonance studies of histidine-containing di- and tripeptides. Estimation of the effects of charged groups on the pKa value of the imidazole ring. *Biopolymers*, 15(2), pp.393–401.

Thomas, P. J., Qu, B. H. & Pedersen, P. L., 1995. Defective protein folding as a basis of human disease. *Trends in Biochemical Sciences*, 20(11), pp.456–459.

Thompson, P. A., Muñoz, V., Jas, G. S., Henry, E. R., Eaton, W. A., Hofrichter, J., 2000. The Helix-Coil Kinetics of a Heteropeptide. *The Journal of Physical Chemistry B*, 104(2), pp.378–389.

Tu, L. & Deutsch, C., 1999. Evidence for dimerization of dimers in K+ channel assembly. *Biophysical Journal*, 76(4), pp.2004–2017.

Umrethia, M., Kett, V. L., Andrews, G. P., Malcolm, R. K., Woolfson, A. D., 2010. Selection of an analytical method for evaluating bovine serum albumin concentrations in pharmaceutical polymeric formulations. *Journal of Pharmaceutical and Biomedical Analysis*, 51(5), pp.1175–1179.

Van Eldik, R., Asano, T. & Le Noble, W. J., 1989. Activation and reaction volumes in solution. 2. *Chemical Reviews*, 89(3), pp.549–688.

Vatassery, G. T., Quach, H. T., Smith, W. E., Benson, B. A., Eckfeldt, J. H., 1991. A sensitive assay of transthyretin (prealbumin) in human cerebrospinal fluid in nanogram amounts by ELISA. *Clinica Chimica Acta; International Journal of Clinical Chemistry*, 197(1), pp.19–25.

Vendruscolo, M., Paci, E., Karplus, M., Dobson, C. M., 2003. Structures and relative free energies of partially folded states of proteins. *Proceedings of the National Academy of Sciences of the United States of America*, 100(25), pp.14817–14821.

Viappiani, C., Abbruzzetti, S., Small, J. R., Libertini, L. J., Small, E. W., 1998. An experimental methodology for measuring volume changes in proton transfer reactions in aqueous solutions. *Biophysical Chemistry*, 73(1-2), pp.13–22.

Viegas, A., Manso, J., Nobrega, F. L., Cabrita, E. J., 2011. Saturation-Transfer Difference (STD) NMR: A Simple and Fast Method for Ligand Screening and Characterization of Protein Binding. *Journal of Chemical Education*, 88(7), pp.990–994.

Wang, L. V. & Hu, S., 2012. Photoacoustic tomography: in vivo imaging from organelles to organs. *Science*, 335(6075), pp.1458–1462.

Wang, T., Du, D. & Gai, F., 2003. Helix–coil kinetics of two 14-residue peptides. *Chemical Physics Letters*, 370(5-6), pp.842–848.

Watters, A. L., Deka, P., Corrent, C., Callender, D., Varani, G., Sosnick, T., Baker, D., 2007. The highly cooperative folding of small naturally occurring proteins is likely the result of natural selection. *Cell*, 128(3), pp.613–624.

Wei, C.-C., Ho, M.-H., Wang, W.-H., Sun, Y.-C., 2005. Molecular dynamics simulation of folding of a short helical peptide with many charged residues. *The Journal of Physical Chemistry. B*, 109(42), pp.19980–19986.

Werner, J. H., Dyer, R. B., Fesinmeyer, R. M., Andersen, N. H., 2002. Dynamics of the Primary Processes of Protein Folding: Helix Nucleation. *The Journal of Physical Chemistry B*, 106(2), pp.487–494.

Westrick, J. A., Goodman, J. L. & Peters, K. S., 1987. A time-resolved photoacoustic calorimetry study of the dynamics of enthalpy and volume changes produced in the photodissociation of carbon monoxide from sperm whale carboxymyoglobin. *Biochemistry*, 26(25), pp.8313–8318.

Wetlaufer, D. B., 1973. Nucleation, rapid folding, and globular intrachain regions in proteins. *Proceedings of the National Academy of Sciences of the United States of America*, 70(3), pp.697–701.

Williams, S., Causgrove, T. P., Gilmanshin, R., Fang, K. S., Callender, R. H., Woodruff, W. H., Dyer, R. B., 1996. Fast events in protein folding: helix melting and formation in a small peptide. *Biochemistry*, 35(3), pp.691–697.

Wilting, J., Kremer, J. M. H., Ijzerman, A. P., Schulman, S. G., 1982. The kinetics of the binding of warfarin to human serum albumin as studied by stopped-flow spectrophotometry. *Biochimica et Biophysica Acta (BBA) - Protein Structure and Molecular Enzymology*, 706(1), pp.96–104.

Wiseman, R. L., Powers, E. T. & Kelly, J. W, 2005. Partitioning conformational intermediates between competing refolding and aggregation pathways: insights into transthyretin amyloid disease. *Biochemistry*, 44(50), pp.16612–16623.

Wishart, D. S., Bigam, C. G., Holm, A., Hodges, R. S., Sykes, B. D., 1995. 1H, 13C and 15N random coil NMR chemical shifts of the common amino acids. I. Investigations of nearest-neighbor effects. *Journal of Biomolecular NMR*, 5(1), pp.67–81.

Wishart, D. S., Sykes, B. D. & Richards, F. M., 1991. Relationship between nuclear magnetic resonance chemical shift and protein secondary structure. *Journal of Molecular Biology*, 222(2), pp.311–333.

Wishart, D. S., Sykes, B. D. & Richards, F. M., 1992. The chemical shift index: a fast and simple method for the assignment of protein secondary structure through NMR spectroscopy. *Biochemistry*, 31(6), pp.1647–1651.

Wlodawer, A. & Sjölin, L., 1983. Structure of ribonuclease A: results of joint neutron and X-ray refinement at 2.0 Å resolution. *Biochemistry*, 22(11), pp.2720–2728.

Wojtczak, A., Cody, V., Luft, J. R., Pangborn, W., 1996. Structures of human transthyretin complexed with thyroxine at 2.0 Å resolution and 3',5'-dinitro-N-acetyl-L-thyronine at 2.2 Å resolution. *Acta Crystallographica. Section D, Biological Crystallography*, 52, pp.758–765.

Wolynes, P., Onuchic, J. & Thirumalai, D., 1995. Navigating the folding routes. *Science*, 267(5204), pp.1619–1620.

Wu, X. & Wang, S., 2001. Helix Folding of an Alanine-Based Peptide in Explicit Water. *The Journal of Physical Chemistry B*, 105(11), pp.2227–2235.

Wüthrich, K., 1986. *NMR of proteins and nucleic acids*. volume 51. John Wiley & Sons, Inc.

Wyman, J. & Gill, S. J., 1990. *Binding and Linkage: Functional Chemistry of Biological Macromolecules*, University Science Books.

Xia, Y., Zhu, Q., Jun, K.-Y., Wang, J., Gao, X., 2010. Clean STD-NMR spectrum for improved detection of ligand-protein interactions at low concentration of protein. *Magnetic Resonance in Chemistry*, 48(12), pp.918–24.

Xu, M. & Wang, L. V., 2006. Photoacoustic imaging in biomedicine. *Review of Scientific Instruments*, 77(4), pp.041101-1–041101-22.

Xu, Y., Oyola, R. & Gai, F., 2003. Infrared study of the stability and folding kinetics of a 15-residue beta-hairpin. *Journal of the American Chemical Society*, 125(50), pp.15388–15394.

Yang, W. Y. & Gruebele, M., 2004. Detection-dependent kinetics as a probe of folding landscape microstructure. *Journal of the American Chemical Society*, 126(25), pp.7758–7759.

Zhang, Y. & Skolnick, J., 2004. Automated structure prediction of weakly homologous proteins on a genomic scale. *Proceedings of the National Academy of Sciences of the United States of America*, 101(20), pp.7594–7599.
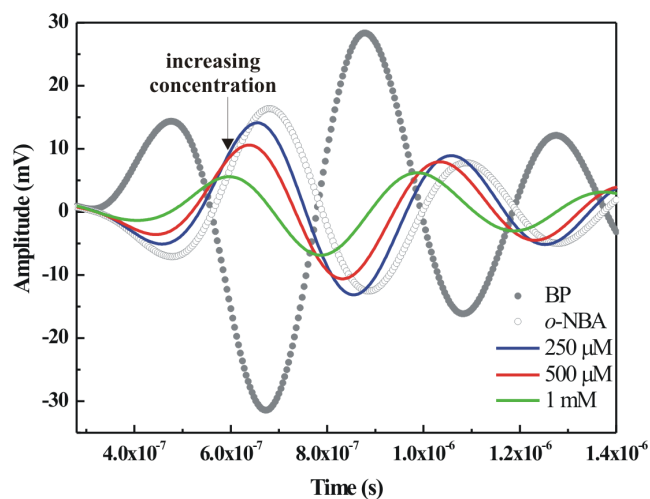
Appendices

Appendix A

## Photoacoustic waves of the amino acid model compounds

Figure A.1: Photoacoustic waves generated after laser irradiation, obtained using the two-temperature method. The signals from the BP and o-NBA are represented by closed circles and open circles, respectively. The signals of the amino acid model compound Ac-Glu-NH$_2$, at different concentrations and in an aqueous solution containing o-NBA, are shown as solid lines. The BP signal was measured at $T_{\beta \neq 0} = 6.0$°C, while the signals from o-NBA and Ac-Glu-NH$_2$ were measured at $T_{\beta=0} = 3.0$°C. The value of the prepulse pH used for solutions of Ac-Glu-NH$_2$ was 5.3.
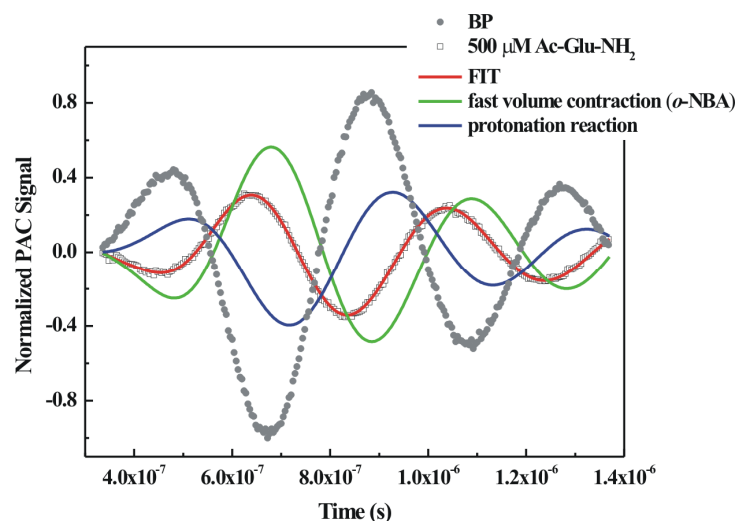
Figure A.2: The photoacoustic wave generated by laser irradiation of 500 μM Ac-Glu-NH$_2$ in an aqueous solution containing *o*-NBA, at prepulse pH around 5. The BP signal is represented by filled circles and the signal from the Ac-Glu-NH$_2$ is represented by open squares. The fit derived from the deconvolution is represented by the red line. The overall fit correspond to the summation of two component waves, which are associated with the fast contraction of *o*-NBA and the protonation reaction, represented by green and blue lines, respectively.
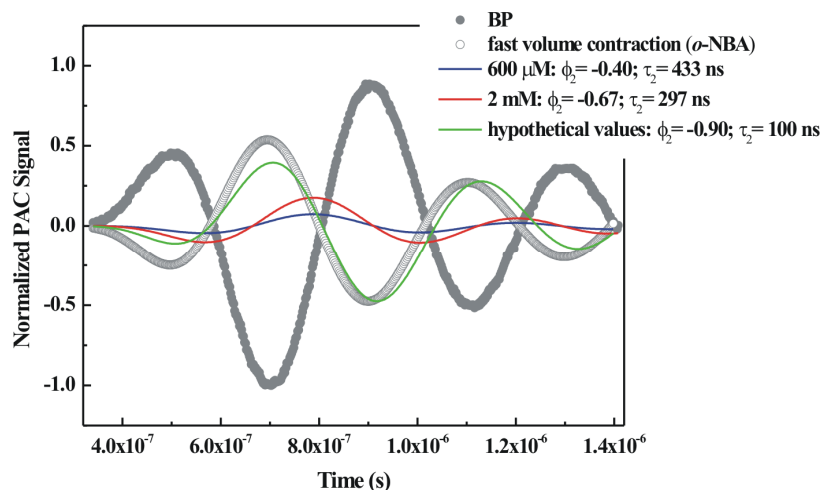
Figure A.3: Simulation of the component waves associated with the photolysis of *o*-NBA and the protonation of Ac-His-NHMe at different concentrations. The simulated waves for 600 μM and 2 mM were obtained from experimental data, while ϕ_2 = -0.9 and τ_2 = 100 ns are hypothetical values. The BP signal is represented by filled circles and the simulated wave for *o*-NBA derived from the results of the deconvolution is represented by open squares. The solid lines represent the simulated waves for the protonation of Ac-His-NHMe. The overall sample signal observed in TR-PAC (Ac-His-NHMe in the presence of *o*-NBA) correspond to the summation of both simulated component waves.

216
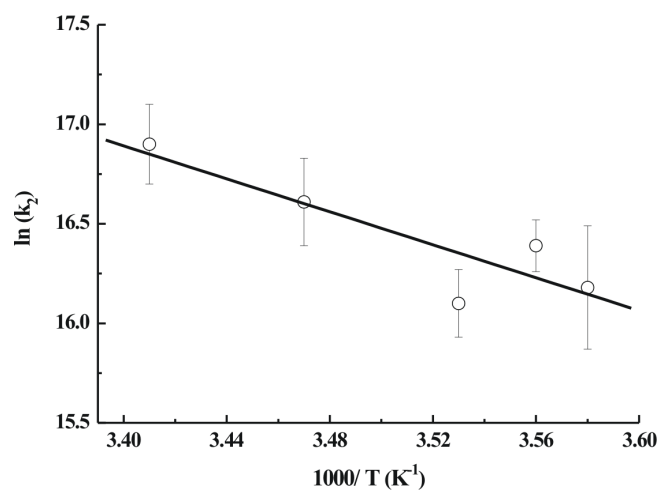
Figure A.4: Arrhenius plot for the protonation of Imidazole (1500 µM), at prepulse pH 7.8. The activation energy (E_a) and frequency factors for each reaction were derived from the linear relationship (solid line) of the rate constants as a function of 1/T (see Equation 4.6) and are reported in Table 4.3.

Appendix B

NMR structure of the RN80 peptide

Table B.1: ^{1}H-NMR assignments* of RN80 in 100 mM NaCl, at pH 5.6 and 3.0 °C.

	H^N	H^α	H^β	Others	
Ala1	8.15	3.91	1.12		
Glu2	8.36	4.08	1.76/1.66	$H^{\gamma2/\gamma3}$	2.01
Thr3	7.87	3.98	4.21	$H^{\gamma2}$	0.99
Ala4	8.37	3.84	1.15		
Ala5	8.15	3.92	1.07		
Ala6	7.79	3.85	1.18		
Lys7	7.97	3.69	1.50	$H^{\delta2/\delta3}$ $H^{\epsilon2/\epsilon3}$	1.34 2.64
Tyr8	7.86	4.05	2.82	$H^{\delta1/\delta2}$ $H^{\epsilon1/\epsilon2}$	6.77 6.37
Leu9	7.84	3.85	1.35	H^{γ} $H^{\delta1/\delta2}$	1.50 0.64
Arg10	7.68	3.84	1.97	$H^{\gamma2/\gamma3}$ $H^{\delta2/\delta3}$ H^{ϵ}	1.32/ 1.42 2.91 7.42
Ala11	7.65	3.89	0.99		
His12	7.69	4.26	2.52/2.97	$H^{\epsilon1/\epsilon2}$ $H^{\delta1/\delta2}$	8.08 6.74
Ala13	7.70	3.97	1.12		
-NH2	7.38/ 6.87				

* Chemical shift values are in ppm referenced from H_2O at 4.69 ppm.

Table B.2: ^{1}H-NMR assignments* of the RN80 in 100 mM NaCl, at pH 2.8 and 3.0 °C.

|	H^N	H$^\alpha$	H$^\beta$	Others	
Ala1	8.16	3.92	1.07		
Glu2	8.34	4.17	1.68/1.84	H$^{\gamma2/\gamma3}$	2.21
Thr3	7.78	3.98	4.14	H$^{\gamma2}$	0.98
Ala4	8.33	3.86	1.14		
Ala5	8.12	3.90	1.12		
Ala6	7.82	3.98	1.13		
Lys7	7.95	3.71	1.48	H$^{\delta2/\delta3}$ H$^{\zeta}$	1.33 7.30
Tyr8	7.84	4.09	2.75/ 2.83	H$^{\delta1/\delta2}$ H$^{\varepsilon1/\varepsilon2}$	6.79 6.39
Leu9	7.85	3.87	1.34	H$^{\gamma}$ H$^{\delta1/\delta2}$	1.46 0.62
Arg10	7.76	3.85	1.55	H$^{\gamma2/\gamma3}$ H$^{\delta2/\delta3}$ H$^{\varepsilon}$	1.34/ 1.43 2.92 7.00
Ala11	7.70	3.89	0.99		
His12	7.81	4.28	2.62/2.99	H$^{\varepsilon1/\varepsilon2}$ H$^{\delta1/\delta2}$	8.15 6.81
Ala13	7.80	3.96	1.11		
-NH2	7.41/ 6.87				

*Chemical shift values are in ppm referenced from H_2O at 4.69 ppm.

Table B.3: ^{1}H-NMR assignments* of RN80 in 100 mM NaCl, at pH 8.7 and 3.0 °C.

|	H^N	H$^\alpha$	H$^\beta$	Others	
Ala1	8.32	3.96	1.07		
Glu2	8.40	4.19	1.65/1.76	H$^{\gamma2/\gamma3}$	2.00
Thr3	7.92	4.41	4.16	H$^{\gamma2}$	0.99
Ala4	8.45	4.32	1.14		
Ala5	8.17	3.91	1.13		
Ala6	7.85	4.35	1.15		
Lys7	7.95	3.73	1.42	H$^{\delta2/\delta3}$	1.35
Tyr8	7.79	4.11	2.78	H$^{\delta1/\delta2}$ H$^{\varepsilon1/\varepsilon2}$	6.80 6.42
Leu9	7.91	4.30	1.32	H$^{\gamma}$ H$^{\delta1/\delta2}$	1.45 0.62
Arg10	7.83	4.49	1.51	H$^{\gamma2/\gamma3}$ H$^{\delta2/\delta3}$ H$^{\varepsilon1}$	1.33/ 1.39 2.92 7.32
Ala11	7.78	4.39	0.99		
His12	7.62	4.60	2.56/2.89	H$^{\varepsilon1/\varepsilon2}$ H$^{\delta1/\delta2}$	7.73 6.65
Ala13	7.77	3.37	1.10		
-NH2	7.29/ 6.87				

* Chemical shift values are in ppm referenced from H_2O at 4.69 ppm.

Table B.4: Three-bond $^3J_{HNH\alpha}$ coupling constants for RN80 in 100 mM NaCl, in different pH conditions and 3.0 °C.

| residue	$^3J_{HNH\alpha}$ / Hz		
	pH 3	pH 5	pH 8
Ala1			7.15
Glu2	7.63	6.10	8.12
Thr3	7.28	6.22	8.17
Ala4	5.11	5.19	7.96
Ala5	6.82	7.02	7.95
Ala6	5.02	4.46	7.27
Lys7	4.99	4.94	8.00
Tyr8	7.12	5.11	7.85
Leu9	8.31	5.52	7.88
Arg10	8.57	5.92	7.09
Ala11	8.95	5.85	8.02
His12	5.81	4.82	8.31
Ala13		6.94	7.41
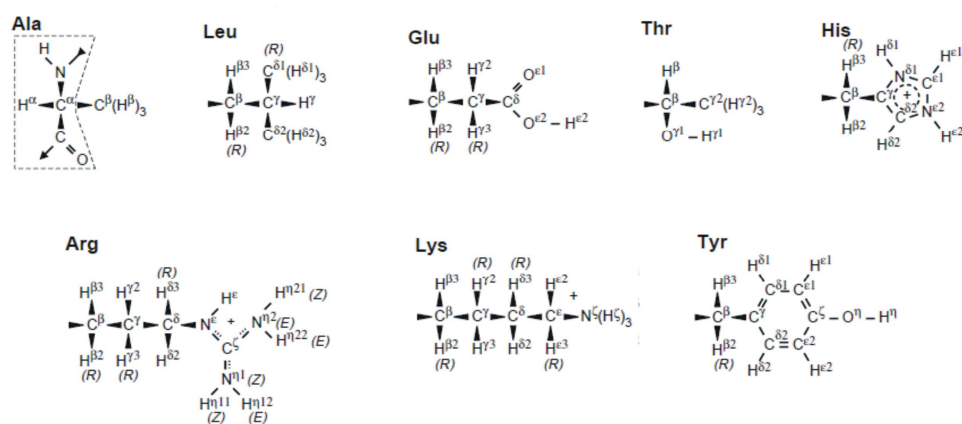
Figure B.1: Recommended atom identifiers following the 1969 IUPAC-IUB guidelines for the eight amino acids present in the sequence of RN80. Adapted from Markley et al. (1998).
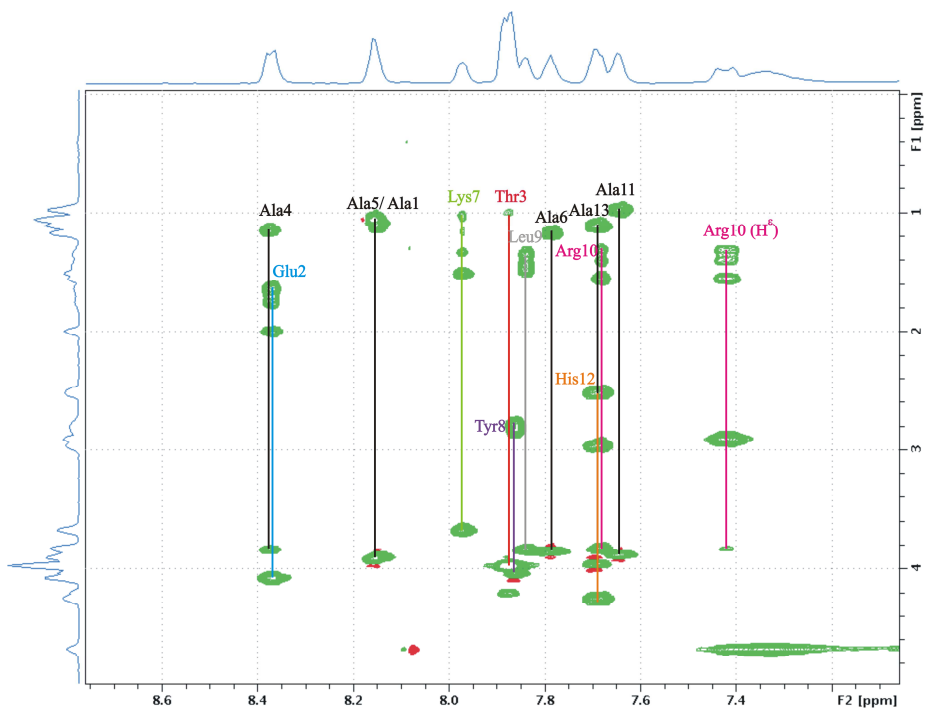
Figure B.2: NH-aliphatic region of the TOCSY spectrum of 3mM RN80 in 90% H_2O / 10% D_2O containing 100 mM NaCl, at pH 5.6 and 3.0°C. Individual spin systems are identified by the standard three-letter amino acid code and the sequential numbers in the amino acid sequence.
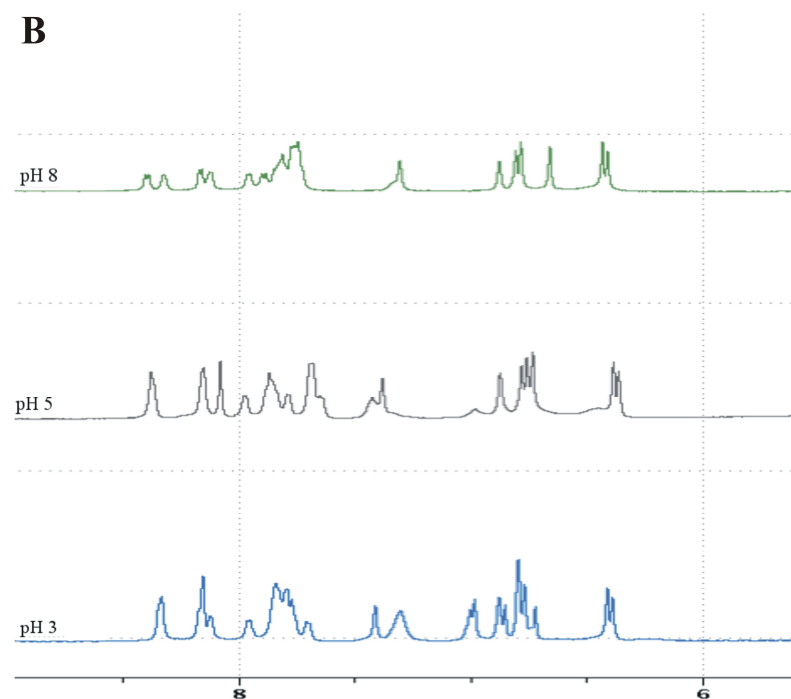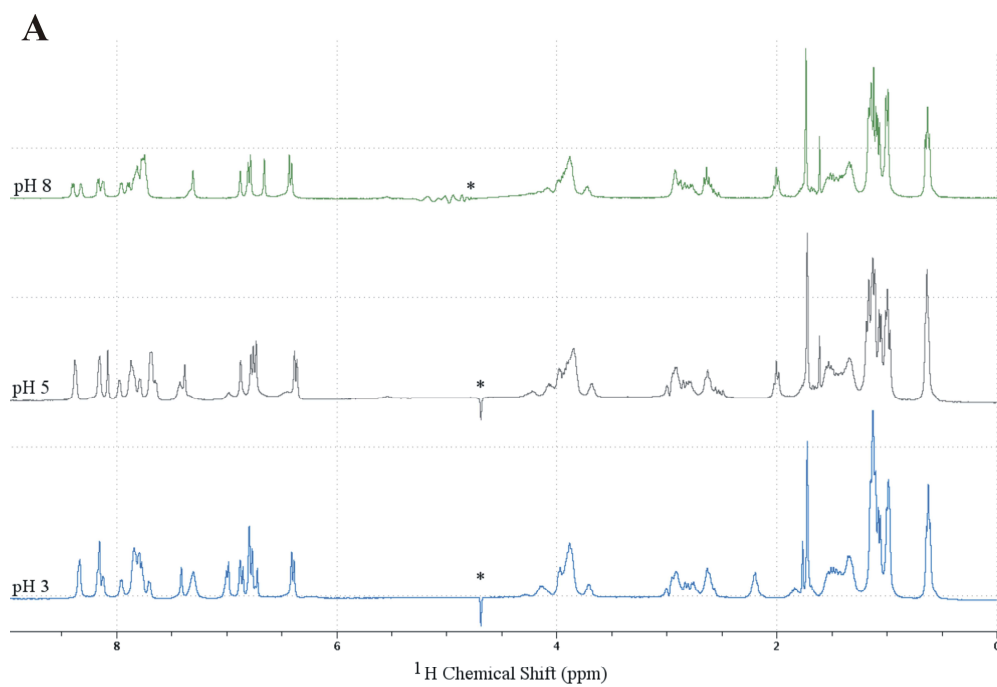
Figure B.3: (A) ^{1}H-NMR spectra of 3 mM RN80 in 90% H_2O/ 10% D_2O containing 100 mM NaCl, at different pHs and 3.0 °C. All spectra were referenced to the solvent signal (marked with an *). (B) Expansion of the ^{1}H-NMR spectra showing the aromatic and amide regions.

Appendix C

Transthyretin refolding mechanism

Although homotetrameric proteins can assemble by several pathways, it is frequently observed the MDT mechanism in which two monomers associate to form a homodimer, and then two homodimers associate to form a homotetramer (Powers & Powers 2003).

Several protein refolding reactions are initiated from the unfolded and monomeric state of the protein (often by dilution from high concentrations of denaturants such as urea, guanidinium hydrochloride or guanidinium thiocyanide). Here, TTR refolding kinetics curves were constructed monitoring the variation in intrinsic tryptophan fluorescence at 380 nm, upon protein dilution into 20 mM sodium phosphate buffer, 150 mM sodium chloride, pH 7.0, to the desired urea and protein concentrations, at 25ºC. It is worth to note that no kinetically significant, unimolecular folding or reorganization steps, such as proline isomerization (Bodenreider et al., 2002), have been observed. Moreover, more complex folding pathways involving more than one intermediate such as dimers and trimers (MDRT mechanism) is also minimized at low protein concentrations (Jaenicke 1987) (Powers & Powers 2003).

The simplest best-fitting and more likely kinetic model for the refolding and assembly of the TTR tetramer was found to be a simple 2-step mechanism:

$$2M_{Denatured} \xrightarrow{k_1} D \qquad\qquad (C.1)$$

$$2D \xrightarrow{k_2} T_{Native} \qquad\qquad (C.2)$$

where M, D and T correspond to monomer, dimer and tetramer, respectively. The system of differential equations associated with this mechanism is:

$$\frac{d[M]}{dt} = -2k_1 [M]^2 \tag{C.3}$$

$$\frac{d[D]}{dt} = k_1 [M]^2 - 2k_2 [D]^2 \tag{C.4}$$

$$\frac{d[T]}{dt} = k_2 [D]^2 \tag{C.5}$$

where the brackets indicate the molar concentration of the enclosed species and t is the time in seconds. Conservation of mass dictates that $C = 4[T] + 2[D] + [M]$, where C is the total concentration of protein subunits. Since we are concerned with homotetramer assembly starting from a pool of unfolded monomers, the initial conditions are $[M]_{t=0} = C$ and $[D]_{t=0} = [T]_{t=0} = 0$. Assuming these considerations, the differential equations were solved and simplified using the program *Mathematica 4*.2 (Wolfram Research, Inc., USA) to obtain the concentrations of M, D and T over time.

The concentration of M over time can be determined solving the differential Equation C.3 and assuming that $[M]_{t=0} = C$:

$$\int_C^{[M]} \frac{d[M]}{[M]^2} = -2k_1 \int_0^t dt \tag{C.6}$$

$$\int_C^{[M]} -\frac{1}{[M]^2} d[M] = 2k_1 t \tag{C.7}$$

$$\left[\frac{1}{[M]} \right]_C^M = 2k_1 t \tag{C.8}$$

$$\frac{1}{[M]} - \frac{1}{C} = 2k_1 t \tag{C.9}$$

$$[M] = C \times \left(\frac{1}{1 + 2Ck_1 t} \right) \tag{C.10}$$

Considering that $[M]_{t=0} = C$ and $[D]_{t=0} = 0$, and using Equation C.10, the concentration of D over time was determined by solving and simplifying the differential Equation C.4:

$$\frac{d[D]}{dt} = k_1\left(C \times \left(\frac{1}{1+2Ck_1t}\right)\right)^2 - 2k_2[D]^2 \qquad (C.11)$$

$$[D] = \frac{C \times \left(\dfrac{1}{1+2Ck_1t}\right) \times \left(1 - \left(\dfrac{1}{1+2Ck_1t}\right)^{\sqrt{1+2\frac{k_2}{k_1}}}\right)}{\left(1 + \sqrt{1+2\dfrac{k_2}{k_1}}\right) \times \left(\dfrac{1}{1+2Ck_1t}\right)^{\sqrt{1+2\frac{k_2}{k_1}}} - 1 + \sqrt{1+2\dfrac{k_2}{k_1}}} \qquad (C.12)$$

Using the conservation of mass assumption and Equation C.5, the value of $[T]$ over time can be determined through the following equations:

$$[T] = \frac{C - [M] - 2[D]}{4} \qquad (C.13)$$

$$[T] = \frac{1}{4}\left(C - C \times \left(\frac{1}{1+2Ck_1t}\right) - \frac{2 \times C \times \left(\dfrac{1}{1+2Ck_1t}\right) \times \left(1 - \left(\dfrac{1}{1+2Ck_1t}\right)^{\sqrt{1+2\frac{k_2}{k_1}}}\right)}{\left(1 + \sqrt{1+2\dfrac{k_2}{k_1}}\right) \times \left(\dfrac{1}{1+2Ck_1t}\right)^{\sqrt{1+2\frac{k_2}{k_1}}} - 1 + \sqrt{1+2\dfrac{k_2}{k_1}}}\right) \qquad (C.14)$$

The time course of fluorescence change was described by the equation:

$$I_f(t) = f_M[M] + f_D[D] + f_T[T] \qquad (C.15)$$

where $I_f(t)$ is the observed fluorescence intensity at time t, and f_T, f_D and f_M are the specific fluorescence intensities of T, D and M, respectively. The concentration of T, D and M ($[T]$, $[D]$, $[M]$) were obtained from equations C.14, C.12 and C.10, respectively. The rate constants k_1 and k_2 were obtained by fitting Equation C.15 to the data, using nonlinear least-squares analysis, and the software package *OriginPro7* (OriginLab Corporation,

USA). The final values of k_1 and k_2 were refined until no further significant improvement to the fit was observed by evaluating the distribution of the residuals.